PREFACE

Progress in astrophysics and astronomy in the last few decades has been phenolmenal and there is therefore little need for justification when a new international journal makes its debut as a rapid means of dissemination of scientific results. This heartening trend arises from major advances in both theory and observation, especially with the revolutionary technological achievements of recent years that have opened up avenues of research over the entire electromagnetic spectrum. In keeping with the general concept of the international character of astronomy, activity in almost all these fields has become a worldwide feature with numerous contributions coming in from areas of the globe that earlier had provided less effective participation. It is our hope that the new journal will provide the additional facility needed for quick publication of the results of research from members of an expanding fraternity. It is also indicative of the measure of optimism we have in the future growth of astronomical endeavour on the international scale.

We invite accounts of original contributions to any area of astronomy and astrophysics, observational and theoretical. There will be no levy of page charges. All papers are refereed and will appear with a minimum publication time-lag after acceptance. It is our wish to aim at a high quality of scientific content and there by contribute to the promotion of astronomical research.

M. K. V. BAPPU

J. Astrophys. Astr. (1980) **1,** 3–16

Comoving Frame Calculations of Spectral Lines formed in Rapidly Expanding Media with the Partial Frequency Redistribution Function for Zero Natural Line Width

A. Peraiah *Indian Institute of Astrophysics, Bangalore* 560034

Received 1980 February 8; accepted 1980 April 7

Abstract. Comoving frame calculations have been used to compute the spectral lines formed in rapidly expanding spherical media. We have employed the angle-averaged partial frequency redistribution function R_I with a two-level atom model in non-LTE atom approximation. A linear velocity law increasing with radius has been employed with maximum velocity at τ=0 being set equal to 30 mean thermal units. It is found that one obtains almost symmetric emission line profiles at large velocities similar to those found in quasars.

Keywords:. radiative transfer—partial redistribution function—comoving frame—spectral lines

1. Introduction

Many stars (such as early type supergiants, Wolf-Rayet stars etc.), quasars and nuclei of Seyfert galaxies show evidence of mass motion in their outer layers. Calculation of spectral lines formed in such media is extremely complicated because of (i) photon redistribution in the line which is again complicated (ii) by the radial mass motion in the medium.

One must calculate accurately the effect of the latter on the former. The calculations become quite involved simply because photons can be redistributed from any given point to any other point in the interval ν_0 $(1-V_{\max}/c)$ to ν_0 $(1+V_{\max}/c)$ where ν_0 is the central frequency of the line and $V_{\max}$ is the maximum gas velocity. In the atmospheres of many OB type stars, the gas velocities may be as large as 2000-3000 km s^{-1}, which would be about 100 times the mean thermal unit. If one intends to simulate profiles formed in such media, one has to consider the bandwidth as large as 200 mean thermal units. Recently Hummer and Kunasz (1974), Peraiah (1978), Peraiah and Wehrse (1978) and Wehrse and Peraiah (1979) attempted to calculate lines in the rest frame of the star. In both cases, the maximum gas velocity employed was only 2 mean thermal units. The reason is that in the rest frame, the frequency-angle mesh should extend from $(-x-V_{max})$ to $(x+V_{max})$ where $x=(\nu-\nu_0)/\Delta_s$, Δ_s being some standard frequency interval. As the velocity V_{max} increases, this interval also increases and so does the number of frequency-angle points and the numerical operations. The excessive numerical operations introduce round-off errors and 'eat' into the real solution. Therefore, one has to restrict to small gas velocities.

However, in a comoving frame, the relative velocities do not exist and therefore we need not consider a large frequency-angle mesh. Mihalas, Kunasz and Hummer (1975, 1976) have solved the transfer equation in the comoving frame with both complete and partial frequency redistribution. However, their calculations are limited to show a comparison between the complete and partial redistribution.

In this paper, we present calculations of line formation in the comoving frame with partial redistribution in the framework of discrete space theory of radiative transfer. This is an extension of the calculations of lines in the comoving frame with complete redistribution (see Peraiah 1980) to partial frequency redistribution.

2. Solution of line transfer in the comoving frame with partial redistribution

We shall consider the radiative transfer equation in the comoving frame with a two-level atom approximation in non-LTE. The comoving terms are (see Mihalas, Kunasz and Hummer 1975)

$$\left\{ (1-\mu^2) \frac{V(r)}{r} + \mu^2 \frac{dV(r)}{dr} \right\} \frac{\partial I(x, \mu, r)}{\partial x}, \tag{1}$$

where $I(x, \mu, r)$ is the specific intensity of the ray with frequency $x=(\nu-\nu_0)/\Delta_s$, (Δ_s being some standard frequency interval and ν_0 is the central frequency of the line) making an angle $\cos^{-1}\mu$ with the radius vector at the radial point r. $V(r)$ is the radial velocity of the gas at r in mean thermal units. The radiative transfer equation in the comoving frame is written after including the terms in equation (1) (see Mihalas, Kunasz and Hummer 1975, 1976)

$$\begin{aligned} \mu \frac{\partial I(x, \mu, r)}{\partial r} + \frac{1-\mu^2}{r} \frac{\partial I(x, \mu, r)}{\partial \mu} &= K(x, r)\, S_L(x, r) \\ &+ K_c(r)\, S_c(r) - [K(x, r) + K_c(r)]\, I(x, \mu, r) \\ &+ \left\{ (1-\mu^2) \frac{V(r)}{r} + \mu^2 \frac{dV(r)}{dr} \right\} \frac{\partial I(x, \mu, r)}{\partial x}, \end{aligned} \tag{2}$$

And for the oppositely directed beam,

$$-\mu \frac{\partial I(x, -\mu, r)}{\partial r} - \frac{1-\mu^2}{r} \frac{\partial I(x, -\mu, r)}{\partial \mu} = K(x, r)\, S_L(x, r)$$

$$+ K_c(r)\, S_c(r) - [K(x, r) + K_c(r)]\, I(x, -\mu, r)$$

$$+ \left\{ (1-\mu^2)\frac{V(r)}{r} + \mu^2 \frac{dV(r)}{dr} \right\} \frac{\partial I(x, -\mu, r)}{\partial x} \ . \tag{3}$$

Here, K_L (x, r) and K_c (r) are the absorption coefficients per unit frequency interval in the line and continuum respectively. The quantities S_L (x, r) and S_C (r) are the line and continuum source functions respectively and are given by

$$S_L(x, r) = \frac{(1-\epsilon)}{\phi(x)} \int_{-\infty}^{+\infty} dx' \int_{-1}^{+1} R(x; x')\, I(x', \mu')\, d\mu' + \epsilon\, B(r), \tag{4}$$

and $$S_c(r) = \rho(r)\, B(r), \tag{5}$$

where $B(r)$ is the Planck function and $\rho(r)$ is model-dependent and is treated as an arbitrary function in this work. K_L (x,r) is given by

$$K_L(x, r) = \phi(x) K_L(r), \tag{6}$$

and the profile function $\phi(x)$ is given by

$$\phi(x) = \int_{-\infty}^{+\infty} R(x, x')\, dx',$$

where $R(x, x')$ is the angle-averaged redistribution function (see Hummer 1962) given by

$$R_{I\text{-}A}(x, x') = \tfrac{1}{2}\, \mathrm{erfc}\,(|\bar{x}|), \tag{7}$$

where $$\mathrm{erfc}\,(|\bar{x}|) = \frac{1}{\sqrt{\pi}} \int_{|\bar{x}|}^{\infty} exp\,(-t^2)\, dt, \tag{8}$$

$\bar{x}$ being the maximum of $|x|$ and $|x'|$ The line profile is normalised so that,

$$\int_{-\infty}^{+\infty} \phi(x)\, dx = 1. \tag{9}$$

The quantity ϵ is the probability per scatter that a photon is lost by collisional de-excitation.

The integration of equations (2) and (3) is performed as described in Grant and Peraiah (1972) and Peraiah (1978, 1980). After discretisation equations (2) and (3) are written as,

$$\mathbf{M}\ [\mathbf{U}^{+}_{n+1} - \mathbf{U}^{-}_{n}] + \rho_c\, [\boldsymbol{\Lambda}^{+}\, \mathbf{U}^{+}_{n+1/2} + \boldsymbol{\Lambda}^{-}\, \mathbf{U}^{-}_{n+1/2}] + \tau_{n+1/2}\, \boldsymbol{\Phi}_{n+1/2}\, \mathbf{U}^{+}_{n+1/2}$$
$$= \tau_{n+1/2}\, \mathbf{S}_{n+1/2} + \tfrac{1}{2}(1-\epsilon)\, \tau_{n+1/2}\, \mathbf{R}_{n+1/2}\, \mathbf{W}_{n+1/2}\, [\mathbf{U}^{+}_{n+1/2} + \mathbf{U}^{-}_{n+1/2}]$$
$$+\ \mathbf{M}_1\ \mathbf{d}\ \mathbf{U}^{+}_{n+1/2}, \tag{10}$$

and $$\mathbf{M}\, [\mathbf{U}^{-}_{n} - \mathbf{U}^{-}_{n+1}] - \rho_c\, [\boldsymbol{\Lambda}^{+}\, \mathbf{U}^{-}_{n+1/2} + \boldsymbol{\Lambda}^{-}\, \mathbf{U}^{+}_{n+1/2}] + \tau_{n+1/2}\, \boldsymbol{\Phi}_{n+1/2}\, \mathbf{U}^{+}_{n+1/2}$$
$$= \tau_{n+1/2}\, \mathbf{S}_{n+1/2} + \tfrac{1}{2}\,(1-\epsilon)\, \tau_{n+1/2}\, \mathbf{R}_{n+1/2}\, \mathbf{W}_{n+1/2}\, [\mathbf{U}^{+}_{n+1/2} + \mathbf{U}^{-}_{n+1/2}]$$
$$+\ \mathbf{M}_1\ \mathbf{d}\ \mathbf{U}^{-}_{n+1/2} \tag{11}$$

Where $$\mathbf{M} = \begin{bmatrix} \mathbf{M}_m & & & \\ & \mathbf{M}_m & & \\ & & \ddots & \\ & & & \mathbf{M}_m \end{bmatrix},\ \mathbf{M}_m = [\mu_j\, \delta_{jl}], \tag{12}$$

μs being the angle quadrature points.

$$\boldsymbol{\Lambda}^{\pm} = \begin{bmatrix} \boldsymbol{\Lambda}^{\pm}_m & & & \\ & \boldsymbol{\Lambda}^{\pm}_m & & \\ & & \ddots & \\ & & & \boldsymbol{\Lambda}^{\pm}_m \end{bmatrix}, \tag{13}$$

$A^{\pm}_{m}$ are the curvature matrices (see Peraiah and Grant 1973). And,

$$\mathbf{U}^{\pm}_{n} = [\mathbf{U}^{\pm}_{1,n}\ ,\ \mathbf{U}^{\pm}_{2,n}\ ,\ \mathbf{U}^{\pm}_{3,n}, \ldots, \mathbf{U}^{\pm}_{i,n}, \ldots, \mathbf{U}^{\pm}_{I,n}]^{T}, \tag{14}$$

$$\mathbf{U}^{+}_{i,n} = 4\pi r^2{}_n \begin{bmatrix} I(\tau_n, +\mu_1, x_i) \\ I(\tau_n, +\mu_2, x_i) \\ \vdots \\ I(\tau_n, +\mu_J, x_i) \end{bmatrix}, \tag{15}$$

r_n being the radius of the nth shell and J and I are the total number of angles and frequency points. The subscript n+½ represents the average of the subscripted parameter over the shell bounded by the radii r_n and $r_{n+1}$is defined as $\tau_{n+1/2}$ is defined as

$$\tau_{n+1/2} = K_L\,(r_{n+1/2})\,\Delta\, r, \tag{16}$$

$$\Delta r \quad = (r_{n+1} - r_n). \tag{17}$$

The quantity $\Phi_{n+1/2}$ is given by

$$\Phi_{n+1/2} = [\Phi_{kk'}]_{n+1/2} = (\beta + \phi_k)_{n+1/2}\,\delta_{kk'}\,, \tag{18}$$

$\beta = K_C \,/\, K_L$ and

$$k = j + (i-1)J;\; 1 \leqslant k \leqslant K = IJ, \tag{19}$$

$$\mathbf{S}_{n+1/2} = (\rho\beta + \epsilon\phi_k)_{n+1/2}\, B'_{n+1/2}, \tag{20}$$

$$\phi_k = \phi\,(x_i,\, \mu_j),$$

$$B'_{n+1/2} = 4\pi r^2_{n+1/2}\, B(r). \tag{21}$$

The quantity $R_{n+1/2}$ is the redistribution function. As we are considering the commoving frame, R^{++} = R^{--}= R^{-+} = R^{+-} = R, which corresponds to the redistribution function in static medium, $W_{n+1/2}$ is given by

$$W_k = a_i\, c_j,\; a_i = \frac{A_i\, R_{kk'}}{\Sigma\, R_{kk'}\, A_i\, C_j}\,, \tag{22}$$

where *A's* and *C*'s are the weights of the frequency and angle quadratures respectively. The quantity ρ_c is the curvature factor given by

$$\rho_c = \Delta r / \bar{r}, \tag{23}$$

where $\bar{r}$ is the mean radius of the given shell. The last two terms in (10) and (11) represent the comoving terms given in (1) and

$$\mathbf{M}_1 = \mathbf{M}^1\,\Delta V_{n+1/2} + \mathbf{M}^2\,\rho_c\, V_{n+1/2}, \tag{24}$$

$$\left.\begin{aligned} \mathbf{M}^1 &= \begin{bmatrix} \mathbf{M}^1_m & & & \\ & \mathbf{M}^1_m & & \\ & & \ddots & \\ & & & \mathbf{M}^1_m \end{bmatrix},\; \mathbf{M}^1_m = [\mu_j^2\,\delta_{jl}] \\ \mathbf{M}^2 &= \begin{bmatrix} \mathbf{M}^2_m & & & \\ & \mathbf{M}^2_m & & \\ & & \ddots & \\ & & & \mathbf{M}^2_m \end{bmatrix},\; \mathbf{M}^2_m = [1-\mu_j^2]\,\delta_{jl} \end{aligned}\right\}\; j,\, l = 1, \ldots, J. \tag{25}$$

$V_{n+1/2}$ is the average velocity in the shell bounded by radii r_n and r_{n+1} and $\Delta V_{n+1/2}$ is given by

$$\Delta V_{n+1/2} = V_{n+1} - V_n. \tag{26}$$

The matrix **d** represents the frequency derivative and its form is determined from the condition of flux conservation in a purely scattering medium (see Peraiah 1980). This is given by

$$\mathbf{d} = \begin{bmatrix} -d_1 & d_1 & & & & \\ -d_2 & 0 & d_2 & & & \\ & -d_3 & 0 & d_3 & & \\ & & \cdot & \cdot & \cdot & \\ & & & \cdot & \cdot & d_{I-1} \\ & & & & -d_I & d_I \end{bmatrix} \tag{27}$$

Where $d_i = (X_{i+1} - X_{i-1})^{-1}$ for $i = 2, 3, \ldots I-1$ and we put

$$d_1 = d_I = 0. \tag{28}$$

By applying the diamond scheme to replace the average intensities $u^{\pm}_{n+1/2}$ in equations (10) and (11) and arranging the resulting equations in the form of the 'interaction principle ' we obtain the reflection and transmission operators(see Appendix). Calculation of the diffuse radiation field in the line in the comoving frame can be done as described in Grant and Hunt (1969).

3. Results and discussion

The calculations a comoving frame can be easily made as the redistribution function does not change when the gas moves unlike that in the rest frame wherein the change in the redistribution function should be taken into account at every radial point in the moving gas (see Peraiah 1978). However, the radiation field obtained in the comoving frame should be tanslated into either (i) the rest frame of the star which describes the solution of radiative transfer in spherical symmetry or (ii) onto the frame of reference of the observer at infinity. In this paper, we have performed the latter type of calculation as these may be useful for direct comparison with observations. In Fig. 1, we have described how the radiation field in the comoving frame has been translated into the frame of reference of the observer at the earth. The procedure is briefly as follows: We solve the radiative transfer equation (see Peraiah 1980) in the comoving frame (see equations (2) and (3)) by assuming a velocity distribution given by

$$V(r) = V_A + \frac{V_B - V_A}{B - A}\,(r - A), \tag{29}$$

where $V(r)$ is the velocity of the gas at the radial point r and V_A and V_B and the velocities at the inner and outer radii A and B of the atmosphere respectively. All velocities are measured in mean thermal unit and we have considered the density varying as

$$\rho(r) \sim 1/[r^2\,V(r)], \tag{30}$$

so that the optical depth varies as $1/r$. When the solution of transfer is obtained, we can calculate the frequency and angle-independent source functions $S(r)$ at every radial point by the relation

$$S_n = \sum_{i=1}^{I} A_i \sum_{j=1}^{J} S(x_i, \mu_j, \tau_n)\, C_j. \tag{31}$$

The optical depth is calculated along the parallel rays as shown in Fig. 1 and not along the radial direction in the atmosphere. With the help of equations (29), (30) and (31) we can calculate the fluxes received at infinity. We have selected

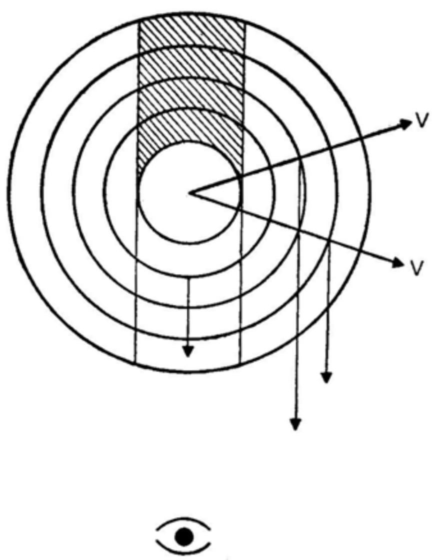

Figure 1. Diagram to show how fluxes are calculated at infinity.

a few representative values of the parameters ϵ, β, V_A, V_B , *B/A*. The total optical depth has been taken to be $\approx 10^3$ at the line centre. For boundary conditions see Peraiah (1978, 1980).

The results are presented in Figs 2 to 9. In Figs 2–5, we give the frequency and angle-integrated source functions for the parameters shown in the figures. In Fig. 2, the source functions are given for $B/A = 3$, and $\epsilon=\beta = 0$ and $V_B = 0,10$ and 30. We notice that the source function is reduced by nearly 4 orders of magnitude at the boundary in the static case, whereas in the case of moving gas it is further reduced to 5 orders of magnitude.

Similar effects have been found when the ratio of outer to inner radii *B/A* is increased to 9. In this case the source function is reduced by 7 orders of magnitude when the velocity reaches 30 at the surface (see Fig. 3). The radiation field is diluted over an extended medium and this effect is further accentuated when the gases in the atmosphere move radially outwards. In Figs 4 and 5, we present the frequency and angle-independent source functions corresponding to the parameters $\epsilon = 10^{-3}$, $\beta = 0$ and $B/A = 3$ and 9. The same effects are found in general as for a purely scattering medium ($\epsilon = 0$, $\beta = 0$). However, the sharp rise in the source function at τ_{max} is due to the nature of the boundary condition we have given *i.e.* no

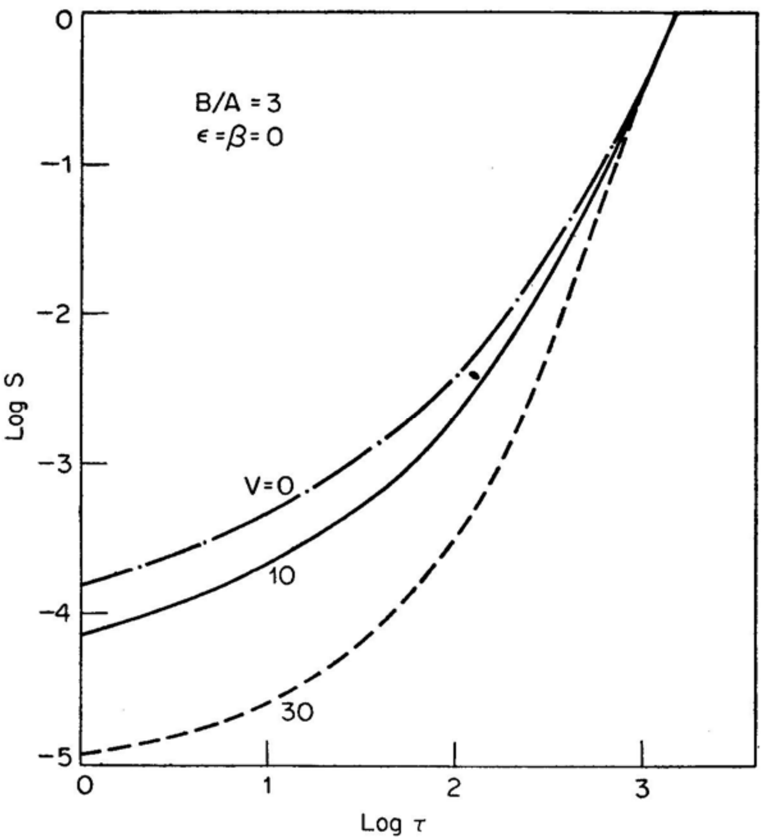

Figure 2. Frequency and. angle independant source functions for *B/A=3*, ϵ=ß=O.

radiation is incident at $\tau = \tau_{max}$. In the vicinity of τ_{max}, in the atmosphere, the source function reaches a maximum as there is line emission ($\epsilon = 10^{-3}$). We present the flux profiles received by the observer at the earth in Figs 6–9. We have plotted F_x ($=F(x)/F(x_{max})$) versus Q ($= x/x_{max}$). The profiles given in Figs 6 and 7 correspond to the source functions given in Figs 2 and 3 and the profiles given in (8) and (9) correspond to the source functions given in Figs 4 and 5. We notice absorption lines in the case of purely scattering medium as seen from Figs 6 and 9. When the velocities increase their line centres are shifted towards the blue side (see Figs 6 and 7). In Figs 8 and 9 the flux profiles for line emission are presented. In a static medium, we obtain an emission line with central absorption. However, when motion is introduced, we notice an emission line with reduced widths. These profiles are quite similar to those observed in some of the quasars, see for example Baldwin (1975) and Baldwin a n d Netzer (1978).

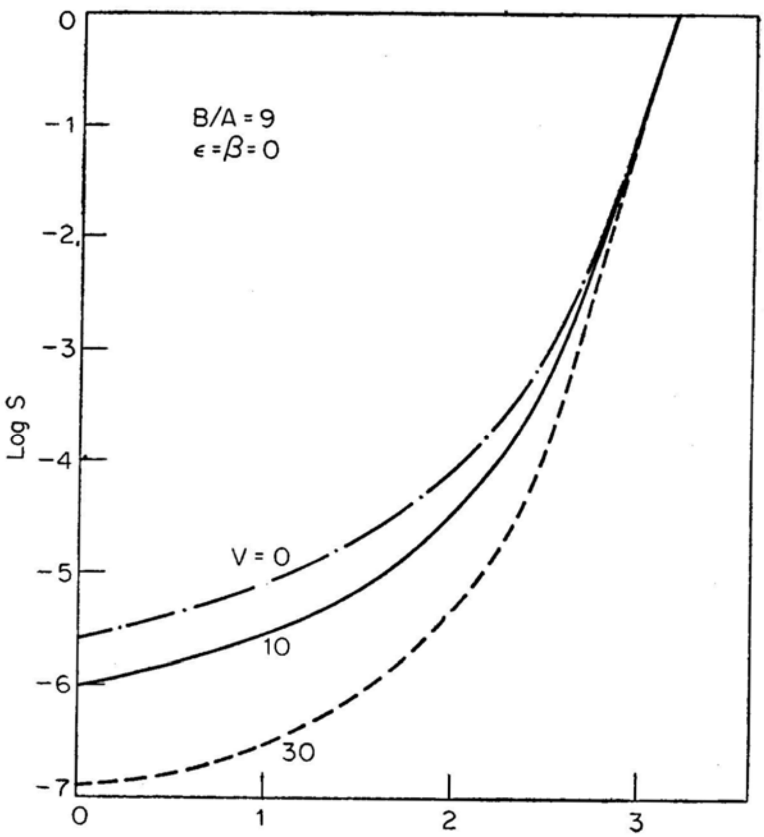

Figure 3. Same as in Fig. 2 with B/A=9.

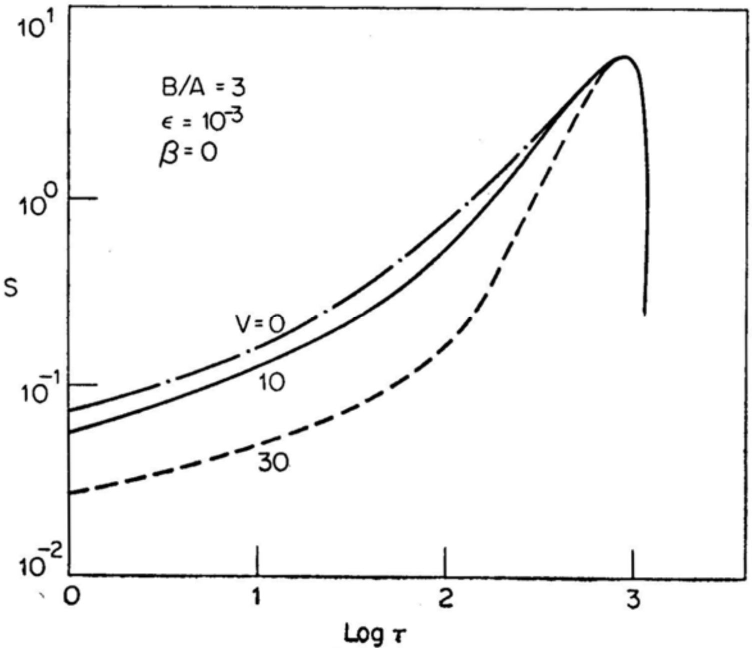

Figure 4. Same as in Fig. 2 with ϵ=10^{-3}.

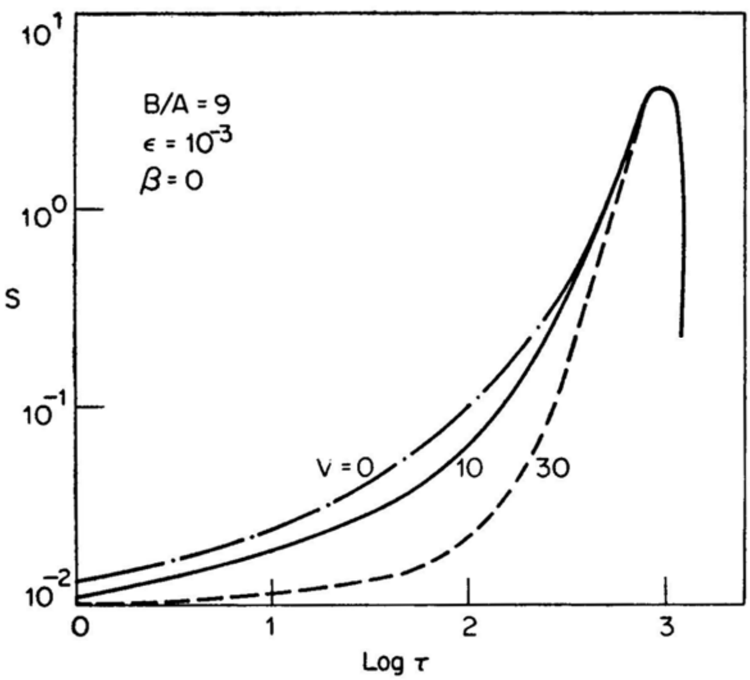

Figure 5. Same as in Fig. 2 with *B/A=9* and ϵ=10^{-3}.

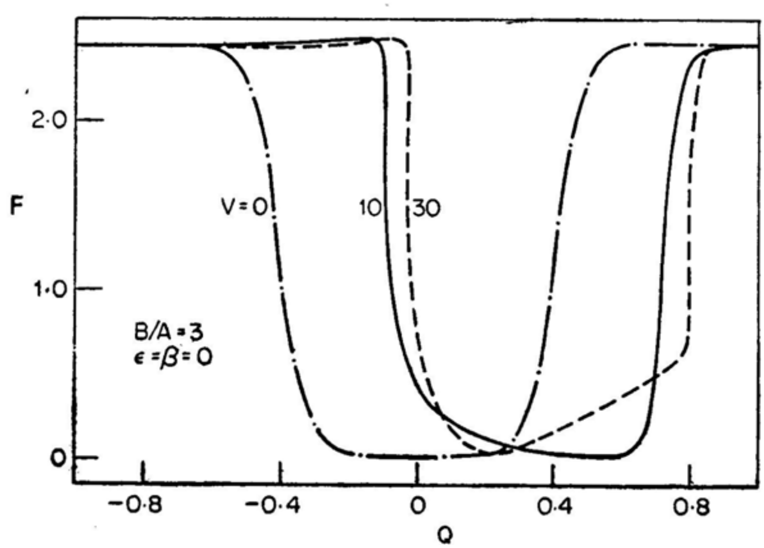

Figure 6. Flux profiles of the lines received at the observer $F = F(x)/F(x_{\max})$ and $Q = x/x_{\max}$ corresponding to the source functions given in Fig. 2.

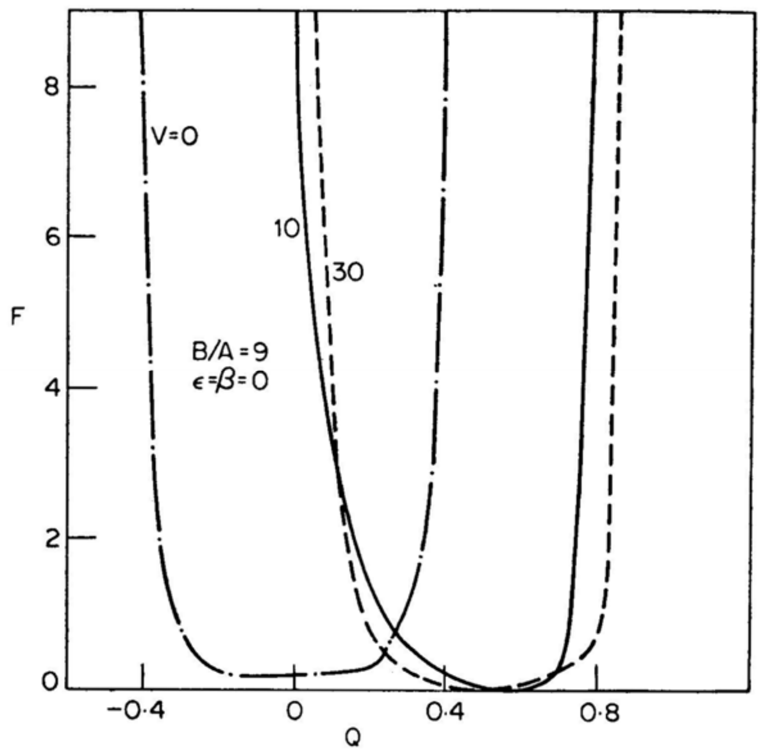

Figure 7. Flux profiles corresponding to the source functions given in Fig. 3.

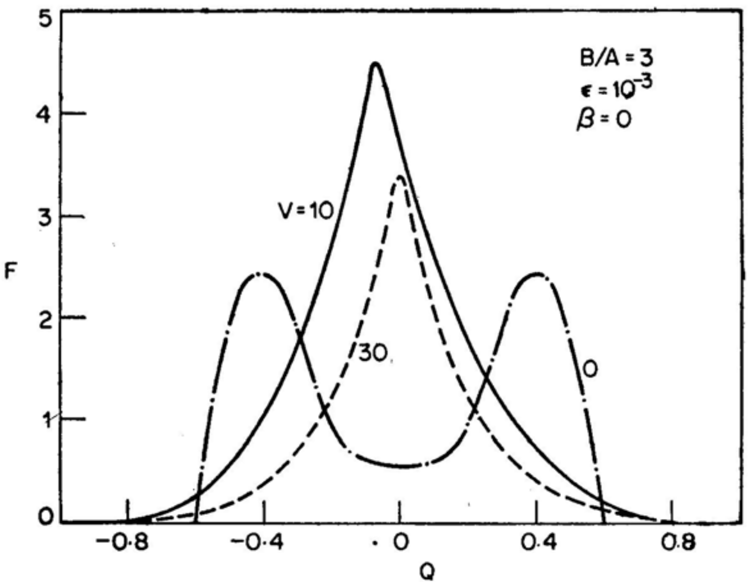

Figure 8. Same as in Fig. 6 but corresponding to the source functions of Fig. 4.

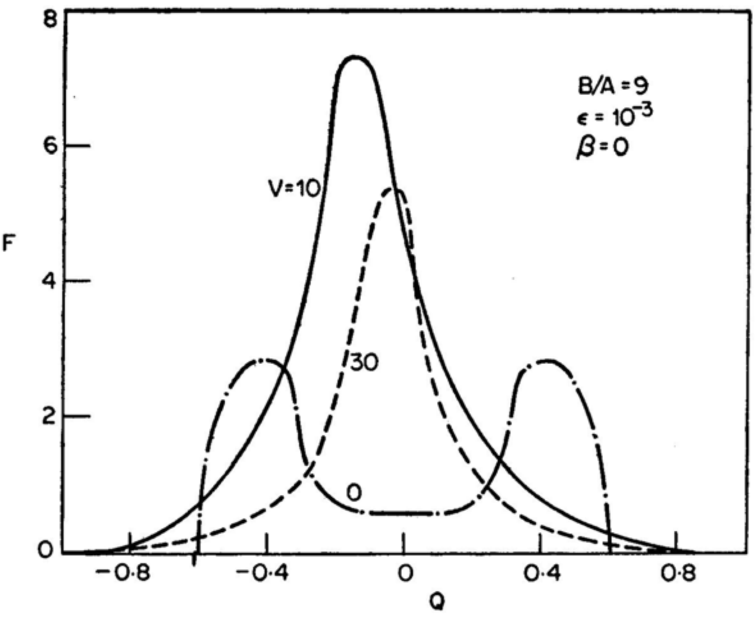

Figure 9. Same as in Fig. 6 corresponding to the source functions given in Fig. 5.

4. Conclusions

Comoving frame calculations have been performed by using the angle-averaged partial frequency redistribution function R_I to obtain flux profiles which can be compared with observations. The profiles calculated with line emission ($\epsilon = 10^{-3}$) resemble those observed in some of the quasars.

Appendix

The transmission and reflection matrices in the basic 'cell' are,

$$\mathbf{t}(n+1, n) = \mathbf{G}^{+-}[\mathbf{\Delta}^{+}\mathbf{A}_{+} + \mathbf{g}^{+-}\mathbf{g}^{-+}],$$

$$\mathbf{r}(n+1, n) = \mathbf{G}^{-+}\mathbf{g}^{-+}[\mathbf{I} + \mathbf{\Delta}^{+}\mathbf{A}_{+}),$$

and the source vector is

$$\sum{}^{+} = \mathbf{G}^{+-}[\mathbf{\Delta}^{+} + \mathbf{g}^{+-}\mathbf{\Delta}^{-}]\,\mathbf{S}\,\tau.$$

Similarly $\mathbf{t}$ $(n, n+1)$, $\mathbf{r}$ $(n, n+1)$ and Σ^{-} can be written by interchanging the subscripts and superscripts, namely the + and – signs (**I** is unit matrix). Also,

$$\mathbf{G}^{+-} = [\mathbf{I} - \mathbf{g}^{+-}\mathbf{g}^{-+}]^{-1}, \ \mathbf{g}^{+-} = \tfrac{1}{2}\tau\,\mathbf{\Delta}^{+}\mathbf{Y}_{-}$$

$$\mathbf{\Delta}^{+} = [\mathbf{M} + \tfrac{1}{2}\tau\,\mathbf{Z}_{+}]^{-1}, \ \mathbf{Z}_{+} = \mathbf{\Phi} - \tfrac{1}{2}\sigma\,\mathbf{R}\,\mathbf{W} + \frac{\rho_c\,\mathbf{\Lambda}^{+}}{\tau} - \frac{\mathbf{M}_1\mathbf{d}}{\tau}$$

$$\mathbf{Z}_{-} = \mathbf{\Phi} - \tfrac{1}{2}\sigma\mathbf{R}\mathbf{W} - \frac{\rho_c\mathbf{\Lambda}^{+}}{\tau} - \frac{\mathbf{M}_1\mathbf{d}}{\tau}$$

$$\mathbf{Y}_{+} = \tfrac{1}{2}\sigma\,\mathbf{R}\,\mathbf{W} + \frac{\rho_c\,\mathbf{\Lambda}^{-}}{\tau}, \ \mathbf{Y}_{-} = \tfrac{1}{2}\sigma\,\mathbf{R}\,\mathbf{W} - \frac{\rho_c\,\mathbf{\Lambda}^{-}}{\tau}$$

$$\mathbf{A}_{+} = \mathbf{M} - \tfrac{1}{2}\tau\,\mathbf{Z}_{+}, \ \mathbf{A}_{-} = \mathbf{M} - \tfrac{1}{2}\tau\,\mathbf{Z}_{-}.$$

Similarly G^{-+}, g^{-+}, Δ^{-}, are written by interchanging the subscripts and superscripts + and – signs. And $\sigma = 1 - \epsilon$.

References

Baldwin, J. A. 1975, *Astrophys. J.,* **201,** 26.
Baldwin, J. A., Netzer, H. 1978, *Astrophys. J.,* **226,**1.
Grant, I. P., Hunt, G. E. 1969, *Proc. R. Soc London Ser. A,* **313,** 183.
Grant, I. P., Peraiah, A. 1972, *Mon. Not. R. astr. Soc.,* **160,** 239.
Hummer, D. G. 1962, *Mon. Not. R. astr. Soc.,* **125,** 21.
Hummer, D. G., Kunasz, P. B. 1974, *Mon. Not. R. astr. Soc.,* **166,** 19.

Mihalas, D., Kunasz, P. B., Hummer, D. G. 1975, *Astrophys. J.*, **202,** 465.
Mihalas, D., Kunasz, P. B., Hummer, D. G. 1976, *Astrophys. J.*, **210,** 419.
Peraiah, A. 1978, *Kodaikanal Obs. Bull Ser. A*, **2**, 115.
Peraiah, A. 1980, *Acta Astr.* (in press)
Peraiah, A., Grant, I. P. 1973, *J. Inst. Math. Its Appl*, **12,** 75.
Peraiah, A., Wehrse, R. 1978, *Astr. Astrophys.*, **70,** 213.
Wehrse, R., Peraiah, A. 1979, *Astr. Astrophys.*, **71,** 289.

J. Astrophys. Astr. (1980) **1,** 17–23

Lines formed in Rotating and Expanding Atmospheres

A. Peraiah *Indian Institute of Astrophysics, Bangalore* 560034

Received 1980 February 23; accepted 1980 April 7

Abstract. Spectral lines formed in a rotating and expanding atmosphere have been computed in the frame of the observer at infinity. Two kinds of velocity laws are employed: (i) a uniform radial velocity of the gas and (ii) velocity increasing with radius (*i.e.* velocity gradients). The atmosphere has been assumed to be rotating with constant velocity. We have considered maximum radial and rotational velocities to be 10 and 3 mean thermal units respectively in an atmosphere whose geometrical thickness is 10 times the stellar radius. The total radial optical depth at line centre is taken to be about 100. In all cases, Doppler profile and a source function which is varying as $1/r^2$ have been used.

Generally, the lines are broadened when rotation is introduced. However, when radial motion is also present, broadening becomes asymmetric and the red emission and blue absorption are enhanced.

Key words: rotating and expanding atmospheres—spectral lines—radiative transfer—P Cygni profiles

1. Introduction

Rotation is a common phenomenon among all the celestial objects. The stellar rotation is evidenced in the broadening of the spectral lines formed in their atmospheres. The rotational aspects of the rings of Be stars are discussed in Slettebak (1979). However, we should consider systems in which the atmosphere is rotating. In addition to rotation, the radial motion of the gas in the atmosphere is also an important factor which could change the shape of the spectral lines. Recently, several methods of calculating spectral lines in a radially moving gas have been developed (see Mihalas 1978; Peraiah 1978). However, the combined effects of rotation of the atmosphere and the radial motion of the gases in the atmosphere are not very well understood. Recently, Dural and Karp (1978) calculated lines with these two effects taken into account in a semi-analytical way. However, they used small velocities of rotation and radial motion with no velocity gradients. They have used the limb darkening law (Gray 1976) to calculate the specific intensities.

In this paper, we compute spectral lines seen by the observer at the earth by using the formal solution of the radiative transfer equation for a medium with radial optical depth of 100 at the line centre, using a maximum rotational velocity of 3 and radial velocity of the gas of 10 mean thermal units. The results are presented in the next section.

2. Computational procedure and discussion of results

The geometry of the calculations is given in Fig. 1. The medium has been divided into several shells. The rotational velocity V_{rot} and the radial velocity V_{rad} at each point on the shells are projected on to the line of sight 1 of the observer. So, the resultant frequency is given by

$$x = x' + \mathbf{v}_{\mathbf{rot}} \cdot \mathbf{l} + \mathbf{v}_{\mathbf{rad}} \cdot \mathbf{l}, \tag{1}$$

where $x' = (\nu' - \nu_0)/\Delta\nu_D, \quad \Delta\nu_D = v_T\,(\nu_0/c).$

v_{rot} and v_{rad} are measured in units of v_T, the mean thermal velocity of the gas. The atmosphere has been divided into several shells as shown in Fig. 1. The optical depth is calculated in each of these shells along the line of sight after taking into

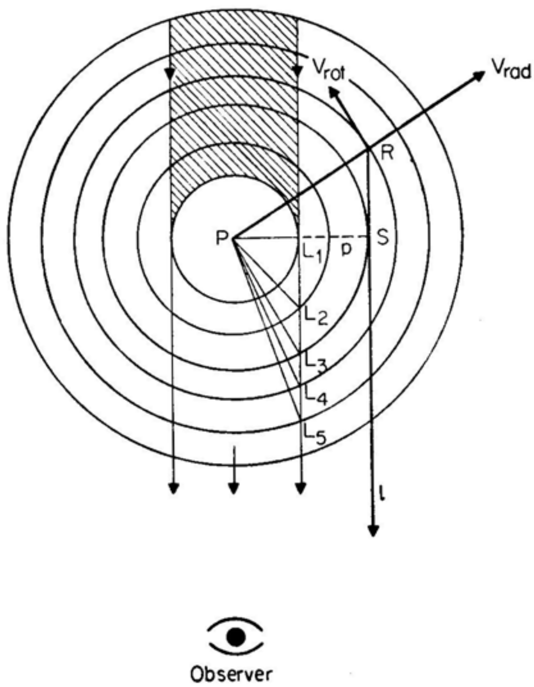

Figure 1. Diagram showing the stellar disc from which radiation is received at infinity.

account the projection of v_{rot} and v_{rad} on to 1 and is given by

$$\tau_L = \frac{\pi e^2}{mc} f \frac{\Delta L}{\Delta \nu_D \sqrt{\pi}} N \exp\left(-x^2/\delta^2\right), \tag{2}$$

where ΔL is the length along the ray between two consecutive shell boundaries (L_1L_2 or L_2L_3 etc.) and $\delta = \Delta\nu_D(r)/\Delta\nu_D$, the ratio of the Doppler widths, is kept equal to. 1. We calculate the transfer of the rays along the line of sight. These are parallel rays cutting across the shell boundaries. N is the particle density. The specific intensity at each shell boundary becomes the incident radiation for the transfer of radiation in the next shell. No incident radiation is given at the outermost boundary. The emergent intensity is calculated by the formal solution of radiative transfer equation and is given by

$$I(\tau_L) = I_0 \exp(-\tau_L) + \int_0^{\tau_L} S(t) \exp\left[-(\tau_L - t)\right] dt, \tag{3}$$

where $S(t)$ is the source function. The radial distribution of the source function is obtained from the solution of the radiative transfer equation in spherical symmetry either in the rest frame of the star or in the comoving frame of the gas. However, as we are investigating the combined effects of rotation and radial motion on the formation of lines qualitatively, we have assumed a source function which varies as $1/r^2$. With this assumption, we can estimate the specific intensity $I(\tau_L)$ at the boundary of each shell. The integral in equation (3) is evaluated by Simpson's rule. Finally we calculate the flux by the integral

$$F(x) = 2\pi \int_A^B I(p, x) p\, dp, \tag{4}$$

where p is the perpendicular distance from the centre of the star P to the ray along the line of sight and A and B are the inner and outer radii of the medium.

We have assumed two types of variations for the velocity satisfying the law of continuity: (i) increasing linearly with radius, *i.e.*

$$V_r = V_A + \frac{V_B - V_A}{B - A}(r - A), \tag{5}$$

where V_A, V_B and V_r are the velocities at A, B and r respectively; and (ii) a constant velocity throughout the atmosphere $V = V_A = V_B$. The density changes as $1/r^3$ in the first case and as $1/r^2$ in the second case such that the equation of continuity is always satisfied. We have assumed constant velocity of rotation in all shells so that the angular velocity changes as $1/r$ (so that angular momentum is conserved on the whole). In the first case, we have set $V_A = 0$ and V_B =0, 1, 3,6and 10 and V_{rot} = 0, 1 and 3 mean thermal units (mtu) whereas in the second case, the values of V_{rot} are the same as in case 1 but with V = 0, 1 and 3 mtu only. The inner and outer radii of the atmosphere are taken to be 10^{12} and 10^{13} cm respectively and the density at radius A is put at 10^6 cm^{-3}.

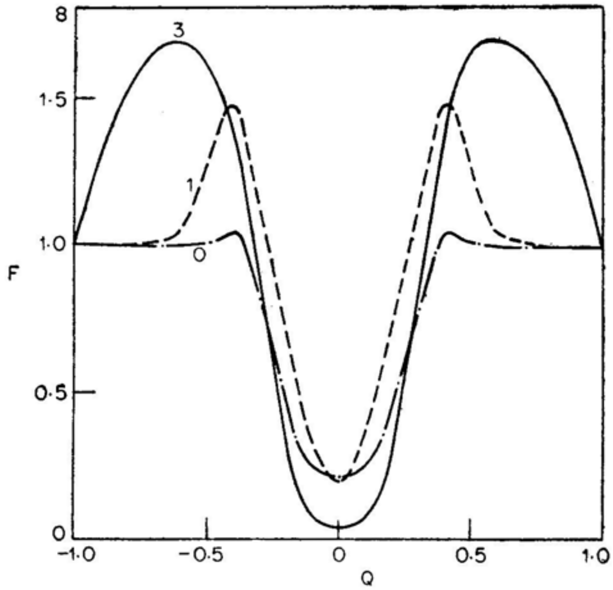

Figure 2. Flux profiles for differential radial velocities with V_B=V_A=*0* and V_{rot}=0, 1 and 3. Q=X/X_{max} and F=flux (X)/flux (X_{max}). The numbers refer to V_{rot} .

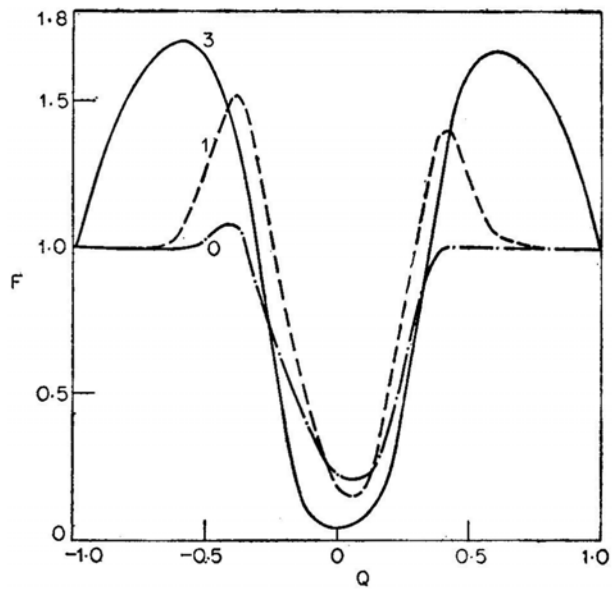

Figure 3. Flux profiles for V_B=*1*, V_A=*0* and V_{rot} =0, 1, 3.

In Fig. 2 we have plotted flux profiles *i.e.* $F(=F(x)/F(X_{max}))$ versus Q (=X/X $_{max}$)for V_B =0 and V_{rot} =0, 1 and 3 mtu. The line for V_{rot} = 0 shows deep absorption but with slight emission (about 5 per cent) in the wings. However, when rotation is introduced, the lines show a large broadened emission of nearly 50 per cent forV_{rot} =1 and 70 per cent for V_{rot} =3 mtu. But the absorption becomes sharper for V_{rot} = 1 and both emission and absorption become broader and deep. When rotation is introduced into the radially moving matter, there will be an artificial extension of the outer layers which means that the side lobes of the atmosphere from which the scattered radiation arrives at the observer, extend and increase the emission.

In Fig. 3 flux profile for V_B=1 mtu and V_{rot}= 0, 1,3 mtu is presented. There is a small red emission for V_{rot} =0 and no emission on the blue side of the centre of the line. However, when rotational velocity is introduced both emission and absorption increase and there is emission on the blue side which is comparable to that on the red side. These features become strong as we increase the radial velo-

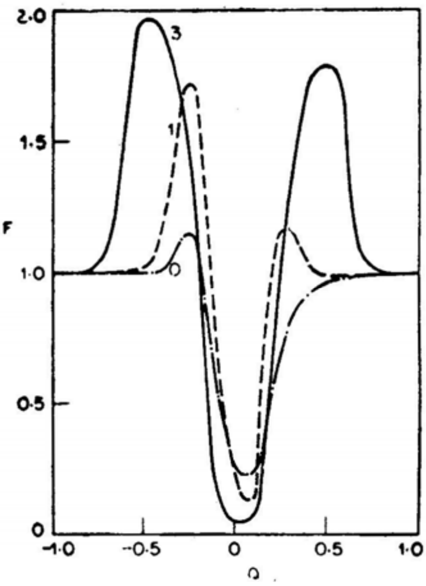

Figure 4. Flux profiles for V_B=3, V_A=0 and V_{rot}=0, 1, 3.

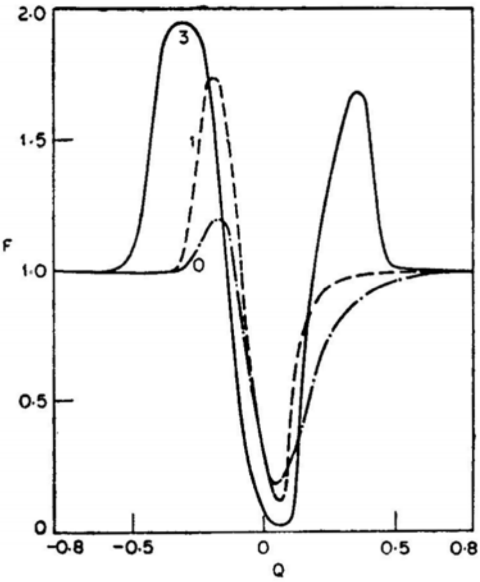

Figure 5. Flux profiles for V_B=6, V_A=0 and V_{rot}=0, 1, 3.

city to 3, 6 and 10 mtu. At V= 10 mtu and V_{rot} = 3, the asymmetry is quite large. These are shown in Figs 4, 5 and 6. In Figs 7 and 8 the flux profiles for the second case (uniform radial motion) are presented. The profiles in Fig. 7 are calculated for V_B =V_A=1 mtu and V_{rot} = 0, 1, 3 mtu. We clearly notice the P Cygni profiles for V_{rot} = 0 and rotation introduces emission in the blue side (compare this with profiles given in Fig. 3). In Fig. 8 we present the profiles for V=3 mtu and V_{rot} = 0, 1, 3 mtu, These profiles exhibit clearly the type of profiles one would expect from P Cygni atmospheres. As the rotational velocity increases, the red emission becomes larger and its peak becomes redder

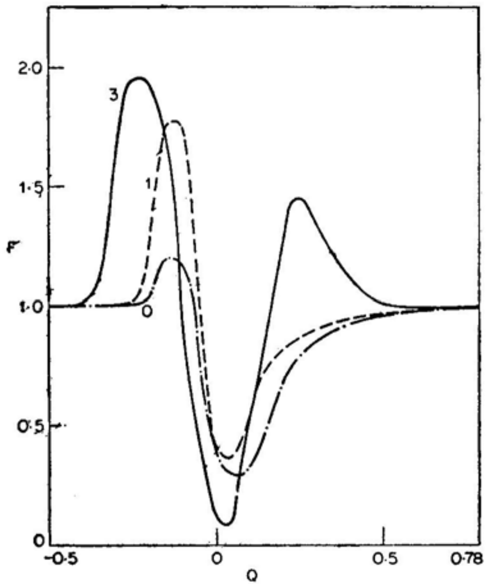

Figure 6. Flux profiles for V_B=10, V_A=0 and V_{rot}=0, 1, 3.

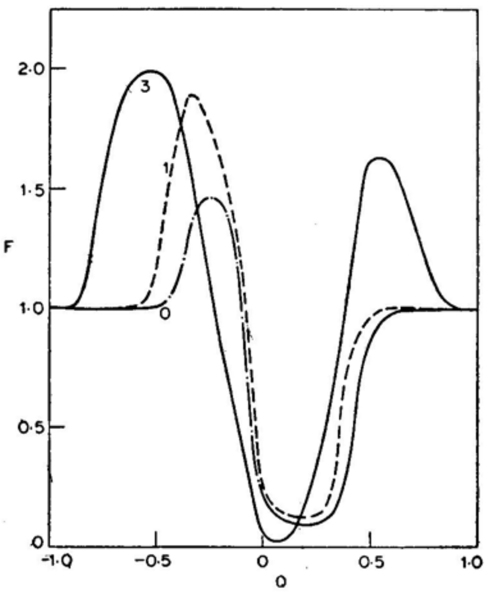

Figure 7. Flux profiles for $V_A = V_B$ =l, V_{rot} =0, **1.**

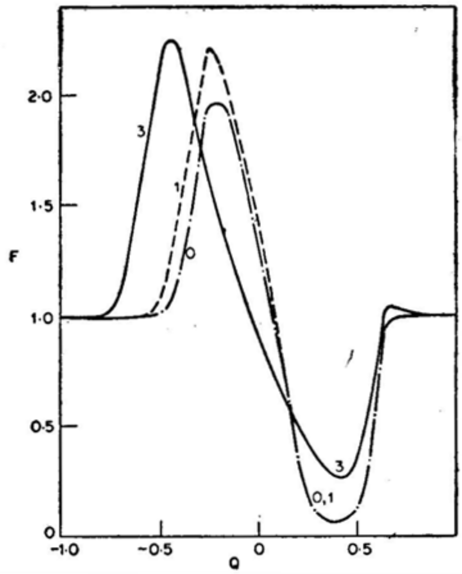

Figure 8. Flux profiles for $V_A = V_B = 3$, $V_{\text{rot}} = 0, 1, 3$.

3. Conclusions

The effects of rotational velocities on the formation of spectral lines formed in an atmosphere with radial velocities, have been investigated. Radial motion of the gases introduce a P Cygni type-shape and rotational motion would increase the emission on either side of the centre of the line although the line remains asymmetric.

References

Dural, P., Karp, A. H. 1978, *Astrophys., J.*, **222,** 220.
Gray, D. F. 1976, *The Observations and Analysis of Stellar Photospheres,* John Wiley, New York.
Mihalas, D. 1978, *Stellar Atmospheres,* 2 edn, Freeman, San Francisco.
Peraiah, A. 1978, *Kodaikanal Obs. Bull. Ser. A*, **2,** 115.
Slettebak, A. 1979, *Space Sci. Rev.,* **23,** 541.

J. Astrophys. Astr. (1980) **1,** 25–32

Pulsar Activity and the Morphology of Supernova Remnants

V. Radhakrishnan and G. Srinivasan *Raman Research institute, Bangalore* 560080

Received 1980 March 17 ; accepted 1980 April 28

Abstract. We use the recently introduced concept of a 'window' of magnetic field strengths in which pulsars can be active to explain the variation in morphology of supernova remnants. The striking difference between shell-type and filled-type remnants is attributed to differences in he magnetic field strengths of the neutron stars left by the respective Supernovae. Field strengths of a value permitting pulsar activity result in particle production and Crab-like centrally concentrated remnants. Other field values lead to strong magnetic dipole radiation and cones-quent shell formation (*e.g.* Cas A). Several apparent inconsistencies concerning pulsar-supernova associations appear to find a logical expla-nation on the basis of this hypothesis.

Key words: pulsars—supernova remnants—magnetic window

1. Introduction

It is generally accepted that supernova explosions are unlikely without the formation of neutron stars. According to this picture there must be a neutron star associated with all supernova remnants (SNR). Because the observed proper motions of pulsars are very much less than the velocity of supernova ejecta, the neutron stars must be inside the SNR while the latter are still young. Since the typical age of pulsars is much larger than the life-time of SNRs, it is to be expected that old pulsars will show no association with SNRs; on the other hand we find it surprising that a radio pulsar has been detected in only 2 of the 120 or so known SNRs. This question has been asked many times in the literature and several arguments have been advanced to explain why a pulsar is not seen inside more, if not all SNRs.

The main arguments are (a) the pulsar may not be beamed at us; (b) a low flux density and large dispersion measure make it difficult to detect; (c) in addition, if it is in a binary system the pulsar may be 'smothered' by the stellar wind from the companion star (see Manchester and Taylor 1977 for a discussion of these effects). These three arguments would reduce the number of pulsars that one would expect to detect from 120 to a much smaller number. However, even if they do explain the absence of *pulsed* radio radiation from the centres of the majority of SNRs, they do not concern themselves with other possible manifestations of a rotating neutron star inside the SNRs.

If the newly born neutron star was functioning as a normal young pulsar (short period and high magnetic field), there should be a copious outflow of relativistic particles (Goldreich and Julian 1969; Sturrock 1971; Ruderman and Sutherland 1975). These should radiate either in the interstellar magnetic field or the field of the low frequency magnetic dipole radiation (Rees and Gunn 1974), giving rise to a central concentration of radio brightness around the neutron star. The Crab Nebula is a classic example of such a central concentration, and Shklovskii (1977) has argued very convincingly that the relativistic particles responsible for the radiation must be produced by the central pulsar.

In recent years, 9 more SNRs resembling the Crab Nebula, and showing no evidence of shell structure, have been reported by various authors and have been compiled by Caswell (1979). All the hundred or so other remnants are of the so-called shell-type, although in several cases the structure is not well delineated in the available radio maps. With one exception (G 326·3–1·8), central concentrations are not found in shell-type remnants and are conspicuously missing in the three youngest known remnants, Cas A, Tycho and Kepler which are among the best examples of well-defined shells with hollow interiors. The non-observability of radio pulsars in these three young remnants could be due to one of the factors such as beaming referred to above, but their distinctly non-Crab-like appearance cannot be a result of the direction from which they are viewed. It is an explanation of this difference in remnant morphology that we are attempting in this paper.

2. Field strengths and pulsar activity

Very reasonable arguments have been advanced that filled-centre supernova remnants may be expected to have lifetimes of ~10,000 years (Weiler and Panagia 1978). Since Cas A, Tycho and Kepler are all less than ~400 years old, the absence of such a nebula in each of them is consistent with the absence of a pulsar at their centres. To reconcile this with our earlier premise that a neutron star must have been formed in each explosion, we advance a new hypothesis relating the activity of neutron stars as pulsars with remnant morphology.

It has been argued recently (Radhakrishnan 1979) that for a neutron star to be active as a pulsar, the surface magnetic field must lie within a small range $2–3 \times 10^{12}$G, and its rotation period must be less than a few seconds. The latter condition will need to be satisfied for the production of a sufficiently high voltage to sustain the sparks which generate the energetic particles which then radiate (Ruderman and Sutherland 1975). In addition, the former condition has to be satisfied to enable reinitiation of the sparking process each time the gap has been re-formed after the previous breakdown. According to this picture, the observed spread in the magnetic fields *derived* from period and period derivative measurements on the assumption of dipole braking and a constant radius, is a reflection of the presence of multipole components and the spread in radii of the neutron stars in question (Shukre and

Radhakrishnan 1980). For the purpose of this paper we shall assume the above picture and explore the consequences for supernova remnants.

One of these consequences is that all neutron stars born with initial fields lying outside the magnetic window referred to above will spend part or all of their lives in ‘ silence ‘. Neutron stars with initial fields below the window can never become pulsars. Those born with a true field very much higher than $2{\cdot}5\times10^{12}$G will also never be pulsars no matter how short their initial rotation period; braking due to magnetic dipole radiation will lengthen the period beyond the limit referred to above by the time the field decays to around $2{\cdot}5\times10^{12}$G. Those with initial fields just above this value may become pulsars depending on the timescale of the decay of the magnetic field. If pulsar dipole fields decay through the formation of multipole components as discussed by Flowers and Ruderman (1977), the characteristic surface magnetic field and its value on the polar cap will not diminish greatly while the dipole component relaxes to a very small value. As discussed by Shukre and Radhakrishnan (1980) such a field will permit pulsar operation even though the dipolar field is below the window value. If the evolution of the field as proposed by Flowers and Ruderman (1977) is sufficiently rapid, we may expect a significant number of neutron stars born with fields above the window to turn on as pulsars with some intermediate value of period, and remain observable until the period lengthens to beyond the cut-off value referred to earlier.

Irrespective of whether the initial field is above or below the magetic window, we propose that in either case this is precisely the reason for the hollow appearance of most shell-type remnants, and in particular Tycho, Kepler and Cas A. We suggest that inside each of these remnants, there is in fact a rapidly spinning neutron star with a surface magnetic field outside the window, and from which pulsed radio radiation would therefore not be observed from any direction or distance; and that the only outlet for the rotational energy of these stars is magnetic dipole radiation as discussed by Pacini (1967) and Gunn and Ostriker (1969).

It is interesting that Woltjer (1974) has suggested that the hollow interior of objects such as Cas A may perhaps be understood as due to the very strong electromagnetic wave field of a pulsar in the centre. In his picture, low frequency electromagnetic waves sweep the relativistic electrons out from the immediate vicinity of the pulsars, which must be spinning very fast but may not be beaming at us. According to our picture, there are no relativistic particles put out by the neutron stars in these remnants, but only a strong low frequency wave field. Depending on the initial strength and decay time of their fields these neutron stars may manifest themselves as pulsars in due course as discussed above. By this time the remnants will almost certainly have dissipated themselves; for them to remain observable would require that the decay time of neutron star magnetic fields be much shorter than generally believed, and of the order of the lifetime of shell-type SNRs ($\sim10^5$ years). In any case, one would not expect to see central concentrations around such ‘turned on’ pulsars, since these nebulae can be sustained only by rapidly spinning young pulsars.

3. Filled remnants

The centrally concentrated remnants listed by Caswell (1979) can now be understood as resulting from those cases where the initial magnetic field of the neutron star lay within the ‘magnetic window’ (Radhakrishnan 1980; Shukre and Radhakrishnan 1980) at birth. The rotational energy of such pulsars goes into the production of relativistic particles and pulsed radiation. The central concentration of radio brightness is the evidence for the operation of the neutron star as a pulsar, and the absence of radio pulses from any of them can now be attributed to one or more of the factors mentioned earlier, namely beaming direction, low flux density, large dispersion measure etc. The smaller number of such centrally concentrated remnants makes these arguments, in our view, more acceptable now than when applied to all the 120 or so observed supernova remnants in the galaxy.

The SNR Vela X associated with the pulsar PSR 0833 — 45 also has a filled interior as seen in the radio emission (Lerche and Milne 1980). Recent observations by HEAO-B (Harnden *et al.* 1979) have revealed an X-ray nebula of angular size ~1’ and centred on the pulsar. Together with the Crab, we thus have two pulsars seen in ~10 such remnants, all presumably powered by pulsars. This is in reasonable accord with the 20 per cent factor usually associated with pulsar beaming.

4. Shell-Type remnants

We shall now discuss the question of the formation of supernova shells. If they are formed by the shock waves and mass ejection which are believed to accompany every supernova explosion, then the absence of shells around the Crab and similar remnants must be due to some other parameter. The presence or absence (at the site of the explosion) of interstellar matter which could be compressed into a shell is one possible reason. Cox and Smith (1974) have in fact proposed that holes in the form of million-degree-bubbles are left in the interstellar medium by previous supernova explosions. The filling factor suggested by them for such bubbles is ~l0 per cent. This could be considered to agree with the ratio of filled to shell-type remnants, although, the much shorter lifetime of the former would really lead to a much larger filling factor, if this were the true explanation.

However, according to this picture, pulsars should be found in either type of remnant; the presence of a shell should depend only on whether there has been a previous explosion in the vicinity. Of the large number of pulsars known today (~300), there are only two (the Crab and Vela) believed by all to be definitely associated with remnants. The probability that both these pulsars would be found in centrally concentrated remnants is less than 1 per cent because the latter form less than a tenth of the population of supernova remnants. For this reason it seems to us much more likely that the morphology of a remnant is, in fact, a consequence of the presence or absence of an active pulsar in it.

We have already discussed the intimate connection between the nature of filled remnants and the particle producing pulsars in them. In a similar manner, if shells were produced by the strong low-frequency dipole radiation put out by neutron stars which are not pulsars, the picture would be complete. Such a mechanism was proposed by Ostriker and Gunn (1971). According to them, supernova explosions are powered by the stored rotational energy in the newly formed neutron stars. The intense low-frequency radiation pushes out the outer envelope of the star and the surrounding interstellar matter and accelerates them for long enough to acquire the kinetic energy associated with observed shells. Thus newly born neutron stars which do not immediately function as pulsars could create the shells seen as most supernova remnants. The radio radiation from these shells can arise from one or more of the mechanisms proposed for both field amplification and particle acceleration in supernova shells (Gull 1973; Scott and Chevalier 1975; Bell 1978; Blandford and Ostriker 1978).

5. Hybrid morphology?

In the above discussion we have categorised neutron stars as either pulsars producing filled remnants, or magnetic dipole radiators producing shell-type remnants, as if these two types of behaviour were mutually exclusive. It is an open question as to whether a rotating magnetised neutron star can put its energy into particle production (Goldreich and Julian 1969; Sturrock 1971; Ruderman and Sutherland 1975), and *simultaneously* into low frequency magnetic dipole radiation (Pacini 1967; Gunn and Ostriker 1969). In almost all discussions in the literature of any of these two processes, the other is carefully neglected as if it did not exist. If a rotating magnet were immersed in a highly conducting medium, Lenz's law would lead us to believe that the electric fields generated by the rotation would set up currents whose magnetic fields neutralised the far field magnetic dipole radiation. The rotational energy would go into the acceleration of the charges whose motion forms the currents.

Kaplan, Tsytovich and Eidman (1974) have discussed this problem for a strongly magnetised rotating neutron star but assuming that the conductivity in the magnetosphere is isotropic. They concluded that turbulence in the relativistic circumpulsar plasma will sharply reduce its conductivity with several consequences including the shielding of the magnetic dipole radiation. It is possible that their assumption of isotropic conductivity invalidates their conclusions. If it does not, then neutron stars will operate in only one mode at a time, either as magnetic dipole radiators (with no particle output), or as pulsars putting out pulses and relativistic particles (but with little or no dipole radiation).

The interesting case of G 326·3–1·8 (Caswell 1979), which shows a weak but well-defined shell in addition to a central feature might be evidence to the contrary. It is unlikely that the central feature is due to the recent turning on of the neutron star as a pulsar and that the shell was produced before pulsar activity started. As discussed earlier, the time within which the field would have had to decay is unacceptably short; a rough age estimate of this remnant based on its diameter etc. (see for example Clark and Caswell 1976) leads to approximately 5000 years. G 326·3–1·8 represents perhaps simply a case of ‘ having a little each way’ in that both low-frequency radiation and pulsar behaviour are present. It is conceivable that the recently discovered class of objects (Ryle *et al.* 1978) wherein very small diameter sources are found at the centres of well-defined shells are also in this special category.

6. Supernovae in binaries

We turn now to neutron stars born in close binary systems. According to the standard picture (van den Heuvel 1977) the system will not disrupt after the first explosion, and the companion star will remain in the main sequence for a few million years. As the stellar wind of the companion will be weak during this phase, we expect the picture relating to the morphology of remnants described above to remain substantially unmodified.

If the neutron star has the right magnetic field to operate as a pulsar, a nebula centred on the pulsar will be produced as before. If the neutron star is not active as a pulsar, a shell will be formed in the usual way. But as the lifetime of shells is much greater than that of central nebulae, further developments are conceivable in this case. In particular, if within the lifetime of the shell the dipole radiation from the neutron star can be absorbed by the stellar wind in its Roche lobe, this will lead to its heating and subsequent reradiation, *i.e.* to the formation of a source of higher frequency radiation surrounding the neutron star.

In the case of the second explosion in binary systems, we believe that its manifestations will be identical to those accompanying a single star explosion. Even in the unlikely event of the system remaining bound, the first neutron star will have very little influence on the newly formed one. Also, even a moderate proper motion would have moved the binary far from the site of the first explosion in the intervening period of several million years; the development of the remnant will therefore not be biased.

7. Conclusions

We have attempted in this paper to relate pulsar activity in neutron stars with the observed morphology of SNRs. We start with the concept of a window of magnetic field strengths only within which neutron stars will display pulsar activity; neutron stars with fields outside the window will put out only magnetic dipole radiation. The former variety emit large numbers of relativistic particles and create centrally concentrated remnants of which type about 10 are known. Neutron stars emitting only dipole radiation create shells around them characteristic of most of the known supernova remnants.

Among the longstanding inconsistencies relating to pulsar-supernova associations are (a) the fact that in only two of all the known remnants have pulsars been observed, and (b) that neither of these pulsars is in shell-type remnants, which form the vast majority. Both these facts find a logical explanation on the basis of our hypothesis. Only the ten or so Crab-like remnants have active pulsars in them, and the various selection effects in operation make only two of them observable.

We are aware that the present hypothesis appears to further increase the already existing difficulty of reconciling the formation rates of pulsars and occurrence rate of Supernovae in the galaxy. Estimates of these two numbers made by different authors are fraught with uncertainties and vary widely, but most of them seem to indicate a higher formation rate for pulsars than if they were produced in supernova explosions (see discussion on p. 168 of Manchester and Taylor 1977). If only some of the neutron stars produced by Supernovae become pulsars, this discrepancy would obviously be widened. It was mentioned earlier that the lifetime of filled remnants is of the order of 10^4 years, whereas that of shell-type remnants is generally believed to be 10^5 to 10^6 years. As the ratio of these two lifetimes is approximately the same as that of the numbers of observed remnants of the two varieties, this indicates that their production rates are roughly equal. In other words, roughly half of the neutron stars produced in Supernovae have initial magnetic fields inhibiting them from functioning as pulsars at birth. If some fraction of these eventually turn on as pulsars after the remnants have dissipated themselves, this would imply that the majority of neutron stars created in supernova explosions do in fact contribute to the pulsar population. Thus, we see that the discrepancy referred to earlier is only marginally affected by the present hypothesis, and the explanation of any serious disagreement must lie elsewhere. We believe in any case, that as more light is thrown on the processes of formation of pulsars and Supernovae, the matter will resolve itself without requiring that every neutron star that is created must immediately function as a pulsar.

Finally, we touch upon the possible implications of our conclusions for the direct measurements of neutron star temperatures by X-ray observations (Murray *et al.* 1979; Harnden *et al.* 1979; Helfand, Chanam and Novick 1980). If, indeed, there are neutron stars at the centres of all SNRs as we have assumed, the upper limits imposed by Xray observations suggest that neutron stars cool much faster than present theories have supposed. Also, if only some neutron stars are active as pulsars as we have proposed, and pulsars operate according to the Ruderman and Sutherland (1975) model, then some difference should be found between the temperatures of the pulsars and of other neutron stars of the same age, due to the extra heating by the particles hitting the surfaces of pulsars.

Acknowledgements

We thank R. D. Ekers, M. M. Komesarorff, P. Morrison, and L. Woltjer for a critical reading of an earlier version of this manuscript.

References

Bell, A. R. 1978, *Mon. Not. R. astr. Soc.,* **182,** 147.
Blandford, R. D., Ostriker, J. 1978, *Astrophys. J.,* **221,** L29.
Caswell, J. L. 1979, *Mon. Not. R. astr. Soc.,* **187,** 431.
Clark, D. H., Caswell, J. L. 1976, *Mon. Not. R. astr. Soc.,* **174,** 267.
Cox, D. P., Smith, B. W. 1974, *Astrophys. J.,* **189,** L105.
Flowers, E., Ruderman, M. A. 1977, *Astrophys. J.,* **215,** 302.
Goldreich, P., Julian, W. H. 1969, *Astrophys. J.,* **157,** 869.
Gull, S. F. 1973, *Mon. Not. R. astr. Soc.,* **161,** 47.
Gunn, J. E., Ostriker, J. P. 1969, *Nature,* **221,** 454.
Harnden, F. R. Jr., Hertz, P., Gorenstein, P., Grindlay, J., Schreier, E., Seward, F. 1979, *Bull. Am. astr. Soc.,* **11,** 424.
Helfand, D. J., Chanam, G. A., Novick, R. 1980, *Nature,* **283,** 337.
Kaplan, S. A., Tsytovich, V. N., Eidman, V. Ya. 1974, *Soviet. Astr.,* **18,** 211.
Lerche, I., Milne, D. K. 1980, *Astr. Astrophys.,* **81,** 302.
Manchester, R. N., Taylor, J. H. 1977, *Pulsars,* Freeman, San Francisco.
Murray, S. S., Fabbiano, G., Fabian, A. C, Epstein, A., Giacconi, R. 1979, *Astrophys. J.,* **234,** L69.
Ostriker, J. P., Gunn, J. E. 1971, *Astrophys. J.,* **164,** L101.
Pacini, F. 1967, *Nature,* **216,** 567.
Radhakrishnan, V. 1980, in *Non-Solar Gamma Rays* (*COSPAR*), Eds R. Cowsik and R. D. Wills, Pergamon Press, Oxford, p. 163.

Rees, M. J., Gunn, J. E. 1974, *Mon. Not. R. astr. Soc.*, **167,** 1.
Ruderman, M. A., Sutherland, P. G. 1975, *Astrophys. J.*, **196,** 51.
Ryle, M., Caswell, J. L., Graham Hine, G. S., Shakeshaft, J. 1978, *Nature,* **276,** 571.
Scott, J. S., Chevalier, R. A. 1975, *Astrophys. J.*, **197,** L5.
Shklovskii, I. S. 1977, *Soviet. Astr.*, **21,** 371.
Shukre, C. S., Radhakrishnan, V. 1980, *Astrophys. J.*, submitted.
Sturrock, P. A. 1971, *Astrophys. J.*, **164,** 529.
van den Heuvel, E. P. J. 1977, *Ann. N. Y. Acad. Sci.*, **302,** 14.
Weiler, K. W., Panagia, N. 1978, *Astr. Astrophys.*, **70,** 419.
Woltjer, L. 1974, in *Supernovae and Supernova Remnants,* Ed. C. B. Cosmovici, D. Reidel, Dordrecht.

J. Astrophys. Astr. (1980) **1,** 33–45

The Role of General Relativity in Astronomy: Retrospect and Prospect*

S. Chandrasekhar *Laboratory for Astrophysics and Space Research, The University of Chicago, Chicago, USA*

My last attendance at a meeting of the International Astronomical Union was forty-four years ago when it met in Paris in 1935. I do not doubt that my being asked to give an invited discourse at this meeting is a personal courtesy extended to me by your distinguished President recalling, perhaps, the years when he and I were colleagues together at the University of Chicago.

I am aware that associated with my absence from these meetings for nearly half a century is the fact that during most of this period—if not all of it—my interests, at different times, have been outside whatever may have been the prevailing trends in the mainstream of astronomy. I am afraid that on this account, the point of view I shall present—retrospectively and prospectively—will not be in conformity with the trends currently prevailing. I must therefore begin by asking for your patience and for your forbearance.

Dr Blaauw, when he invited me to give one of the three discourses at this meeting, suggested that in selecting a topic I might wish to take into account the fact that this year is the centennial of Einstein's birth. The subject of my discourse is in accordance with that suggestion.

The general theory of relativity was conceived by Einstein in the faith that laws appropriate to the different domains of the physical sciences must be mutually and harmoniously consistent with one another. Since Newton's laws of gravitation are based on the notion of instantaneous action at a distance, it is discordant with the precepts of the special theory of relativity derived, in the first instance, from Maxwell's laws governing electrodynamics. Therefore, argued Einstein, the Newtonian laws of gravitation must be modified to eliminate this discordance by allowing for the finiteness of the velocity of light.

Besides, at the base of the Newtonian theory was the enigmatic fact of the equality of the inertial and the gravitational mass—an empirically found equality to which Newton gave its deserved prominence by stating it in the opening sentences of his *Principia.* Einstein wished to eliminate this element of magic in the Newtonian theory by some general principle. The general principle is, of course, his principle of equivalence.

*Invited discourse delivered at the Seventeenth General Assembly of the International Astronomical Union held at Montreal, Canada and reprinted with the permission of the author, the International Astronomical Union and D. Reidel Publishing Company.

Even with the principle of equivalence as a base and the special theory of relativity as a guide, the formulation of a consistent theory of gravitation is fraught with ambiguities. But Einstein succeeded in formulating his general theory of relativity by a combination of physical reasoning and mathematical arguments of simplicity and elegance. It was, as Weyl stated, a triumph of speculative thought. And the fact that Einstein was able to arrive at a complete and a coherent physical theory by such speculative thought is the reason why, when we follow his thoughts, we feel as though a 'wall obscuring truth has collapsed'—quoting Weyl once again.

The element of controversy and doubt, that have continued to shroud the general theory of relativity to this day, derives precisely from this fact, namely, that in the formulation of his theory Einstein incorporates aesthetic criteria; and every critic feels that he is entitled to his own differing aesthetic and philosophic criteria. Let me simply say that I do not share these doubts; and I shall leave it at that.

The general theory of relativity is a theory of gravitation; and like the Newtonian theory of gravitation, which it refines and broadens, its natural home is astronomy. It is, therefore, not surprising that the early interest in the general theory was related to the verification of the small departures from the Newtonian theory which it predicts in the astronomical domain.

As is well known, the three classical tests relate to:

(i) the dependence of the rate of a clock on the value of the gravitational potential at its location;

(ii) the deflection that light must experience as it traverses a gravitational field; and

(iii) the slow precession which the Kepler orbit described by a planet must experience.

Of these three tests, the first is not really a test of the particular form of Einstein's equations; it is rather a test of the principle of equivalence.

Perhaps the best way to explain what particular features of the theory are verified by the different tests is to consider the coefficients of the metric to which they refer.

We all know that in space, free of any gravitational field, the appropriate geometry is that of special relativity, associated with the Minkowskian metric,

$$ds^2 = -c^2dt^2 + (dx^2 + dy^2 + dz^2), \tag{1}$$

where c denotes the velocity of light. The principle of equivalence requires that we must replace this metric by

$$ds^2 = -c^2dt^2\,(1 - 2U/c^2) + (dx^2 + dy^2 + dz^2), \tag{2}$$

where U *is* the gravitational potential determined by Poisson's equation:

$$\nabla^2 U = -4\pi G\rho. \tag{3}$$

By this generalisation, the intervals of the proper time, $d\tau_1$ and $d\tau_2$, at locations where the gravitational potentials are U_1 and U_2, are in the ratio

$$d\tau_1/d\tau_2 = [(1 - 2U_1/c^2) / (1 - 2U_2/c^2)]^{1/2} = 1 - (U_1 - U_2)/c^2 \tag{4}$$

—a relation which implies the slowing down of a clock as it is transported to regions of higher gravitational potential. This predicted slowing down of a clock has, as is known, been experimentally confirmed by the experiments of Pound and Rebka.

If one supposes that the metric (2) is adequate to determine the deflection of a light ray as it traverses a gravitational field, then one would find, as Einstein found in 1911, that a light ray grazing the solar disc must be deflected by 0·83". Indeed, Einstein thought in 1911 that 0·83" was the amount of the deflection to be expected; and an expedition which had set out to verify this early prediction was aborted by the beginning of World War I.

The full theory of Einstein requires that for the purposes of predicting the deflection of light, the metric must be modified to the form

$$ds^2 = -c^2(1 - 2U/c^2)dt^2 + (1 + 2U/c^2)(dx^2 + dy^2 + dz^2). \tag{5}$$

The factor $(1+2U/c^2)$ in front of the spatial element $(dx^2 + dy^2 + dz^2)$ represents the curvature of space and is a genuine general relativistic effect. It is only when this additional modification of the metric is taken into account, do we find that the theory predicts a deflection of 1·7" for a light ray grazing the sun's disc.

As is well known, this latter value for the deflection of light, rather than 0·87″ or 3·4″, was confirmed by the British eclipse expeditions of 1919 under circumstances which catapulted Einstein to world renown.

In recent times this prediction concerning the deflection of light has received much more precise confirmation from long base-line interferometric radio observations of the two quasars 3C 273 and 3C 279 which are 9° apart and which are occulted by the sun every year in October. The latest analysis of these observations confirms the predictions of the general theory of relativity to a fraction of a per cent. A related test consists in measuring the round-trip radar travel-time in the solar system; and the results of these experiments by Shapiro and his associates again confirm the predictions of the general theory (based on the metric (5)) to within experimental errors.

The last of the major tests relates to the precession of a Keplerian orbit. This effect depends on completing the metric (4) so that it may provide consistent equations of motion allowing for all first-order departures from the Newtonian theory. The appropriate form of the metric then takes the form

$$\begin{aligned} ds^2 = &-[1 - 2U/c^2 + (\ldots)/c^4](dx^\circ)^2 + (P_\alpha/c^3)dx^\circ dx^\alpha \\ &+ (1 + 2U/c^2)[(dx^1)^2 + (dx^2)^2 + (dx^3)^2], \\ &(x^\circ = ct,\ x^1 = x,\ x^2 = y,\ x^3 = z) \end{aligned} \tag{6}$$

where the terms of order c^{-4} and c^{-3} depend on the distribution of matter and motion in the central mass. In particular, P_α depends only on the presence of internal motions and we may neglect it in evaluating the rate of precession of the Keplerian orbit of a planet round the sun since its rotation is slow and hardly makes any contribution.

The observed precession of 43″ per century of the orbit of Mercury was shown, already by Einstein in his first publication, to be in perfect accord with the predictions of his theory.

More recently, in the binary pulsar discovered by Hulse and Taylor, the rate of precession of the orbit, as determined by these authors, is 4·2° per year. And this observed rate would lead one to infer that the total mass of the binary pulsar is 2.83 ☉. I should however point out that the recent observations by Crane, Nelson, and Tyson suggest that the companion of Hulse and Taylor's pulsar may have been optically detected; and if the indicated presence of an optical companion should be confirmed, then inferences that have been drawn concerning this pulsar require a re-evaluation.

May I at this point emphasise that the confirmations of the general theory of relativity of which I have spoken relate only to the first non-trivial departures from the Newtonian theory predicted by the general theory and as such they refer only to two or at most three of the coefficients of the terms of the lowest order in a post-Newtonian expansion of the metric beyond those required by the principle of equivalence. It is clear that there is no hope, in the foreseeable future, to verify the coefficients of the terms of higher order that are present in approximations beyond the post-Newtonian. On this account, the principal question which is currently debated, in the context of the elaborate and the expensive experiments conducted to verify the general theory, is not whether the predictions of the general theory are confirmed; it is, rather, the viability or otherwise of the innumerable theories, alternative to Einstein's, that continue to proliferate. Before the present precise confirmations of the particular predictions of the general theory, to which I have made reference, were available, one had to contend with theories which were *ad hoc* on. all accounts. Now, the only difference is that authors of alternative theories must arrange that they agree with Einstein's theory in the lowest order *i.e.* with the two or three coefficients in the post-Newtonian expansion of the metric which are involved. When I view these theories, I am reminded of what E. A. Milne once told me: Given a finite set of observational constraints, ' It cannot be beyond the wit of man to construct theories which will meet those constraints.' And certainly there has been no lack of wit in constructing theories alternative to Einstein's. I hope you will forgive me if I recall in this connection an admonition of Eddington's, 'The off chance that posterity may find wisdom in our words is no reason for making meaningless noises.'

I now turn to the role which general relativity plays in our understanding of the largescale structure of the universe *i.e.* in the realm of cosmology. I think it can be fairly said that the only aspect of general relativity with which most astronomers were concerned, up until the early sixties, is in the cosmological models it provides for interpreting the results of observations. To a large extent the role, as perceived, was an exaggerated one; and for the following reasons.

The basic facts one was concerned with in cosmology before the discovery of the microwave background-radiation are the following:

(i) In a first approximation the distribution of the extragalactic nebulae is locally homogeneous and isotropic.

(ii) The galaxies are receding from us and one another with velocities which are proportional to their mutual distances—relations codified in Hubble's law.

As was pointed out and emphasised by E. A. Milne, these facts have a very simple interpretation which requires no special appeal to any particular theory. The facts imply that all the nebulae, we now observe, must have been, at one time, collected together in a small volume of space. This inference is no more than the common inference which one would draw from a swarm of bees flying radially outward from a tree, namely, that there was a beehive in the tree! However, (again, as Milne emphasised) a homogeneous swarm of particles radially expanding from one of the particles has a remarkable property. A simple application of the parallelogram of velocities shows that the description will be the same with respect to any other particle in the swarm provided one does not go too near the boundary. In such a system, every local observer can, in the words of Eddington, consider himself as the plague-spot of the universe! In other words, a cosmological principle must prevail. This is a straightforward interpretation of very simple facts. What is remarkable about the application of general relativity to the cosmological problem is that requirements of homogeneity and isotropy do not allow a static universe: it can only be an expanding (or a contracting) one in which, locally, a Hubble relation must obtain. In making this assertion, I am, of course, supposing that the cosmical constant is zero. It will be recalled that Einstein introduced the cosmical constant with the sole purpose of permitting a static homogeneous universe in the framework of his theory. With a nonvanishing cosmical constant, one has an additional adjustable parameter. If the cosmical constant had not been invented, much of the game in which cosmologists, both theoretical and observational, have indulged themselves would have been spoiled.

I need not at this point go over the facts which must be familiar to all of you, namely, that the postulates of homogeneity and isotropy yield, in the framework of general relativity, the Friedmann models associated with the Robertson-Walker metric.

The Friedmann model commonly described as the ' big-bang ' model for the universe, strictly interpreted, implies that the universe began in an initial singularity and, if the universe should be a closed one, will end in a future singularity. The fundamental question in this context is how seriously one should take the predicted singularities. One could well be sceptical of extrapolating the Friedmann models backwards to the time when the radius of the universe was zero, and in the case of the closed models, forward to the time when the radius of the universe will again tend to zero. For, the Friedmann models assume *strict* spherical symmetry, *strict* homogeneity, and *strict* isotropy; and none of these assumptions is strictly realised or can be realised. One can therefore argue that some slight inhomogeneity, some slight anisotropy, and some slight departures from exact spherical and strict radial flow will replace the singularity by a state of high mean density which need not transcend any ' reasonable' limit which we may wish to impose. This scepticism was widespread during the fifties and the early sixties; and it was maintained by some of the most perceptive cosmologists of the time, McCrea and Lifshitz and Khalatnikov, for example. Thus, in a survey of cosmological theories written by McCrea in 1962, we find the statement: ' There, is no known feature of the universe that gives any indication of its ever having been in a state of extreme congestion as required by the Friedmann models.'

One's views with respect to the occurrence of singularities in solutions describing the evolution of gravitating physical systems in general relativity changed radically in 1965 when Roger Penrose proved that, so long as matter obeys certain very reasonable conditions (such as that the energy density as measured by an observer, in a frame of reference in which he is at rest, is always positive), singularities are inevitable once a process of collapse has started and a point of no return has been reached. (Subsequent theorems by Penrose and Hawking have succeeded in relaxing the original conditions of Penrose.)

The essential reason for the occurrence of singularities in general relativity is that every force which operates against collapsing to a singularity in the Newtonian theory (such as pressure or rotation) only adds to the inertia of the system and enhances the very gravitational force which is the cause of the collapse.

I shall return to the problem of gravitational collapse presently, but the point I wish to emphasise now is that the deduction that the universe very likely did begin in an initially singular state is not based solely on the discovery of Penzias and Wilson as is commonly believed. What their discovery does imply is that the present observed homogeneity and isotropy of the universe can be extrapolated backwards to a time when the radius of the universe was a 1000–2000 times smaller than it is at present and the physical conditions of density and temperature were such that the recombination of protons and electrons into hydrogen atoms took place, radiation and matter got decoupled, and the present matter dominated era began.

With the assurance that the present homogeneity and isotropy prevailed at the time of the electron-proton recombination, the singularity theorems of Penrose and Hawking give us the needed confidence to extrapolate further back in time. As is well known, this extrapolation backwards to three minutes from the initial singularity allows us to account for the cosmic abundance of helium and deuterium provided—and this is an important proviso—we incorporate in the calculations the empirically determined ratio of 10^9 for the number of photons to the number of baryons in the universe.

The densities and temperatures at which nucleosynthesis took place and the present abundance of helium was established are by no means extreme: the densities are comparable to, in fact much less than, what they are in atomic nuclei. But if the universe was in that state, the singularity theorems of Penrose and Hawking place no limit on the densities and temperatures to which we may—indeed must—extrapolate backward.

It is generally thought that quantal effects will require modifications of the general theory of relativity when we wish to discuss phenomena which may occur (rather will occur) in regions whose linear dimensions are of the order of the Planck length $(\hbar G/c^3)^{1/2} \sim 1{\cdot}6\times10^{-33}$cm and in intervals of time of the order of Planck length/velocity of light ($\sim 5{\cdot}3 \times 10^{-44}$s). It appears that at these extreme densities and temperatures there will be spontaneous creation of particles even as they occur at the horizons of black holes as Hawking radiation. One of the most interesting aspects of general relativity, in its applications to cosmology, is this interface which it provides for a unification of general relativity, quantum theory, and elementary particle physics. Regardless of the final outcome of these investigations, it would appear that the occurrence of cosmological singularities in the framework of general relativity raises some of the deepest questions in current physical thought.

I now turn to what has become one of the central problems of astronomy, namely, that of gravitational collapse.

While one can readily concede that much of the detailed calculations carried out at present depend on information concerning the physical state of dense nuclear matter derived in recent years, the basic reason for considering gravitational collapse in the context of the late evolution of stars was clearly recognised and stated more than forty-five years ago.

As is well known, stars with masses exceeding a certain limit do not have finite equilibrium states determined by electron degeneracy. This limiting mass is 14 $\odot$ if a mean molecular weight of 2 per electron is assumed. The existence of this limiting mass in turn implies that in the final stages of the evolution of stars, their contraction cannot be arrested by the zero-point degeneracy pressure of the electrons. This result appeared so secure that statements such as these were made at the time.

‘ *Given an enclosure containing electrons and atomic nuclei* (*total charge zero*), *what happens if we go on compressing the material indefinitely* ?’ (1932).

‘ The life history of a star of small mass must be essentially different from the life history of a star of large mass. For a star of small mass the natural white-dwarf stage is an initial step towards complete extinction. A star of large mass cannot pass into the white-dwarf stage and one is left speculating on other possibilities.’ (1934)

Eddington clearly recognised that the existence of this upper limit to the mass of completely degenerate configurations, *if accepted*, implied inevitably the occurrence of black holes as the end products of the evolution of massive stars at least in some instances. He thus stated in January 1935:

‘ The star apparently has to go on radiating and radiating and contracting and contracting until, I suppose, it gets down to a few kilometers radius when gravity becomes strong enough to hold the radiation and the star can at last find peace.’

But he went on to say:

‘ I felt driven to the conclusion that this was almost a *reductio ad absurdum* of the relativistic degeneracy formula. Various accidents may intervene to save the star, but I want more protection than that. I think that there should be a law of nature to prevent the star from behaving in this absurd way.’

Indeed, since Eddington considered the conclusion derived from the Fermi degeneracy of electrons, allowing for the effects of special relativity, as leading to a *reductio ad absurdum*, he modified the relativistic degeneracy formula so that finite equilibrium states will be possible for all masses.

It is difficult to understand why Eddington, who was one of the early enthusiasts and staunchest advocates of general relativity, should have found the conclusion that black holes may be formed during the course of the evolution of stars so unacceptable. But the fact is that Eddington’s supreme authority in those years effectively delayed the development of fruitful ideas along these lines for some thirty years.

I hope you will forgive me if I recall on this occasion that at the last meeting of the International Astronomical Union in 1935 that I attended, Eddington stated his views, that I have quoted, in no uncertain terms in a report he gave at a meeting of the Commission on the Internal Constitution of the Stars. I passed on a note to Henry Norris Russell, who was presiding on that occasion, requesting that I be allowed to express views contrary to Eddington's. But I was denied that request.

The question whether the contraction of a massive star in excess of the critical mass can be arrested at a stage when matter attains nuclear density of 10^{13} g cm^{-3} was in part answered by an investigation of Oppenheimer and Volkoff in the late thirties on the equilibrium states of neutron stars. This investigation required, of course, the application of the equations of hydrostatic equilibrium in the framework of general relativity. But it is an entirely general consequence of the relativistic equations of equilibrium that the range of allowed masses must necessarily have an upper limit. I shall explain the origin of this upper limit a little later. The actual value of the maximum mass of a neutron star depends on the exact form of the equation of state; but upper limits to the attainable maximum can be set as Hartle and others have shown. But regardless of what this upper limit may be, it is clear that sufficiently massive stars must, in some cases at least, find that peace which Eddington considered as a *reductio ad absurdum.*

There are many different groups of investigators who are now exploring the mechanics of gravitational collapse to answer questions such as these. What is the nature of the remnants that will be left behind during such collapse ? To what extent is it justifiable to consider such remnants as the remnants of supernova explosions? What may be the amount of energy radiated as gravitational waves during such collapse? These and other related questions are being discussed at various sessions at this meeting. I shall say no more about them, but pass onto what the general theory of relativity provides as solutions appropriate for black holes.

A solution describing a stationary black hole must have the following properties. It must partition space into two regions: an inner region bounded by a smooth surface which is the envelope of null geodesies; and an outer region which becomes asymptotically flat *i.e.* it becomes the familiar spacetime of the special theory of relativity. The bounding surface separating the two regions defines the horizon of the black hole; and it is a necessary consequence of the definition that the space interior to the horizon is incommunicable to the space outside.

It is a startling fact that with these simple and necessary restrictions on a solution to describe a black hole, the general theory of relativity allows only a single unique two-parameter family of solutions. This is the Kerr family of solutions in which the two parameters are the mass and the angular momentum of the black hole. It includes Schwarzschild's solution as a limiting case appropriate for zero angular momentum.

Karl Schwarzschild derived his solution in December 1915 within a month of the publication of Einstein's series of four short papers outlining his theory. Schwarzschild sent his paper to Einstein for communicating it to the Berlin Academy. In acknowledging the manuscript, Einstein wrote, 'I had not expected that the exact solution to the problem could be formulated. Your analytical treatment of the problem appears to me splendid.'

Roy Kerr derived his solution in 1962. I should include this discovery of Kerr as among the most important astronomical discoveries of our time. It is, in my judgement, the only discovery in astronomy comparable to the discovery of an elementary particle in physics.

I shall now briefly consider the nature of the spacetimes around black holes described by the Schwarzschild and the Kerr solutions. The best way to visualize them is to exhibit the 'light-cone structure' in the manner of Roger Penrose.

Imagine that at a point in space, a flash of light is emitted. Consider the position of the wave front of the emitted flash of light at a fixed short interval of time later. In field-free space, the wave front will be a sphere about the point of emission. But in a strong gravitational field, this will not be the case. The sphere will be distorted by the curvature of spacetime about the point of emission.

Fig. 1 displays these wave fronts at various distances from the centre of symmetry of the Schwarzschild black hole. The section of the wave fronts by a plane through the centre of symmetry is illustrated. One observes that the sections of the wave fronts are circles far from the centre as one should expect; they are, however, progressively displaced asymmetrically inward as one approaches the centre. And on the *horizon* the wave front is directed entirely inward towards the centre with the point of emission on the wave front—the wave front has become tangential to the horizon. This is clearly the reason why light emitted from the horizon of a black hole does not escape to infinity. The situation in the interior of the horizon is even more remarkable. The wave front does not include the point of emission:

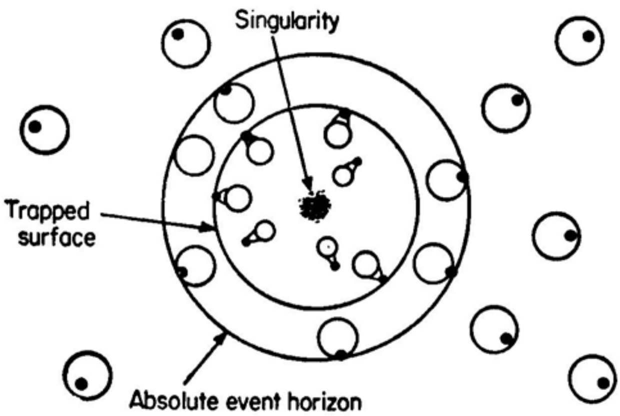

Figure 1. Effect of the curvature of spacetime on the propagation of light from points in the neighbourhood of a Schwarzschild, (nonrotating) black hole.

the wave front has detached itself. And since no observer can travel with a speed faster than that of light, it follows that there can be no stationary observers within the horizon—the inexorable propulsion of every material particle towards the singularity at the centre cannot be avoided.

Turning next to the geometry of the spacetime in Kerr geometry, we illustrate in Fig. 2 sections of the wave fronts of light emitted at various points on the equatorial plane of the Kerr black hole. The singularity in this case is a ring around the centre in the equatorial plane. In contrast to the Schwarzschild geometry, we have to distinguish, besides the horizon—where the wave front is entirely inside the horizon—a second surface where the wave front just manages to be attached to the source of emission. This second surface describes what has been called the ergosphere. In the region between the ergosphere and the horizon, while the wave front has detached itself from the point of emission, it is still possible for a particle, with a sufficient velocity suitably directed, to escape to infinity. The importance of this intermediate region is that it is possible for a particle entering this region from infinity to break up in two in such a way that one of the fragments is absorbed by the black hole, while the other escapes to infinity with an energy which is in excess of that of the incident particle. This is the so-called Penrose process for extracting the rotational energy of the Kerr black hole. An analogous phenomenon occurs when electromagnetic or gravitational waves of sufficiently small frequencies are incident on the black hole in suitable directions. In these cases, the reflection coefficient for such incident waves exceeds unity and is called super-radiance.

One of the questions that has been extensively studied in the context of black holes concerns the amount of energy that can be radiated as gravitational waves when objects fall into black holes or, indeed, when two black holes collide. It appears from the investigations of Detweiler that substantial energies can be radiated away only in collisions in which the object circles the black hole, at least once, before it falls in. I shall not discuss these questions any further. And I shall not also discuss, for lack of time, the many astrophysical questions relating to the physical phenomena, such as the emission of Xrays, which may be manifested during the accretion of matter around black holes; nor shall I consider the interesting dynamical questions relating to the altered distribution of stars around massive black holes that are presumed to occur at the centres of active galaxies.

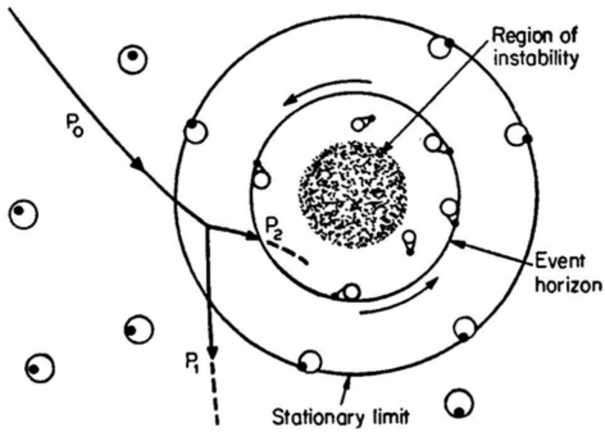

Figure 2. Equatorial cross-section of a Kerr (rotating) black hole. The positions of the wave fronts of light signals emitted at various points should be contrasted with those shown for the Schwarzschild black hole in Fig. 1. The rotational energy of the Kerr black hole can be extracted by a particle (P_0) that crosses thestationary limit from outside: the particle divides into two particles, one of which (P_2) falls into the black hole while the other (P_1) escapes from the ergosphere with more mass energy than the original particle (P_0).

I now turn to consider what the prospects may be for general relativity in astronomy. I am aware that it is a dangerous pastime for anyone to put on the cloak of a prophet; and it is certainly not my intention to play that part. What I do wish to say is more in the nature of reflections. I hope you will forgive me if they appear to you no more than a reflection of my own personal attitudes.

The general theory of relativity is a theory of gravitation and as I said at the outset, its natural home is in astronomy in the sense that its manifestations, whatever they may be, must be in the realm of astronomy. On this account one may be safe, I think, in expecting that the true role of general relativity in astronomy will be in providing as a basis for our understanding, its consequences under well-defined conditions, consequences so secure that we may incorporate them, on an equal footing, with other established facts of observation. In making this statement I am envisaging a role for theory in astronomy which is largely unrecognised and largely not practised. Since this is the case, I should like to clarify what I mean in the context of certain consequences which follow from the general theory of relativity.

Eddington once told me that his interest in the internal constitution of the stars arose from his interest in developing a pulsation theory for Cepheid variability; and how this interest led him to a study of the radial oscillations of gaseous stars in radiative equilibrium. It is therefore natural that one of the first problems in relativistic astrophysics which was considered in the early sixties was precisely the problem of the radial oscillations of a gaseous star in the framework of general relativity. This happens to be a particularly simple problem. Indeed, Eddington could have solved it in 1918; and certainly in 1934. The solution to this problem at once led to a qualitative difference in the criterion for the dynamical stability which follows from the Newtonian theory and from the general theory of relativity. Allow me to take a little time to explain the nature of this difference.

It is well known that in the framework of the Newtonian theory, the condition for the dynamical instability of a star derived from radial perturbations is that the effective ratio of the specific heats γ or more precisely some average of it, is less than 4/3; and dynamical stability is guaranteed if γ, or some average of it, is in excess of 4/3. But this result is changed in the framework of general relativity. A star with a ratio of specific heats γ, no matter how high, will become unstable if its radius falls below a certain determinate multiple of the Schwarzschild radius. It is this fact which accounts for the existence of a maximum mass for a neutron star to which I referred to earlier; and, indeed, for the instability of *all* equilibrium configurations as they approach the value 9/8 of the Schwarzschild radius. (For a solar mass, the Schwarzschild radius is 2½ km; and it increases linearly with the mass.)

I may parenthetically note here that this important result that configurations in stable hydrostatic equilibrium in general relativity must have radii in excess of 9/8 of the Schwarzschild radius, was established by Karl Schwarzschild in February 1916 in his second paper devoted to general relativity and published just three months before he died.

This instability of relativistic origin has never been directly observed. Yet, one can be so confident of the predicted instability that we can incorporate it along with other more conventionally established facts in our attempts to understand astrophysical phenomena. Let me give an example.

As I have said, instability of relativistic origin will set in whenever the ratio of the specific heats is close to four thirds. This is the case for degenerate configuretions near the limiting mass; and the application of the relativistic criterion shows that they become dynamically unstable before the limiting mass is reached. Precisely what happens is the following. On the Newtonian theory, it can be shown that the period of radial pulsation decreases monotonically to zero as we approach the limiting mass; but in the framework of general relativity, because of the instability it causes, the period attains a minimum, just prior to the limiting mass and before the sequence becomes unstable. In other words, while general relativity does not modify to any appreciable extent the structure derived from the Newtonian theory, it changes qualitatively the period mass relation; it exhibits a minimum period that was absent in the Newtonian theory. This minimum period is about seven-tenths of a second. Since pulsars are known to have periods much shorter than this minimum value, the possibility of their being white dwarf configurations was ruled out; and this was a deciding factor in our concluding that pulsars are neutron stars.

I should add that instabilities of relativistic origin occur also in stars clusters; and it is clear that these theoretically predicted instabilities must be included in any discussion pertaining to the evolution of large agglomerations of mass, be they individual stars, clusters of stars, or clouds of gas.

I should next like to consider a second example in the same genre.

It is, I believe, a matter of common knowledge, that at some point along the Maclaurin sequence of rotating homogeneous oblate spheroidal masses, the triaxial Jacobian sequence branches off. And as Kelvin pointed out, already in 1883, the Maclaurin spheroid, while not dynamically unstable, is nevertheless secularly unstable at the point of bifurcation in the sense that any dissipative mechanism that may be operative will induce an instability and propel it along the Jacobian sequence. Thus if the rotating mass is viscous, then the e-folding time of the secular instability varies inversely as the coefficient of viscosity so that it becomes infinite in the limit of zero viscosity. While all these are relatively well known, it was not generally known, until recently, that at the point of bifurcation of the Maclaurin sequence, there are, in fact, two alternative sequences along which evolution may proceed: besides the Jacobin sequence, there is a second congruent Dedekind sequence. These ellipsoids of Dedekind, unlike the ellipsoids of Jacobi, are stationary in the inertial frame and owe their triaxial figures to internal vortical motions. Dedekind discovered these ellipsoids in 1860; but they were forgotten and ignored, along with a beautiful theorem which he discovered in this context, for more than a hundred years.

The relevance of the Dedekind sequence for astronomy emerged only recently in the context of general relativity. In general relativity, a dissipative mechanism is built into the theory in the sense that a non-axisymmetric perturbation which induces a variable quadrupole, or higher, moment will dissipate energy and angular momentum as a result of radiation-reaction and emission of gravitational radiation. On examination, it was found that this source of dissipation will induce a secular instability of the Maclaurin spheroid at the point of bifurcation and propel it along the Dedekind sequence. This was an unexpected result. But a far greater surprise was yet to come. In a paper of remarkable power and insight, John Friedman has proved that all rotating objects, I mean, *all* rotating objects, are unstable in the framework of general relativity by virtue of the same radiation-reaction. In my judgement, next to the discovery of Kerr's solution, Friedman's theorem is of the most far-reaching significance that has been proved in general relativity in the realm of astronomy.

To emphasise the generality of Friedman's theorem, let me only point out that our rotating earth is unstable in the framework of general relativity. The reason why, in spite of its instability, the earth has endured over a billion years is simply that the *e*-folding time of the relativistic instability is to be measured in billions of billions of years. But the security we on the earth have enjoyed cannot be shared by objects which during a process of gravitational collapse, or some other cause, attain radii of a few times their Schwarzschild radii. Clearly the instability predicted by Friedman must be taken into account in all discussions pertaining to gravitational collapse or the early formation of galaxies and stars.

In my attempt to clarify my views on the prospective role of general relativity in astronomy, I have left myself no time to discuss questions in the domain of general relativity which are currently actively being pursued. I am referring in particular to the continuing efforts, both theoretical and experimental, concerned with the detection of gravitational waves from astronomical sources. These efforts are not only in the building of detectors of greater sensitivity, but also in estimating the wavelengths and the amounts of gravitational radiation which we may expect from likely astronomical sources. And one dreams that eventually we may be able to detect a universal background of gravitational radiation similar to the universal background of microwave radiation. These are all specific questions which require specific answers. I have not dealt with them since there are others in the audience who can address themselves to these questions with a competence which I do not have. I have chosen instead to address myself to the nature of the larger role which general relativity may play in astronomy.

I began this discourse by stating that the real home of general relativity is astronomy. May I conclude by suggesting the likelihood that, in time, some of the fundamental aspects of astronomy will find their natural home in the general theory of relativity.

J. Astrophys. Astr. (1980) **1,** 47–66

Evidence for a Large Population of Shocked Interstellar Clouds

V. Radhakrishnan and G. Srinivasan *Raman Research institute, Bangalore* 560080

Received 1980 April 14; accepted 1980 May 29

Abstract. A 21 cm absorption measurement over a long path length free of the effects of differential galactic rotation indicates the existence of two distinct cloud populations in the plane. One of them consisting of cold, dense clouds has been well studied before. The newly found hot clouds appear to be at least five times more numerous. They have a spin temperature of ~ 300 K, an rms velocity of ~ 35 km s^{-1}, twice the total mass, and hundred times the kinetic energy of the cold clouds. Over long path lengths, the hot clouds have N_H/kpc ~ 2 × 10^{21} cm^{-2} kpc^{-1}, and are estimated to have individual column densities ⩽ 10^{20} cm^{-2}. We propose that they are shocked clouds found only within supernova bubbles and that the cold clouds are found in the regions in-between old remnants, immersed in an intercloud medium. We conclude that the solar neighbourhood must be located between old supernova remnants rather than within one.

Key words: 21 cm absorption—shocked clouds—spin temperature—high velocities

1. Introduction

A recent analysis (Radhakrishnan and Sarma 1980; hereafter Paper I) of the H I absorption spectrum of Sgr A obtained with the Parkes interferometer (Radhakrishnan *et al.* 1972a) has revealed, in addition to the other well known features, an unexpected, very wide, low optical depth feature, at zero velocity. According to these authors, the new feature represents an amount of neutral hydrogen in the Galaxy comparable to that in dense cold concentrations, and it contains most of the energy in mass motions of the interstellar gas. In this paper, we shall discuss and elaborate on these two statements and also present their implications for other studies of the interstellar medium.

We reproduce in Fig. 1 that part of the profile from Paper I relevant to the present discussion. The narrow central feature, Fig. 1b, represents typical cold concentrations such as have been extensively studied in other directions in the Galaxy and whose properties have been described by Radhakrishnan and Goss (1972). It is the wide feature (Fig. 1d) whose interpretation is the main subject of the pre sent discussion. We also list in Table 1, the parameters describing these two features that we shall use. here. The spin temperature characterising the hydrogen in the wide features was only mentioned in Paper I as being a few hundred degrees kelvin. We give in Table 1 a more specific value obtained as described in the Appendix by a comparison of the interferometer measurement (Fig. 2a) with the single dish measurement of Sanders, Wrixon and Mebold (1977) (Fig. 2b).

Two additional parameters of interest that follow from Table 1 are the average values of number and energy densities of the hydrogen in the wide feature

$$\langle n_H \rangle \approx 0{\cdot}5\ \mathrm{cm}^{-3},\ \text{and}\ (3/2)\,\rho\,\langle v^2 \rangle \approx 1{\cdot}5 \times 10^{-11}\ \mathrm{erg\ cm}^{-3}.$$

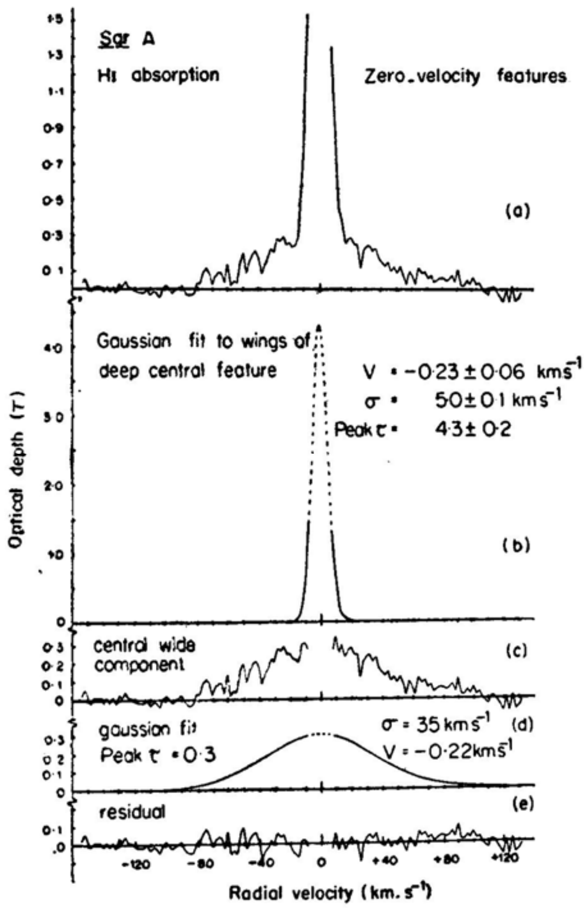

Figures 1a to e. Resolution of the zero velocity features a, in the H I absorption spectrum of Sgr A into two Gaussian b and d; the residuals c and e after subtraction of these components.

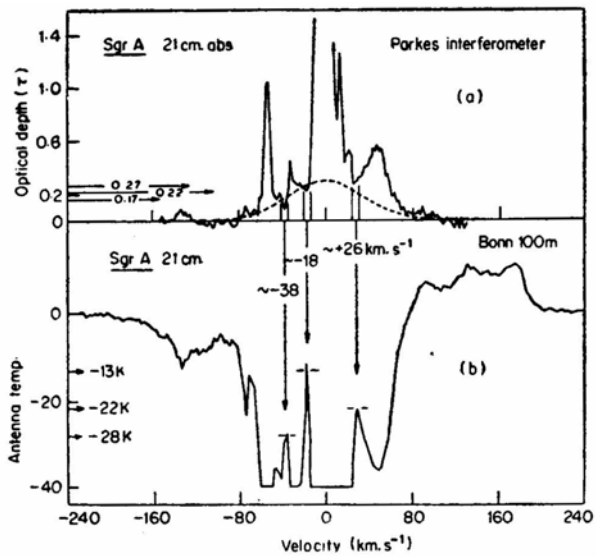

Figures 2a and b. The total HI optical depth profile obtained in the direction of Sgr A with the Parkes interferometer (from Paper I) a, and the antenna temperature profile obtained in the same direction with the Bonn 100 metre telescope (Sanders, Wrixon and Mebold 1977) **b**. See Appendix for discussion.

Table 1. Parameters of the Gaussian components fitted to the zero velocity features of the HI absorption spectrum of Sgr A (From Paper I).

Fig. No.	Velocity km s^{-1}	Peak τ	σ km s^{-1}	N_H/T_s 10^{19} cm^{-2} K^{-1}	T_s^* K	N_H 10^{21} cm^{-2}
1b	−0·23	4·3	5·0	9·8	80	8
1d	−0·22	0·3	35	4·9	300±50	15

*Taken from Radhakrishnan *et al.* (1972b) for the clouds in the narrow feature, and derived in the Appendix for the wide feature.

In the next section we shall identify the wide feature with low-optical-depth clouds distributed globally in the Galaxy; this is as opposed to a ‘ local’ origin, for example at the galactic centre. We shall then attempt to show that these clouds must have acquired their characteristics from collisions with the shock fronts of expanding supernova remnants. This will be followed by a discussion of the implications for some other theoretical and observational studies of the interstellar hydrogen; our conclusions will be summarised in the final section.

2. On the global origin of the wide feature

We shall repeat first the argument advanced in Paper I supporting a distributed origin for the wide feature (Fig. 1d), namely that the mean velocity was indistinguishably different from that of the narrow feature (Fig. lb) and from zero. The spin temperature of the wide feature, ~ 300 K, implies for pressure balance, about a fourth of the number density of atoms found in cold clouds. This combined with the high column density of ~ 15×10^{21} cm^{-2} requires the gas to be distributed in a large number of clouds; a single concentration would be too massive. All the gas associated with the galactic centre is known, from various studies of this region, to have velocities differing significantly from zero. On the other hand, a large number of clouds, or cloudlets, each with its own peculiar motion, if distributed along the line of sight to the centre, could be reasonably expected to have a mean velocity of zero.

The next argument we offer is through a comparison with optical observations, One of the earliest studies of the motions of interstellar clouds was carried out by Blaauw (1952) who analysed the measurements of Adams (1949) to determine the distribution of radial motions. The observed blends were separated into individual components, and both an exponential and a Gaussian were tried as fits to the distribution of velocities (Fig. 3). Although he had noted that the intensity of the

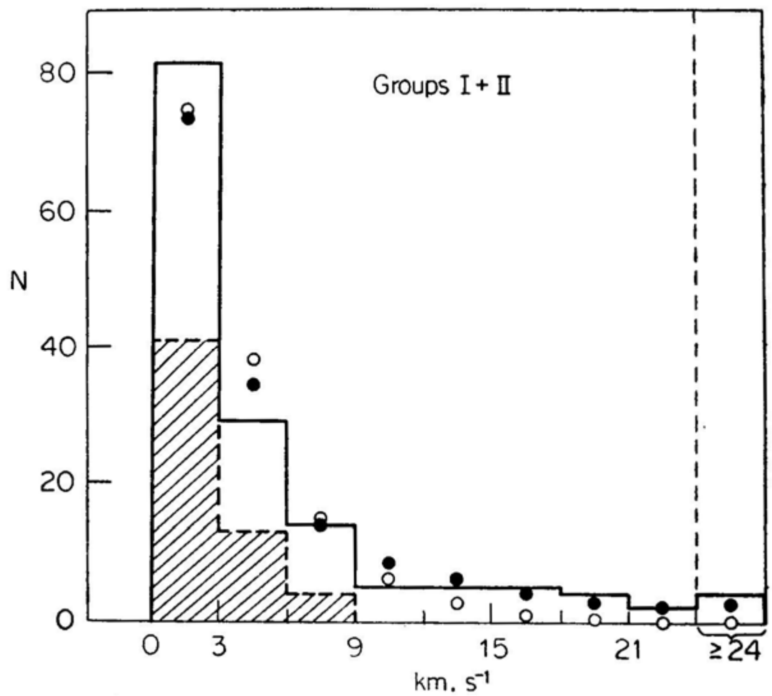

Figure 3. Reproduced from Blaauw (1952). Groups I+II represent stars whose distances were < 500 pc. The smooth curve represents the observed numbers of velocities in intervals of 3 km s^{-1} in groups I + II. The dashed curve represents the contribution due to the components with intensities > 6 in ADAMS' scale.
Circle : numbers computed on the basis of hypothesis A with $n = 3$, $\sigma = 5.5$ km s^{-1}.
Dots : numbers based on hypothesis B with $n = 3$, $\eta = 5.0$ km s^{-1}.

Ca II lines showed a correlation with velocity, in that those clouds with large peculiar velocities had weaker lines on the average, he did not attempt to separate them into two distributions. He concluded that the radial motions were satisfactorily described by a single exponential (Blaauw 1952).

An indication that there was more than one type of interstellar cloud (identifiable by its motion) was the correlation found by Routly and Spitzer (1952), of the ratio of sodium I to calcium II column densities with large peculiar velocities relative to the local standard of rest. The sodium-to-calcium ratio decreases with increasing velocity. This correlation was further investigated and confirmed by Siluk and Silk (1974) using more recent data for 64 stars. We show in Fig. 4a histogram constructed from the data in their paper of the velocities observed in the direction of these stars. The velocity range is much larger than in the sample of Blaauw (Fig. 3), and the histogram is much more suggestive of two distinct distributions, one of which can be well approximated by the Gaussian shown in Fig. 4'. The other distribution is clearly seen to be a wide one, but its shape cannot be reliably determined because of the poor statistics of this sample.

We show in Fig. 5 a folded version of the optical depth plot of Fig. la, and the similarity between it and Figs 3 and 4 clearly suggests that the low wide H I absorption feature is due to the higher velocity clouds discussed above which show weak lines and a sodium I to calcium II anomaly. In comparing these figures it must be remembered that in the optical case it is the numbers of clouds with a given velocity that are being summed, whereas in the H I profile it is the optical depths that are being added together. It may be noted that the fluctuations in the wings of the wide H I feature (Fig. 1c) are somewhat greater than would be expected from noise, and suggest individual cloudlike contributions rather than say from a uniform diffuse medium. As the optical observations were made in many directions in the

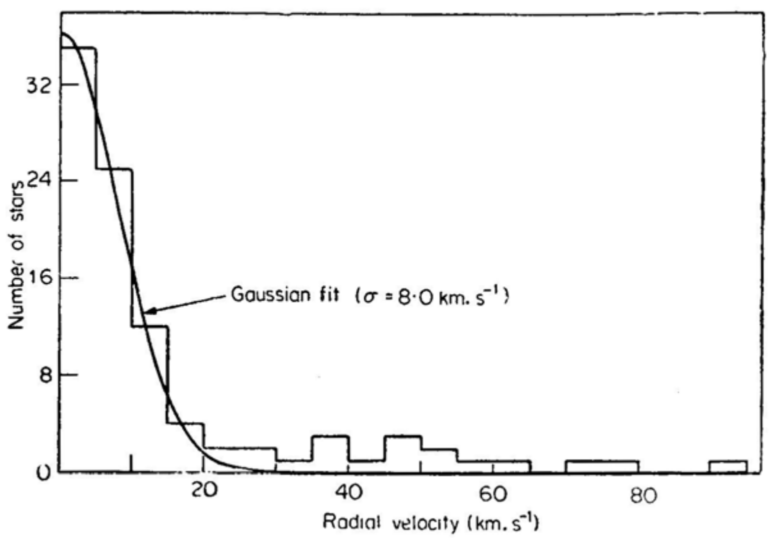

Figure 4. Histogram of radial velocities observed in the direction of 64 stars from the data in Siluk and Silk (1974). The low velocity features can be approximated well by the Gaussian shown. The higher velocity features are associated with anomalous ratios of sodium I to calcium II column densities.

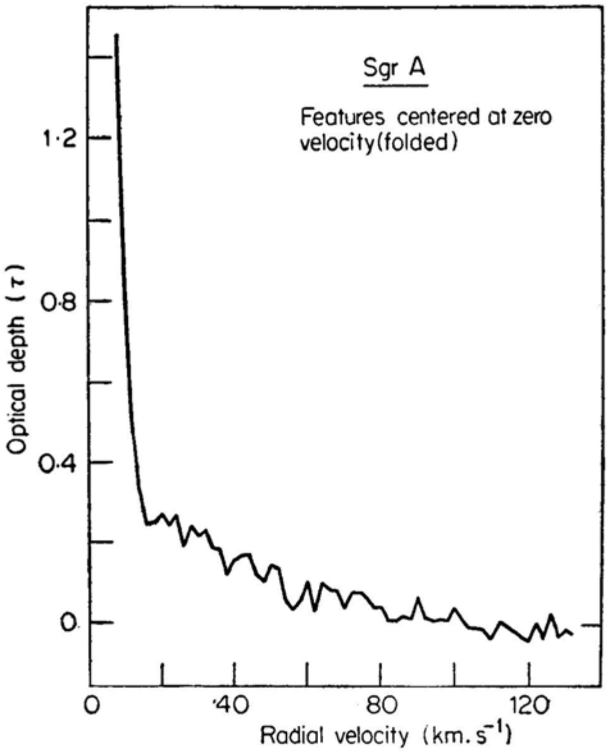

Figure 5. A folded version of the optical depth distribution of Fig. la. A similarity with the distributions of Figs 3 and 4 is evident, as also the presence of two distinct distributions.

Galaxy, the velocities are unconnected with motions near the galactic centre and are representative of all directions.

On the basis of an early study of H I absorption in a number of sources, Clark (1965) had already surmised that the narrower Gaussian distribution of cloud velocities obtained from 21 cm studies differed from the exponential found by Blaauw (1952) because the components at higher velocities were missed in the hydrogen study. A significant increase in the temperature of hydrogen clouds and the consequent decrease in their optical depths would make them harder to detect in absorption. On the other hand, the 21 cm *emission* from such optically thin clouds would be independent of temperature and therefore easily detectable A comparison of line velocities obtained both optically and at 21 cm led Heiles (1974) to note that optical absorption lines should perhaps be associated with emission rather than absorption lines obtained at 21 cm. Also Mast and Goldstein (1970), from a study of 21 cm emission features away from the plane, concluded that an exponential was a good fit for the velocity distribution they obtained. With hindsight, these two conclusions can be understood if there are also clouds at a higher temperature and with a lower column density (as we shall show presently) than those responsible for the typical 21 cm absorption lines. The reason that Mast and Goldstein (1970), as also Blaauw (1952), considered a single exponential an acceptable fit for the combined distribution was that it was limited in its velocity range ($\leqslant$ 30 km s^{-1}). The higher velocity features, which were missed because they were weaker, would have brought to light the existence of two distinct distributions.

The mean temperature of the clouds making up the wide feature is 300 K±50 as shown in Table 1. Since the gas is optically thin, this value must truly represent the harmonic mean temperature of these clouds. There is undoubtedly a distribution of clouds with temperatures from somewhat below to presumably much higher than 300 K. But as the typical temperature for cold concentrations is of the order of 80 K, we see that the higher velocity clouds are definitely hotter by a factor of 4. If overall pressure equilibrium is invoked, the number density n_H in these clouds should be approximately four times less than in the cold clouds. If N_H (cold) and N_H (hot) are the typical column densities per cloud of each variety, then

$$\frac{N_H\ \text{(hot)}}{N_H\,\text{(cold)}} \approx \left(\frac{M\ \text{(hot)}}{M\ \text{(cold)}}\right)^{1/3} \left(\frac{T_{\text{hot}}}{T_{\text{cold}}}\right)^{-2/3}.$$

The dependence on the mass ratio is weak as we see, but as $T_{\text{hot}} \approx 4T_{\text{cold}}$, the optical lines should be weaker in the hot clouds by at least a factor ~ 2·5. We estimate the hydrogen column densities to lie in the range 5–10 × 10^{19} cm^{-2}. For the 21 cm line however, the integral over velocity of the optical depth

$$\int \tau\, dv \propto \frac{N_H}{T_s}.$$

The ratio of the optical depths for equal masses is thus

$$\left(\frac{T_{\text{hot}}}{T_{\text{cold}}}\right)^{-5/3} \approx 1 : 10.$$

A lower mass, and increased turbulence, will be two additional factors that contribute to decreasing the *peak* optical depth of features due to hot clouds by over an order of magnitude from those of typical cold clouds.

There has been a longstanding difference in the number of clouds per kpc estimated from optical and radio measurements. Blaauw (1952) found 8–12 clouds per kpc while Radhakrishnan and Goss (1972) found only 2·5 per kpc even after allowing for various selection effects. Although the correction for instrumental blending applied by Blaauw has been criticised (see Heiles 1974), there is no question that there is a large difference in the numbers obtained. This serious discrepancy can now be understood in terms of the discussion in the previous paragraph, and is yet another argument supporting the picture presented above. If the majority of clouds along any given line of sight belong to the hotter and higher velocity category, they would have been below the sensitivity limit of the 21 cm survey on which the statistics were based.

Finally it may be noted that the total mass in such clouds is greater than in the lower velocity clouds. From Table 1 we see that the column density of the gas producing the wide feature is twice that of the gas represented in the narrow feature.

Assuming that this will be true over any long path length in the Galaxy, we are led to the conclusion that there is twice as much gas, and hence total mass, in the higher velocity clouds.

We wish to avoid confusion with the so-called high velocity clouds (HVC) and intermediate velocity clouds (IVC), referring to gas in differing velocity ranges and usually observed at *high latitudes*. We shall use the terms fast and/or hot in referring to the clouds we have just described, characterised by a $V_{\mathrm{rms}} \sim 35$ km s^{-1}, a T_{spin} of a few hundred degrees, and which are found in the *galactic plane*.

3. Association with supernova remnants

We have argued in the preceding section that the gas represented by the wide feature in the Sgr A profile consists of a large number of clouds characterised by a lower optical depth, a higher temperature and a higher velocity than typical cold clouds. They are more numerous, contain twice as much total mass, and are distributed as widely as the colder variety. If this picture is accepted, we shall now show that a connection with supernova remnants is inescapable.

The dominant role that supernova explosions must play in the dynamics of the interstellar gas has been stressed repeatedly by Spitzer (1956, 1968, 1978). That they must also play an important role in maintaining the heat balance was revealed by the Copernicus measurements. In addition to the discovery of the widespread coronal gas at temperatures close to a million degrees, and soft X-ray emission, it was possible to firmly establish that cosmic rays played little or no role in heating the interstellar gas (Williamson *et al.* 1974; Jenkins and Meloy 1974; York 1974; Spitzer and Jenkins 1975).

Several theoretical investigations in recent years have pointed out that the effects of supernova shocks must pervade most of galactic space. Cox and Smith (1974) proposed that the remnants would overlap each other and connect up in a network of tunnels filled with hot coronal gas. McKee and Ostriker (1977) have put forward the most comprehensive model yet for the interstellar medium in which three components are regulated by supernova explosions in an inhomogeneous substrate. In their model, as in other studies along the same lines (*e.g.* McKee, Cowie and Ostriker 1978) there is a natural and intimate connection between the heating of clouds and their acceleration as a whole. Earlier models while preoccupying themselves with temperatures, pressure equilibrium, etc. had said very little about the motions of the gas, because their heating mechanisms were independent of motions. In supernova models, on the other hand, clouds are accelerated by the same shock wave that also heats them up as they pass through it.

It has been recognised for many years that even to explain the motions of cold clouds with relatively low velocities, supernova energy was required as an input. Spitzer (1978) estimates that supernova shocks acting with 3 per cent efficiency can explain the observed cloud motions; he mentions specifically that the motions of ‘high velocity clouds’ have not been taken into account in his discussion. If all the spiral arm regions are pervaded by shock fronts, and if all standard-cloud motions and gas heating are to be attributed to them, one must surely appeal to the same source to explain the properties of a hotter, more numerous and more energetic population of clouds.

In the previous section we identified the clouds under discussion with those in the tails of the velocity distribution observed by Blaauw (1952), and a similar distribution from the more recent observations of Siluk and Silk (1974). The latter authors proposed, in fact, that these clouds were inside supernova remnants and returned to the more numerous data of Adams (1949) to substantiate their suggestion. Considering only velocities > 20 km s^{-1}, the number of clouds having an absolute velocity greater than V was found to be proportional to $1/V^2$. According to Siluk and Silk (1974), this would be in reasonable agreement with the acceleration of clouds in the adiabatic phase of the expansion of remnants.

A direct comparison between our profile and their distribution is not possible because, as stated earlier, it is the atoms and not clouds that have been added together in the 21 cm profile. A distribution of masses with different temperatures (and hence optical depths) would further modify the distribution. Although distributions other than a Gaussian, like that of Siluk and Silk (1974), provide a reasonable fit over the higher velocity part of the profile, the available signal-to-noise ratio is not adequate to enable a meaningful distinction to be made. Finally, theoretical work in this complicated field is short of providing an unambiguous radial velocity distribution to be expected for clouds accelerated by one or more shocks.

The reasonable fit to a Gaussian, as seen in Fig. 1, makes possible however, a very simple computation of the total energy in these clouds, and provides the strongest argument we have for associating them with supernova remnants. As the thermal energies form a minor contribution for both the narrow and wide components in the profile, we could directly compare the energies associated with the 'peculiar' motions of the H I atoms themselves. The dispersion of the wide component (σ_W ~ 35 km s^{-1}) is 7 times greater than that of the narrow component (σ_N ~ 5 km s^{-1}), and it contains twice as much mass. The ratio of kinetic energies is therefore $(\sigma_{W/}\ \sigma_N) \times (m_w\ /\ m_n) \approx 100$; the gas in the wide component has two orders of magnitude more energy than the cold clouds.

It would appear therefore that the motions of this population of clouds form the main reservoir of kinetic energy in interstellar neutral gas, as indicated in Paper I. If an input of supernova energy at a low efficiency is required to maintain even the motions of the cold clouds, we have no alternative but to ascribe the higher velocities of these hotter clouds to a more efficient utilisation of most of the energy in supernova shocks. Any theoretical model of the interstellar medium must, it appears to us, primarily account for their velocities, and for the difference from the velocity distribution of cold clouds.

If collisions between clouds are mainly responsible for dissipating the energies of their motions, then calculations such as by McKee and Ostriker (1977) (equations (58) to (61) of their paper), leading to a root mean square velocity of ~ 8 km s^{-1}, will have to be modified to explain the velocity spectrum of the hot clouds. The dissipation rate calculated on t h e basis of a *random* distribution of velocities of the order of 35 km s^{-1} leads to an embarrassingly high dissipation rate, much higher than the total input rate of energy from supernova explosions. On the other hand, if cloud-cloud collisions took very much longer, because clouds accelerated by the same shock tend to be moving in the same direction, then the dissipation rate would be reduced considerably.

That clouds probably do not move randomly, and hence rarely collide if ever, has also been concluded from observational studies of their motions by Heiles (1974), but in this case referring to colder material. In any event, we conclude that collisions between hot clouds must be relatively rare, and most likely less frequent than collisions with supernova shocks. As a consequence, many clouds may suffer several consecutive collisions with shocks, leading to faster, hotter and less massive clouds, to be found in the tail of the total distribution of velocities. Although the velocities of such clouds may be highly correlated in any particular region, a long line of sight will intersect many such domains and tend to produce a distribution with zero mean.

4. Discussion

4.1 *The Number of Hot Clouds*

We shall now discuss some of the implications of the conclusions reached in the preceding sections. We have seen that the total mass and the harmonic mean temperature of the gas in the hot clouds are approximately twice and four times the corresponding values in typical cold clouds. With these inputs, some constraints can be placed on the ratio of the number of clouds of each variety along a given line of sight. If the hot clouds are produced by the action of one or more shocks on cold clouds, we would expect their masses to be no higher than those of cold clouds, and very likely less, because of the evaporation which must accompany this process (McKee and Ostriker 1977).

Given the typical mass of such clouds, the radius will depend on the number density of atoms which will be about a fourth of that in cold clouds, if pressure equilibrium has established itself; the temperature in these clouds is four times that in cold clouds. The resulting ratio of the number of clouds per unit line of sight of each variety can be arrived at easily, and is given by

$$\nu_H / \nu_C = (\langle n_H \rangle / \langle n_C \rangle)\ (T_H / T_C)^{2/3}\ (M_C / M_H)^{1/3} = 5\ (M_C / M_H)^{1/3},$$

where ν is the number of clouds, $\langle n \rangle$ the average number density, T the temperature, M the mass, and the subscripts H and C refer to the hot and cold clouds respectively.

It varies from 5 to 1 for no change in mass but an increase in radius commensurate with pressure balance, and 6 to 1 for a decrease in mass to half that of cold clouds, and pressure balance. If there are 2·5 cold clouds per kpc, we could therefore expect a total of both varieties of 15 and 19 clouds per kpc respectively, for the two cases discussed above.

The number of clouds per kpc observed optically depends on the particular type and sensitivity of the observations. As mentioned earlier, Blaauw (1952) obtained 8 to 12 per kpc from the Ca II observations of Adams (1949). A recent photometric study by Knude (1979), in which special attention was paid to clouds producing only small reddening, yielded 6 to 8 clouds per kpc along a line of sight. Clouds not belonging to this special category would therefore contribute to substantially increasing this number.

High resolution interferometric observations by Hobbs (1974a) of the KI λ7699 line showed that there were 4·6 clouds per kpc (Hobbs 1974b). The choice of this particular line for the purpose of studying the properties of interstellar clouds was based on other considerations, and not for determining the frequency of occurrence of all types along the line of sight. That many clouds not producing a detectable KI λ7699 line exist, is seen from observations by the same author (Hobbs 1974a), in which the number of stars toward which the D_2 and λ7699 lines were observed were 77 and 17 respectively. This ratio suggests that the number of clouds per kpc producing D_2 lines could be as high as $77/17 \times 4{\cdot}6$ or ~21.

As the analysis by Blaauw (1952) was based on the early measurements of Adams (1949), of much lower sensitivity than the measurements of Hobbs (1974a), we feel that a reasonable estimate of the total number of clouds per kpc would be 15 to 20. Admittedly, our calculation of the number of clouds to be expected along a line of sight involved assumptions such as that clouds are spherical, which are certainly not borne out by observations. Our purpose was really to get a feeling for the increase in number, which we conclude is in good agreement with the other estimates, if the masses of, and number densities in hot clouds are typically less than those of the cold clouds.

Such a large number of hot clouds per kpc raises immediately the possibility of their being observable at intermediate and high galactic latitudes. We estimated a ratio of hot to cold clouds of ≈ 5:1, and it was found from the Parkes survey (Radhakrishnan *et al.* 1972b) that cold clouds are typically separated along a line of sight by one full scale-thickness of the galactic disk. We would therefore expect to see 2 to 3 hot clouds per half-thickness of the galactic disk, assuming for the moment that conditions in the solar neighbourhood are no different from the average over a long line of sight in the galactic plane. Several such clouds should therefore be encountered along any line of sight at intermediate and even high galactic latitudes; the optical depths of such clouds should be typically below 0·1, and the spin temperatures in the hundreds of kelvins.

Dickey, Salpeter and Terzian (1978) have carried out a 21 cm absorption survey at high and intermediate galactic latitudes with the upgraded Arecibo telescope, and found a number of absorption features with optical depths in the range 0·1 to 0·01 and spin temperatures of a few hundred degrees. They have also surmised (Dickey, Salpeter and Terzian 1979), that a substantial part of the optically thin hydrogen they saw in emission, but whose optical depth was below their limits of detection, consists of low density, warm, intermediate velocity clouds. These results are in good qualitative agreement with what would be expected on the basis of our previous conclusions.

4.2 *Spin Temperatures*

We turn now to a discussion of spin temperatures. A connection between spin temperatures and optical depths, in that hotter clouds would tend to be optically thinner, is certainly to be expected on general grounds. The simple-minded relationship derived earlier on the assumption of pressure balance predicts that $\tau \propto M^{1/3} \times T^{-5/3}$. If there was a dependence of mass on temperature of the form $M \propto T^{\beta}$, this would modify the relationship between τ and T depending on the value of β. If $\beta = -1$, meaning that the masses of clouds are inversely proportional to their temperature, this would lead to $\tau \propto T^{-2}$. The relationship derived empirically by Dickey, Salpeter and Terzian (1978) from their sample, with values of $(1 - e^{-\tau})$

spanning two orders of magnitude, reduces to this for small values of τ. While this might appear to be reasonably in agreement with what is expected, we have some reservations however.

The temperatures of ~ 30 clouds measured in the Parkes survey showed no discernible correlation with their optical depths which lie in the range $-1{\cdot}0 < \log(1 - e^{-\tau}) < -0{\cdot}1$. A better sample of over 40 clouds having $-1{\cdot}4 < \log(1 - e^{-\tau}) < -0{\cdot}1$ measured recently by Mebold *et al.* (1980) also shows no correlation of their spin temperatures with optical depth. These measurements are shown in Figs 6a and 6b. Thus, although a correlation of spin temperature with optical depth might be expected in any optical depth range, it appears that for clouds limited to the range $\log(1 - e^{-\tau}) \geqslant -1.0$, a significant empirical relationship of T_{spin} with τ is yet to be established.

If we assume that the principal reason for a difference in spin temperatures of interstellar clouds, is whether they belong to one or other of the two categories we have proposed, the measurements of Dickey, Salpeter and Terzian (1979) can be reconciled with those represented in Figs 6a and 6b. If this interpretation is correct, then the rms velocity for the higher temperature—and lower optical depth—features

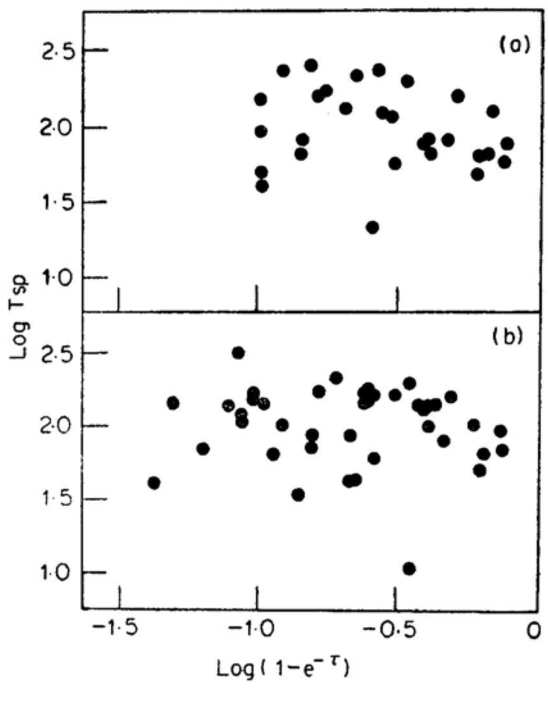

Figure 6a and b. The distribution of spin temperature versus optical depth for approximately 30 clouds measured in the Parkes survey (Radhakrishnan *et al.* 1972 b) a ; and for ~ 40 clouds measured recently by Mebold *et al.* (1980) b. For clouds with optical depths in this range, no definite trend is apparent in either distribution.

Found by them should by greater than for the lower temperature ones. This is precisely what was found by Dickey, Salpeter and Terzian (1978) as discussed at the end of § 4 of their paper and shown in Fig. 45 of the same.

A value of log $(1 - e^{-\tau}) = -1{\cdot}0$ appears to be a reasonable dividing line below which hot, shocked clouds begin to make their appearance. The less sensitive surveys selected the cold clouds with higher optical depths, which apparently have little or no correlation with their spin temperatures. On the other hand, the Arecibo survey with its greater sensitivity, included several of the hot clouds; but a reliable empirical relationship between T and τ for the hot clouds alone may have to await the detection of larger numbers of this variety. In any case, the clear difference in rms velocities noted by Dickey, Salpeter and Terzian (1978), is further confirmation of our hypothesis of two distributions of clouds. The increased number of clouds per kpc found in the Arecibo survey, as compared to the Parkes value, is also in agreement with the picture we have outlined.

4.3 *Emission from Hot Clouds*

A serious quantitative disagreement exists however, between our picture and the amount of emission from optically thin hydrogen observed at intermediate and high latitudes. The average column density of optically thin material normalised to $|b| = 90°$, is $\sim 1{\cdot}4 \times 10^{20}$ cm^{-2} (Radhakrishnan *et al.* 1972b; Mebold 1972; Dickey, Salpeter and Terzian 1979). If the column density per unit path length of the hot clouds we see in the direction of the centre, were also to hold in the solar neighbourhood, there should be in *these clouds alone,* twice this observed value. If all the observed emission is attributed to them, this would imply that there is no intercloud gas at all, and we would still have accounted for only half the expected amount. Further, if they are separated clouds, as suggested by the optical evidence, they will not contribute to the pressure required to hold the cold clouds together, and which must therefore come only from hot coronal gas.

It seems to us that there is no compelling reason why the density of hot clouds in the solar neighbourhood should conform to the average obtained over a long line of sight. One would, in fact, expect fluctuations over a length scale comparable to the size of remnants at the stage when the shocks have become too weak to effecttively accelerate clouds; also, over distances comparable to the separation between old remnants. The size of the solar neighbourhood observable at intermediate and high latitudes could well be of the order of the latter. If fluctuations can occur in the amount of hot-cloud material, as we find from its local deficiency, it is possible that the amount of intercloud material in any locality can also fluctuate over such distances. It is not inconceivable that there is an inverse correlation between the two, particularly if clouds of the two varieties are generated in different regions. We shall advance reasons for proposing such a separation in a later part of this section.

4.4 *Velocities of the Emitting gas*

We believe that a separation of the optically thin gas at intermediate and higher latitudes into an intercloud and hot cloud components may be possible by a careful analysis of emission profiles in different directions. Most of the optically thin gas observed in the Parkes survey, and attributed entirely to an intercloud medium, has an internal dispersion of approximately 11km s^{-1}; its mean velocity is separated from the velocity of absorbing clouds in the same direction by a typically smaller value, as is immediately evident from an inspection of the spectra (example page 43 of the Parkes survey). Such a correlation in velocities has also been noted in the more recent Arecibo data by Dickey, Salpeter and Terzian (1979), and has been interpreted by them as evidence against an ‘ extreme two-phase’ model. Any two-phase model against which such a correlation can be construed as evidence, will indeed have to be extreme, in that it must require total independence in velocity space of the two phases. As far as we know, no theoretical model or observational study of the intercloud gas has required or claimed such independence.

The simplest considerations lead one in fact to expect a correlation of velocities. Whether the intercloud gas has been left over from cloud condensation, or created from evaporation of clouds, some sharing of the motions would be natural. Even if a cloud were injected into a motionless medium, some of its motion should gradually be imparted to the immediately surrounding intercloud gas. If a cloud were to move through a rarified—but hotter—medium with a velocity comparable to the thermal velocities in the medium, the pressure balance will be upset and a shock would be set up. In addition to slowing down the cloud through drag, it is likely to disrupt it. According to Chevalier (1977) and references there in (Gurzadyan 1970; Richtmyer 1960; Woodward 1976), the boundary between high and low density regions is unstable after being shocked and the deceleration of a dense gas by a low density gas leads to its breakup as it is penetrated by the low density gas. If clouds co-exist with a medium, and have velocities comparable to the thermal velocities in the medium, one must therefore expect to find much smaller differential velocities, or in other words a correlation of the velocities.

Returning now to the optically thin gas seen in emission in the solar neighbourhood, we said earlier that it could have contributions both from hot clouds and true intercloud gas. We have established that the hot clouds occupy a very much larger volume in velocity space than the cold clouds. If they are concentrations of gas like the cold clouds, but different only in their temperature and their velocities, their motions will be independent in velocity space. If all the gas seen in emission were due to hot clouds, it would be most reasonable to expect near-total decorrelation of the velocities. As pointed out above, the observations show that there is considerable correlation. We interpret this as strong evidence that a considerable fraction of the emitting gas is intercloud material (see also recent discussion by Heiles 1980).

In profiles representing only optically thin material, we expect the hot cloud contributions to have a wider dispersion (~ 35 km s^{-1}) than the intercloud medium (~ 10 km s^{-1}). The combined contributions, when not clearly separable, would mimic an exponential, as discussed earlier in the case of the two cloud populations. Evidence of this may be seen in Fig. 3 of Dickey, Salpeter and Terzian (1979), where they show the normalised emission averaged over different source directions at intermediate and high galactic latitudes.

4.5 *Where are the Clouds Found ?*

If we are right in thinking that cloud velocities will tend to be lower than the sonic speed m a surrounding medium, we are then forced to the interesting conclusion that the hot clouds with speeds of the order of 60 km s^{-1} cannot last in a neutral intercloud medium where the temperatures are believed to be typically 8000 K. On the other hand, if they were immersed in coronal gas with temperatures approaching a million degrees, the problem does not arise. In a recent study, McKee, Cowie and Ostriker (1978) discuss the production of fast clouds of neutral hydrogen with column densities ~ 10^{19} cm^{-2} accelerated by the ram pressure of the expanding interior shocked gas. These clouds will of course be moving in the hot coronal gas inside the remnant.

The evidence presented in this paper for two distinct cloud populations seems to point strongly to a picture in which the fast and slow clouds are immersed respectively in hot coronal gas and a warm intercloud medium in separated regions in the galactic disk. Such a separation would facilitate the explanation of many observed facts beginning with the deficiency of hot clouds in the solar neighbourhood. These clouds would clearly acquire their velocities from the supernova shocks which overtook them, and within which they will be found. On the other hand, if the low velocities of the cold clouds were typical of the velocities of gas in the regions where they are formed, we would have a natural explanation of their motions. Cloud-cloud collisions dissipating part of the energy available before the collision, need not be invoked to produce a ‘ thermalised ‘ distribution with $\sigma \sim 5$ km s^{-1}.

The mean velocity of the gas caught and compressed between the shock fronts of adjacent remnants in their late stages will be roughly half the difference in the velocities of these shocks, when the sum of their radii equals the distance between the explosion sites. A simpleminded calculation assuming a 30 year period for the occurrence rate of Supernovae in the Galaxy leads to the relation $\Delta T_6 \approx 2 \times 10^3\ D_{pc}^{-2}$, where ΔT_6 is the time difference in millions of years between supernova explosions separated by a distance D in pc, calculated on the basis of a 50 per cent probability. It has been assumed that the effective area of the galactic disk in which Supernovae occur is that of a circle of radius 10 kpc. Thus, to within a factor of 2 or so, there is a 50 per cent chance that remnants differing in age by less than a million years, will be separated in distance by less than ~ 50 pc. A proper calculation of the mean velocity of gas in the meeting area of the two shocks will involve the appropriate equations from a theory for the development of remnants in their late stages. But a rough estimate seems to suggest that the velocities will be of the order of the velocities of cold clouds. We therefore propose that the regions between old and neighbouring supernova remnants provide the conditions and occupy enough volume to account for the formation of the cold clouds.

This picture is not too different from that proposed by McKee and Ostriker (1977) for the formation of cold clouds. According to them, condensation of cold matter will typically occur only on the clouds passed by shocks during the late stages of supernova remnant expansion. A slight modification of this picture is one in which clouds caught between two old SNRs will act as nucleii for the condensation of the swept up material leaving cold dense clouds with a low velocity. The gas which has not condensed onto the clouds will remain as a neutral intercloud medium. Conditions in such regions may be very similar to those considered by Field, Goldsmith and Habing (1969), with the only difference that cosmic rays play no part in heating the gas. If so, cold clouds will spontaneously condense out of the medium; further they will show the poor T_{spin} versus τ correlation illustrated well in Fig. 6b, because they are attempting to reach an equilibrium temperature. Such clouds, in course of time, when passed by subsequent but rapid shocks will suffer heating, partial evaporation of their masses, and acceleration to many times their velocities thus moving them into the population of hot, shocked clouds we identify with the wide feature of our absorption spectrum.

Finally we note that there does exist independent observational evidence in support of a picture in which dense cold neutral hydrogen is always found in shells. From a detailed study of Per OB2 and Sco OB2, Sancisi (1974) proposed that the birth places of these stellar associations were shells of neutral hydrogen surrounding old and strongly decelerated supernova remnants. From a very extensive survey of the 21 cm emission over a large part of the sky, Heiles (1976) concluded that the number of shells is large, and that nearly every H I density concentration appears to be part of a large arc and therefore a shell. He has also made the point that the existence of shells or sheets of interstellar gas has previously been deduced by many different techniques.

5. Conclusions

The main contribution of the present work is the identification of a component of the interstellar gas which should assume the central role in any picture describing its energetics. We started with the new wide feature detected in the Gaussian analysis of the 21 cm absorption spectrum of Sgr A (Paper I). The spin temperature of the gas was derived by a comparison with observations" on the Bonn 100 metre telescope by Sanders, Wrixon and Mebold (1977), and found to be 300 K±50. We showed that the gas represented by this feature must be globally distributed in the galaxy, by arguments involving its near-zero mean velocity, its column density, and by a comparison with velocity distributions obtained by optical and radio observations in many other directions in the Galaxy. The exponential form attributed to these other velocity distributions was shown to be a consequence of the superposition of two distributions, one narrow and one wide, the latter of which was incompletely sampled.

The column density of the wide feature was shown to indicate that in the hot clouds it represented, there was twice as much total hydrogen as found in cold clouds. We then argued that an association of these hot clouds with supernova shocks was inevitable. We based this argument on the correlation of cloud temperatures with velocity, the sodium I to calcium II anomaly observed in high velocity optical clouds and attributed to the effects of shocks on grains (Spitzer 1978), and most importantly on the high kinetic energy contained in these clouds, ~ 100 times that in cold clouds.

If most of the mass in interstellar clouds was moving with an rms velocity of 35 km s^{-1}, some constraints can be placed on the randomness of these velocities. Cloud-cloud collisions at such velocities would lead to an excessively high dissipation rate of energy if the motions were random, but the velocities are more likely to be correlated because of acceleration by large shock fronts. It was concluded that collisions of clouds with supernova shocks would be more likely than with other clouds.

The number of hot clouds estimated from the total column density, the temperature, and some assumptions of the masses, was predicted to be 15–20 clouds per kpc along a line of sight, in rough agreement with a number estimated from the optical measurements of Hobbs (1974a, b). The observations of Dickey, Salpeter and Terzian (1978) of clouds with low optical depth, high spin temperature, and a high velocity were shown to be in agreement with our picture. We proposed however, that the relationship of spin temperature with optical depth may be different in different optical depth ranges, as suggested by a comparison with the measurements of Mebold *et al.* (1980).

We found that the solar neighbourhood is deficient in the emission expected from hot clouds alone by at least 50 per cent. Fluctuations in the composition of interstellar gas occur therefore over volumes of the order of that of the solar neighbourhood, as would be expected in a supernova dominated picture of the interstellar medium.

The velocity correlation between the optically thin gas seen only in HI emission, and the optically thick gas seen in absorption, was interpreted as evidence that a substantial fraction of the optically thin gas in the solar neighbourhood must be intercloud material. If all of it was due to hot clouds alone, the motions would be independent and no velocity correlation would have been observed with the motions of the cold clouds. It was suggested that a careful analysis of the emission from optically thin hydrogen might enable a separation into true intercloud and hot cloud components. The hot cloud emission should show a much wider dispersion than the intercloud emission and hence permit a separation. Some evidence for this was already present in the measurements of Dickey, Salpeter and Terzian (1978).

It was argued that hot clouds are not likely to be found in regions with intercloud gas, as their velocities in this medium would be highly supersonic. In the interior of remnants, the high temperature of the coronal gas would make such velocities subsonic. It was proposed therefore that the two varieties of clouds would be generally found in separated regions; the interior of remnants would contain hot clouds heated and accelerated by the shocks which overtook them, and cold clouds would be found in the regions in-between remnants where intercloud gas will also exist. The cold clouds probably condense out of the intercloud gas between supernova remnants due to instabilities such as discussed by Field, Goldsmith and Habing (1969). If clouds formed in this manner, they would tend to acquire an equilibrium temperature, and hence show a poor correlation with optical depth as indicated by the observations.

The low velocities of cold clouds were attributed to the velocities of the gas from which they condense, and it was argued that such gas caught between neighbouring remnants in their late stages would have rms velocities of ~ 5 km s^{-1}. The presence of a substantial amount of intercloud gas, and the deficiency of hot clouds in the solar neighbourhood was attributed to its location in-between old supernova remnants, rather than within one.

To sum up, an analysis of the 21 cm absorption spectrum of a strong continuum source well placed in the galaxy has led to a model in which the volume of the galactic disk contains, in addition to the hot bubbles representing supernova remnants (Cox and Smith 1974), cooler in-between regions. Clouds with $N_H \leqslant 10^{20}$ cm^{-1}, N_H / kpc ~ 2 $\times 10^{21}$ cm^{-2} kpc^{-1}, T_s ~ 300 K, and speeds of ~ 60 km s^{-1} are found inside bubbles. Outside of them, we have regions filled with an intercloud medium imbedded in which are cold dense clouds with N_H ~ 4$\times$ 10^{20} cm^{-2}, N_H */kpc* ~ 10^{21} cm^{-2} kpc^{-1}, T_s typically between 50 and 100 K, and speeds ~ 8 km s^{-1}.

Acknowledgements

We are grateful to R. H. Sanders and U. Mebold for providing us with measurements obtained with the Bonn 100 metre telescope in the direction of Sgr A; also to U. Mebold, A. Winnberg, W. M. Goss and P. M. W. Kalberla for providing us with the measurements shown in Fig. 6b in advance of publication, and for permission to reproduce the same. We thank M. Vivekanand for much assistance with calculations and Rajaram Nityananda for discussions.

Appendix

The spin temperature of the wide component

We shall estimate the spin temperature of the gas in the wide component by combining the Parkes interferometer optical depth measurements with the antenna temperatures obtained by Sanders, Wrixon and Mebold (1977) with the Bonn 100 metre telescope. These measurements are shown in Figs 2a and 2b. We see in 2a the total optical depth profile obtained in the direction of Sgr A from Paper I, and superimposed on it (dashed line) the Gaussian fitted to the wide component (Fig. 1d of this paper). It will be seen that in the narrow velocity ranges centred at approximately —38 km s^{-1}, –18 km s^{-1}, –18 km s^{-1} and + 26 km s, the contribution to the total optical depth is, to within the errors of the measurement, only from the wide component. The optical depths at these velocities are indicated in Fig. 2a and the Bonn antenna temperatures at the same velocities are indicated in Fig. 2b. The optical depths are reasonably low at all 3 velocities, and the harmonic mean spin temperatures can be derived from the single dish antenna temperatures which contain both emission and absorption contributions. At any given velocity,

$$T_A = -T_c(1-e^{-\tau}) + \eta\, T_s(1-e^{-\alpha\tau}),$$

$$\text{or }\; T_s = \frac{T_A + T_c(1-e^{-\tau})}{\eta\,(1-e^{-\alpha\tau})},$$

where T_A is the Bonn antenna temperature from Fig. 2b,

T_c, 600 K 50 the continuum antenna temperature on Sgr A (provided by Mebold),

η is the beam efficiency 70 ± 3 per cent (Mebold and Hills 1975),

τ taken from Fig. 2a,

α taken to be 2·35 ± 0·35 (see below).

The emission contribution will come both from the path length to the galactic centre, and also from beyond the galactic centre all along the direction *1*= 0, b 0. The factor a is the ratio of the emission to absorption path lengths involved. As the uncertainty in this quantity is large, we have taken α to vary from 2 to 2·7 in estimating our total errors. We have assumed here that the emission contribution from behind the galactic centre is not diminished in any way by the continuum source –a very reasonable assumption considering the relative sizes of source and antenna beam, and the optical thinness of most continuum sources at this frequency. The spin temperatures derived on this basis are 290 ± 35, 400±40, and 350 ±40 at the three velocities.

There appears to be a correlation of the derived spin temperatures at the three velocities with the optical depths or | V | ; as the absorption profile is centred at zero, these latter quantities vary together. No significant correlation with optical depth is to be expected over the central portion of the wide feature, as there will be a mixture of clouds of all speeds, of which we are measuring only one component of the motion. Some correlation with velocity is to be expected however, due to a contribution to the antenna temperature from the wings of the emission profile from true intercloud gas along the line of sight. While the intercloud emission should be negligible at —38 km s^{-1}, there would be some contribution at smaller velocities.

A recalculation of the temperatures was therefore carried out, allowing for intercloud emission including its partial absorption by hot clouds. Based on measurements obtained in the Parkes survey, the dispersion of intercloud gas was taken to be 11 km s^{-1} in a direction free of galactic rotation effects, and its total column density to the far end of the Galaxy was taken to be $N_{1CM} \approx 1{\cdot}4 \times 10^{22}$ cm^{-2}. The new values of temperature obtained were 290 K, 230 K and 300 K, respecttively for the three velocities given earlier.

These new values would represent a gross overcorrection if there were no intercloud gas at all in the Galaxy. As discussed in § 4 we believe there is, but perhaps somewhat less than we have assumed here. We conclude that 300 K ± 50 is therefore a very reasonable estimate of the harmonic mean temperature of the gas in the wide feature.

References

Adams, W, S. 1949, *Astrophys. J.*, **109,** 354.
Blaauw, A. 1952, *Bull, astr. Inst. Netherl,* **11,** 459.
Chevalier» R. A. 1977, *A. Rev. Astr, Astrophys.,* **15,** 175.
Clark, B. G. 1965, *Astrophys. J.*, **142,** 1398.
Cox, D. P., Smith, B. W. 1974, *Astrophys. J.,* **189,** L105.
Dickey, J. M., Salpeter, E. E., Terzian, Y. 1978, *Astrophys. J. Suppl Ser.,* **36,** 77.
Dickey, J. M., Salpeter, E. E., Terzian, Y. 1979, *Astrophys. J.,* **228,** 465.
Field, G. B., Goldsmith, D. W., Habing, H. J. 1969, *Astrophys. J.*, **155,** L149.
Gurzadyan, G. A. 1970, *Planetary Nebulae,* D. Reidel, Dordrecht.
Heiles, C. 1974, in *Galactic Radio Astronomy,* Eds F. J. Kerr and Simonson III, D. Reidel, Dordrecht, p. 13.
Heiles, C. 1976, *Astrophys. J.*, **208,** L137.
Heiles, C. 1980, *Astrophys. J.*, **235,** 833.
Hobbs, L. M. 1974a, *Astrophys. J.,* **191,** 381.
Hobbs, L. M. 1974b, *Astrophys. J.*, **191,** 395.
Jenkins, E. B., Meloy, D. A. 1974, *Astrophys. J.*, **193,** L121.
Knude, J. 1979, *Astr. Astrophys.,* **71,** 344.
Mast, J. W., Goldstein, S. J. Jr. 1970, *Astrophys. J.,* **159,** 319.
McKee, C. F., Ostriker, J. P. 1977, *Astrophys. J.*, **218,** 148.
McKee, C. F., Cowie, L. L., Ostriker, J. P. 1978, *Astrophys. J.*, **219,** L23.
Mebold, U. 1972, *Astr. Astrophys.,* **19,**13.

Mebold, U., Hills, D. L. 1975, *Astr. Astrophys.,* **42,** 187.
Mebold, U., Winnberg, A., Goss, W. M., Kalberla, P. M. W. 1980, preprint.
Radhakrishnan, V., Goss, W. M. 1972, *Astrophys. J. Suppl. Ser.,* **24,** 161.
Radhakrishnan, V., Goss, W. M., Murray, J. D., Brooks, J. W. 1972a, *Astrophys. J. Suppl. Ser.,* **24,** 49.
Radhakrishnan, V., Murray, J. D., Lockhart, P., Whittle, R. P. J. 1972b, *Astrophys. J. Suppl. Ser.,* **24,** 15.
Radhakrishnan, V., Sarma N. V. G. 1980, *Astr. Astrophys.,* **85,** 249.
Richtmyer, R. D. 1960, *Commun. Pure Appl. Math.,* **13,** 297.
Routly, P. M.. Spitzer, L. Jr. 1952, *Astrophys. J.,* 115, 227.
Sancisi, R. 1974, in *Galactic Radio Astronomy,* Eds F. J. Kerr and Simonson III, D. Reidel, DOrdrecht, p. 115.
Sanders, R. H., Wrixon, G. T., Mebold, U. 1977, *Astr. Astrophys.,* **61,** 329.
Siluk, R. S., Silk, J. 1974, *Astrophys. J.,* **192,** 51.
Spitzer, L. Jr. 1956, *Astrophys.J.,* **124,** 20.
Spitzer, L. Jr. 1968, *Diffuse Matter in Space,* Wiley Interscience, New York.
Spitzer, L. Jr. 1978, *Physical Processes in the Interstellar Medium,* Wiley-Interscience, New York
Spitzer, L. Jr., Jenkins, E. B. 1975, *A. Rev. Astr. Astrophys.,* **13,** 133.
Williamson, F. O., Sanders, W. T., Kraushaar, W. L., McCammon, D., Borken, R., Bunner, A. N. 1974, *Astrophys. J.,* **193,** L133.
Woodward, P. R. 1976, *Astrophys.J.,* **207,** 484.
York, D. G. 1974, *Astrophys. J.,* **193,** L127.

J. Astrophys. Astr. (1980) **1,** 67–70

A Search for OB Stars in Supernova Remnants

Sidney Van den Bergh *Dominion Astrophysical Observatory, Herzberg Institute of Astrophysics, Victoria, B.C., Canada*

Received 1980 April 30; accepted 1980 May 20

Abstract. A massive binary, in which the primary becomes a supernova, should leave a luminous secondary near the centre of its remnant. Contrary to expectation no statistically significant excess of OB stars is, however, found near the centres of optically visible galactic supernova remnants.

Key words: Supernovae—supernova remnants—binaries

1. Introduction

Recently van den Heuvel, Ostriker and Petterson (1980) have presented a model in which SS 433 is considered to be a binary system consisting of an evolved early-type star and an old neutron star. Since many massive early-type stars are binaries a major fraction of all Supernovae of type II should leave early-type stars near the centres of their remnants. Even if these left over OB stars become runaway objects (Blaauw 1961; Zwicky 1957) they will still remain close to the centres of the supernova remnants in which they are located. This is so because the ejection velocity of a runaway star ($\sim 10^2$ kms^{-1}) is so much lower than the initial expansion velocity ($\sim 10^4$ km S^{-1}) of supernova remnants. A search for OB stars near the centres of supernova remnants therefore seemed promising.

2. Expected number of OB stars in SNR's

From data collected by Tammann (1974) it is seen that Supernovae of type II outnumber those of type I by factors of 4/3 and 21/13 in Sb and Sc galaxies respectively. Since the Galaxy is generally considered to be of morphological type intermediate between types Sb and Sc ~ 60 per cent of all galactic SNR's should have been produced by SN II. Of the 34 presently known optical SNR's in the Galaxy ~20·4 should therefore have been formed by the explosion of the massive (*cf.* Maza and van den Bergh 1976) precursors of SN II. According to Garmany, Conti and Massey (1980) ⩾ 37 per cent of all O stars are, on the basis of their radial velocities, certain or probable binaries. If it is assumed* that all primaries *and* secondaries become SN II then a fraction ⩾ 37/(63 + 37 + 37) = 0·27 of all galactic SN II remnants were produced by primaries and should still contain OB secondaries. On the basis of this assumption ⩾ 5·5 of the optically visible galactic SNR's should contain an OB star near their centres. The real number of OB stars in SNR's will be even greater than this because a large fraction of all OB stars are known to be members of wide physical double or multiple systems (Salukvadze 1979) such as the Orion Trapezium.

Since both OB star surveys and searches for optical SNR's extend to similar distances† it seemed worthwhile to undertake a search for OB stars near the centres of supernova remnants. Such objects would be particularly valuable because they might provide accurate distance determinations for supernova remnants.

3. Search for OB stars in SNR's

The O star catalogue of Cruz-González *et al.* (1974) was used to search for O-type stars located within 1·5 R_m (in which R_m is the larger of the optical and radio semi-

Table 1. Identified galactic supernova remnants.

Designation	Name	R_m (arcmin)	Designation	Name	R_m (arcmin)
G 004·5 + 6·8	Kepler	1·5	G 180·3 − 1·7	S 147	100
G 006·5 − 0·1	W 28	15	G 184·6 − 5·8	Crab	7
G 039·7 − 2·0	W 50	44	G 189·0 + 3·0	IC 443	27
G 053·6 − 2·2	3C 400·2	10	G 205·6 − 0·1	Monoceros	105
G 065·3 + 5·7	S 94	120	G 206·9 + 2·3	PKS 0646+06	40
G 068·8 + 2·6	CTB 80	20:	G 260·4 − 3·4	Puppis	40
G 074·3 − 8·5	Cygnus Loop	120	G 263·4 − 3·0	Vela	150
G 078·2 + 2·1	DR 4	31	G 284·2 − 1·7	MSH 10–5$\underline{3}$	25
G 111·7 − 2·1	Cas A	2·1	G 292·0 + 1·8	MSH 11–5$\underline{4}$	2·7
G 116·9 + 0·2	CTB 1	22	G 296·1 − 0·7	...	8
G 119·5 + 9·8	CTA 1	45	G 296·5 + 10·0	PKS 1209–52	40
G 120·1 + 1·4	Tycho	4	G 315·4 − 2·3	RCW 86	28
G 130·7 + 3·1	3C 58	5	G 320·4 − 1·0	RCW 89	5
G 132·7 + 1·3	HB 3	70	G 326·3 − 1·8	MSH 15–5$\underline{6}$	18
G 160·4 + 2·8	HB 9	78	G 327·6 + 14·5	Lupus	17
G 166·1 + 4·4	OA 184	45	G 332·4 − 0·4	RCW 103	5
G 166·3 + 2·5	VRO 42·05·01	38	G 342·0 + 0·1	Kes. 45	15

*Some support for this assumption is provided by the work of Bohannan and Garmany (1978) who find a real lack of low amplitude binary systems. Taken at face value their results indicate that O-type close binaries tend to have similar masses.

†Twelve of the SNR's listed in Table 1 have distances determined by Clark and Caswell. For these objects the mean and median distances are 2·7 and 2·0 kpc respectively. For a random sample of O stars in the catalogue of Cruz-González *et al.* (1974) the mean and median distances are 2·4 and 2·2 kpc respectively. There may, however, be some bias in favour of distance determinations for the nearer SNR's in the Clark and Caswell compilation. For the 12 SNR's in Table 1 with distances $\langle R_m \rangle$ =45' compared to $\langle R_m \rangle$ =35' for the 22 SNR's without distances.

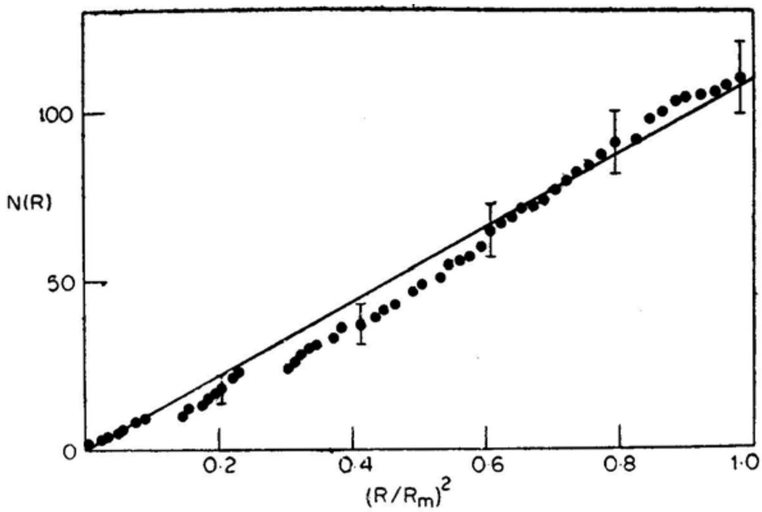

Figure 1. Comparison of the observed and expected (uniform) distribution of R/R_m values. The observations show no significant deviation from a uniform distribution.

major axes) of the centres of optical SNR's. Data on the adopted positions and R_m values of all 34 presently known optical supernova remnants are collected in Table 1. A total of 23 O stars were found to be located within 1·5 R_m of the centres of these SNR's. The distribution of these objects, as a function of their distance R from the centres of the remnants, is compiled in Table 2. The data in this table show that the observed distribution of R/R_m values does not differ significantly from that expected for a uniform distribution of O stars out to R/R_m = 1·5. Note in particular that only one O star has R/R_m < 0·25 compared to 0·6 expected for a uniform distribution. This star is the O 7·5 IIIf star HD 47125 (Plaskett's star), which is located 20′ from the centre of the Monoceros SNR. The fact that this star (Abhyankar 1959; Hutchings and Cowley 1976) is a double-lined spectroscopic binary shows that it is *not* the secondary surviving member of a close binary system.

Possibly the majority of ' missing ' central stars in SNR's are B stars or evolved early-type supergiants rather than O stars. The Hamburg/Warner and Swasey catalogue of *Luminous Stars in the Northern Milky Way* was therefore checked for objects with R/R_m < 1·0. The distribution of the R/R_m values of the 110 objects in volumes I, II, IV, V, VI of this catalogue, that are located in supernova remnants,

Table 2. Distribution of O stars within supernova remnants.

R/R_m	N (Observed)	N (Predicted)
0·00–0·25	1	0·6
0·26–0·50	2	1·9
0·51–0·75	3	3·2
0·76–1·00	4	4·5
1·01–1·25	9	5·8
1·26–1·50	4	7·0

is shown in Fig. 1. The observed distribution of R/R_m values within SNR's is seen to be indistinguishable from a uniform distribution. In particular only four stars are observed to have $R/R_m < 0{\cdot}20$, compared to 4·4 expected for a uniform distribution. In addition to Plaskett's star the following objects are found to have $R/R_m < 0{\cdot}20$:+42° 1286(B 0·5V)in HB 9and +27° 828, +27° 830(OB–) in S 147.

The Hamburg/Warner and Swasey identification charts show that spectral classification is still possible in the brightest part of the Cygnus Loop. This shows that the observed distribution of OB stars within SNR's is probably little affected by emission nebulosity.

No plausible explanation, other than the perversity of small-number statistics presents itself for the unexpected lack of OB stars at or near the centres of galactic supernova remnants.

References

Abhyankar, K. D. 1959, *Astrophys. J. Suppl. Ser.,* **4,** 157.
Blaauw, A.1961, *Bull. astr. Inst. Netherl.,* **15,** 265.
Bohannan, B., Garmany, C. D. 1978, *Astrophys. J.,* **223,** 908.
Clark, D. H., Caswell, J. L. 1976, *Mon. Not. R. astr. Soc.,* **174,** 267.
Cruz-Gonzalez, C, Recillas-Cruz, E., Costero, R., Peimbert, M., Torres-Peimbert, S. 1974, *Rev. Mexicana de Astronomia y Astrofisica,* **1,** 211.
Garmany, C. D., Conti, P. S., Massey, P. 1980, preprint.
Hutchings, J. B., Cowley, A. P. 1976, *Astrophys. J.,* **206,** 490.
Maza, J., van den Bergh, S. 1976, *Astrophys. J.,* **204,** 519.
Salukvadze, G. N. 1979, *Astrofizika,* **14,** 30.
Tammann, G. A. 1974, in *Supernovae and Supernova Remnants,* Ed. C. B. Cosmovici, D. Reidel, Dordrecht.
van den Heuvel, E. P. J., Ostriker, J. P., Petterson, J. A. 1980, *Astr. Astrophys.,* **81,** L7.
Zwicky, F. 1957, *Morphological Astronomy,* Springer-Verlag, Berlin, p. 258.

J. Astrophys. Astr. (1980) **1,** 71–78

XX Cam—The Inactive R CrB Star

N. Kameswara Rao *Indian Institute of Astrophysics, Bangalore* 560034
N. M. Ashok and P. V. Kulkarni *Physical Research Laboratory, Ahmedabad* 380009

Received 1980 May 8; accepted 1980 May 29

Abstract. Infrared observations obtained six years apart of the R CrB type star XX Cam do not show any infrared excess, unlike all the other members of the class. The observed colours match a 7000 K black body energy distribution quite well. From the year 1898 till todate, apparently XX Cam has undergone only one visual light minimum in 1940. The lack of infrared excess, the abundance peculiarities and further lack of small amplitude light variations with periods of few tens of days, which are characteristic of R CrB type stars, are discussed in terms of theoretical pulsation models of helium stars.

Key words: R CrB star—infrared excess

1. Introduction

XX Cam is one of the brighter members of R CrB class of variable stars which characteristically shows under-abundance of hydrogen, overabundance of carbon and undergoes at irregular intervals, sudden decreases in visual light from 2 to 7 mag. Bidelman (1948) was the first to point out the similarities of the spectrum of XX Cam and R CrB. A search for light variability on Harvard plates by Yuin (1948) from 1898 to 1948 showed only one light minimum of 1·7 mag depth during 1939-40. Until today, it is the only recorded minimum of the star reported in the literature, quite in contrast to the other R CrB type stars which it resembles spectroscopically like R CrB and RY Sgr. On the average R CrB shows a visual light minimum once in 750 days and RY Sgr once in 1000 days (Table 1). Even though the occurrence of light minima in this class of star is very irregular, and sometimes an interval of about ten years exists between the minima of R CrB (Mayall 1960), XX Cam has so far the longest duration in between minima.

The visual light minima of R CrB stars are thought to be caused by a circumstellar cloud or shell of dust particles (probably formed at the time of the minimum) coming in the line of sight between the star and the observer (O'Keefe 1939, Feast 1975). The dust (probably carbon dust) around the star absorbs a fraction of the stellar radiation and reradiates it at a lower temperature (800–900 K) giving rise to the infrared excess. After the initial discoveries of infrared excess in R CrB and RY Sgr (Stein *et al.* 1969*;* Lee and Feast 1969) it is now known that almost all the bonafide R CrB stars show infrared excesses (Feast and Glass 1973; Glass 1978; Gaustad 1972; Rao 1980b). However, Humphreys and Ney (1974) suggested that the infrared excess of R CrB is due to the presence of a cool companion which mainly radiates in IR. Their suggestion was based on the following results. (1) The energy distribution in the infrared of R CrB seems to resemble that of CIT 6 (a carbon star). (2) The variation of flux at 3·5μ of about 1·5 mag was not accompanied by any visual light variations and also it seems to follow a period of 3·5 years. Particularly there was no change of the infrared flux at the time of the 1972 visual light minimum. Simultaneous visual and infrared observations of RY Sgr by Feast *et al.* (1977) show that this binary model is not applicable to RY Sgr. They observed that the infrared light curve (L mag) mimics the Cepheid-like visual light variations of 38·6 day period synchronously, thus showing the infrared excess to be due to the circumstellar dust.

If infrared excesses are due to dust formed around the star from the ejected gas, some correlation between visual light minima and infrared excess is to be expected in the average properties. A parameter e is defined as the product of the average frequency of the occurrence of visual light minima (*i.e.* $1000/\bar{P}$ days) and the average visual extinction ($\overline{\Delta V}$ in mag). This parameter is given in Table 1 along with the average amount of infrared excess (ΔL) in the $3{\cdot}5\mu$ L band, for four stars R CrB, RY Sgr, GU Sgr and S Aps. The amount of infrared excess ΔL is obtained as the difference of the average $\bar{L}_{obs}$ and L_{BB} magnitudes; L_{BB} is estimated for a black body from the $(V–J)_0$ index observed at light maximum after correction for interstellar extinction. As can be seen from Table 1, ϵ and ΔL both increase together showing a qualitative relation between visual extinction and the infrared excess. Further support for this relation comes from the IR observations for hydrogen-poor carbon-rich non-variable stars (HdC) HD 182040 and HD 173409,

Table 1. Photometric parameters of R CrB stars

Star	Sp. Type	$\bar{P}$ (days)*	$\overline{\Delta V}$ (mag)*	ϵ	$\bar{L}_{obs}$ mag.**	L_{BB} mag	$\Delta L = \bar{L}_{obs} - L_{BB}$ mag	T_{BB}† K
R CrB	F81b	750	5·8	7·6	2·2	4·64	2·4	7200
RY Sgr	GoIb	999	5·4	5·4	2·62 – 3·0	4·85	2·23 — 1·85	7000
GU Sgr		1493	2·3	1·45	6·08 — 5·86	7·68	1·82—1·6	6000
S Aps	R3	1761	3·4	1·95	5·07	6·25	1·18	4265
XX Cam		>14832	1·7	~0				

*The light curve data are taken from the following sources: R CrB–Mayall (1960) and AAVSO Publications, RY Sgr–Mayall (1972), GU Sgr–Bateson and Jones (1973) and S Aps–Waters (1966).

***L* and (*V–J*) for GU Sgr, S Aps are obtained from Glass (1978); for RY Sgr–from Glass (1978) and Feast et al. (1977); for R CrB from Humphreys and Ney (1974) and Stecker (1975) and Glass (1978). The interstellar reddening is from Glass (1978).

†T_{BB} *is* the black body temperature.

which are spectroscopically similar to R CrB stars. Feast and Glass (1973) show that these non-variable HdC stars do not possess any infrared excesses. For XX Cam the e value obtained is close to zero and from the above relation very little or no infrared excess is to be expected. To check this, the following infrared observations were obtained.

2. IR observations

Observations of XX Cam in the *J*, *K* bands were obtained by B. J. McNamara in December 1973 at NKR's request, with the 127-cm telescope at Kitt Peak. M. Cohen has also kindly obtained observations of XX Cam at 2·2μ, 3·6μ and I0μ, with the 152-cm telescope at Mt. Lemmon in February 1974 at NKR's request. Further observations in *J*, *H*, *K* bands were obtained by us after six years, on 17 February 1980 with the 102-cm telescope at Kavalur using a liquid nitrogen cooled In Sb detector. These three sets of observations seem to agree with each other within the observational errors (±0·07 mag). The observed magnitudes and fluxes are given in Table 2, along with the mean *UBV* magnitudes given by Fernie, Sherwood and DuPuy (1972).

The interstellar reddening of XX Cam is estimated by Pugach (1977) as *E* (*B–V*) of 0·5 to 0·6 mag based on the distribution of the colour excess in the galactic plane given by Fitzgerald (1968). If a value of *E*(*B–V*) of 0·5 is adopted, the colours of XX Cam become too blue when compared with R CrB. Since the spectra of both R CrB and XX Cam look very similar (see Plate 12 of Yamashita, Nariai and Narimoto 1977), we assume that XX Cam has the same intrinsic (*B–V*) as that of R CrB (*B* – *V*= 0·52 mag) and thus obtain *E*(*B–V*) = 0·30 mag. The energy distribution is shown in Fig. 1 after correcting for the interstellar reddening of *E*(*B* – *V*) = 0·30 mag and using the reddening relations corresponding to van de Hulst's curve No. 15 (Johnson 1968). Also shown in Fig. 1 is the black body energy distribution for temperature of 7000 K. As can be seen from the figure, the energy distribution of XX Cam follows closely that of a black body at 7000 K and does not show any appreciable infrared excess, thus confirming the earlier expectation. Observations obtained six years apart do not show any variations greater

Table 2. Energy distribution of XX Cam.

Filter	λ (μ)	mag	F (watts/cm^2 μ)	Date
U	0·36	8·48	$1{\cdot}76 \times 10^{-15}$	
B	0·44	8·20	$3{\cdot}78 \times 10^{-15}$	
V	0·55	7·35	$4{\cdot}50 \times 10^{-15}$	
J	1·25	5·63	$1{\cdot}90 \times 10^{-15}$	Dec. 1973
K	2·2	5·36	$2{\cdot}80 \times 10^{-16}$	Dec. 1973
	2·2	5·5	$2{\cdot}47 \times 10^{-16}$	Feb. 1974
	3·6	5·38	$4{\cdot}16 \times 10^{-17}$	Feb. 1974
	10	4·5*	$2{\cdot}06 \times 10^{-18}$*	Feb. 1974
J		5·80	$1{\cdot}627 \times 10^{-15}$	Feb. 1980
H		5·70	$5{\cdot}972 \times 10^{-16}$	Feb. 1980
K		5·55	$2{\cdot}350 \times 10^{-16}$	Feb. 1980

*10 micron measurement is an upper limit to the flux.

than that which can be attributed to observational errors. In this respect XX Cam is more like the non-variable HdC stars.

3. Spectrum

The spectrum of XX Cam has been analysed by Orlov and Rodriguez (1974) in some detail, and further reanalysis of Orlov and Rodriguez's data was done by

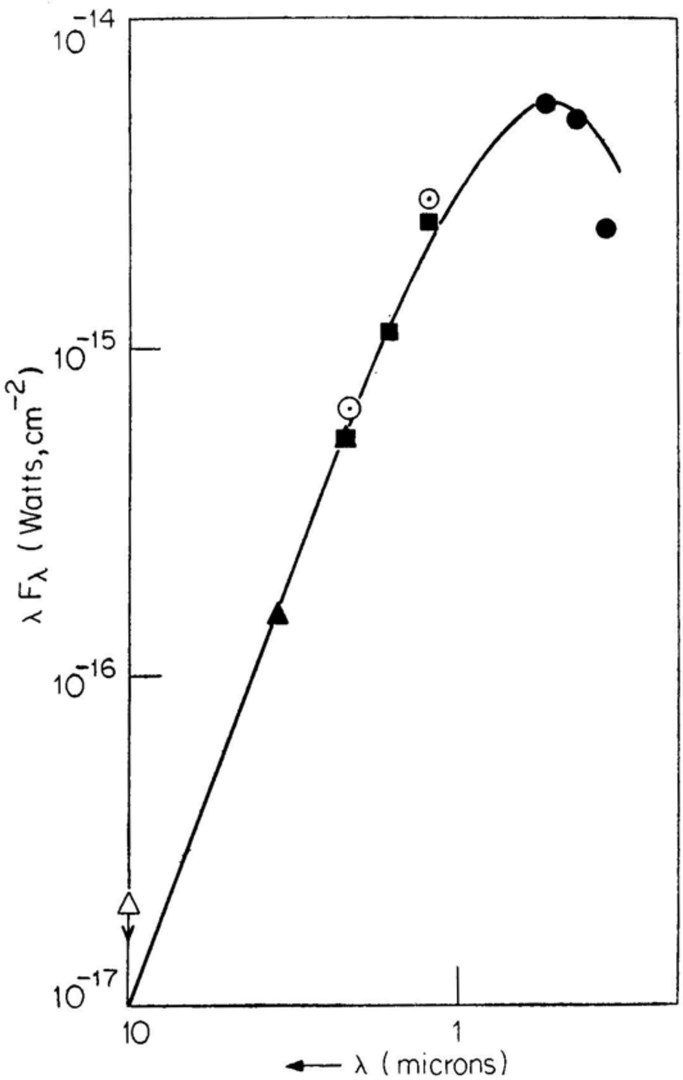

Figure 1. Energy distribution of XX Cam (Table 2) corrected for E (B — V) = 0·30. The curve represents a black body energy distribution (full line) for 7000 K which is made to agree with the observations at 0·55 microns.

● –Mean *UBV* observations given by Fernie, Sherwood and DuPuy (1972).

⊙–Observations in Dec. 1973.

▲–Observations in Feb. 1974. Open triangle denotes the upper limit.

■ –Observations in Feb. 1980.

Schönberner(1975) with the help of model atmospheres. The effective temperature obtained by Schönberner of 7200 ± 600 K is in good agreement with the black body temperature of 7000 K estimated from the colours earlier. He also derives a mean micro-turbulent velocity of 9·5 km S^{-1}. Within the uncertainties of the analysis, all the three stars R CrB, RY Sgr and XX Cam have the same effective temperature of 7000 K and log g = 0·15. Although no observations of hydrogen lines were available in XX Cam, Schönberner estimated that hydrogen is more deficient in XX Cam than in RY Sgr and R CrB.

It is of importance to establish the C/H ratio in R CrB stars for an understanding of the stage of evolution and the process of mixing of surface and interior material. Moreover, it was noticed earlier that there might be a relation between C/H ratio and the Li abundance (Rao 1975). To estimate these parameters in XX Cam, a coudé spectrogram of 16Å mm^{-1} dispersion centred at λ 6600 was obtained on 1972 September 11, using the cooled Varo-image intensifier and the 61-cm coudé auxiliary telescope of Lick Observatory. The following equivalent widths are obtained; Hα λ 6562·8 = 0·52Å, CI λ 6587·7 = 0·70Å, the feature at λ 6707·8 of Li = 0·112Å. These could be compared with the value of RY Sgr obtained by Danziger (1965): Hα = 0·72Å, CI λ 6587·75= 0·354 Å and Li λ 6707 = 0·124Å. From a differential curve of growth analysis done with respect to RY Sgr, similar to that by Danziger, we obtained from the CI λ 6587·7 and Hα lines the (C/H) ratio Log $[(C/H)_{RY\ Sgr} / (C/H)_{XX\ Cam}] \simeq -$ 1·16. This value roughly agrees with the value of – 0·9 estimated by Schönberner. Thus we see that in XX Cam, carbon is a little more abundant and hydrogen more deficient than in RY Sgr.

In his study of Li abundances, Zappala (1972) found that the equivalent widths obtained for the Li feature on Varo-spectrograms (the same equipment used here) are systematically larger by 0·08 in log W_λ/λ, when compared to conventional spectrograms of the same dispersion (16 Å mm^{-1}). If this correction is applied to the equivalent width of Li feature in XX Cam, the corrected equivalent width is obtained as 93 mÅ; this may be compared with 124 mÅ in RY Sgr (Danziger 1965) and 220 mÅ in R CrB (Keenan and Greenstein 1963). Thus the Li abundance in XX Cam seems to be less than in RY Sgr. In both the stars the equivalent widths fall on the linear part of the curve of growth and differences in continuous opacity and excitation temperatures are small.

From the equivalent widths of four neutral oxygen lines observed by Danziger in RY Sgr, Schönberner (1975) found oxygen to be under-abundant by a factor of 2·5 relative to the oxygen abundance in normal B stars. For R CrB, Keenan and Greenstein (1963) show that the neutral oxygen lines are much stronger than in the normal F5 Ib super-giant star α Per, and thus oxygen might even be over-abundant when compared with solar abundance. The equivalent widths for two O I lines are as follows for R CrB measured on a 16Å mm^{-1} coudé spectrogram obtained by Herbig with the 3 meter telescope: λ 6454 = 210 m Å and λ 6453 = 135 mÅ as compared to 80 mÅ for both the lines obtained by Danziger for RY Sgr. (The equivalent widths of nearby Ca I lines λ 6437, λ 6462 and λ 6432 of Fe II are roughly equal to the equivalent widths of the same lines obtained in RY Sgr by Danziger within ± 0·02 in log W_λ/λ. The other two O I lines used by Danziger in RY Sgr λ 6154 and λ 6156 are very badly blended in the spectrogram of R CrB.) An order of magnitude estimate of the oxygen abundance for R CrB from the equivalent widths, thus shows that it is the same as in normal B stars. In XX Cam, the neutral oxygen line λ 7774 is much stronger than in R CrB. The equivalent width of this feature obtained from the Varo-spectrograms obtained at 33Å mm^{-1} dispersions are 2·40 and 1·90Å for XX Cam and R CrB respectively (Rao and Mallik 1978). It is well known that the λ 7774 feature is sensitive to luminosity of the star. Since Schönberner's analysis gives roughly the same effective gravity for both XX Cam (log g = 0·20) and R CrB (log g = 0·15), the difference in the equivalent widths might thus reflect differences in the oxygen abundance. In any case the oxygen abundance in XX Cam is the same as or even more than that of R CrB. (Although the O I lines λλ 6453, 6454 are present on the Varo-spectrogram of XX Cam mentioned earlier, they are very much blended.) Thus the qualitative study of the red spectrograms of XX Cam shows that it has less hydrogen, less lithium, more carbon and normal or more oxygen abundances when compared to RY Sgr and R CrB.

4. Light variability

There is another characteristic which seems to distinguish XX Cam from other R CrB stars, namely the variability in the visual light even at the time of normal light maximum. Most of the R CrB stars seem to show a cepheid type (?) light variability of 0·2 to 0·5 mag in a period of a few tens of days (Feast 1975). RY Sgr, the best studied star in this respect, shows pulsations with a period of 38·6 days (Alexander *et al.* 1972). Both R CrB itself (Fernie, Sherwood and DuPuy 1972) and UW Cen (Bateson 1972) have been reported to have periods around 40 days. GU Sgr also seems to show a periodicity of 38 days with amplitude of 0·3 mag (Bateson and Jones 1973; Rao 1980a). Sherwood (1975) has shown that there is a variability in light of 0·2 to 0·4 mag in *V* for all the other confirmed members of R CrB class, with periods of few tens of days. However, the two non-variable HdC stars HD 137613 and BD–10° 2179 which were specifically looked for light variability, do not show any light variations greater than 0·1 mag in *V*, with a period of a few tens of days (Rao 1980a). *UBV* observations of XX Cam have been obtained by Fernie, Sherwood and DuPuy (1972), Landolt (1968, 1973) and Rao (1980a), extending from 1967 to 1972. These observations, although scattered in time do not reveal any light variations greater than 0·1 mag in *V*. Even the Harvard photographic observations reported by Yuin (1948) do not show any prominent periodic variations of few tens of days. Except for the 1·7 mag drop in 1939-40, the only other light variability that has been reported of XX Cam, is the irregular light variation of about 0·1 mag or less in timescales of about 10 minutes on some nights by Totochava (1973, 1975). Apparently on some other nights such, rapid light variations are not present (Robinson 1974, personal communication; Totochava 1975). Our own observations of continuous monitoring of the star, for 3 hours on two nights through a *B* filter with the 102-cm reflector, do not show any variability greater than 0.03 mag. The significance of these short period irregular light variations is not clear at present; in any case these are small in amplitude. Thus XX Cam again shows characteristics similar to that of non-variable HdC stars.

5. Discussion

The lack of infrared excess in XX Cam implies lack of the presence of (or production of) circumstellar dust, and this behaviour is similar to that of non-variable HdC stars like HD 182040. Such an inference also derives support from the polarisation observations. The polarisation observations of XX Cam obtained at different times do not seem to show any changes in either the percentage of polarization or position angle of the electric vector or wavelength dependence (Kolotilov, Orlov and Rodriguez 1974). Moreover, these observations can be explained as due to the interstellar extinction. Although XX Cam has the same $T_{\rm eff}$ and log g as R CrB and RY Sgr the lack of production (or very infrequent production) of dust is puzzling.

The R CrB type variation of large drops in visual light and the pulsations (light variations) with periods of few tens of days seem to be related phenomena. All stars which show R CrB type variations also seem to show some sort of periodic variations in light (pulsations?). It might even be that the pulsations cause the R CrB type activity. The absence of such pulsations or periodic variations light in XX Cam and in the non-variable HdC stars might indicate that they lie just outside the instability strip. The presence of such an instability strip has been postulated by Trimble (1972) from her theoretical studies of pulsations in helium stars. However, non-variable and variable (R CrB stars) HdC stars seem to have the same M_v of – 4·0 mag (Feast 1972; Richer 1975) $T_{\rm eff}$ and thus occupy the same position in the HR diagram. This might be related to the fact that XX Cam and even all the cool non-variable HdC stars (Warner 1967) have hydrogen much more deficient (except HD 148839) and carbon enhanced in abundance than R CrB and RY Sgr. The theoretical pulsation calculations of Trimble (1972) show that increasing the carbon content is like increasing Z, the metallicity parameter and the effect of this on the pulsational properties of helium stars is such that for a given $T_{\rm eff}$ a star with large Z will be less likely to pulsate than one with smaller Z. Thus XX Cam with a higher carbon content (also oxygen) and less hydrogen might be more stable than R CrB and RY Sgr. However, more observational studies regarding the chemical composition of HdC stars coupled with better theoretical pulsation models are needed, before the above conjecture can be properly justified.

Although at present the evolutionary phase of R CrB stars is not clear (see Bond, Luck and Newman 1979; Paczynski 1971; Sackman, Smith and Despain 1974; Schönberner 1975; Wheeler 1978), the deficiency of hydrogen and lithium and enhancement of carbon (probably oxygen too) in XX Cam as well as the non-variable HdC stars might indicate in a stage of evolution later than of R CrB and RY Sgr.

Acknowledgements

We would like to express our thanks to M. K. V. Bappu, M. Cohen, G. Herbig, E. Harlan, B. McNamara and Sushma Mallik, for their help and advice.

References

Alexander, J. B., Andrews, P. J., Catchpole, R. M., Feast, M. W., Lloyd Evans, T., Menzies, J. W., Wisse, P. N. I., Wisse, M. 1972, *Mon. Not. R. astr. Soc.*, **158,** 305.

Bateson, F. W. 1972, *Inf. Bull. Var. Stars,* No. 661.

Bateson, F. W., Jones, A. F. 1973, *R. astr. Soc. New Zealand, Var. Stars Sec. Circ.,* No. 193.

Bidelman, W. P. 1948, *Astrophys. J.,* **107,** 413.

Bond, H. E., Luck, E. R., Newman, M. J. 1979, *Astrophys. J.* **233,** 295.

Danziger, I. J. 1965, *Mon. Not. R. astr. Soc.,* **130,** 199.

Feast, M. W. 1972, *Mon. Not. R. astr. Soc.,* **158,** 11 p.

Feast, M. W. 1975, *Variable Stars and Stellar Evolution,* Eds V. E. Sherwood and L. Plant, D. Reidel, Dordrecht, p. 129.

Feast, M. W., Glass, I. S. 1973, *Mon. Not. R. astr. Soc.,* **161,** 293.

Feast, M. W., Catchpole, R. M., Lloyd Evans, T., Robertson, B. S. C., Dean, J. F., Bywater, R. A. 1977, *Mon. Not. R. astr. Soc.,* **178,** 415.

Fernie, J. D., Sherwood, V., DuPuy, D. L. 1972, *Astrophys. J.,* **172**, 383.

Fitzgerald, P. M. 1968, *Astr. J.,* **73,** 983.

Gaustad, J. 1972, *Mem. Soc. R. Sci. de Liege 6^e^ Serie,* Tome III, 87.

Glass, I. S. 1978, *Mon. Not. R. astr. Soc.,* **185,** 23.

Humphreys, R. H., Ney, E. P. 1974, *Astrophys. J.,* **190,** 339.

Johnson, H. L. 1968, *Nebulae and Interstellar Matter* Eds. B. M. Middlehurst and L. H. Aller, University of Chicago Press, Chicago, p. 167.

Keenan, P. C., Greenstein, J. L. 1963, *Contr. Perkins. Obs. Ser II,* No. 13, 199.

Kolotilov, E. A., Orlov, M. Ya, Rodriguez, M. H. 1974, *Soviet Astr.,* **17,** 615.

Landolt, A. U. 1968, *Publ. astr. Soc. Pacific,* **80,** 318.

Landolt, A. U. 1973, *Publ. astr. Soc. Pacific,* **85,** 606.

Lee, T. A., Feast, M. W. 1969, *Astrophys. J.,* **157,** L173.

Mayan, M. W. 1960, J. *R. astr. Soc. Can.,* **54,** 193.

Mayall, M. W. 1972, *R. astr. Soc. Can*., **66,** 233.

O'Keefe, J. A. 1939, *Astrophys. J.,* **90,** 294.

Orlov, M. Ya, Rodriguez, M. H. 1974, *Astr. Astrophys*., **31,** 203.

Paczynski, B. 1971, *Acta Astr.,* **21,** 1.

Pugach, A. F. 1977, *Variable Stars* (*Russian*) **20,** 391.

Rao, N. K. 1975, *Bull. astr. Soc. India,* **3,** 50.

Rao, N. K. 1980a, *Astrophys. Sp. Sci.,* **70,** 480.

Rao, N. K. 1980b, *Observatory*, (in press).

Rao, N. K., Mallik, S. G. V. 1978, *Mon. Not. R. astr. Soc.,* **183,** 211.

Richer, H. B. 1975, *Astrophys. J.,* **197,** 611.

Sackman, I. J., Smith, R. L., Despain, K. H. 1974, *Astrophys. J.,* **181,** 555.

Schönberner, D. 1975, *Astr. Astrophys.,* **44,** 383.

Sherwood, V. E. 1975, *in IAU Symp.* 67: *Variable Stars and Stellar Evolution* Eds V. E. Sherwood and L. Plant, D. Reidel, Dordrecht, p. 147.

Stein, W. A„ Gaustad, J. E., Gillet, R C., Kanacke, R. F. 1969, *Astrophys. J.,* **155,** L3.

Totochava, A. G. 1973, *Astr. Circ. USSR* No. 791.

Totochava, A. G. 1975, *IAU Symp.* 67: *Variable Stars and Stellar Evolution* Eds V. E. Sherwood and L. Plaut, D. Reidel, Dordrecht, p. 161.

Trimble, V. 1972, *Mon. Not. R. astr. Soc.* **156,** 411.

Warner, B. 1967, *Mon. Not. R. astr. Soc.* **137,** 119.

Waters, B. H. J. 1966, *R. astr. Soc. New Zealand, Var. Stars Sec. Circ.,* No. 119.

Wheeler, T. C. 1978, *Astrophys. J.,* **225,** 212.

Yamashita, Y., Nariai, K., Narimoto, Y. 1977, *An Atlas of Representative Stellar Spectra,* University of Tokyo Press, Tokyo.

Yuin, E. 1948, *Astrophys. J.,* **107,** 413.

Zappala, R. R. 1972, *Astrophys. J.,* **172,** 51.

J. Astrophys. Astr. (1980) **1,** 79–95

A Dispersion Relation for Open Spiral Galaxies

G. Contopoulos *Astronomy Department, University of Athens, Athens, Greece*

Received 1980 March 20; accepted 1980 April 25

Abstract. The Lin-Shu dispersion relation is applicable in the (asymptotic) case of tight spirals (large wave number k_R). Here we reconsider the various steps leading to the Lin-Shu dispersion relation in higher approximation, under the assumption that the wave number k_R is not large [$(k_R r) = O(1)$], and derive a new dispersion relation. This is valid for open spiral waves and bars. We prove that this dispersion relation is the appropriate limit of the nonlinear self-consistency condition in the case where the linear theory is applicable.

Key words: galaxies—density waves—dispersion relation

1. Introduction

The basic dispersion relation of Lin and Shu (1964) for spiral density waves was derived on the asymptotic assumption of a large wave number k_R, *i.e.* of a small pitch angle (tight spirals). However, this assumption is not applicable to open spirals, or to bars.

As we will see below in the response calculations the wave number k_R enters through the combination $kr\epsilon$, where

$$\epsilon = \langle \dot{r}^2 \rangle^{\frac{1}{2}} / \kappa r \tag{1}$$

is the epicyclic small parameter, with $\langle \dot{r}^2 \rangle^{½}$ the dispersion of velocities and κ the epicyclic frequency. In the Lin-Shu dispersion relation the quantity $[k_R r \epsilon]$ is about 1 at co-rotation. Thus it is smaller than 1 in the whole 'long wave' branch of the dispersion relation from the inner Lindblad resonance up to co-rotation, as well as in the extension of the 'short wave' branch beyond co-rotation up to the outer Lindblad resonance.

The various steps and assumptions used in deriving the Lin-Shu dispersion relation were analysed in the Maryland Notes on the *Dynamics of Spiral Structure*

(Contopoulos 1972). There, however, only a first order epicyclic theory in ϵ was used.

In order to find a dispersion relation appropriate for relatively small k_R ($k_R r = O(1)$, or smaller), we will need a second order epicyclic theory.

In §2 we derive the response density in the case of a flat (two-dimensional) galaxy. Then, using also Poisson's equation, we derive, in §3, the new dispersion relation. We show that this dispersion relation agrees with the self-consistency conditions derived for nonlinear waves (Contopoulos 1979) in the limit where the linear theory can be applied.

2. The response density

We write the potential of the spiral galaxy V in the form

$$V = V_0 + V_1 \tag{2}$$

where $V_0 = V_0(r)$ is the axisymmetric background and

$$V_1 = V_1^*(r) \exp [i(\omega t - 2\theta)], \tag{3}$$

Represents a two-armed spiral mode with eigenvalue $\omega = 2\Omega_s$, where Ω_s is the angular velocity of the spiral pattern. We write

$$V_1^*(r) = \exp [i\Phi(r)]. \tag{4}$$

where Φ is complex; the derivative of Φ is the complex wave number

$$\Phi' = k = k_R + ik_I. \tag{5}$$

(Accents mean derivatives with respect to r). The imaginary part K_I is related to the amplitude A of the potential by the relation

$$k_I = -d \ln A/dr. \tag{6}$$

Thus k_R is the wave number used by Lin and Shu. In our case k_R is of $0(r^{-1})$ and it may even be zero (bar).

The corresponding density response is given by Shu (1968)

$$r\sigma_1^*(r) = \iint d\dot{r}\, dJ_0 \left\{ \frac{\partial f}{\partial E} V_1^*(r) - \frac{\left(2\dfrac{\partial f_0}{\partial J_0} + \omega \dfrac{\partial f_0}{\partial E_0}\right)}{2 \sin (\omega\tau_0 - 2\theta_0)} \right.$$

$$\left. \times \int_{-\tau_0}^{\tau_0} V_1^*(\tilde{r}) \exp [i(\omega\tilde{\tau} - 2\tilde{\theta})]\, d\tilde{\tau} \right\}, \tag{7}$$

where f_0 is the axisymmetric distribution function, given as a function of the energy

$$E_0 = \tfrac{1}{2}(\dot{r}^2 + J_0^2/r^2) + V_0(r), \tag{8}$$

and the angular momentum

$$J_0 = (r_0^3\, V_0')^{1/2} = r_0^2\, \Omega_0. \tag{9}$$

Here τ_0 is the half-period of the unperturbed orbit, θ_0 the angle between the pericentron and apocentron of an epicyclic orbit going through a given point (r, θ) at time τ_0. The quantity r_0 is defined by equation (9).

A second order epicyclic theory gives (Contopoulos 1975)

$$\tilde{r} = s_0 + s_1 \cos\theta_1 + s_2 \cos 2\theta_1, \tag{10}$$

and $$\dot{\tilde{r}} = -\frac{\pi}{\tau_0}(s_1 \sin\theta_1 + 2s_2 \sin 2\theta_1), \tag{11}$$

where $$\theta_1 = \frac{\pi}{\tau_0}(\tilde{\tau} - \tau_1) = \gamma - \gamma_1, \tag{12}$$

with $$\gamma = \tilde{\tau}\,\frac{\pi}{\tau_0},\ \gamma_1 = \tau_1 \frac{\pi}{\tau_0}, \tag{13}$$

τ_1 being the time of the apocentron passage (where θ_1=0). This orbit goes through $\tilde{r}$=r, with radial velocity $\dot{\tilde{r}}$ = r (defined by equation (8) if E_0 is given) at time $\tilde{\tau} = \tau_0$, *i.e.* for $\theta_1 = \pi - \gamma_1$.

We have further

$$s_2/s_1^2 = \frac{1}{12\kappa_0^2}\left(\frac{d\kappa_0^2}{dr_0} - \frac{3\kappa_0^2}{r_0}\right), \tag{14}$$

where κ_0 is the 'epicyclic frequency'

$$\kappa_0 = \left(\frac{3V_0'}{r_0} + V_0''\right)^{1/2} \tag{15}$$

and $$s_0 = r_0 - 3s_2. \tag{16}$$

We can see that s_1/r_0 is of $O(\epsilon)$, while $s_2/r_0 = O(\epsilon^2)$.

The value of τ_0 is given by

$$\pi/\tau_0 = \kappa_0\,(1 + a_0\, s_1^2), \tag{17}$$

But the expression of a_0 will not be needed.

Using these relations, and omitting terms of $O(\epsilon^3)$ we find

$$\tilde{r} - r = R_1 + R_2, \tag{18}$$

where $R_1 = (r_0 - r)(1 + \cos\gamma) - \frac{\dot{r}}{\kappa_0}\sin\gamma,$ (19)

and $$R_2 = \frac{s_2}{s_1^2}\left\{-2\left[(r_0 - r)^2 + \frac{2\dot{r}^2}{\kappa_0^2}\right]\cos\gamma - 4(r_0 - r)\frac{\dot{r}}{\kappa_0}\sin\gamma\right.$$

$$\left. + \left[(r_0 - r)^2 - \frac{\dot{r}^2}{\kappa_0^2}\right]\cos 2\gamma - 2(r_0 - r)\frac{\dot{r}}{\kappa_0}\sin 2\gamma - 3\left[(r_0 - r)^2 + \frac{\dot{r}^2}{\kappa_0^2}\right]\right\}. \tag{20}$$

We have also

$$\dot{\tilde{r}} = \dot{R}_1 + \dot{R}_2, \tag{21}$$

where the dot means differentiation with respect to $\tilde{\tau}$. Hence, in this approximation,

$$s_1^2 = (r_0 - r)^2 + \frac{\dot{r}^2}{\kappa_0^2}, \tag{22}$$

therefore $(r_0 - r)/r$ and $\dot{r}/\kappa r$ are of $0(\epsilon)$.

The dispersion of velocities $\langle \dot{r}^2 \rangle^{1/2}$ cannot be smaller than a minimum value $(0{\cdot}2857)^{1/2}\kappa/k_T$, necessary for axisymmetric stability (Toomre 1964), where

$$k_T = \kappa^2/2\pi G \sigma_0, \tag{23}$$

And σ_0 is the surface density. Thus we write

$$\langle \dot{r}^2 \rangle^{1/2} = Q(0{\cdot}2857)^{1/2}\kappa/k_T, \tag{24}$$

Where $Q \geqslant 1$. In realistic models Q may be of order 2. For $Q = 1$ (marginal stability) the small parameter ε in our galaxy varies between 0·26 at $r = 4$kpc and 0·10 at $r = 20$kpc, while for $Q = 2$ it varies between 0·5 and 0·2.

In equation (7) we need also the expression (derived from the formulae of Appendix A of contopoulos 1975):

$$\omega\tilde{\tau} - 2\tilde{\theta} = (\omega\tau_0 - 2\theta_0)\frac{\gamma}{\pi} + \Lambda_1 + \Lambda_2, \tag{25}$$

where $\theta_0 = \tau_0 \Omega_0\left(1 + \frac{\kappa_0'}{r_0\kappa_0}s_1^2\right),$ (26)

$$\Lambda_1 = \frac{4\Omega_0}{r_0\kappa_0}\left[\frac{\dot{r}}{\kappa_0}(1 + \cos\gamma) + (r_0 - r)\sin\gamma\right], \tag{27}$$

and $$\Lambda_2 = \frac{8\Omega_0 s_2}{r_0 \kappa_0 s_1^2}\left\{2(r_0 - r)\frac{\dot{r}}{\kappa_0}(1+\cos\gamma) - \left[(r_0-r)^2 + \frac{2\dot{r}^2}{\kappa_0^2}\right]\sin\gamma\right\}$$
$$+\frac{4\bar{s}_2}{s_1^2}\left\{2(r_0 - r)\frac{\dot{r}}{\kappa_0}\sin^2\gamma - \left[(r_0-r)^2 - \frac{\dot{r}^2}{\kappa_0^2}\right]\sin\gamma\cos\gamma\right\}, \tag{28}$$

where $\bar{s}_2 = O(\epsilon^2)$. As we will see the terms containing $\bar{s}_2$ do not contribute in the response integral, thus its value is not given.

We write further

$$\omega\tau_0 - 2\theta_0 = \nu_0\pi = \pi(1 - a_0 s_1^2)\left(\bar{\nu}_0 - \frac{2\Omega_0\kappa_0'}{r_0\kappa_0^2}s_1^2\right), \tag{29}$$

where $$\bar{\nu}_0 = (\omega - 2\Omega_0)/\kappa_0. \tag{30}$$

In the last integral of equation (7) we have also

$$V_1^*(\tilde{r}) = V_1^*(r)\exp[i\Phi(\tilde{r}) - i\Phi(r)] = V_1^*(r)\exp\{i[k(R_1 + R_2 + \ldots)$$
$$+\tfrac{1}{2}k'(R_1 + R_2\ldots)^2 + \ldots]\}. \tag{31}$$

Thus equation (7) is written

$$r\,\sigma_1^*(r) = V_1^*(r)\int_{-\infty}^{\infty} d\dot{r}\int_0^{\infty} dr_0\frac{dJ_0}{dr_0}\left[\frac{\partial f_0}{\partial E_0} - \frac{\left(2\dfrac{\partial f_0}{\partial J_0} + \omega\dfrac{\partial f_0}{\partial E_0}\right)}{2\sin(\nu_0\pi)}\frac{\tau_0}{\pi}\right.$$
$$\left.\times\int_{-\pi}^{\pi} d\gamma\exp\{i[\nu_0\gamma + \Lambda_1 + \Lambda_2 + k(R_1 + R_2) + \tfrac{1}{2}k'R_1^2 + \ldots]\}\right], \tag{32}$$

where k, k' … are calculated at r.

We introduce not the unperturbed distribution function (Shu 1970)

$$f_0 = \frac{2\Omega_0\sigma_0(r_0)}{\kappa_0 2\pi\langle\dot{r}^2\rangle_0}\exp\left[-\frac{(E_0 - E_{00})}{\langle\dot{r}^2\rangle_0}\right], \tag{33}$$

where E_0, J_0 are given by equations (8) and (9) and

$$E_{00} = \frac{1}{2}\frac{J_0^2}{r_0^2} + V_0(r_0). \tag{34}$$

Thus $$E_0 - E_{00} = \frac{1}{2}\left[\dot{r}^2 + \kappa_0^2(r - r_0)^2 + \frac{4\kappa_0^2 s_2}{s_1^2}(r - r_0)^3 + \ldots\right]. \tag{35}$$

After some operations we find

$$2\frac{\partial f_0}{\partial J_0}+\omega\frac{\partial f_0}{\partial E_0}=-\frac{f_0}{\langle \dot r^2\rangle_0}\left(\bar\nu_0\,\kappa_0-T\langle \dot r^2\rangle_0\right), \tag{36}$$

where $$T=\frac{4\Omega_0}{\kappa_0^2 r_0}\left[\frac{d\ln}{dr_0}\left(\frac{\Omega_0\,\sigma_0\,(r_0)}{\kappa_0\,\langle \dot r^2\rangle_0}\right)+\left(\frac{E_0-E_{00}}{\langle \dot r^2\rangle_0}\right)\left(\frac{d\ln\,\langle \dot r^2\rangle_0}{dr_0}\right)\right]. \tag{37}$$

Further

$$\bar\nu_0\,\kappa_0\,\frac{\tau_0}{\pi}=\nu_0+\frac{2\Omega_0\kappa_0'}{r_0\,\kappa_0^2}\,s_1^2. \tag{38}$$

Using these values in equation (32) together with the expressions

$$dJ_0/dr_0=\kappa_0^2\,r_0/2\Omega_0, \tag{39}$$

and $$\partial f_0/\partial E_0=-f_0/\langle \dot r^2\rangle_0, \tag{40}$$

we find $$r\sigma_1^*(r)=V_1^*(r)\int_{-\infty}^{\infty}d\dot r\int_0^{\infty}dr_0\,\frac{\kappa_0 r_0\sigma_0(\tau_0)}{2\pi\langle \dot r^2\rangle_0^2}\exp\left[-(E_0-E_{00})/\langle \dot r^2\rangle_0\right]$$

$$\times\left[-1+\frac{1}{2\sin(\nu_0\pi)}\left(\nu_0+\frac{2\Omega_0\,\kappa_0'}{r_0\kappa_0^2}\,s_1^2-\frac{T\langle \dot r^2\rangle_0}{\kappa_0}\right)\int_{-\pi}^{\pi}d\gamma\right.$$

$$\left.\times\exp\left\{i[\nu_0\gamma+\Lambda_1+\Lambda_2+k(R_1+R_2)+\tfrac12 k'R_1^2]\right\}\right]. \tag{41}$$

This is the basic ‘response equation’. From this equation we can easily derive the Lin-Shu formula (1974) under the following assumptions and simplifications:

(i) We assume that $|kr|$ is large, of $0(\epsilon^{-1})$.

(ii) We assume that we are not close to the Lindblad resonances or the particle resonance, *i.e.* $\sin(\nu_0\pi)$ is not of $0(\epsilon^2)$ or smaller.

(iii) We write $\xi=r_0-r$ and integrate ξ from $-\infty$ (instead of $-r$) to ∞.

(iv) We omit all terms except those of the lowest order.

Then we find the well-known formula

$$\sigma_1^*=-\frac{V_1^*\,\sigma_0}{\langle \dot r^2\rangle}\left(1-\frac{\nu\pi}{\sin(\nu\pi)}\,G_\nu\,(\chi_R)\right) \tag{42}$$

where $$G_\nu\,(\chi_R)=\frac{1}{2\pi}\int_{-\pi}^{\pi}d\gamma\,\cos(\nu\gamma)\exp\left[-\chi_R\,(1+\cos\gamma)\right] \tag{43}$$

and $\quad X_R = k_R^2 \langle \dot{r}^2 \rangle / \kappa^2.$ (44)

The various quantities like v, κ are calculated at r, while the corresponding quantities v_0, K_0 are calculated at r_0. [An exception to this rule is the unperturbed surface density σ_0, which means $\sigma_0(r)$, while the surface density at r_0 is written explicity $\sigma_0(r_0)$]. In the next approximation in ε we use also in equation (41) the terms kR_2 and $\frac{1}{2}k'R^2_1$ and the cubic term in $(E_0 - E_{00})$. After several operations we find

$$\sigma_1^* = -\frac{V_1^* \sigma_0}{\langle \dot{r}^2 \rangle} \left\{ 1 - \frac{\nu\pi}{\sin(\nu\pi)} \left[G_\nu(X) - \frac{iX}{kr} \frac{dG_\nu}{dX} \frac{d \ln}{d \ln r} \left(\frac{dG_\nu}{dX} \frac{\sigma_0 k_R r \nu\pi}{\kappa^2 \sin(\nu\pi)} \right) \right] \right\}, \tag{45}$$

where k is now complex. This formula is essentially that of Shu (1970) if we set $k = k_R + ik_I$ and omit terms of $O(k_I^2)$.

In fact, if k is complex, we can write

$$X = k^2 \langle \dot{r}^2 \rangle / \kappa^2 = X_R(1 + i2k_I/k_R),$$

omitting terms of $O(k_I^2)$, and

$$G_\nu(X) = G_\nu(X_R) + \frac{i2k_I r}{k_R r} X_R \frac{d\,G_\nu}{dX}. \tag{46}$$

But $2k_I r = -d \ln A^2 / d \ln r$, thus the response density (45) becomes

$$\sigma_1^* = -\frac{V_1^* \sigma_0}{\langle \dot{r}^2 \rangle} \left\{ 1 - \frac{\nu\pi}{\sin(\nu\pi)} \left[G_\nu(X_R) - \frac{iX_R}{k_R r} \frac{d\,G_\nu}{dX} \right.\right.$$
$$\left.\left. \times \frac{d \ln}{d \ln r} \left(\frac{d\,G_\nu}{dX} \frac{\sigma_0\, k_R r \nu\pi A^2}{\kappa^2 \sin(\nu\pi)} \right) \right] \right\}. \tag{47}$$

We can check that this form is exactly that of Shu (1970).

In deriving eq. (45) we notice that the epicyclic terms of $O(\epsilon^2)$, namely the terms containing s_2/s_1^2 do not contribute in the response density. The same can be seen in Shu's (1970) derivation of the dispersion relation.

We come now to the case where $kr=O(1)$ *i.e.* kr is not large. In this case we start again with equation (41), assuming now $\mathbf{\Lambda}_1$ and kR_1 of $O(\epsilon)$ and $\mathbf{\Lambda}_2$, kR_2, and $\frac{1}{2}\, k'R^2_1$ of $O(\epsilon^2)$.

As regards sin $(v_0\pi)$ it can be away from zero (non-resonant case) or close to zero (resonant cases). We consider here the non-resonant case and leave a special resonant case ($v_0 \simeq 0$) for the Appendix.

We develop the last exponential of (41) and sort out the terms of various orders. The terms of orders $O(\epsilon^{-2})$ and $O(\epsilon^{-1})$ in the second member of (41) give

$$\frac{V_1^* \sigma_0}{\langle \dot{r}^2 \rangle} \left[-1 + \frac{\nu}{2 \sin(\nu\pi)} \int_{-\pi}^{\pi} d\gamma \, \exp(i\nu\gamma) \right] \tag{48}$$

and this is equal to zero.

In the next higher order, $O(1)$, we find

$$r\sigma_1^*(r) = V_1^*(r)\int_{-\infty}^{\infty} d\dot{r}\int_0^{\infty} dr_0\,\frac{r_0\kappa_0\sigma_0(r_0)}{2\pi\langle\dot{r}^2\rangle_0^{\frac{3}{2}}}\exp\Big\{-\frac{1}{2\langle\dot{r}^2\rangle_0}\Big[\dot{r}^2+\kappa_0^2(r_0-r)^2$$

$$-\frac{4\kappa_0^2\,s_2}{s_1^2}\,(r_0-r)^3\Big]+O_2\Big\}\Big[-1+\frac{\nu_0}{2\sin(\nu_0\pi)}\Big\{1-\frac{T_1\langle\dot{r}^2\rangle_0}{\kappa_0\,\nu_0}$$

$$+\frac{1}{\kappa_0\,\nu_0}\Big(\frac{2\,\Omega_0\,\kappa_0'}{r_0\,\kappa_0^3}-T_2\Big)[\dot{r}^2+\kappa_0^2\,(r_0-r)^2]\Big\}\int_{-\pi}^{\pi}d\gamma\exp(i\nu_0\,\gamma)$$

$$\times\Big\{1+i(\Lambda_1+kR_1)+i(\Lambda_2+kR_2)-\tfrac{1}{2}(\Lambda_1+kR_1)^2+\frac{ik'}{2}R_1^2\Big\}\Big] \tag{49}$$

where $$T_1=\frac{4\Omega}{\kappa^2r}\,\frac{d\ln}{dr}\Big(\frac{\Omega\kappa}{\sigma_0}\Big),\; T_2=\frac{4\Omega}{\kappa^2r}\,\frac{d\ln}{dr}\,(\sigma_0/\kappa), \tag{50}$$

and O_2 is a term containing the factor $(r_0-r)^4/\langle\dot{r}^2\rangle_0$.

If we use the values (19), (20), (27) and (28) for R_1, R_2, Λ_1, Λ_2 and perform the integration with respect to $\dot{r}$, we find

$$r\sigma_1^*(r)=V_1^*(r)\int_0^{\infty}dr_0\,Z_0\exp\Big[-\frac{\kappa_0^2\,(r_0-r)^2}{2\langle\dot{r}^2\rangle_0}+\frac{2\kappa_0^2s_2\,(r_0-r)^3}{s_1^2\,\langle\dot{r}^2\rangle_0}+O_2\Big]$$

$$\times\Big[-1+\frac{\nu_0}{2\sin(\nu_0\pi)}\Big\{1-\frac{T_1\langle\dot{r}^2\rangle_0}{\kappa_0\nu_0}+\frac{1}{\kappa\nu}\Big(\frac{2\Omega_0\kappa_0'}{r_0\kappa_0^3}-T_2\Big)\,[\langle\dot{r}^2\rangle_0$$

$$+\kappa_0^2\,(r_0-r)^2]\Big\}\int_{-\pi}^{\pi}d\gamma\exp(i\nu_0\gamma)\Big\{1-\frac{i2\,\bar{s}_1}{s_1}\,(r_0-r)\sin\gamma$$

$$+ik\,(r_0-r)\,(1+\cos\gamma)+\frac{i4\,\bar{s}_1}{s_1^3}\,s_2\,\sin\gamma\Big[(r_0-r)^2+\frac{2\langle\dot{r}^2\rangle_0}{\kappa_0^2}\Big]$$

$$-\frac{i4\,\bar{s}_2}{s_1^2}\Big[(r_0-r)^2-\frac{\langle\dot{r}^2\rangle_0}{\kappa_0^2}\Big]\sin\gamma\cos\gamma$$

$$-\frac{ik\,2\,s_2}{s_1^2}\Big[(r_0-r)^2+\frac{2\,\langle\dot{r}^2\rangle_0}{\kappa_0^2}\Big]\cos\gamma+\frac{iks_2}{s_1^2}\Big[(r_0-r)^2$$

$$-\frac{\langle\dot{r}^2\rangle_0}{\kappa_0^2}\Big]\cos 2\gamma-\frac{ik\,3\,s_2}{s_1^2}\Big[(r_0-r)^2+\frac{\langle\dot{r}^2\rangle_0}{2\,\kappa_0^2}\Big]-\frac{\langle\dot{r}^2\rangle_0}{2\kappa_0^2}\Big[\frac{2\,\bar{s}_1}{s_1}\,(1+\cos\gamma)$$

$$+ k \sin \gamma \Big]^2 - \frac{(r_0 - r)^2}{2} \Big[-\frac{2\,\bar{s}_1}{s_1} \sin \gamma + k(1 + \cos \gamma) \Big]^2$$

$$+ \frac{ik'}{2} \Big[\frac{\langle \dot{r}^2 \rangle_0}{\kappa_0^2} \sin^2 \gamma + (r_0 - r)^2 (1 + \cos \gamma)^2 \Big] \Big\} \Big], \tag{51}$$

where $\bar{s}_1 = -2\,\Omega_0 s_1 /\, r_0 \kappa_0,$ (52)

and $Z_0 = \dfrac{r_0 \kappa_0 \sigma_0 (r_0)}{(2\pi \langle \dot{r}^2 \rangle^3)^{1/2}}.$ (53)

We set now $r_0 - r = \xi$ and expand every quantity around $\xi = 0$. Thus

$$\exp \left[-\frac{\kappa^2 (r_0 - r)^2}{2 \langle \dot{r}^2 \rangle} + \frac{2 \kappa_0^2 s_2 (r_0 - r)^3}{s_1^2 \langle \dot{r}^2 \rangle_0} + O_2 \right]$$

$$= \exp \left(\frac{\kappa^2 \xi^2}{2 \langle \dot{r}^2 \rangle} \right) \left\{ 1 + \frac{\kappa^2}{\langle \dot{r}^2 \rangle} \left[\frac{2\, s_2}{s_1^2} - \frac{d \ln}{2\, dr} \left(\frac{\kappa^2}{\langle \dot{r}^2 \rangle} \right) \right] \xi^3 + O_2 \right\}, \tag{54}$$

where the last O_2 contains terms with $\xi^4/\langle \dot{r}^2 \rangle$ and $\xi/\langle \dot{r}^2 \rangle^2$.

Also

$$Z_0 = Z \left(1 + \frac{Z'}{Z} \xi + \frac{Z''}{2Z} \xi^2 \right), \tag{55}$$

with $Z = \dfrac{r \kappa \sigma_0 (r)}{(2\pi \langle \dot{r}^2 \rangle^3)^{1/2}},$ (56)

$$\frac{\nu_0}{\sin (\nu_0 \pi)} = \frac{\nu}{\sin (\nu \pi)} \left[1 + \frac{d \ln}{dr} \left(\frac{\nu}{\sin (\nu \pi)} \right) \xi + \frac{\sin (\nu \pi)}{2 \nu} \frac{d^2}{dr^2} \left(\frac{\nu}{\sin (\nu \pi)} \right) \xi^2 \right] \tag{57}$$

and $\exp \; (i \nu_0 \gamma) = \exp \; (i \nu \gamma) \left(1 + i \gamma \nu' \xi + \dfrac{i \gamma \nu''}{2} \xi^2 - \dfrac{\gamma^2 \nu'^2 \xi^2}{2} \right.$. (58)

Further $\bar{s}_1/s_1$, calculated previously at r_0, is replaced by

$$\bar{s}_1/s_1 + \frac{d}{dr} (\bar{s}_1/s_1)\, \xi$$

where now $\bar{s}_1/s_1$ is calculated at $r(\xi = 0)$.

If we integrate now over ξ from $-\infty$ to $+\infty$ (replacing the lower limit by $-\infty$ as done by Lin and Shu) we see that the terms of $O(\epsilon^{-2})$ are zero. The terms of $O(\epsilon^{-1})$ are odd in ξ, thus they are also zero. After some operations we find

$$\sigma_1^* = \frac{V_1^* \sigma_0\, \nu}{r \kappa^2 \sin (\nu \pi)} \int_{-\pi}^{\pi} d\gamma \exp\, (i \nu \gamma) \left\{ \left[\frac{d \ln}{dr} \left(\frac{\nu}{\sin (\nu \pi)} \right) + i \gamma \nu' - \frac{i 2 \bar{s}_1}{s_1} \sin \gamma \right. \right.$$

$$+ ik\,(1+\cos\gamma)\Big]\Big[\frac{Z'}{Z}+\frac{6s_2}{s_1^2}-\frac{3}{2}\frac{d\ln}{dr}\left(\frac{\kappa^2}{\langle\dot{r}^2\rangle}\right)\Big]+\frac{d\ln}{dr}\left(\frac{\nu}{\sin(\nu\pi)}\right)$$

$$\times\Big[i\gamma\nu' - \frac{i2\bar{s}_1}{s_1}\sin\gamma + ik\,(1+\cos\gamma)\Big] + i\gamma\nu'\Big[-i\frac{2\bar{s}_1}{s_1}\sin\gamma + ik\,(1+\cos\gamma)\Big]$$

$$+\frac{\sin(\nu\pi)}{2\nu}\frac{d^2}{dr^2}\left(\frac{\nu}{\sin(\nu\pi)}\right)+\frac{1}{\nu}\Big[\frac{4\,\Omega\,\kappa'}{r\kappa^2}-\kappa\,(T_1+2T_2)\Big]+\frac{i\gamma\nu''}{2}-\frac{\gamma^2\,\nu'^2}{2}$$

$$-i\,\frac{2d}{dr}\left(\frac{\bar{s}_1}{s_1}\right)\sin\gamma+\frac{i12\bar{s}_1 s_2}{s_1^3}\sin\gamma-\frac{ik6s_2}{s_1^2}(1+\cos\gamma)-\Big[\left(\frac{2\bar{s}_1}{s_1}\right)^2+k^2\Big](1+\cos\gamma)$$

$$+ik'\,(1+\cos\gamma)\Big\}\,. \tag{59}$$

Using now the values of Z, s_2/s_1^2, $\bar{s}_1/s_1$ and T_1, given by (56), (14), (52) and (50), we finally find

$$\sigma_1^* = \frac{V_1^*}{2\pi Gr}\left\{\frac{d}{dr}\Big[\frac{r}{k_T\,(1-\nu^2)}\left(i\,k-\frac{4\,\Omega\,\nu}{\kappa r}\right)\Big]-\frac{r}{k_T\,(1-\nu^2)}\Big[k^2+\left(\frac{4\Omega}{\kappa r}\right)^2\Big]\right.$$

$$\left.+\frac{4\Omega}{k_T\,\kappa\nu}\,\frac{d}{dr}\left(\frac{\Omega}{k_T}\right)\right\}. \tag{60}$$

We notice that this response is by two orders in $\varepsilon\,\sigma$ smaller than the response of Lin and Shu (42). However the present formula is valid for $k_R\, r$ not large, namely for $k_R\, r = O(1)$.

3. Dispersion relation

We find the dispersion relation if we set the response density given by equation (60), equal to the imposed density derived by solving Poisson's equation.

Kalnajs (1971) solved Poisson's equation in the case of a flat galaxy, by finding a relation between the Mellin transforms of the 'reduced potential' $r^{1/2}\,V_1$ and the 'reduced surface density' $r^{1/2}\,\sigma_1$. In the case of a potential of the form

$$V_1 = \exp\,[(i\alpha-\tfrac{1}{2})\ln r + i\,(\omega t-2\theta)], \tag{61}$$

the corresponding density is

$$\sigma_1 = -\frac{1}{2\pi GK(\alpha,2)}\,\exp\,\Big[\left(i\alpha-\frac{3}{2}\right)\ln r + i\,(\omega t-2\theta)\Big], \tag{62}$$

where, approximately

$$K(\alpha, r) \simeq (\alpha^2+4)^{-\frac{1}{2}}. \tag{63}$$

The approximation is very good for $|\alpha|$ large, while the greatest error occurs for $\alpha = 0$ and is less than 3 per cent.

As the form of most spiral galaxies is close to a logarithmic spiral we can use a formula of the form (61) and derive

$$kr = \alpha + \frac{i}{2}. \tag{64}$$

In Kalnajs' calculations α is considered real.

However one can extend these formulae to complex α provided that the imaginary part of α is small (Contopoulos 1980).

We write the solution of Poisson's equation in the form

$$\sigma_1^* = -\frac{V_1^*}{2\pi Gr}\left[\left(kr - \frac{i}{2}\right)^2 + 4\right]^{1/2} \tag{65}$$

with k complex.

Using (65), (60) and (23) we find

$$\left[\left(kr - \frac{i}{2}\right)^2 + 4\right]^{1/2} + \frac{d}{dr}\left[\frac{r}{k_T(1-\nu^2)}\left(ik - \frac{4\Omega\nu}{\kappa r}\right)\right]$$
$$-\frac{r}{k_T(1-\nu^2)}\left[k^2 + \left(\frac{4\Omega}{\kappa r}\right)^2\right] - \frac{4\Omega}{k_T\kappa\nu}\frac{d\ln}{dr}\left(\frac{\Omega}{k_T}\right) = 0. \tag{66}$$

This is the required dispersion relation. It is valid away from the main resonances of the galaxy (where $\nu^2 = 1$ or $\nu = 0$), provided $k_R\, r$ is of $0(1)$, and $(k_T\, r - ½)^2 < (k_R\, r)^2 + 4$.

If we disregard the quantity $i/2$ in the first term of (66) the dispersion relation becomes

$$\operatorname{sgn}(k_R)\, kr\left(1 + \frac{4}{k^2r^2}\right)^{1/2} + \frac{d}{dr}\left[\frac{r}{k_T(1-\nu^2)}\left(ik - \frac{4\Omega\nu}{\kappa r}\right)\right]$$
$$-\frac{r}{k_T(1-\nu^2)}\left[k^2 + \left(\frac{4\Omega}{\kappa r}\right)^2\right] - \frac{4\Omega}{k_T\kappa\nu}\frac{d\ln}{dr}\left(\frac{\Omega}{k_T}\right) = 0. \tag{67}$$

In this form the dispersion relation was given without proof by Contopoulos (1973)

A resonant form of the dispersion relation valid near the particle resonance is given in the Appendix.

It is of interest now to compare our dispersion relation (66) or (67) with the classical Lin-Shu dispersion relation

$$\frac{|k|}{k_T\chi}\left[1 - \frac{\nu\pi}{\sin(\nu\pi)}G_\nu(X)\right] = 1, \tag{68}$$

which is derived by solving Poisson's equation for large real k, in which case (65) gives $\sigma_1^* = -V_1^* |k|/2\pi G$, and inserting this value in (42).

We notice that

$$\chi = (kr)^2 \epsilon^2. \tag{69}$$

In our case, where $kr = O(1)$, we have $\chi = O(\epsilon^2)$. Thus we can expand the exponential in (43) and write $\exp[-\chi(1+\cos\gamma)] = 1 - \chi - \chi\cos\gamma$.
Then we find, up to terms of $O(\epsilon^2)$,

$$1 - \frac{\nu\pi}{\sin(\nu\pi)} G_\nu(X) = \frac{\chi}{1-\nu^2}, \tag{70}$$

and the dispersion relation becomes

$$|k| = k_T (1-\nu^2). \tag{71}$$

This dispersion relation contains only a few of the terms of our dispersion relation (66). On the other hand if in (66) we consider kr real and large the most important terms give again the relation (71).

We conclude that the Lin-Shu dispersion relation for kr not large tends to our dispersion relation (66) for large kr. This establishes a continuity between the two formulae but indicates clearly that the dispersion relation (66) is the correct one if kr is of $O(1)$, or smaller, and not large of $O(\epsilon^{-1})$.

We will prove now that the dispersion relation (66) can be derived as the limiting case of the nonlinear self-consistency equations derived by Contopoulos (1979).

If we are not very near resonance the self-consistency equations (80) and (81) of Contopoulos (1979) are written, in the present symbolism,

$$\frac{\sigma_0 \sin q_+ x}{k_R A} \left\{ \left(-k_I + \frac{4\Omega}{\kappa r}\right) \left[\frac{1}{r}\left(\frac{2\Omega}{\Omega - \Omega_s} - 1\right) - \frac{\sigma_0'}{\sigma_0} - \frac{x'}{x}\right] + (k_R + q_+') k_R \right\} = \frac{1}{2\pi G r} \mathrm{Re} \left[\left(kr - \frac{i}{2}\right)^2 + 4\right]^{1/2}, \tag{72}$$

and

$$\frac{\sigma_0 \sin q_+ x}{k_R A} \left\{ k_R \left[\frac{1}{r}\left(\frac{2\Omega}{\Omega - \Omega_s} - 1\right) - \frac{\sigma_0'}{\sigma_0} - \frac{x'}{x}\right] - \left(k_R + q_+\right) \times \left(-k_I + \frac{4\Omega}{kr}\right) \right\} = \frac{1}{2\pi G r} \mathrm{Im} \left[\left(kr - \frac{i}{2}\right)^2 + 4\right]^{\frac{1}{2}}, \tag{73}$$

where x is the deviation of a periodic orbit from a circle, and

$$\cot q_+ = \frac{1}{k_R}\left(-k_I + \frac{4\Omega}{\kappa r}\right). \tag{74}$$

Combining (72) and (73) in one complex equation we find

$$\left[\left(kr-\frac{i}{2}\right)^2+4\right]^{1/2}=\frac{\kappa^2 r\sin q_+ x}{k_T k_R A}\left\{\left(ik+\frac{4\Omega}{\kappa r}\right)\left[\frac{2\Omega}{r(\Omega-\Omega_s)}\right.\right.$$

$$\left.\left.-\frac{1}{r}-\frac{\sigma_0'}{\sigma_0}-\frac{x'}{x}+\left(k_R+q_+'\right)\left(k-\frac{i4\Omega}{kr}\right)\right\}.\tag{75}$$

In the linear approximation the deviation x is (Contopoulos 1979)

$$x=\frac{Ak}{2\kappa^2(1+\nu)\sin q_+}.\tag{76}$$

If we insert this value of x in (75) we find, after some operations

$$\left[\left(kr-\frac{i}{2}\right)^2+4\right]^{\frac{1}{2}}=\frac{r}{2k_T(1+\nu)}\left\{\left(ik+\frac{4\Omega}{\kappa r}\right)\left[\frac{2\Omega}{r(\Omega-\Omega_s)}-\frac{1}{r}-\frac{\sigma_0'}{\sigma_0}\right.\right.$$

$$\left.\left.+\frac{2\kappa'}{\kappa}+\frac{\nu'}{1+\nu}-ik\right]-\left(ik+\frac{4\Omega}{\kappa r}\right)'\right\}.\tag{77}$$

In the general neighbourhood of the inner Lindblad resonance (for which our theory was mainly developed) we have

$$1+\nu=\eta\ \text{(small)}.\tag{78}$$

If we keep only terms of $0(\eta^{-2})$ and $0(\eta^{-1})$ in the second member of (77), we can write $\Omega-\Omega_s=-\frac{1}{2}\kappa\nu$, hence

$$\left[\left(kr-\frac{i}{2}\right)^2+4\right]^{1/2}=\frac{r}{2k_T\,\eta}\left\{\left(ik+\frac{4\Omega}{kr}\right)\left(-\frac{1}{r}-\frac{\sigma_0'}{\sigma_0}+\frac{2\kappa'}{\kappa}+\frac{\nu'}{\eta}\right)\right.$$

$$\left.+k^2+\left(\frac{4\Omega}{kr}\right)^2-\left(ik+\frac{4\Omega}{\kappa r}\right)'\right\}.\tag{79}$$

Exactly the same formula is derived from the dispersion relation (66) in the same approximation, *i.e.* including only terms of $0(\eta^{-2})$ and $0(\eta^{-1})$. This provides a verification both of the dispersion relation (66) and of the self-consistency conditions of our previous paper.

This coincidence provides also the necessary continuity between the non-linear theory and the linear theory. Very close to the resonance the value of x given by (76) increases very much and tends to infinity as $\nu\to 1$. This is not possible, and the nonlinear theory provides the correct value of x there. However, further away from resonance the linear theory is sufficient and one can use the linearised self-consistency conditions or the dispersion relation (66). We must remember here that the nonlinear theory of Contopoulos (1979) was developed for kr not large,

while the corresponding theory for large kr (tight spirals) is much more complicated (Mertzanides 1976).
We finish this section by writing the dispersion relation in the case of a bar ($k_R = 0$):

$$\left[4-\left(k_I r-\frac{1}{2}\right)^2\right]^{\frac{1}{2}}-\frac{d}{dr}\left[\frac{r}{k_T\,(1-\nu^2)}\left(k_T+\frac{4\,\Omega\,\nu}{\kappa\,r}\right)\right]$$
$$-\frac{r}{k_T\,(1-\nu^2)}\left[-k_I^2+\left(\frac{4\,\Omega}{kr}\right)^2\right]-\frac{4\,\Omega}{k_T\,\kappa\nu}\frac{d\ln}{dr}\left(\frac{\Omega}{k_T}\right)=0. \tag{80}$$

The first term represents approximately the function $[K(\alpha, 2)]^{-1}$ of Kalnajs (1971) and is valid if

$$\left|k_I\,r-\frac{i}{2}\right|<2.$$

A better representation of $[K(\alpha, 2)]^{-1}$ is the expansion

$$2\left[1-\frac{(k_I\,r-\frac{1}{2})^2}{8}-\frac{(k_I\,r-\frac{1}{2})^4}{128}\right]$$

Which is approximately valid for $|k\,r - \frac{1}{2}| \lesssim 2{\cdot}2$.

4. Conclusions

We summarise here the main conclusions of the present paper.

(i) We found a dispersion relation which is valid for relatively open spirals and bars.

However, it is expected that this dispersion relation is approximately valid also for smaller pitch angles, of the order of 20°. The evidence is derived from the fact that the linear theoretical formula (76) above, gives good numerical results for pitch angles even less than 20° (Contopoulos 1979, Appendix C).

(ii) Our dispersion relation has a common limit with the Lin-Shu (1964) dispersion relation. Namely the Lin-Shu dispersion relation for kr not large coincides with our dispersion relation for large kr.

(iii) Our dispersion relation is the limit of the nonlinear self-consistency conditions (Contopoulos 1979) when the linear approximation is valid, namely not very near resonances.

(iv) The dispersion relation is in complex form, therefore it contains two equations that have to be satisfied simultaneously. These equations correspond to the self-consistency conditions, requiring that the phase and amplitude of the response density should coincide with the phase and amplitude of the imposed density.

In the case of a bar we have only one equation, that refers to the amplitude of the bar.

(v) The complex second order dispersion relation of Shu (1970) depends only on the first order epicyclic orbits and not on the second order epicyclic terms.

On the other hand in our dispersion relation we have also contributions from the epicyclic orbits of $O(\epsilon^2)$.

(vi) In the Appendix we give a dispersion relation valid near the particle resonance.

Numerical applications of the new dispersion relations will be given in another paper.

Appendix

We will apply now the basic response equation (41) to the neighbourhood of the particle resonance. In this case the result (60) is not valid because it contains ν in the denominator which tends to zero as r tends to the particle resonance r_* . The Lin-Shu formula (42) gives the impression that no singularity occurs at ν=0 because $\nu\pi/\sin(\nu\pi) \rightarrow 1$ as $\nu \rightarrow 0$. However, the singularity appears in the amplitude A if we solve Shu's (1970) complex dispersion relation.

A more careful examination of the basic response equation (41) shows that if ν_0 is small, of $O(\epsilon^2)$, then we cannot disregard the other terms of $O(\epsilon^2)$, besides ν_0, in the coefficient of the last integral. This coefficient contains the denominator $\sin(\nu_0 \pi)$, therefore it tends to infinity as $\nu_0 \rightarrow 0$.

One way to avoid the singularity is to consider ν_0 complex

$$\nu_0 = \nu_R + i\nu_I, \tag{Al}$$

where $\nu_R = 2(\Omega\ \tau_0 - \theta_0)/\pi$ and

$$\nu_I = \frac{\tau_0}{\pi}\omega_I \simeq \frac{\omega_I}{\kappa} < 0, \tag{A2}$$

i.e. we assume that the eigenvalue ω is complex

$$\omega = 2\Omega_s + i\omega_I, \tag{A3}$$

containing a small negative imaginary part ($\omega_I < 0$), corresponding to a slightly growing wave. As we will see this method is valid also if $\omega_I \rightarrow 0$, *i.e.* if a neutral wave is considered as the limit of a growing wave.

Near the resonance ν_0 can be replaced by

$$\nu_0 \simeq \nu'_* (\xi - \xi_*) + i\nu_I, \tag{A4}$$

where $\xi = r_0 - r,\ \xi_* = r_* - r.$ (A5)

This approach was used in the case of the Lindblad resonances by Mark (1971). If ν_I is small the major contribution to the integral over $\xi = r_0 - r$ comes from the region near $\xi - \xi_*$.

In equation (51) the lowest order terms in the expression for σ^*_1 that become infinite as $\nu_0 \to 0$ are

$$\frac{V_1^*}{r}\int_0^\infty dr_0\, Z_0 \exp\left[-\frac{\kappa_0^2\,(r_0-r)^2}{2\langle\dot r^2\rangle_0}\right]\frac{1}{2\sin(\nu_0\pi)}\left\{-\frac{T_1\langle\dot r^2\rangle_0}{\kappa_0}+\frac{1}{\kappa_0}\left(\frac{2\Omega_0\kappa_0'}{r_0\kappa_0^3}-T_2\right)\right.$$

$$\left.\times\left[\langle\dot r^2\rangle_0+\kappa_0^2(r_0-r)^2\right]\right\}\int_{-\pi}^{\pi} d\gamma\, \exp\,(i\nu_0\gamma). \tag{A6}$$

These terms are of $O(\epsilon^2)$. Introducing the above expression (A4) and omitting higher order terms we find

$$\frac{V_1^* Z}{\kappa r\,\nu_*'}\int_{-\infty}^{\infty}\frac{d\xi}{(\xi-\xi_p)}\exp\left(-\frac{\kappa^2\xi^2}{2\langle\dot r^2\rangle}\right)\left[\left(-T_1+\frac{2\Omega\kappa'}{r\kappa^3}-T_2\right)\langle\dot r^2\rangle\right.$$

$$\left.+\,\kappa^2\left(\frac{2\Omega\kappa'}{r\kappa^3}-T_2\right)\xi^2\right], \tag{A7}$$

where $\xi_p = \xi_* - i\nu_I/\nu_*'.$ (A8)

The integral extends from $-\infty$ (instead of $-r$) to $+\infty$, as in the case of Lin and Shu.

Using the w function (Abramowitz and Stegun 1965)

$$w(z)=\frac{i}{\pi}\int_{-\infty}^{\infty}\frac{\exp\,(-t^2)\,dt}{z-t}, \tag{A9}$$

we find $\dfrac{V_1^* Z}{\kappa r\nu_*'}\left\{i\pi w\,(u_p)\left[\left(-T_1+\dfrac{2\Omega\kappa'}{r\kappa^3}-T_2\right)\langle\dot r^2\rangle+\left(\dfrac{2\Omega\kappa'}{r\kappa^3}-T_2\right)\kappa^2\xi_p^2\right]\right.$

$$\left.+\,\kappa\xi_p\,(2\pi\langle\dot r^2\rangle)^{\frac12}\left(\frac{2\Omega\kappa'}{r\kappa^3}-T_2\right)\right\} \tag{A10}$$

where $u_p=\kappa\xi_p/(2\langle\dot r^2\rangle)^{\frac12}.$ (A11)

Assuming that $\nu_I \to 0$ we have for a neutral wave, considered as a limit of growing waves, $u_p = u_*$, where

$$u_*=\kappa\xi_*/(2\langle\dot r^2\rangle)^{\frac12}. \tag{A12}$$

Thus the last term of the response density (60) must be replaced by

$$\frac{V_1^*\sigma_0 2\Omega}{\kappa^2 r\nu_*'}\left\{\frac{i\pi w(u_*)}{(2\pi\langle\dot r^2\rangle)^{1/2}}\left[\frac{d\ln}{dr}\left(\frac{\kappa}{\Omega^2}\right)+\frac{\kappa^2\xi_*^2}{\langle r^2\rangle}\frac{d\ln}{dr}\left(\frac{k_T^2}{\kappa}\right)\right]+\left[\frac{\kappa\xi_*}{\langle\dot r^2\rangle}\frac{d\ln}{dr}\left(\frac{k_T}{\kappa}\right)\right]\right\}, \tag{A13}$$

and the final form of the dispersion relation near the particle resonance is†

$$\left[\left(kr-\frac{i}{2}\right)^2+4\right]^{1/2}+\frac{d}{dr}\left[\frac{r}{k_T(1-\nu^2)}\left(ik-\frac{4\Omega\nu}{\kappa r}\right)\right]-\frac{r}{k_T(1-\nu^2)}$$
$$\times\left[k^2+\left(\frac{4\Omega}{\kappa r}\right)^2\right]+\frac{2\Omega}{k_T\nu'_*}\left\{\frac{i\pi w(u_*)}{(2\pi\langle\dot{r}^2\rangle)^{1/2}}\left[\frac{d\ln}{dr}\left(\frac{\kappa}{\Omega^2}\right)+\frac{\kappa^2\,\xi_*^2}{\langle\dot{r}^2\rangle}\frac{d\ln}{dr}\left(\frac{k_T^2}{\kappa}\right)\right]\right.$$
$$\left.+\frac{\kappa\xi_*}{\langle\dot{r}^2\rangle}\frac{d\ln}{dr}\left(\frac{k_T^2}{\kappa}\right)\right\}. \qquad \text{(A14)}$$

References

Abramowitz, M., Stegun, I. A. 1965, *Handbook of Mathematical Functions,* Dover, p. 297.

Contopoulos, G. 1972, *The Dynamics of Spiral Structure,* Lecture Notes, University of Maryland.

Contopoulos, G. 1973, in *Dynamical Structure and Evolution of Stellar Systems,* Eds L. Matrinet and M. Mayor, Geneva Observatory, P. 1.

Contopoulos, G. 1975, *Astrophys. J.,* **201,** 566.

Contopoulos, G. 1979, *Astr. Astrophys.,* **71,** 221.

Contopoulos, G. 1980, In preparation.

Kalnajs, A. 1971, *Astrophys. J.,* **166,** 275.

Lin,C.C, Shu, F.H.1964, *Astrophys. J.,* **140,** 646.

Mark, J. 1971, *Proc. nat. Acad. Sci. Am.,* **68,** 2095.

Mertzanides, C. 1976, *Astr. Astrophys.,* **50,** 395.

Shu, F. H. 1968, *PhD thesis,* Massachusetts Institute of Technology.

Shu, F.H.1970, *Astrophys. J.,* **160,** 99.

Toomre, A. 1964, *Astrophys. J.,* **139,** 1217.

†This dispersion relation was given without proof by Contopoulos (1973) but with an erratum: A factor κ should be put in front of $w\,(u_*)$ there.

J. Astrophys. Astr. (1980) **1,** 97–100

Comments on the Source Function Equality in (Zeeman)-Multiplets

L. G. Stenholm and R. Wehrse *Institut für Theoretische Astrophysik, im Neuenheimer Feld 294, D 6900 Heidelberg, Federal Republic of Germany*

Received 1980 June 18; accepted 1980 June 23

Abstract. The conditions for the source functions of a multiplet to be equal are studied for plasmas with and without magnetic fields. It is found that source function equality holds—in addition to the case of collisional predominance—only when the redistribution functions are all identical and no interlocking with other lines occurs. When magnetic fields are present, the assumption of source function equality leads to a violation of the invariance conditions of the scattering matrix and should therefore not be made.

Key words: radiative transfer—non-LTE—Zeeman effect—polarization

Non-LTE calculations for the radiative transfer of multiplet lines have recently been studied by several authors for plasmas without magnetic fields (*cf.* Mihalas 1978) and with magnetic fields (see *e.g.* Landi Degl'Innocenti 1975; Stenholm and Stenflo 1978; Auer, Heasley and House 1978). Many of these calculations, in particular those for Zeeman lines, are based on the assumption that the source functions of the lines are frequency-independent and equal. For the field-free case it is shown by Jefferies (1968), Athay (1972), Mihalas (1978) and others that source function equality occurs when the collision rates between the fine structure levels of the upper term are much larger than the collision rates between these levels and the ground state. In the general case equality is only possible when the mean intensities

$$\bar{J}_{ij} = \tfrac{1}{2} \int_{-\infty}^{\infty} \int_{-1}^{+1} \phi_{vi} (\tau, \mu, v)\, I (\tau, \mu, v)\, d\mu dv$$

scale as

$$
\begin{aligned}
&(B_{12}\,\bar{J}_{12}+C_{12}):(B_{13}\,\bar{J}_{13}+C_{13}):(B_{14}\,\bar{J}_{14}+C_{14})= \\
&\qquad(C_{21}+C_{23}+C_{24}-C_{32}-C_{42}+A_{21}): \\
&\qquad(C_{31}+C_{34}+C_{32}-C_{23}-C_{43}+A_{31}): \\
&\qquad(C_{41}+C_{42}+C_{43}-C_{24}-C_{34}+A_{41}).
\end{aligned}
\tag{1}
$$

(A_{ij}, B_{ij} and C_{ij} are the Einstein *A* and *B* coefficients and the collision rates for transitions $i\rightarrow j$). Equation (1) is easily derived from the statistical equations (*e.g*. Mihalas 1978) under the assumption that the upper levels are equally populated and that the induced emission can be neglected.

It is evident that equation (1) is satisfied—except for singular cases—only if no line of the multiplet is blended with other lines and the redistribution functions are identical. In stellar atmospheres or gas clouds with magnetic fields the last condition is not satisfied, since the absorption coefficients for the Zeeman components have a quite different angle dependence (*cf. e.g.* Stenholm and Stenflo 1978 ; see also equation (6) below). Obviously this may introduce very large deviations from an equal population of the upper levels, in particular for low density configurations (collision rates small!) of spherical geometry (finite optical depth).

In addition, the basic invariants of the scattering matrix (Abhyankar and Fymat 1969) are not conserved, when identical source functions are used. This can be seen as follows: Let us start with the redistribution matrix F (Stenholm and Stenflo 1978)

$$
\mathbf{F}=\begin{pmatrix}
K_I\,K_I' & K_I\,K_Q' & K_I\,K_U' & K_I\,K_V' \\
K_Q\,K_I' & K_Q\,K_Q' & K_Q\,K_U' & K_Q\,K_V' \\
K_U\,K_I' & K_U\,K_Q' & K_U\,K_U' & K_U\,K_V' \\
K_V\,K_I' & K_V\,K_Q' & K_V\,K_U' & K_V\,K_V'
\end{pmatrix},
\tag{2}
$$

K'_x refers to the absorption for the Stokes vector x=(*I, Q, U, V)* and K_x is the corresponding quantity for re-emission). For this F, the calculation of the invariants leads to 9 equations between K_x and K_x' (Abhyankar and Fymat 1969), of which only two are different from each other:

$$
K_I^2=K_Q^2+K_U^2+K_V^2,\qquad K_I'^2=K_Q'^2+K_U'^2+K_V'^2.
\tag{3}
$$

When K_x = K'_x these equations reduce to one. Under the assumption of source function equality the K_x are defined as sums over the three components so that

$$K_I = \tfrac{1}{2}\,[\phi_0 - \tfrac{1}{2}(\phi_+ + \phi_-)]\,(1-\mu^2) + \tfrac{1}{2}(\phi_+ + \phi_-),$$
$$K_Q = \tfrac{1}{2}\,[\phi_0 - \tfrac{1}{2}(\phi_+ + \phi_-)]\,(1-\mu^2)\cos 2\chi, \tag{4}$$
$$K_U = \tfrac{1}{2}\,[\phi_0 - \tfrac{1}{2}(\phi_+ + \phi_-)]\,(1-\mu^2)\sin 2\chi,$$
$$K_V = \tfrac{1}{2}(\phi_- - \phi_+)\,\mu.$$

ϕ are the profiles of the components, χ is the azimuthal angle and μ=cos θ, where θ is the inclination angle relative to the radius vector. For simplicity we have chosen the magnetic field to be radially directed. Inserting these expressions into equation (3) we obtain

$$-\phi_0 = \frac{2\phi_+\,\phi_-\,\mu^2}{(\phi_+ + \phi_-)\,(1-\mu^2)}, \tag{5}$$

which cannot be fulfilled.

Equation (5) shows that for magnetized plasmas even when the upper levels are equally populated the assumption of source function equality leads to results that are not physically realistic. Consequently, whenever scattering is important in plasmas containing magnetic fields such an assumption should not be used. It is therefore unavoidable that we treat the components as separate but interacting analogous to the calculation for fluorescence lines (*cf. e.g.* Weyman and Williams 1969): For this purpose we introduce three redistribution matrices $\mathbf{F_0}$, $\mathbf{F_+}$, $\mathbf{F_-}$ with elements

$$\begin{aligned}
K_{0I} &= \tfrac{3}{8}\,\phi_0\,(1-\mu^2) & K_{\pm I} &= \tfrac{3}{4}\,\phi_\pm\,(1+\mu^2)\\
K_{0Q} &= \tfrac{3}{2}\,\phi_0\,(1-\mu^2)\cos 2\chi & K_{\pm Q} &= \tfrac{3}{4}\,\phi_\pm\,(1-\mu^2)\cos 2\chi\\
K_{0Q} &= \tfrac{3}{2}\,\phi_0\,(1-\mu^2)\sin 2\chi & K_{\pm U} &= \tfrac{3}{4}\,\phi_\pm\,(1-\mu^2)\sin 2\chi\\
K_{0V} &= 0 & K_{\pm V} &= \mp\,\tfrac{3}{2}\,\phi_\pm\,\mu.
\end{aligned} \tag{6}$$

They are normalized so that

$$\frac{1}{4\pi}\int_0^{2\pi}\int_{-1}^{+1} K_I\,d\mu\,d\kappa = 1$$

i.e. the number of photons is conserved in scattering processes. By elementary calculations it can now be shown that the invariance relations for $\mathbf{F_0}$, $\mathbf{F_+}$ and $\mathbf{F_-}$ are fulfilled identically.

In order to be consistent the transfer equation has now to be written

$$\begin{aligned}
\frac{dI_\nu}{dz} &= \kappa_0\,\mathbf{F}_0\,\mathbf{1}\,S_0 + \kappa_+\,\mathbf{F}_+\,\mathbf{1}\,S_+ + \kappa_-\,\mathbf{F}_-\,\mathbf{1}\,S_-\\
&\quad - (\kappa_0\,\mathbf{F}_0 + \kappa_+\,\mathbf{F}_+ + \kappa_-\,\mathbf{F}_-)\,I_\nu.
\end{aligned} \tag{7}$$

with

$$(\mathbf{1})_{ij} = \begin{cases} 1 \text{ for } i = j = 1 \\ 0 \text{ for all other } i, j, \end{cases}$$

$$\kappa_0 = (u_1 B_{13} - u_3 B_{31}) \frac{h\nu}{4\pi} ,$$

$S_0 = n_3 A_{31}/(n_1 B_{13} - n_3 B_{31})$, and

$k_\pm$ and $S_\pm$ are defined in an analogous way.

We note that in these equations the random phase approximation is used. This is justified for thermal plasmas, when the magnetic field is so high that the components are separated in the reference system of the atom.

In conclusion we state that for non-LTE plasmas containing magnetic field the source functions for the lines of a Zeeman triplet are *not equal* and calculations based on this assumption should be considered with caution. For radiative transfer calculations it is therefore necessary to consider the lines as being separate, but blended. The corresponding equations, which fulfill the invariance and normalization conditions, are given above.

Acknowledgement

This work has been performed as part of the programme of the Sonderforschungsbereich 132 'Theoretische und Praktische Stellarastronomie' which is sponsored by the Deutsche Forschungsgemeinschaft.

References

Abhyankar, K. D., Fymat, A. L. 1969, *J. Math. Phys.*, **10,** 1935.
Athay, R. G. 1972, *Radiation Transport in Spectral Lines*, D. Reidel, Dordrecht.
Auer, L. H., Heasley, J. N., House, L. L. 1978, *Astrophys. J.*, **216,** 531.
Jefferies, J. 1968, *Spectral Line Formation,* Blaisdel, Waltham.
Landi Degl' Innocenti, E. 1975, *Astr. Astrophys.*, **45,** 269.
Mihalas, D. 1978, *Stellar Atmospheres*, 2 edn, Freeman, San Francisco.
Stenholm, L. G., Stenflo, J. O. 1978, *Astr. Astrophys.*, **67,** 33.
Weyman, R. J., Williams, R. E. 1969, *Astrophys. J.*, **157,** 1201.

J. Astrophys. Astr. (1980) **1,** 101–111

An Iterative Simultaneous Solution of the Equations of Statistical Equilibrium and Radiative Transfer in the Comoving Frame

A. Peraiah *Indian Institute of Astrophysics, Bangalore 560034*

Received 1980 June 20; accepted 1980 October 30

Abstract. A direct iteration has been performed to obtain a simultaneous solution of the equations of line transfer in an expanding spherically symmetric atmosphere in the comoving frame with statistical equilibrium for a non-LTE, two-level atom. The solution converges in three or four iterations to an accuracy of 1 per cent of the ratio of the population densities of the two levels. As initial values, the upper level population was set equal to zero or to the LTE densities. The final solution on convergence indicates enhanced population of these levels over the initial values assumed, Large velocity gradients enhance this effect whereas large geometrical sizes of the atmospheres tend to reduce it.

Key words*:* statistical equilibrium equation—radiative transfer—co-moving frame—iterative solution—velocity gradients

1. Introduction

In solving the transfer equation in spectral lines, several assumptions are made in advance regarding the distributions of velocity, density and other physical variables. These supply the necessary base for a solution of the equation of transfer, no matter how inconsistent the assumptions may be as compared to the real physical situation. Such procedures have been adopted because of several limitations. To obtain the solution of the transfer equation itself is a formidable task. In addition to it, one should understand the extent to which the numerical and physical constraints restrict the usefulness of the solution.

In recent years, there has been a considerable amount of progress in the technique of obtaining a numerical solution of a non-LTE line transfer equation in expanding spherical atmospheres (Simmonneau 1973; Mihalas, Kunasz and Hummer 1975; Peraiah 1979, 1980a) with several assumptions, some of which need not represent the real situation in an extended stellar atmosphere. One should consider the stellar atmosphere in its entirety to obtain a consistent model, because of the fact that the radiation field and other physical parameters are interdependent. For example the absorption characteristics of the medium could be modified by the stellar radiation field that is incident on the atmospheric material. Again, the new excitation and ionization structure will modify the radiation field which will be noticed in the emergent radiation. Mihalas and Kunasz (1978) attempted to get a simultaneous solution of radiative transfer equation (in the comoving frame) and statistical equilibrium equation using the equivalent two-level atom approach. However, it appears that this takes about 10–15 iterations to obtain convergence of the simultaneous solution. Recently, Kegel (1979) has done extensive calculations towards understanding of the OH masers. He employed a large number of levels in the statistical equation and iterated these with a spatially independent solution of the radiative transport equation. He obtains several interesting results and concludes that the radiative transfer effects are rather important in the study of masers.

In this paper, we try to obtain a simultaneous solution by means of direct iteration of the line transfer equation in comoving frame and with statistical equilibrium equation for a two-level atom.

2. Brief description of the computational procedure

The solution of the transfer equation in comoving frame has been described in detail for complete redistribution and for partial frequency redistribution in the framework of discrete space theory (Peraiah 1980 a, b). The transfer equation in the commoving frame for a non-LTE, two-level atom is given by,

$$\mu \frac{\partial I(x,\mu,r)}{\partial r} + \frac{1-\mu^2}{r}\frac{\partial I(x,\mu,r)}{\partial \mu} = K_L\,[\beta+\phi(x)]\;[S(x,r)-I(x,\mu,r)] + \left\{(1-\mu^2)\frac{V(r)}{r} + \mu^2 \frac{dV(r)}{dr}\right\}\frac{\partial I(x,\mu,r)}{\partial x}, \tag{1}$$

and

$$-\mu \frac{\partial I(x,-\mu,r)}{\partial r} - \frac{1-\mu^2}{r}\frac{\partial I(x,-\mu,r)}{\partial \mu} = K_L[\beta+\phi(x)] \times [S(x,r)-I(x,-\mu,r)] + \left\{(1-\mu^2)\frac{V(r)}{r} + \mu^2 \frac{dV(r)}{dr}\right\}\frac{\partial I(x,-\mu,r)}{\partial x}, \tag{2}$$

where $I\,(x,\mu,r)$ is the specific intensity at the radial point r, making an angle $\cos^{-1}\mu$ with the radius vector. $V(r)$ is the gas velocity at r in terms of mean thermal velocity units (mtu). The quantity x is equal to $(\nu - \nu_0)/\Delta s$ where Δs is a standard frequency interval. The profile function $\phi(x)$ is normalized such that

$$\int \phi(x) dx = 1. \tag{3}$$

$S(x, \mu, r)$ is the source function given by (Grant and Peraiah 1972)

$$S(x, r) = \frac{\phi(x)}{\beta + \phi(x)} S_L(r) + \frac{\beta}{\beta + \phi(x)} S_C(r), \tag{4}$$

where β is the ratio K_C/K_L of opacities in the continuum and line per unit interval of x, and $S_L(r)$ and $S_C(r)$ are the line and continuum source functions respectively. S_L is given in terms of population densities of the two levels

$$S_L(r) = A_{21} N_2(r)/[B_{12} N_1(r) - B_{21} N_2(r)]. \tag{5}$$

The absorption coefficient $K_L(r)$ at line centre is given by

$$K_L(r) = \frac{h \nu_0}{4\pi \Delta s} (N_1 B_{12} - N_2 B_{21}), \tag{6}$$

where A_{21}, B_{12} and B_{21} are the Einstein coefficients and $N_1(r)$ and $N_2(r)$ are the population densities of the lower and upper levels respectively. The statistical equilibrium equation for the two levels is given by

$$\begin{aligned} N_1 \left[B_{12} \int_{-\infty}^{+\infty} dx\, \phi(x) \tfrac{1}{2} \int_{-1}^{+1} I(\mu)\, d\mu + C_{12} \right] \\ = N_2 \left[A_{21} + C_{21} + B_{21} \int_{-\infty}^{+\infty} dx\, \phi(x) \tfrac{1}{2} \int_{-1}^{+1} I(\mu)\, d\mu \right]. \end{aligned} \tag{7}$$

The frequency independent line source function $S_L(r)$ in equation (5) can also be written as

$$S_L(r) = (1 - \epsilon) \int_{-\infty}^{+\infty} \phi(x) J(x)\, dx + \epsilon B, \tag{8}$$

where B is the Planck function and ϵ is the probability that a photon is lost by collisional de-excitation in one scattering. This is given by $\epsilon = C/(C + A_{21})$ where $C = C_{21}[1 - \exp(-h\nu/kT)]$.

We are primarily interested in finding out the capabilities of this method in handling iterative problems. We have, therefore, chosen an isothermal atmosphere with $T_{\text{eff}} = 30{,}000$ K. The atomic parameters of hydrogen Lyman Alpha line have been chosen. The inner radius of the atmosphere is set equal to 10^{12} cm. As we are using a velocity law, where the velocity increases linearly with radius, we have adjusted the electron density $N_e(r)$ and neutral atom density $N(r)$, ($N(r) = N_1(r) + N_2(r)$ where $N_1(r)$ and $N_2(r)$ are the neutral atoms in level 1 and 2 respectively) at every radial point such that they always satisfy the equation of continuity. As the velocity increases outwards the optical depth decreases and we have $dV/d\tau<0$. The number of neutral atoms are calculated by using the Saha equation (Aller 1963)

$$\log \frac{N_1}{N_0} P_e = -\theta I + 2{\cdot}5 \log T - 0{\cdot}48 + \log 2\, u_1(T)/u_2(T), \tag{9}$$

where I is the ionization potential in volts, P_e is the electron pressure in dynes cm^{-2}, θ is equal to $5040/T$ and u's are the partition functions. We have set $N_e = 10^{14}$ cm^{-3}. The rates of collisional excitation and de-excitation are calculated by the relations (Jefferies 1968)

$$C_{12} \simeq 2{\cdot}7 \times 10^{-10}\, \alpha_0^{-1.68} \exp(-\alpha_0)\, T^{-3/2}\, A_{21} \frac{g_2}{g_1} (I_H/\chi_0)^2\, N_e, \tag{10}$$

and

$$C_{21} = 2{\cdot}7 \times 10^{-10}\, \alpha_0^{-1.68}\, T^{-3/2}\, A_{21} (I_H/\chi_0)^2\, N_e, \tag{11}$$

where χ_0 is the excitation energy E_{12} and $\alpha_0 = \chi_0/kT$. I_H is the ionization potential of hydrogen. We have considered two cases (1)$\beta = 0$ and $\epsilon \ll 1$ and (2) $\beta \sim \tau_{\text{shell}}^{-1}$ and $\epsilon \ll 1$. We have kept $N_2 = 0$ or its LTE value and the absorption coefficient is calculated by using equation (6) and hence the optical depth in a given shell. With these initial data, equations (1) and (2) are solved to obtain the mean intensities J_x. These mean intensities $J_x(r)$ are used to obtain a new set of $N_1(r)$ and $N_2(r)$ by solving the statistical equilibrium equation (7) and keeping $N(r) = N_1(r)+N_2(r)$. The new absorption coefficient is estimated with the help of equation (6), by which the transfer equations (1) and (2) are solved again. This process has been repeated until the population densities N's, at each radial point converge within 1 per cent in two successive iterations.

3. Discussion of the results

As we are treating only the statistical equilibrium equation and the equation of radiative transfer, we need several parameters to be specified in advance. We have chosen the quantity B/A (where B and A are the outer and inner radii of the medium) to be 3, 10 and 20. we have used a velocity law

$$V(r) = V_A + \frac{V_B - V_A}{B - A}(r - A), \tag{12}$$

where V (r), V_A and V_B are the velocities at r, A and B respectively. V_A is set equal to zero and V_B is set equal to 0, 5, 10, 30, 60 and 100 mtu.

In the first iteration we started with $N_1(r) = N(r)$ and $N_2(r) = 0$. In the second iteration the new values of N_1 (r) and N_2 (r) are employed to calculate the radiation field and this process is continued until convergence is achieved. We have chosen the population density as the criterion for the convergence because the absorption and emission characteristics are dependent on these quantities. The whole medium has been divided into 30 shells of equal geometrical thickness and it is ensured that at all the shell boundaries the quantities N_1 (r) and $N_2(r)$ in two successive iterations do not differ by more than 1 per cent.

In Figs 1 and 2, we have presented the ratio N_2/N_1 and the line source function calculated by equation (5) with respect to the optical depth in the medium for B/A=3 and 10 respectively. We have set $\beta = 0$ and $\epsilon \ll 1$. The maximum velocities we have used are $V_B = 0, 5, 10, 30, 60$ mtu. We notice a close similarity between the variation of S_L and N_2/N_1 with optical depth. At maximum τ we have maximum N_2/N_1 and S_L. The absolute value of N_2/N_1 is less than 10^{-2} whereas for the same temperature the equilibrium value is $7{\cdot}8 \times 10^{-2}$. This solution converged, in three iterations to the same ratio of N_2/N_1 irrespective of the fact

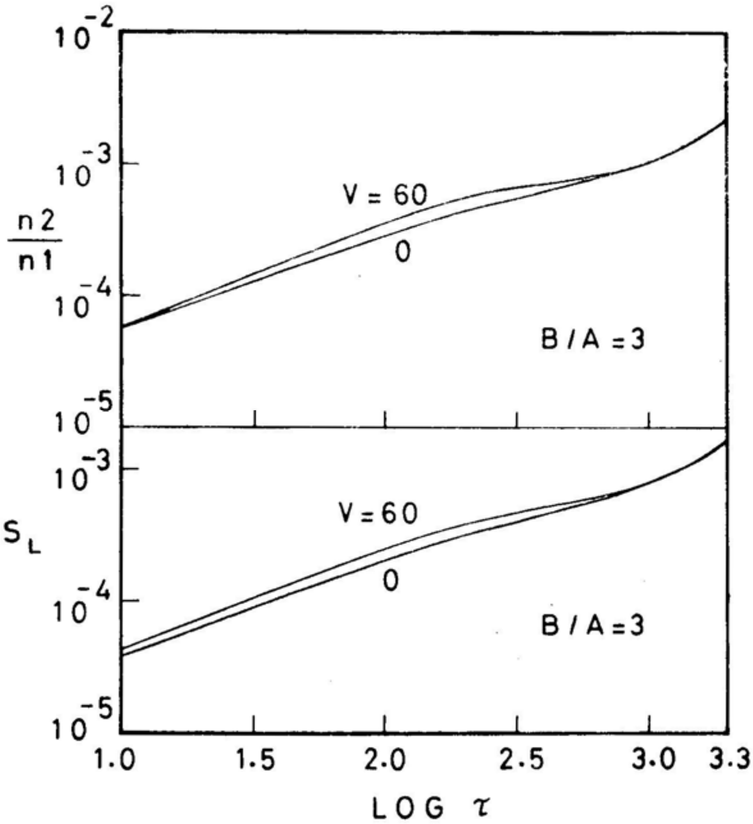

Figure 1. The line source functions S_L and N_2/N_1 are plotted against the optical depth for B/A=3 and V_B =0 and 60.

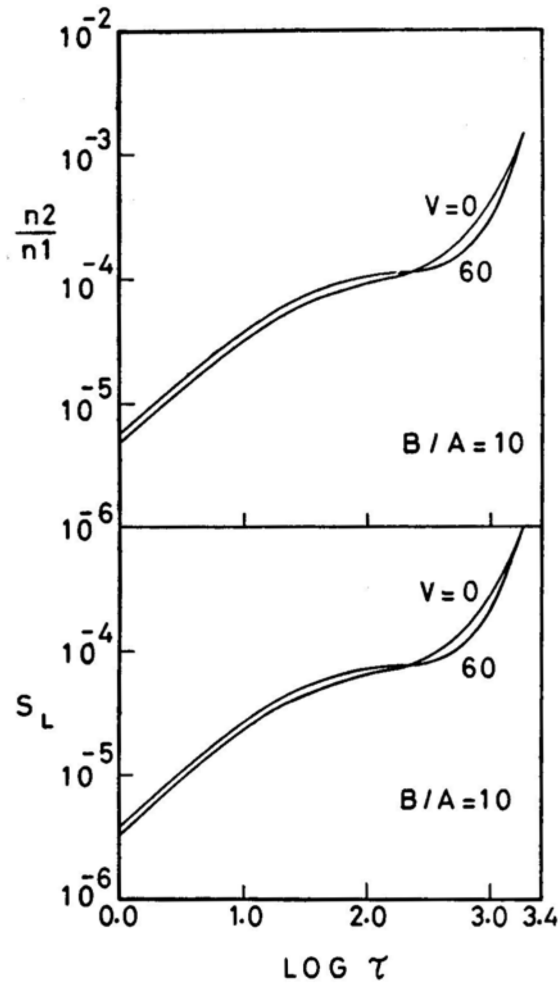

Figure 2. The line source functions S_L and N_2/N_1 are plotted against the optical depth for $B/A = 10$.

whether or not the initial N_2/N_1 is zero or the LTE value. The change in the maximum velocities does not seem to have much effect and therefore we have presented only those results that can be clearly seen in the figures. Fig. 3 gives us the flux profiles at infinity. For $V_B = 0$ (*i.e.* stationary medium) we obtain emission profiles with central absorption. However, when motion is introduced, the central absorption is replaced by emission. This is because of the fact that when more matter moves radially outwards into the side lobes the amount of scattering increases and this enhances the emission in the line (Peraiah 1980b).

In Fig. 4, we have plotted $\Delta N/N_1$, where $\Delta N = N_2 — N_1$, against the optical depth for $B/A = 3$ and $V_B = 0$, 5, 30, 60 and 100 mtu. We have set $\beta = \tau^{-1}_{\text{shell}}$ Therefore β changes between 10^{-2} and 10^{-4} in the medium. In spite of the fact that we have started the iteration with $N_2(r)=0$, the converged solution shows that $N_2(r)$ *is* nearly

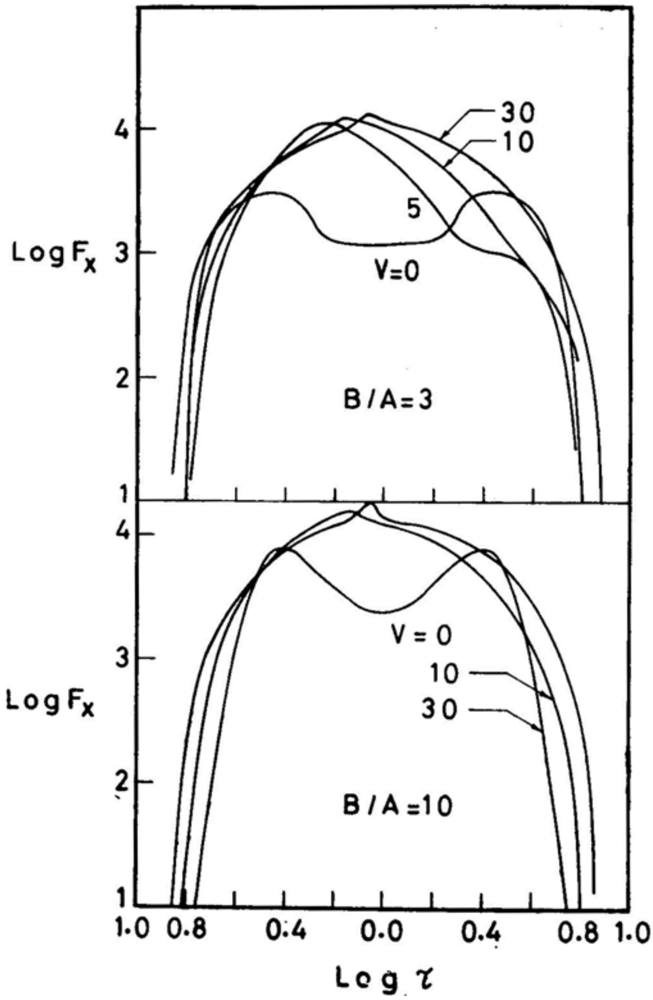

Figure 3. Flux profiles at infinity are given corresponding to the source functions given in Figs 1 and 2.

equal to $N_1(r)$. At =0, N_1 $N_1(r) > N_2(r)$ and the quantity $\Delta N/N_1$ falls off slowly, while at $\tau = \tau_{max}$ there is a sharp fall in $N_2(r)$. If we compare the results of Fig. 1 with those of Fig. 4, we notice that $N_2 N_1 \ll (N_2/N_1)_{LTE}$ in the former case and $N_2^{/}N1_1 \ll (N_2/N_1)_{LTE}$ in the latter. These differences arise because of the high mean intensities in the medium with $\beta > 0$. Results of Fig. 1 represent a medium with scattering whereas the results of Fig. 4 represent the medium with both line emission and scattering. The ratio N_2/N_1 is given by

$$\frac{N_2}{N_1} = \frac{B_{12}\int J_x \phi_x \, dx + C_{12}}{A_{21} + C_{21} + B_{21}\int J_x \phi_x \, dx}.$$

In this case, C_{12}, $C_{21} \ll B_{12}$, B_{21} and A_{21}. Therefore,

$$\frac{N_2}{N_1} = \frac{B_{12} \int J_x \phi_x \, dx}{A_{21} + B_{21} \int J_x \phi_x \, dx}. \tag{13}$$

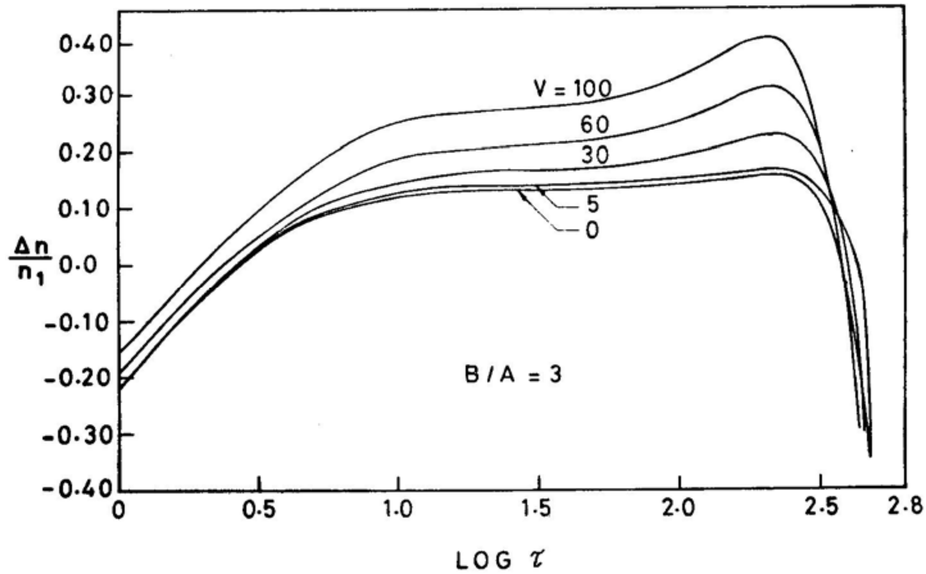

Figure 4. $\Delta N/N_1$ where $\Delta N = N_2 - N_1$ are plotted against total optical depth τ for B/A=3.

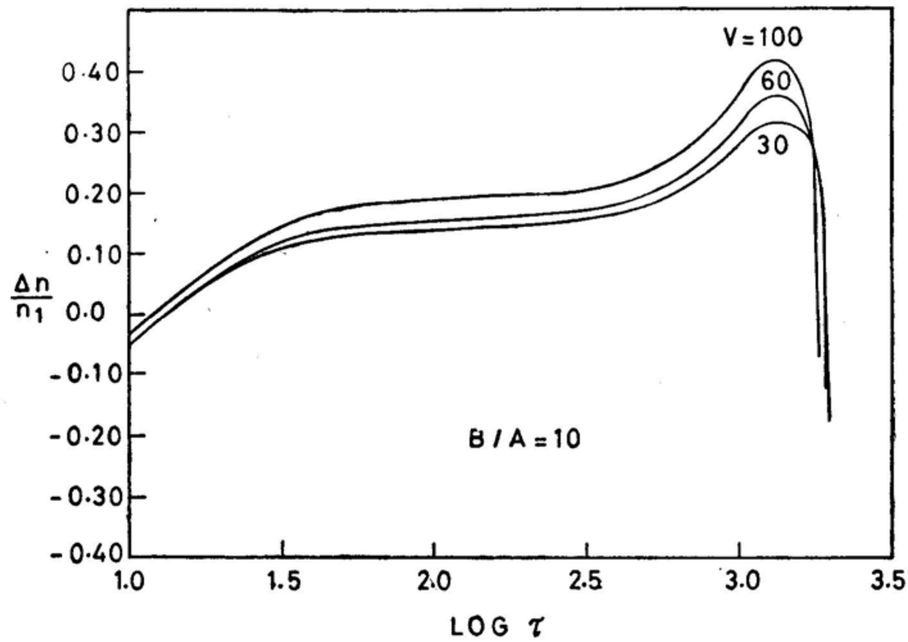

Figure 5. $\Delta N/N_1$ are given against total τ for B/A=10.

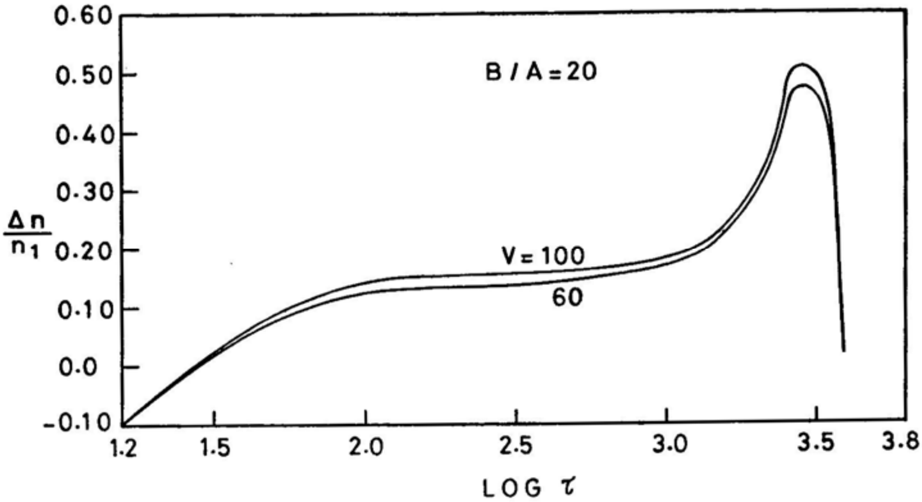

Figure 6. $\Delta N/N_1$ are given against total τ for B/A=20.

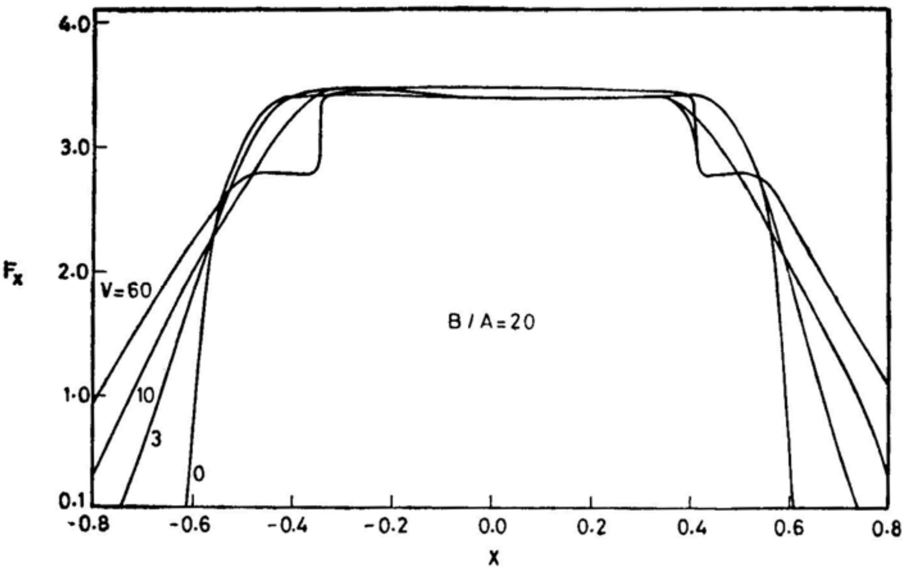

Figure 7. The flux profiles are plotted corresponding to the population density distribution given in Fig. 4. The abscissa is $Q = X/X_{\max}$.

One can estimate approximately the order of magnitude of N_2/N_1 using equation (13). In both the cases, for hydrogen L_α line at 30,000K, at some point in the atmosphere, we obtain, $N_2/N_1 \sim 10^{-4}$ in the first case and $N_2/N_1 \sim 1$ in the second case. This is so because the mean intensities are reduced considerably in the scattering medium with β=0 and $\epsilon \ll 1$, while in the emitting medium with $\beta > 0$ the mean intensities are much higher.

It is very interesting to notice that as $|dV/d\tau|$ increases the ratio $\Delta N/N_1$ increases and this is accentuated at large optical depth. For V_B = 100 mtu of the gas velocity, the maximum value of $\Delta N/N_1$ is as great as 0.4. In Figs 5 and 6, we have plotted $\Delta N/N_1$ for B/A=10 and 20 respectively. One observes immediately that the curves tend to converge for various values of $|dV/d\tau|$, and that they become unresolvable graphically until V_B=60 mtu of the gas velocity. The effects of high velocities which we noticed in Fig. 4 seem to be slightly reduced because of high curvature factors. As we are considering a much larger geometrical thickness, other factors being kept constant, the optical depth increases as B/A increases. We can also notice that the curves become flatter as B/A increases. In all other respects the results of Figs 2 and 3 are similar to those given in Fig. 1.

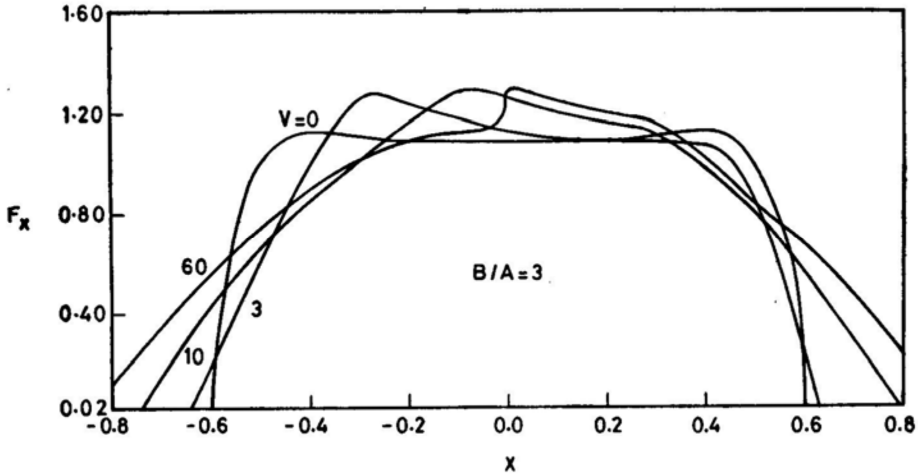

Figure 8. The flux profiles corresponding to the population distribution given in Fig. 5.

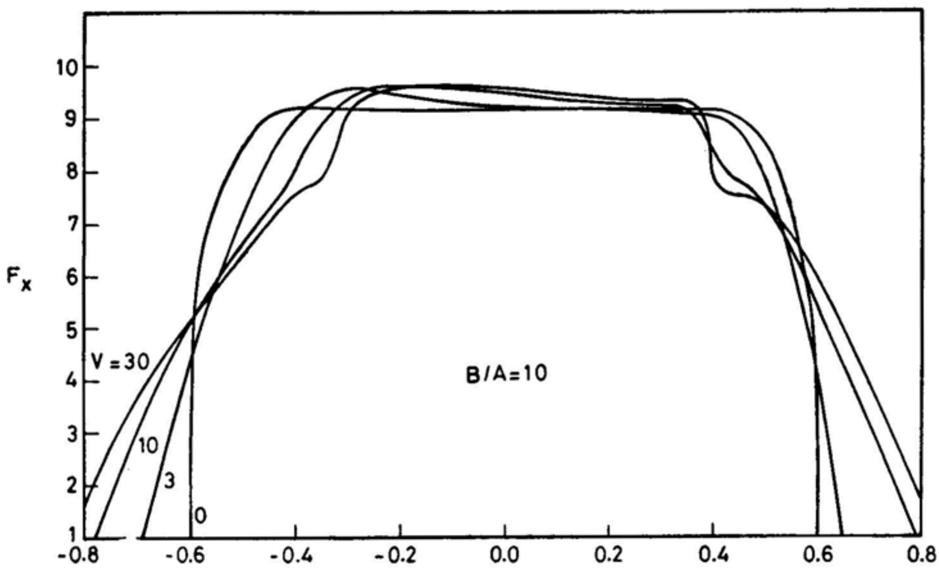

Figure 9. Same as those given in Figs 7 and 8 but corresponding to the population density distribution given in Fig.6.

The line source function $S_L(r)$ is calculated either from equation (5) or from equation (8) and the total source function is computed from equation (4). The line profiles seen by an observer at infinity are computed by using the total source function (Peraiah 1980b). These are given in Figs 7–9, for B/A =3, 10 and 20 respectively. For stationary medium, symmetric emission emerge for all values of B/A. However, for small $|dV/d\tau|$ when B/A=3, a small amount of asymmetry arises with red emission. For large B/A'*s* and $|dV/d\tau|$ we obtain almost symmetric profiles.

Acknowledgements

The author would like to thank Prof. Dr. W. H. Kegel, Dr. R. Wehrse and a referee for their useful comments.

References

Aller, L. H. 1963, *Astrophysics: The Atmospheres of the Sun and Stars,* 2 edn, Ronald, New York.
Grant, I. P., Peraiah, A. 1972, *Mon. Not. R. astr. Soc,* **160,** 239.
Jefferies, J. 1968, *Spectral Line Formation,* Blaisdel, Waltham.
Kegel, W. H. 1979, *Astr. Astrophys. Suppl. Ser.*, **38,** 131.
Mihalas, D., Kunasz, P. B. 1978, *Astrophys. J.,* **219,** 635.
Mihalas, D., Kunasz, P. B., Hummer, D. G. 1975, *Astrophys. J.,* **202,** 465.
Peraiah, A. 1979, *Kodaikanal Obs. Bull. Ser.* ***A*****, 2,** 115.
Peraiah, A. 1980a, *Acta Astr.*, (in press).
Peraiah, A. 1980b, *J. Astrophys. Astr.*, **1,** 3.
Simmonneau, E. 1973, *Astr. Astrophys.*, **29,** 357.

J. Astrophys. Astr. (1980) **1,** 113–117

Effects of High Velocities on Photoionization Lines

A. Peraiah and G. Raghunath *Indian Institute of Astrophysics, Bangalore 560034*

Received 1980 July 8; accepted 1980 October 27

Abstract. We have treated formation of spectral lines in a commoving frame where photoionization is predominant over collisional processes. We have assumed that the radiation field for causing photoionization is a function of Planck function. We have also considered the situation in which the continuum contributes to the radiation in the line. In all the models the quantity B/A (ratio of outer to inner radii) is kept equal to 10 and the total optical depth is taken to be 10^3. The velocity is assumed to be varying according to the law $dV/d\tau \sim — 1/\tau$ where τ is the optical depth ($\tau > 0$) in the given shell. The velocities at the innermost radius ($r = A$) are set equal to 0 and at the outermost radius ($r = B$), the maximum velocities are taken to be 0, 1, 3 and 10 Doppler units. The calculated line profiles are those seen by an observer at infinity. *P* Cygni-type profiles are observed in the case of a medium with no continuum absorption. For a medium with continuum absorption double peaked asymmetric profiles are noticed when the velocities are small; the two emission peaks merge into a single asymmetric peak for larger velocities.

Key words: photoionization lines—comoving frame—radiative transfer equation

1. Introduction

Thomas (1957) first studied the photoionization effects on the formation of lines. Jefferies and Thomas (1959) extended these calculations to obtain source functions in a photoionization-dominated line in a semi-infinite atmosphere with a chromospheric temperature rise. However, most of the attempts are aimed at investigating the line formation in a static medium. Recently, Vardavas and Cannon (1976) investigated the effects of partial frequency redistribution on the formation of these lines in a plane parallel atmosphere in which the gases move with differential velocities, Although they have employed moving media, their main purpose was to establish the differences in the emergent radiation field of the line in which the photon redistribution takes place according to R_{II} and R_{III} functions. However, in these calculations, the velocity employed is only one mean thermal unit although it is possible that in reality the gases move with velocities many times more than one unit of mean thermal velocity.

To obtain the solution of line transfer in high velocity media, one must solve it in the comoving frame and the radiation field should then be translated to a point at infinity. We present in the next section the results of such calculations.

2. Results and discussion

The solution of the radiative transfer equation in a comoving frame has been described earlier (Peraiah 1980). The line source function which we have employed in the transfer equation is as given by (Mihalas 1978)

$$S_L(r) = \frac{\int J_x \phi_x \, dx + \epsilon B + \eta B^*}{1 + \epsilon + \eta}, \tag{1}$$

where ϕ_x is the profile function of the line and $x = (\nu - \nu_0)/\Delta s$ Δs being some standard frequency interval. The quantitiesf ϵB, ϵ and η and ηB^* are the collisional and photoionization source and sink terms respectively (see Athay 1972). As our main interest is to see how the photoionization lines form, we have always set $\epsilon = 0$ and in the case of the model with continuum absorption, we have set β (the ratio of the continuum absorption to that in the line per unit frequency interval) equal to 10^{-6}. The frequency-dependant source function is computed by the formula (Grant and Peraiah 1972)

$$S(r, x) = \frac{\phi(x)}{\phi(x) + \beta} S_L(r) + \frac{\beta}{\phi(x) + \beta} S_C(r), \tag{2}$$

where $S_C(r)$ is the continuum source function which is set equal to the Planck function B and B^* is put equal to f_r B where $f_r \leqslant 1$. The velocity is considered to be changing as $dV/d\tau \sim -1/\tau$ where τ is the optical depth in the shell $|\tau| > 0$ and V is the average velocity of the gas over this shell. However, we have set $V_A = 0$ when $\tau = \tau_{max}$ and $V_B = 0, 1, 3, 10$ mtu at $\tau = 0$. A Doppler profile has been chosen with total optical depth at line centre as 10^3 and the factor η is put equal to 10^{-3} in all cases. The Planck function is taken to be unity and the quantity B/A (ratio of outer to inner radii) is set equal to 10.

In Fig. 1 (a, c, d), the total source functions are presented for the parameters shown in the respective figures. At $\tau = \tau_{max}$, we notice that the source functions are maximum. When the photoionizing radiation is equal to the Planck radiation that is, f_r=1, the source function falls off by about 5 orders of magnitude. When the quantity $f_r = 10^{-2}$, the source function falls one order of magnitude more than in the previous case and those corresponding to higher velocities are reduced much more. A small amount of continuum emission ($\beta = 10^{-6}$) is introduced and the corresponding source functions are given in Fig. 1 (b) for f_r=1. Here, again, we see the same

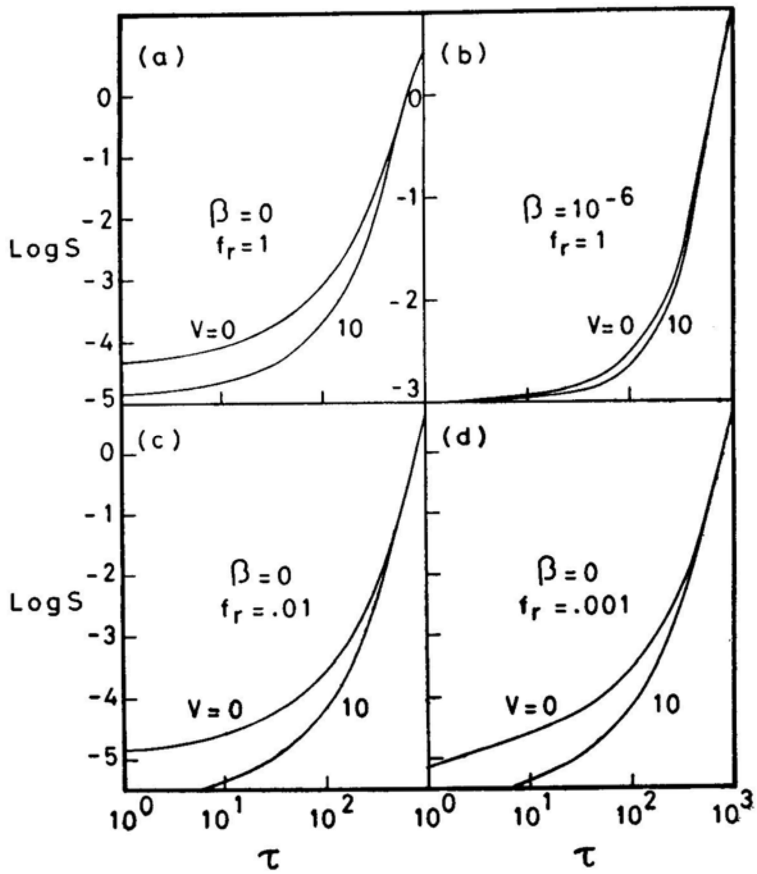

Figure 1. Source function dependence on optical depth for different values of f_r and β. The ratio of outer to inner radii of the atmosphere $B/A = 10$.

type of variation as shown in Fig. 1 (a, c and d) with the exception that the fall is steeper at larger optical depths and that the source function at $\tau = 0$ is only about three orders of magnitude less than that at $\tau = \tau_{\max}$. In this case, the variations in the amount of gas velocity do not introduce substantial changes in the source functions. We notice that the source functions are reduced considerably, particularly at $\tau = 0$. This is due to the fact that as the atmosphere expands, the density of the matter and hence the radiation field in the outer layers are correspondingly reduced so that equation of continuity is satisfied. The results for the cases $f_r = 10^{-2}$ and 10^{-3} are quite similar to those presented in Fig. l(b), and, therefore, are not shown here. The line profiles emerging from the medium are presented in Fig. 2. In Fig. 2 (a) the flux profiles for f_r =l are described. When $V_B = 0$, we notice that the profile is symmetric with small wing emission and self-reversal at the central absorption. However, this disappears when motion is introduced and we see an absorption core and an emission on the red side. A further increase in the velocity changes the profiles to imitate that of a *P* Cygni star. Fig. 2(b) and (c) give the profiles for $f_r = 10^{-2}$ and 10^{-3} respectively and we do not notice any self-reversal even when the gas is not in motion. These profiles have very deep absorption cores and a small amount of emission on the red

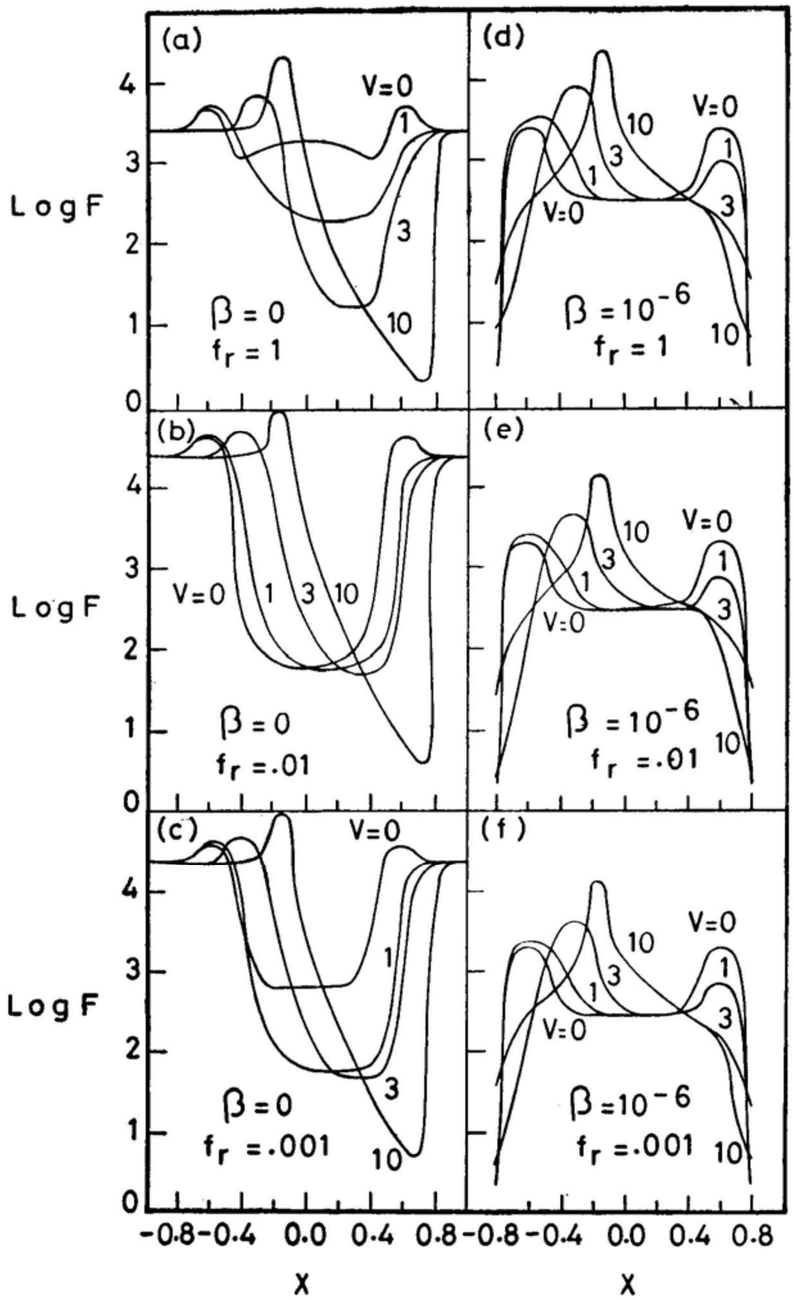

Figer 2. Flux profiles at infinity for different values of the parameters β and f_r In all cases B/A=10, $F=F_x/F_{\min}$, where F_x is the flux at frequency point x.

side. It should be noticed that when $f_r = 10^{-2}$ (Fig. 2b) the depth of the absorption cores for V_B=0, 1, 3 do not differ substantially and when f_r is reduced by a factor of 10, the depths of absorption cores are progressively increased. As the velocity increases, the *P* Cygni nature of the profiles becomes quite evident. Fig. 2 (d, e, f) contain the profiles corresponding to the case with $\beta=10^{-6}$. The flux profiles of Fig. 2(d, e, f) are in emission whereas those in Fig. 2 (a, b, c) are in absorption. This is because we have introduced emission in the continuum and this is shown in the profiles. We notice another important effect, that is, for smaller velocities, the profiles have emission in the wings, and when the velocity increases, we get one single emission peak at the centre of the line. The main reason for this kind of result is, when the atmosphere expands, more matter is transferred into the side lobes of the star and therefore more radiation is scattered into emission.

Reference

Athay, R. G. 1972, *Radiation Transport in Spectral Lines*, D. Reidel, Dordrecht.
Grant, I. P., Peraiah, A. 1972, *Mon. Not. R. astr. Soc.*, **160,** 239.
Jefferies, J. T., Thomas, R. N. 1959, *Astrophys. J.*, **129,** 401.
Mihalas, D. 1978, *Stellar Atmospheres*, 2 edn, Freeman, San Francisco.
Peraiah, A. 1980, *Acta Astr*., (in press).
Thomas, R. N. 1957, *Astrophys. J.*, **125,** 260.
Vardavas, M., Cannon, C. J. 1976, *Astr. Astrophys.*, **53,** 107.

J. Astrophys. Astr. (1980) **1,** 119–128

The Structure of Integrated Pulse Profiles

M. Vivekanand and V. Radhakrishnan *Raman Research Institute, Bangalore 560080*

Received 1980 July 8; accepted 1980 October 9

Abstract. We offer two possible explanations to account for the characteristics of integrated pulse profiles, in particular their degree of complexity, their variation from pulsar to pulsar, their stability, and the tendency of complex profiles to be associated with older pulsars.

It is proposed that the pulse structure could be a reflection of surface irregularities at the polar caps, and it is shown how the surface relief can affect the number of positrons released into the magnetosphere which are subsequently responsible for the observed radio radiation. The electrons produced in the vacuum break-down in the gap carry enough energy to allow creating such a surface relief in ~ 10^6 years, and one way in which this could be achieved is discussed.

Alternatively, the presence of multipole components in the magnetic fields of older pulsars could lead to significant variations in the curvature of the field lines across the gap, and hence to structure in the integrated pulse profiles. An assessment of the two hypotheses from observed pulse profiles seems to favour the polar cap relief picture.

Key words: pulsars—integrated pulse profiles—polar cap model

1. Introduction

One of the many remarkable features of pulsar radio radiation is the integrated pulse shape. Barring mode changes which we shall not discuss here it has been well established that the integrated pulse profiles are reproducible at any time; in other words they are stable for periods of time long compared with those over which pulsars have been observed so far. Further it has been noted (Taylor and Huguenin 1971) that in general pulsars with periods less than 0·75 seconds have simple pulse profiles while those with longer periods tend to have complex pulse profiles. This correlation clearly suggests that the pulse profile becomes more complex as the pulsar ages, but no satisfactory explanation has hitherto been advanced either for the existence of such structure or its evolution with pulsar age. This is in contrast to the microstructure of pulses, drifting sub-pulses, and other short period phenomena for which a number of possible explanations have been advanced.

The observed stability of the integrated pulse structure requires that the information determining its details be stored somewhere on the pulsar. In this paper we investigate two possible ways in which this information could be stored: (a) as surface irregularities at the magnetic polar cap of the pulsar, and (b) as magnetic field variations over the polar cap. We also discuss how this information can become more complex with increasing pulsar age to account for the observed correlation referred to above. We will restrict our discussion to the framework of the RS model (Ruderman and Sutherland 1975) for pulsars and its subsequent modifications (*e.g.* Cheng and Ruderman 1980).

In the model we put forward in this paper, surface irregularities are created by the effect of sparks on local regions in the polar cap. Such irregularities build up over a long period of time and in turn affect the strength of sparks over different areas and the intensity of the associated radio radiation. The minimum scale length of irregularities created by sparks will clearly depend on the area of individual sparks. As a consequence, the maximum number of features so created within the polar cap will depend on the ratio of the polar cap area to that of a spark. The typical area of an individual spark thus plays an important role in the model, and we therefore begin in the next section by estimating it from observations of the pulse microstructure. This is followed by a discussion of the effect of height variations on spark development and the number of positrons released into the magnetosphere by sparks.

In Section 4 we argue that under the combined influence of the temporary heating under a spark and the tension in the surface layer dueto the charge on it, the surface is likely to be deformed by a small amount. It is shown that the deformation required per spark is very small and that enough energy is available to achieve such deformations.

In Section 5 we consider an alternative explanation for the pulse structure based on the presence of multipole components in the magnetic field which are expected to make their appearance with the decay of the pulsar dipole magnetic field (Flowers and Ruderman 1977). In the last section we discuss the relative merits of the two mechanisms and conclude that the presence of several components in the integrated pulse profile of some pulsars favours the polar cap relief model.

2. Microstructure and spark areas

In the RS model the current from the polar cap is interrupted due to the non-availability of positive charges (Fe^{56} ions) which are not pulled off the surface by the electric field generated by the rotation of the neutron star. This causes a vacuum gap to form above the polar cap, about 10^4 cm in both height G and radius L, in which electron-positron pairs are created by any gamma ray photons which happen to be there. These pairs in turn produce photons by curvature radiation which produce more pairs.

This process goes on until the vacuum gap is broken by an avalanche of particles which is called a ‘spark’. The positrons travel away from the star to produce the radiation that we see while the electrons go to the polar cap to complete the pulsar homopolar circuit. The gap is now reformed and breaks down again by the same process. Such sparks occur about 10^5 times per second providing positron bursts which give rise to the pulsar microstructure, and whose average characteristics are reflected in the integrated pulse profile. We shall now attempt to derive the mean area of a spark from the observations of pulsar microstructure.

Let the area of each spark be a cm^2, and let A cm^2 be the area of the polar cap. Then there are A/a independent sparking regions on the polar cap. If sparks occur at 10 μs intervals, then each area is revisited by a spark after every $A/a \times 10$ μs on the average. Thus an observer would record radiation from sparks at a given location only every $A/a \times 10 \mu$s ($=\tau_1$). The radiation would last for a time τ_2, which, we shall discuss later. If sparks occur randomly on the polar cap, the rate of observed sparking would remain the same whether the observer is stationary at a particular longitude on the polar cap or moving across it.

If $\tau_2 < \tau_1$, radiation due to individual sparks can be resolved in each individual pulse of the pulsar, provided the observations are made with fine enough time resolution. If $\tau_2 > \tau_1$, we would only observe a continuous distribution of radiation. If $\tau_2 \approx \tau_1$, we would just resolve individual sparks, but we would interpret $\tau_2 (=\tau_1)$ as a single time scale of intensity variation. All three effects are observed in PSR 0950+08 (Hankins 1971) in which micropulses are spaced from a few hundred μs to 1 ms apart. Their duration ranges from a few hundred μs to as low as 10μs.

We associate the quasi-periodicities of $\lesssim 1$ ms in PSR 1133+16 (Ferguson *et al* 1976) and in PSR 0950+08 (Hankins 1971) and PSR 2016+28 (Cordes 1976) with the time separation τ_1 of observed sparks. For these pulsars the number of independent sparks area A/a can therefore be estimated to be of the order of $(\tau_1/10\ \mu\text{s}) \lesssim (1\ \text{ms}/10\ \mu\text{s}) = 100$. We thus conclude from the microstructure observations of pulsars that typically there are ten to hundred independent sparking areas on the polar cap. A similar conclusion was reached by Cheng and Ruderman (1977) who found from the widths of drifting subpulses that the fractional area of the polar cap occupied by a spark lies between 10^{-1} and 10^{-2}. We shall take the area of each spark to be $\approx \pi \times 10^6$ cm^2 and the radius of a spark area, assumed circular, to be $R \approx 10^3$cm.

In passing, a few remarks might be appropriate on the duration τ_2 of the observed microstructure (a few hundred microseconds) which is large compared to the supposed duration of sparks ($\approx 10\mu$s). In the RS model bunches of relativistic particles emit curvature radiation at a particular frequency from a certain extent of the magnetosphere which we will call the radiating zone for that frequency. Thus bunches travelling through the two extremities of this radiating zone would give out radiation which would reach the observer with a spread in time τ_2 which depends upon its extent. Thus τ_2 will depend on the net excess distance travelled by particles to and radiation from one extremity of the radiation zone, over that corresponding to the other.

3. Variations in the polar cap relief

We consider first the possibility that the surface of the polar cap deviates from that of a smooth sphere. It can be shown that the maximum height H of a conical hill on a base of the same material cannot exceed $3\pi\ Y\rho g$ where Y is the yield stress.

The value of H depends therefore on Y, ρ, and g all of which have uncertainties associated with them. The value of the Young's modulus for pulsar crustal material was estimated by Irvine (1978) as 10^{19} dynes cm^{-2} based on the value given by Chen, Ruderman and Sutherland (1974) for the binding energy. In view of the later work of Flowers *et al.* (1977) which indicates a decrease in the binding energy, a similar estimate would give a lower value.

If we assume that the yield stress Y is given by the Young's modulus, and lies in the range 10^{18} to 10^{19} dynes cm^{-2}, this leads to a value of H somewhere in the range 1 to 10 cm. We shall assume for the present purpose that H can have a value as high as 10 cm, and discuss later whether and how such irregularities are likely to result from the sparking process. For the moment we shall merely assume that the mean height of a spark area can differ from area to area by as much as 10 cm. The polar gap can then be likened to a parallel plate capacitor of separation G cm whose lower surface has bumps of height H cm and radius l cm. As $G \gg l \gg H$ the fractional excess electric field over the bumps would be $(\Delta\Phi/\Phi) \simeq H/l \approx 1$ per cent effective for a height $l \approx 10^3$ cm from the lower plate.

Since the gap height $G \approx 10^4$ cm, a hill of height 10 cm on the polar cap results in an average excess electric field of 0·1 per cent in the volume of the gap directly above it. We shall now show that even such a small excess electric field can significantly alter the number of charged particles produced in the gap.

Let us think of the spark discharge as developing in time 'steps' where the number of charges multiply by a constant factor at the end of each step. During the development of the discharge there is continuous leakage of charges from the gap as they reach one or other ' plate ' of the capacitor. If for some reason the number of charges effective for further multiplication in each step were increased, say by a fraction ϵ, then in each step, the number of charges participating in the avalanche breakdown would be $(1 + \epsilon)$ times more; in m steps the fractional increase in the total number of charges produced would be $(1+\epsilon)^m$.

In the RS model the fraction of charges effective in the multiplication is determined by the gap height $\lambda=\lambda_e+\lambda_{ph}$ where λ_e is the mean free path for charges to radiate a photon of the appropriate energy and λ_{ph} the mean free path for this photon to produce a pair in the gap magnetic field. We now define the time step as $G/2c$, which is the mean time taken by particles presently in the gap to leave it and be replaced by the next generation. If the density of charges is assumed uniform in the gap it will be seen that the fraction that will contribute to the next generation is $\eta \approx (I - \lambda/G)$; if $\lambda > G$, avalanche growth cannot occur. Now the charged particles radiate all along their path (except for the first λ_e cm) on the curved magnetic field lines even as they are accelerated by the gap electric field. An excess electric field in the gap would give the charges a little more energy at each point on their path provided that their energy is not limited by radiation reaction. This would result in an increased gamma of the charges accelerated over hills, where $\gamma = E/mc^2$. For 0·1 per cent average excess field,

$$\frac{\Delta\gamma}{\gamma} \approx 1/1000.$$

But curvature photon energy (E_{ph}) is proportional to γ^3. Therefore

$$\frac{\Delta E_{ph}}{E_{ph}} \approx \frac{3\Delta\gamma}{\gamma} \approx \frac{3}{1000}.$$

This would reduce λ_{ph}which is given by $\lambda_{ph} \propto e^{4/3\chi}$, where χ is proportional to the energy of the photon, and is typically $\approx$ 1/15(Ruderman and Sutherland 1975). We thus have

$$\frac{\Delta\chi}{\chi} \approx \frac{3}{1000},$$

$$\text{or } -\frac{\Delta\lambda_{ph}}{\lambda_{ph}} \approx 0{\cdot}06.$$

If we assume

$$\lambda_e < \lambda_{ph}, \frac{\Delta\lambda}{\lambda} \approx \frac{\Delta\lambda_{ph}}{\lambda_{ph}}$$

and we can compare η in the two cases, which differ in the values of λ in the following form:

$$\epsilon = \Delta\eta/\eta = -\frac{\Delta\lambda}{G} \times \Theta \text{ where } \Theta = \frac{1}{\left(1 - \frac{\lambda}{G}\right)}.$$

If we assume $\lambda \approx 5 \times 10^3$ cm (Ruderman and Sutherland 1975) $\Theta \approx 2$ but could be much larger if λ were closer to G. Spark discharges over a hill therefore would contain $\left(1 + \frac{2\,\Delta\lambda}{G}\right)$ times more charges at the end of each 'step'. As the time for one spark discharge $\approx 10^{-5}$ s the number of 'steps' in which the avalanche growth is completed is $\frac{10^{-5} \times 2c}{G} \approx 60$. In 60 steps the fractional increase in the total number of charges in the gap is

$$\left(1 + 2\frac{\Delta\lambda_{ph}}{G}\right) = (1 + 0.06)^{60} \approx 30.$$

As the radio emission is produced by positrons subsequent to their entering the magnetosphere the average radio intensity could well be expected to depend on the number of particles. Further because of the coherent nature of the radio radiation it is not unreasonable to expect it to be proportional to some power (larger than 1) of the number of particles that are produced in each spark. At the present state of understanding it is difficult, if not hopeless, to take into account all these considerations and to calculate the expected increase in average pulse intensity produced by sparks over hills. Our aim has been merely to show that such an increase is likely, critically dependent on the electric field in the gap, and easily capable of accounting for the observations which show a variation in intensities across the pulse window by factors of the order of $\approx 10^3$. It should be noted however that unless hills of height at least 5 cm (half the assumed value) can be supported on pulsar polar caps, the mechanism described above cannot satisfactorily account for the observations.

4. Deformation of the polar cap by sparks

In this section we will discuss the possible effect of sparks on the polar cap. In the vacuum gap both electrons and positrons are produced and are accelerated towards opposite ends of the gap. Since both types of charges are accelerated by the same electric field they gain similar energies. Therefore the electrons striking the polar cap surface must carry the same energy as the positrons which produce the observed radiation from the pulsar. As the typical total luminosity of a pulsar is $\geqslant 10^{30}$ erg s^{-1} we can expect the electrons in the spark to dump this order of energy onto the polar cap of the pulsar. Any damage done to the surface by these electrons will depend upon the structure and composition of the surface material and the details of the energy dissipation process.

We could begin by asking what are the various things that could happen to the surface as a result of a spark at a certain point on it. One possibility is what has been generally believed so far, *i.e.*, there will be local heating, consequently some excess radiation of photons and no change in the topography. At the other extreme it is conceivable that a pit is formed at the position of a spark and pieces of the crust are thrown up and scattered around the pit. A more likely possibility, however, is a very slight deformation of the crustal surface with the matter remaining bound at all stages; the energy required to create slips is very much less than the energy required to break the bonds between iron atoms.

If the energy available in each spark can effect some rearrangement of matter due to flow of material after sparking, we suggest that the result of a spark on the polar cap will be to *raise* the surface at that point by a minute amount. Although such a hypothesis might seem unlikely by analogy with the effect of meteorites and other energetic solid matter impinging on the surface of planets, we propose that it can happen in the case of pulsars. The very strong electric field at the surface of the polar cap is operative in the sense of trying to tear out ions from it against the force of gravity. The very basis of the RS model is the inability of this electric field to do so simply because of the high binding energy in the presence of strong magnetic fields. The positively charged outer crust at the magnetic polar cap may be likened to a pressurised balloon with a thin solid surface. A dimunition of the binding energy must therefore work in the sense of aiding a movement away from the centre of curvature of the crust. The duration of a spark can therefore be thought of as a short interval of time during which the cohesive energy of the lattice has been decreased, thus making it possible for the electric field to have its way and raise a tiny bump at the position of maximum heating.

The most favourable manner of raising bumps would involve stripping of atomic electrons by the intense beam of spark electrons. This would *momentarily* leave the crust under the spark with a much higher positive charge. A variation of particle density across the spark would effect a similar variation in the extra surface charge density of the softened crustal material leading to a differential upward force. If, the spark were densest in the middle, as one would expect, then a small bump on the polar cap should be left behind by a spark. We saw in the previous section that surface variations on the polar cap of the order of 10 cm could lead to the intensity variations observed across integrated pulse profiles. If an individual spark can be effective in creating a minor deformation in the polar cap, then with time the amplitude of this deformation would increase even if sparking were completely random. An upper limit for Δh, the deformation required per spark, can be obtained from the observed correlation of complex pulse profiles with pulse periods in excess of 0·75 s. The typical age of a pulsar with a period of 0·75 seconds is $\geqslant 10^6$ years and this may be taken as the time for the surface relief of the polar cap to have build up to a root mean square value of ~10 cm. Since there occurs one spark per millisecond on the average over any point on the polar cap, we have 3×10^{16} sparks corresponding to 10^6 years. On a purely random basis the peaks in the surface relief would have a height $\geqslant \sqrt{3\times10^6}\times\Delta h \approx 10$ cm. This leads to a value of $\Delta h \approx 10^{-7}$ cm or the incredibly small value of 10 Å.

In other words, if a single spark managed to increase the height at its centre of impact by 10 Å, then over a period of the order of a million years the surface of the polar cap must end up with variations in height of the order of 10 cm and lead to the consequences discussed in the previous section. The amount of matter under a spark area that must be rearranged to obtain a bump of height 10 Å is $\sim 10^{26}$ atoms. The question is whether enough energy can be imparted to the surface layer in a way that will make it temporarily mobile and allow the electric tension to rearrange it.

Notions regarding the stability of the crustal material have been changing since the early work of Chen, Ruderman and Sutherland (1974) who derived a value for the cohesive energy for each iron atom of ~ 10 keV. This number was revised by Flowers *et al*. (1977) according to whom the cohesive energy of iron per atom in a field of $\sim 10^{12}$ gauss is ~2 keV. If a spark can impart at least this amount of energy to each of more than say 10^{26} atoms directly under the spark, there is then the possibility of rearrangement under the effect of the electric tension. The amount of energy carried by the electrons to the surface is 10^{30} erg s^{-1}. At the rate of 10^5 sparks per second, there is thus in each spark about 10^{25} erg. The area of the spark is $\pi \times 10^6$ cm^2. Assuming the generally accepted upper limit of 10^5 g cm^{-3} for the density at the surface, there is enough energy in the spark to give ~ 2 keV per atom down to a depth of 1 cm. It is seen therefore, that if the energy is deposited in a much shorter distance, the atoms are bound to acquire much more than their cohesive energy immediately after each spark thus permitting a slight deformation within the radiation cooling time of the surface.

The heating of the surface under a spark has been discussed recently by Cheng and Ruderman (1980). According to them ‘ if a pair production discharge occurs above the polar cap an intensive flux of 10^{12} eV electrons is directed onto the surface causing strong local heating. This energy is deposited within $d \gtrsim 10$ radiation lengths (of the order of 10^{-3} cm in 10^5 g cm^{-3} of Fe) of the surface. It is largely reradiated locally from the area under the discharge.’ The temperature quoted by these authors for the surface is a quarter keV $\approx 2{\cdot}5 \times 10^6$K. This implies a total radiation loss of ~10^{30} erg s^{-1} over the whole of the polar cap commensurate with our assumptions in the preceding paragraph.

If the energy in sparks is indeed *deposited* within 10^{-3} cm as suggested by Cheng and Ruderman (1980), then it appears to us that even allowing for the energy taken up by electrons and that radiated as photons, and errors in the various estimates, we must still have a much larger number of mobile atoms than we need. Under these circumstances an eventual modification of the polar cap relief seems inevitable.

It may be mentioned that *increase in height* of an area due to a spark on it represents a positive feed-back mechanism, since subsequent sparks over this area will carry more energy than sparks over neighbouring depressions. Although the extra energy may appear tiny, the effect is significant over the timescales required to build up a hill by a purely random process. As a result the minimum step required per spark will actually be less than the Δh = 10Å which we estimated conservatively earlier. It may also be pointed out that for a similar reason it would be harder to build up surface relief if sparks created pits instead of bumps, in which case the feed-back would be negative.

We have seen how polar cap surface modification by sparks can lead to structure in the integrated pulse profile over the timescale in which pulsars acquire such profiles. By the same token it may be noted that the profiles will remain stable over such periods. From the number of spark areas within the polar cap we can arrive at the minimum scale length for surface irregularities as of the order of 10 metres. The maximum number of hills that one can expect to find along the diameter of a typical polar cap would therefore be ~ 10, and along a chord somewhat fewer. This is in good agreement with observations which show that the maximum number of major components in an integrated pulse profile is about 5. PSR 2045—16 has three major components and PSR 1237–25 has two major and three minor components. In the next section we shall discuss how similar structure in integrated profiles can result from minor magnetic field variations over the polar cap.

5. Magnetic field variations

In an earlier section we showed how the number of charges produced in a spark discharge depended critically on λ, the total path length within the gap for a charge to be accelerated, produce a photon, and for the photon to produce a pair. In that case, the variation in λ resulted mainly from the variation in λ_{ph}, the path length for a photon to produce a pair. It was also seen earlier that λ_{ph} depends critically on the energy of the photon, since $\lambda_{ph} \propto e^{4/3\chi}$, and χ is proportional to the photon energy In this expression, χ is also proportional to the strength of the perpendicular component of the magnetic field. The angles made by the field lines within the gap with the trajectory of the gamma ray photons are very small, and the perpendicular component is therefore directly proportional to this small angle. Even a small change in this angle will therefore have a large effect on λ_{ph} with a consequent change in the total number of particles produced as discussed earlier. For example, an increase of 3 parts per thousand in the small angle made by the field lines with the photon trajectory will result in the same increase of a factor ≈ 30 in the total number of charges, as calculated earlier for a similar increase in the photon energy.

Given a pure dipole magnetic field the curvature of the field lines will vary smoothly across the polar cap and will lead to pulse profiles that do not have a complicated or random structure. However, if pulsar fields evolve with time as discussed by Flowers and Ruderman (1977) multipole components will make their appearance in due course. Such multipole components even if present to a very small degree will significantly modify the curvature of the field lines in the polar cap. For the reasons discussed above this will then be strongly reflected in the intensity of the sparks produced at different longitudes *i.e.* structure in the integrated pulse profile.

To predict the effect of multipole components on the pulse structure is difficult because of the number of parameters involved in the addition of even a quadrupole component. Simple trial models seem to suggest that the major effect of the introduction of a quadrupole component in the gap field would be asymmetry in the pulse profile. The general result is to increase the curvature of the field linens on one side and to decrease it on the other. It seems much harder to create variations in the curvature of the field lines across the gap that could lead to a complex profile with many components as seen in several pulsars.

We note that if multipole fields in older pulsars are as inevitable and as strong as suggested by Flowers and Ruderman (1977), they must have a dominating influence on the pulse profile according to the conclusions drawn above. However, for the reasons just discussed the net result might be merely to make one part or region of the polar cap very much more effective than the rest. In such a case the observed profile would be interpreted as having a smaller duty cycle and might not be recognised as one modified by a complicated field structure in the gap. In any case we note that it multipole components can be shown to be responsible for variations in pulse structure, then this provides an observational method for determining the timescale for the evolution of the magnetic fields from the age of the pulsars which show such effects

6. Discussion and conclusions

We have outlined two possible ways in which the complex variation of the mean intensity within pulse profiles could be explained. In one case, minute local deformations of the surface due to individual sparks lead to a build-up of a surface relief pattern on the polar cap; this in turn causes small variations in the electric field intensity within the gap leading to much larger variations of the number of positrons produced by the sparks. The second possibility invokes the presenee of multipole components which modify the curvature of the magnetic field lines from point to point within the gap leading to the same conclusions as above.

Either mechanism provides general agreement with the observations in that the complicated pulse structure is correlated with older pulsars, and is stable for long periods. Also, the polarisation variation would be independent of the intensity structure within the pulse. In one case, the magnetic field structure would be unaffected by surface variations over the polar cap. For the other, multipole fields would need to modify the dipole pattern only marginally to account for the pulse intensity structure. Further, since they fall off much faster than the dipole field, their contribution in the radiating region at some distance from the pole will be greatly reduced. Hence for both mechanisms the sweep of the position angle of polarisation would be independent of the intensity variations across the pulse, as has been noted and emphasised by Manchester (1979).

To make an assessment from the observations of the importance of either of the two proposed mechanisms, one must take into account the pulse shapes obtainable in the absence of these or other such mechanisms. In magnetic pole models involving radiation into a hollow cone, both single and double pulse structures are easily explained in terms of edge and central cuts of the hollow cone by the line of sight, Many of the symmetry properties observed in pulses can be well accounted for by the circular symmetry of such a hollow cone. As pulses with complicated structure are generally from older pulsars, the radiating region would be further from the light cylinder than in younger (and faster) pulsars, and hence the asymmetry expected from sweeping back of the field lines would also be less. It is the presence of marked asymmetries and/or multiple components that cannot be accounted for in this way, and which we are attempting to explain in this paper.

We have seen earlier that a quadrupole component of the magnetic field can introduce a strong asymmetry, but is unlikely to create a complex pulse profile with many features. On the other hand, surface variations in the polar cap can produce both a large number of components and also asymmetry, since no particular symmetry will result from an essentially random process. Complex profiles, found (for example) in PSR 1237+25, seem therefore to strongly favour the polar cap relief hypothesis, whether or not the other mechanism also contributes. As mentioned earlier this is based on the assumption, which is hard to either prove or disprove at the moment, that the surface irregularities of the order of 10 cm can be supported on the polar cap. Further understanding of the structure and strength of neutron star crusts might show such an assumption to be untenable. If so, this would indicate that the alternative mechanism we have discussed is the operative one, and that the magnetic field structure of older pulsars can have at least some contributions of higher order than a quadrupole moment.

Acknowledgements

We thank Rajaram Nityananda and Ramesh Narayan for numerous discussions and help rendered during the course of this investigation. We are also grateful to D. Morris for a critical reading of the manuscript and to P.A.G. Scheuer for an elegant derivation relating to the maximum possible heights of hills.

References

Chen, H. H., Ruderman, M. A., Sutherland, P. G. 1974, *Astrophys. J.*, **191,** 473.

Cheng, A. F., Ruderman, M. A. 1977, *Astrophys. J.*, **214,** 598.

Cheng, A, F., Ruderman, M. A. 1980, *Astrophys. J.*, **235,** 576.

Cordes J. M 1976, *Astrophys. J.*, **208,** 944.

Ferguson, D. C, Graham, D. A., Jones, B, B., Seiradakis, J. H., Weilebinski, R. 1976, *Nature*, **260**,25.

Flowers, E.G., Lee, J. F., Ruderman, M. A., Sutherland, P. G., Hillebrandt, W., Muller, E. 1977, *Astrophys. J.*, **215,** 291.

Flowers, E. G., Ruderman, M. A. 1977, *Astrophys. J.*, **215,** 302.

Hankins, T. H. 1971, *Astrophys. J.*, **169,** 487.

Irvine, J. M. 1978, *Neutron Stars*, Clarendon Press, Oxford.

Manchester, R. N. 1979, *New Zealand J. Sci.*, **22,** 479.

Ruderman, M. A., Sutherland, P. G. 1975, *Astrophys. J.*, **196,** 51.

Taylor, J. H., Huguenin, G. R. 1971, *Astrophys. J.*, **167,** 273.

J. Astrophys. Astr. (1980) **1,** 129–154

Central Regions of Sérsic-Pastoriza Galaxies: A Photographic Study

T. P. Prabhu *Indian Institute of Astrophysics, Bangalore 560034*

Received 1980 August 6; accepted 1980 October 24

Abstract. A classification scheme is proposed for the central regions of Sérsic-Pastoriza galaxies based on high resolution photographs of 50 objects in the integrated light (4000 Å–8700 Å). Structures of two different linear scales are recognized: (1) nucleus($\lesssim$1 kpc) and (2) perinuclear formation (~1·5 kpc). The perinuclear formation is weak in class κ while the nucleus is too faint to detect in class ι. In the intermediate classes ϵ and σ both the components are bright. Class ϵ has an elliptical perinuclear formation with little gas while the class σ consists of bright H II complexes and dust. Observations of a few galaxies in the infrared and the blue ends of the image tube response show that the nucleus is generally redder than its surroundings. Equal intensity contours and the luminosity profiles are presented for the central regions of 27 galaxies. A comparison of their axial ratios with those of the parent galaxies indicates that the perinuclear formations are prolate or barlike. The dependence of the peak surface brightness of the central formation on the size of the bar is investigated as also the dependence of the central surface brightness of the bar on the size of the bar. The following major conclusions are drawn:

(1) The peak central surface brightness of the perinuclear formation varies as the square of the bar length. This relation implies that the bar induces the infall of gas from the bar-disk region.

(2) The formations of class σ move towards class ϵ as star formation ceases and the massive stars die.

(3) The class ι differs from class σ in the intensity of the burst of star formation. Low luminosity of the parent galaxies in class ι implies less infall of gas and higher domination of the bar potential on the perinuclear formation. Thus the class ι structures are more prolate than those of class σ.

(4) The central brightness of the bars varies directly as the length of the bar.

Key words: galaxies—central regions—bursts of star formation—surface photometry

1. Introduction

Morgan (1958) noticed that the central regions of some spiral galaxies consist of clusters of bright spots which he termed ‘nuclear hot spots’. Early spectroscopic work showed that the hot spots are mere complexes of H II regions (Burbidge and Burbidge 1960, 1968). A wealth of spectroscopic information has been accumulated in recent years (Osmer, Smith and Weedman 1974; Oka *et al.* 1974; Pastoriza 1975; Turnrose 1976; Alloin and Kunth 1979; Wakamatsu and Nishida 1980). One concludes from these data that the central regions of some spiral galaxies have recently received a fresh supply of gas and a burst of star formation has been triggered.

Sérsic and Pastoriza (1965) and Sérsic (1973) have systematized and enlarged upon Morgan’s list. Their criterion of ‘peculiar nucleus’ is ‘ a change in the slope of luminosity profile and evidence of some structure ’ (Sérsic 1973). This definition is broader than Morgan’s and hence includes in addition to the conventional hot-spot systems, the ‘amorphous nuclei’ or ‘ spherical formations surrounded by diffuse asymmetric structure ’. Though not complete to any given magnitude limit, nor to any part of the sky, Sérsic’s finding list has the advantage of selection of central regions of spiral galaxies based on a unique criterion. It is hence unfortunate that despite the coinage of the term ‘ Sérsic-Pastoriza (S-P) galaxies’ (Osmer, Smith and Weedman 1974) the central regions generally studied are only the hot-spot subclass of Sérsic’s list. A closer examination of a larger number of S-P galaxies and an enlargement of Sérsic’s finding list is urged by the following information on the central regions of spiral galaxies:

(1) Sérsic’s criterion of ‘ a change in the luminosity profile ’ compares well with the ‘ nucleus-shoulder-arms ’ structure of Seyfert galaxies (Morgan, Walborn and Tapscott 1971).

(2) Intense emission lines are quite common in the hot-spot galaxies and differ from the spectra of Seyfert galaxies mainly in their breadth. Véron *et al.* (1979, 1980) and Véron, Véron and Zuiderwijk (1980) have seen faint broad components in the emission line profiles of several ‘ emission line galaxies ’ and suspect that a Seyfert nucleus may at times be hidden within a giant H II region.

(3) Large infrared (10 μm) excess is observed in the central regions of several hot-spot galaxies: NGC 2903, 3627, 4258, 4303, 5236 (Rieke and Lebofsky 1978); 3504, 4051 (Rieke and Low 1972); 4064 (Kleinmann and Low 1970); and 7552 (Kleinmann and Wright 1974). The near infrared observations of NGC 1365 and 1808 by Glass (1976) also show excess over the stellar radiation. The excess is interpreted to be due to the reemission by dust heated by the radiation from H II complexes (Telesco and Harper 1980). The amount of the excess is midway between the excess in Seyfert nuclei and in the Galactic nucleus. Some S-P galaxies exhibit an activity of such an intermediate degree in X-rays: NGC 1097 (Ku *et al.* 1979), 1365 (Ward *et al.* 1978) and 1672 (Griffiths, Feigelson and van Speybroeck 1979) are examples of this category. Weak compact central radio sources similar to the ones contained in Seyfert galaxies are found by van der Kruit (1973) in several S-P galaxies (NGC 1300, 2903, 3310, 4258, 4321 and 5383). Two S-P galaxies, NGC 4051 and 4151 are also Seyferts and exhibit the above characteristics.

Our aim to investigate a sample of 50 S-P galaxies (Section 2) has been

(a) to recognize and establish a class of events in the central regions of S-P galaxies,

(b) to arrive at a morphological classification scheme which may provide clues to the strength of and the evolutionary stage of the event (Section 3) and

(c) to investigate the photometric parameters of the central substructure and to search for the clues to the mechanism of the infall of gas.

The observational data are presented in the form of equal intensity contours and equivalent luminosity profiles in Section 4. The distribution of colours using a wide base line (blue and image tube infrared) has been presented for six of the programme galaxies in Section 5. The geometrical and the photometric parameters of the sample are discussed in Section 6 followed by a summary of the results.

2. Observations

We have photographed the central regions of 50 S-P galaxies at the f/13 Cassegrain focus of the 102-cm reflector telescope at the Kavalur Observatory. A Varo 8605 image tube with an S-20 photocathode was employed in a cathode-grounded configuration. The image tube has a P-20 phosphor and input and output face plates of fiber optics. The image scale in the central region of the image tube is 15·5 arcsec mm^{-1}. Kodak IIa-D plates were used in contact with the output face plate. The resolution of the image tube and also of the photographic emulsion is 60 1p mm^{-1} which corresponds to 0·24 arcsec at the image scale mentioned above. Thus the final resolution is limited only by the astronomical seeing which was close to one arcsec on an average. The large image scale results in several instrumental resolution elements per seeing disc (~ 17 on an average) and hence considerably improves the signal-to-noise ratio.

The response of the image tube extends from 4000Å (fiber optics cut-on) to 8700Å A blue region (4000Å–4600Å) was isolated employing 2 mm of Schott BG12 filter while a Wratten 89B filter enabled the isolation of an infrared region (7000Å-8700Å). Six of the programme galaxies were observed in both these bands. The star-like nucleus and the stellar population of the substructure surrounding the nucleus are visible better in the infrared than in the blue. The hot spots are on the other hand seen more distinctly in the blue. All the 50 programme galaxies were photographed in the integrated light of 4000Å–8700Å; they represent the nucleus, the stellar population and also the hot spots.

The exposure times ranged from 1 to 10 minutes in integrated light, 5 to 20 minutes in the blue band and 3 to 15 minutes in the infrared. Several graded exposures were obtained (3 in the majority of cases). The thermal background of the image tube was negligible in all the observations. The sky background was also very low except on the longest exposures. The radial and azimuthal variations in the sensitivity of the image tube, as also the pin cushion distortion have not introduced significant variation over the small sizes of interest ($\lesssim 4$ mm). The images were geometrically centred well near the maximum of tube sensitivity. Different exposures were obtained by shifting the position of the image slightly. Whenever the chicken-mesh due to fiber optics was superposed on the images, plates were discarded. The instances were rare since the contrast of the chicken-mesh was generally very low.

Calibration to relative intensities was achieved by photographing the spectrum of a tungsten lamp through a rotating sector on a separate piece of the same photographic plate as was used for the exposure of the galaxy. The image tube was not employed in this exposure and its response to intensity was assumed to be linear.

3. Classification

The seeing-limited photographs obtained by us reveal two distinct components in the central regions of S-P galaxies:

(a) Nucleus: A bright unresolved or barely resolved formation of $\lesssim 4$ arcsec extent. It is generally redder than the surrounding region.

(b) Perinuclear formation: A substructure of 10–30 arcsec radius around the nucleus.

The relative brightness of these two subsystems varies from one galaxy to another. We propose here a classification scheme for S-P galaxies in which we distinguish between different types according to the relative brightness of the nuclear and the perinuclear region. The central regions with bright nucleus and a very faint perinuclear region are classified as type κ, while those with a very faint nucleus and a bright perinuclear region are classified as type ι. The central regions that show both the components are assigned intermediate classes according to the morphological appearance of the perinuclear formation. A high degree of concentration is assumed to be an indication of the presence of the nucleus even when the latter is not clearly discernible. The classification criteria are listed in Table 1. The central formations of typical members of the major classes (κ, ϵ, σ, ι) are shown in Fig. 1. The class $\epsilon\sigma$ is of intermediate nature between the classes ϵ and σ and $\sigma\iota$ between σ and ι. This classification of 50 S-P galaxies is presented in Table 3 in Section 6.

The above classification scheme was induced by the great degree of regularity noticed in the structure of the perinuclear formations. The hot-spots are generally contained within a region that appears elliptical or oval in class σ and generally follow the pattern of a pseudo-ring formed by two tight spiral arms. The sense of opening can often be traced to be similar to that of the main spiral arms of the galaxy. The hot spots in class ι are aligned in a straight line, and are contained within a barlike region. The perinuclear formations of class ϵ are elliptical or oval structures with smooth distribution of intensity. Morphologically there is a great resemblance

Table 1. Morphological classification scheme for the central regions of Sérsic-Pastoriza galaxies.

Class	Nucleus	Perinuclear formation
κ	very bright	very faint or absent
ϵ		bright bright with elliptical boundary and smooth intensity distribution
$\epsilon\sigma$	bright	bright smooth intensity distribution without a well-defined boundary
σ	bright	bright, distinct or fairly distinct hot spots; a spiral pattern is often evident in dark lanes, hot spots, or in underlying red population
$\sigma\iota$	faint	barlike, generally resolved into hot spots
ι	very faint or absent	barlike formation of faint hot spots

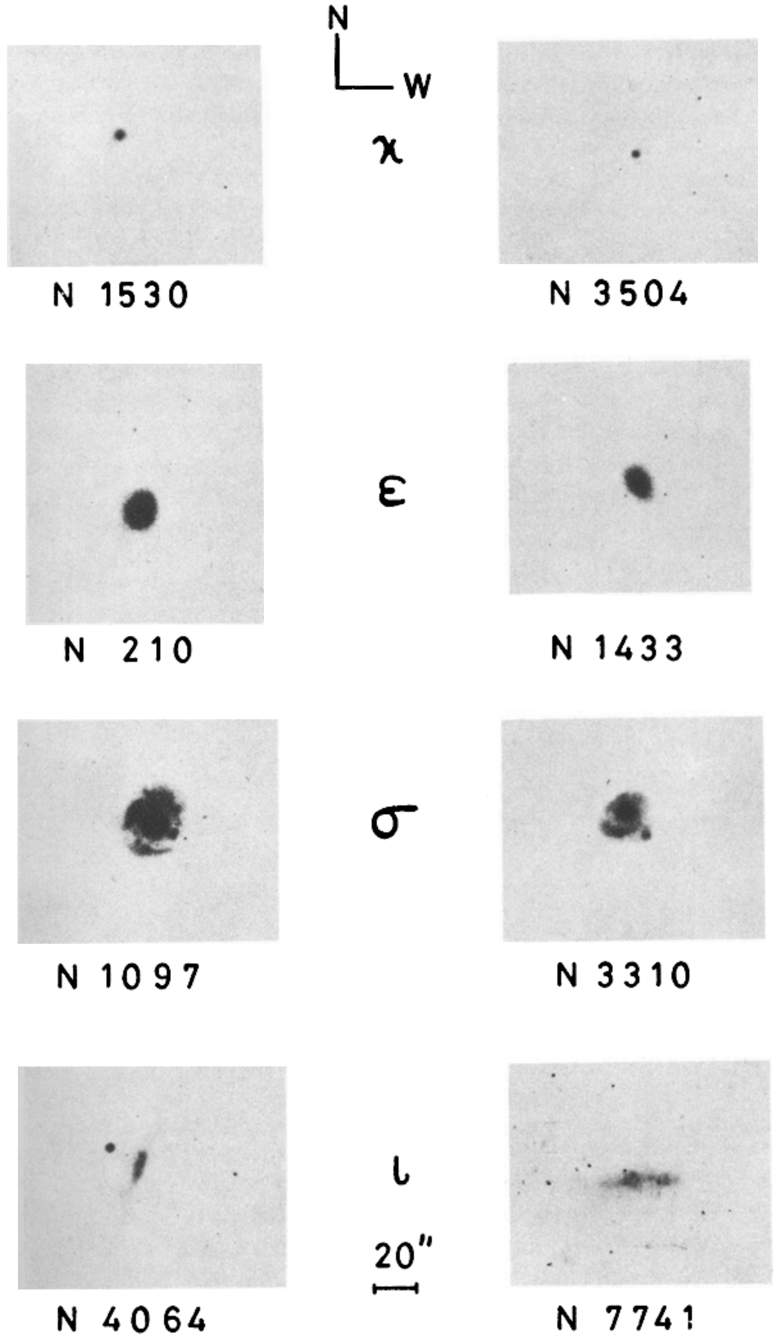

Figure 1. Contrast prints of the central regions of typical members of the major classes of S-P galaxies. The orientation and the scale are the same for all the galaxies.

PRABHU

between our classification scheme for perinuclear regions and the Hubble scheme for galaxies. We have hence drawn the nomenclature from this similarity: ϵ for elliptical, σ for spiral, ι for irregular. Our class κ resembles Zwicky's red compact galaxies.

Sérsic (1973) classified the central regions into two types: (1) HS: Structures with distinct hot spots, and (2) AN: 'amorphous nuclei or spherical formations surrounded by diffuse asymmetric structure'. He also included the dumb-bell like formation (dB) of NGC 1087 and NGC 1140 as a variant of AN. We classify these two objects as $\sigma\iota$ since they appear to contain two faint hot spots. This classification is however not very certain. Among the 50 galaxies classified by us, Sérsic (1973) has classified 41 as AN or HS and two as dB. The galaxies NGC 1415 and NGC 1433 are both classified as AN by Sérsic and Pastoriza (1965). We show in Fig. 2 the fraction of galaxies of Sérsic types AN or HS in each of our class. The dB galaxies are excluded. A high degree of correlation is seen in the sense that the AN contains mostly the earlier classes (ϵ) while the HS contains the later ones (σ, ι). Thus our classification scheme is only an enlargement of Sérsic's scheme.

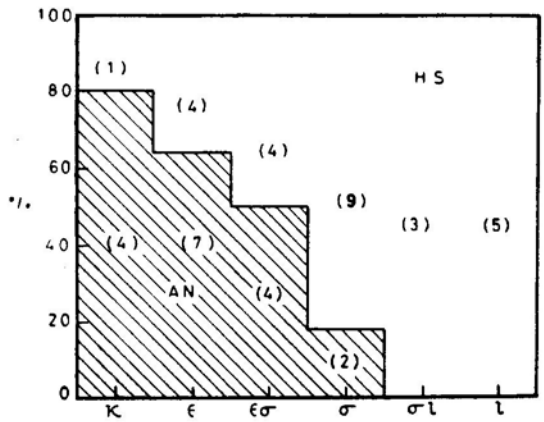

Figure 2. Distribution of Sérsic's classes AN and HS against the classification scheme presented in this paper.

The mean Yerkes type is *g* for class ϵ, *fg* for class σ and *af* for class ι (Prabhu 1979). Thus the central concentration decreases along our classification scheme.

A comparison of outer morphology with the inner structure reveals that the occurrence of barred or intermediate nature (*B*, *AB*) is higher in ϵ,$\epsilon\sigma$ and σ (90 per cent) as compared to $\sigma\iota$ and ι (63 per cent). The latter figure is comparable to the fraction of *A* and *AB* types (59 per cent) in the entire sample of spiral galaxies with $V_r \lesssim 5000$ km s^{-1} from de Vaucouleurs, de Vaucouleurs and Corwin (1976). The frequency of outer rings stays constant between the different classes (average: 20 per cent) but is higher than the corresponding figure for the entire sample (8 per cent). The distribution of the ' varieties ' *r*, *rs*, and *s* is not different from the larger sample, and does not show any variation between different classes. There is a systematic trend however in the mean Hubble type or the DDO luminosity class of each of our class (Prabhu 1979). As one moves from ϵ to ι the mean Hubble type changes from *Sab* to *Sc*; the luminosity class varies from I-II to III (We leave out class κ because of

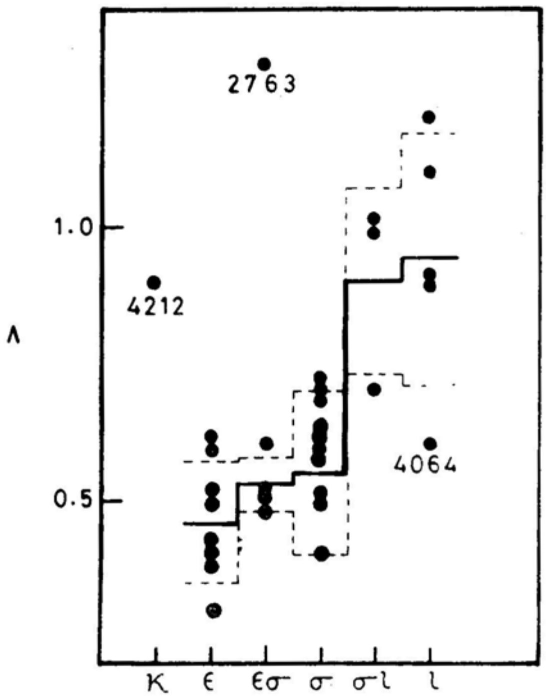

Figure 3. The distribution of the luminosity index of the parent galaxies as a function of the class of the central substructure. The solid line represents the mean luminosity index for each class and the dashed line one standard deviation limits on either side. NGC 2763 is excluded while obtaining the mean for class $\epsilon\sigma$. Galaxies which lie too far away from the mean are labelled.

the lack of statistics on luminosity class). This is as expected since the Hubble type and the DDO luminosity class are correlated. We show in Fig. 3 the distribution of de Vaucouleurs (1977) luminosity index $\Lambda = \frac{1}{10}(T+L)$ where T and L are Hubble type and DDO luminosity class respectively. It is evident from the figure that the classes σ and ι appear more often in low luminosity galaxies (higher Λ) while the classes ϵ, $\epsilon\sigma$ and σ prefer high luminosity ones.

It is significant that the formations of class ϵ generally present only absorption lines in their spectra (except for the emission of [O II] 3727Å). Among the central regions, of 21 S-P galaxies observed spectroscopically by Prabhu (1978, 1979) all the class ϵ formations (NGC 210, 2196, 2935, 3627, 5850) failed to show H_α in emission. Among the remainder all but one (NGC 2763, Class $\epsilon\sigma$) showed the emission line of H_α Other observations of class galaxies also do not show Balmer emission (NGC 4124: Sandage 1978; NGC 1433: de Vaucouleurs and de Vaucouleurs 1961). The only known exception is the class ϵ galaxy NGC 6951 (Burbidge 1962) which shows H_α though not the lines of [O III]. Published information exists on the presence of emission lines in many more non-ϵ class formations. The lack of emission lines in class ϵ makes their central regions appear redder than other systems both in U—B and B—V colours (Prabhu 1979). Corroborating the fact that no dust lanes are prominent in class ϵ formations we conclude that the gas and dust content and the number of hot stars are low in class ϵ systems.

4. Isophotometry

We present in this section the surface intensity distribution in integrated light (4000Å–8700Å) of the central regions of 27 S-P galaxies. These include six formations of type ϵ (NGC 210, 1300, 1433, 2196, 2935 and 3627), three of type $\epsilon\sigma$ (NGC 1326, 1415, 1672), ten of type σ (NGC 613, 1097, 1365, 1808, 2903, 2997, 3177, 3310, 3351, 5236), four of type $\sigma\iota$ (NGC 255,922,1087, 1140), three of type ι (NGC 3955, 4064, 7741) and one of type κ (NGC 1530).

Agfacontour Professional film was employed for obtaining the equidensity contours. The method has been explained by Geyer (1978). We have employed a yellow filter to narrow down the density width of a contour to 0·15 D in the first order and to 0·02 D in the second order. Third order contours were used only in isolated instances and were otherwise avoided because they add to the photometric noise. Fig. 4 shows the characteristic curve of the film as determined by us. The superposition of different pairs of contours was achieved by centering the contours of field stars.

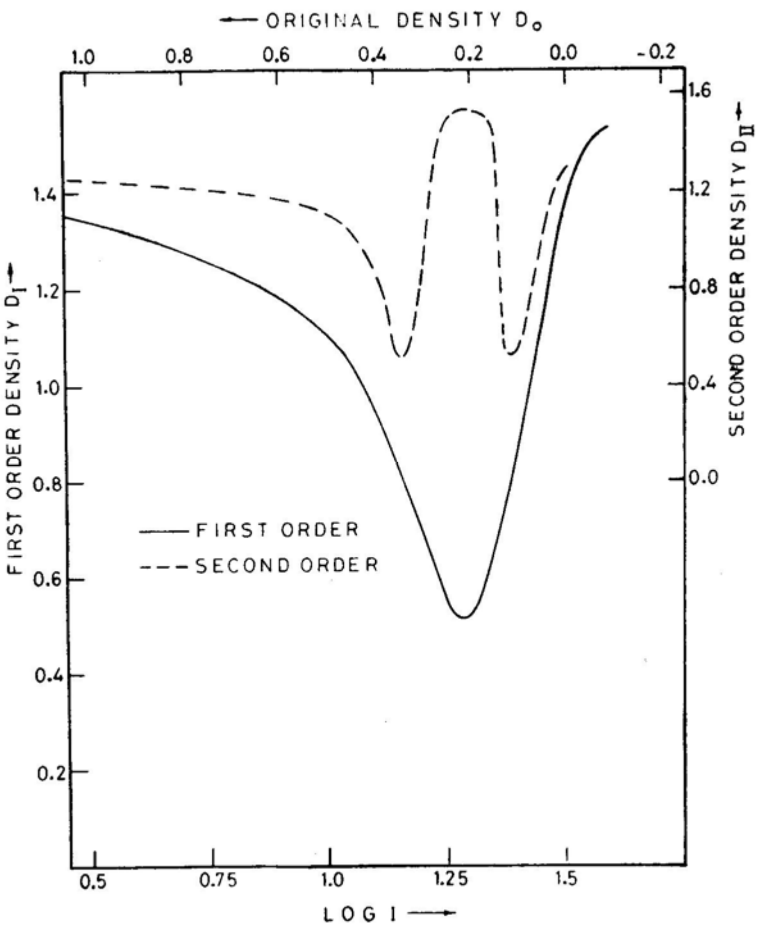

Figure 4. The first and the second order characteristic curves for the Agfacontour film obtained under conditions similar to the ones used in obtaining the equidensity contours.

The reductions to the relative intensity were achieved by reducing a microphotometer scan across the image of the galaxy, using a charactersitic curve obtained from the calibration plate. The orientation of the scan path was determined with the help of the field stars to an accuracy of 0°·1. It passed through the nucleus with an estimated accuracy of 10 μm (0·16 arcsec). The scanning aperture was

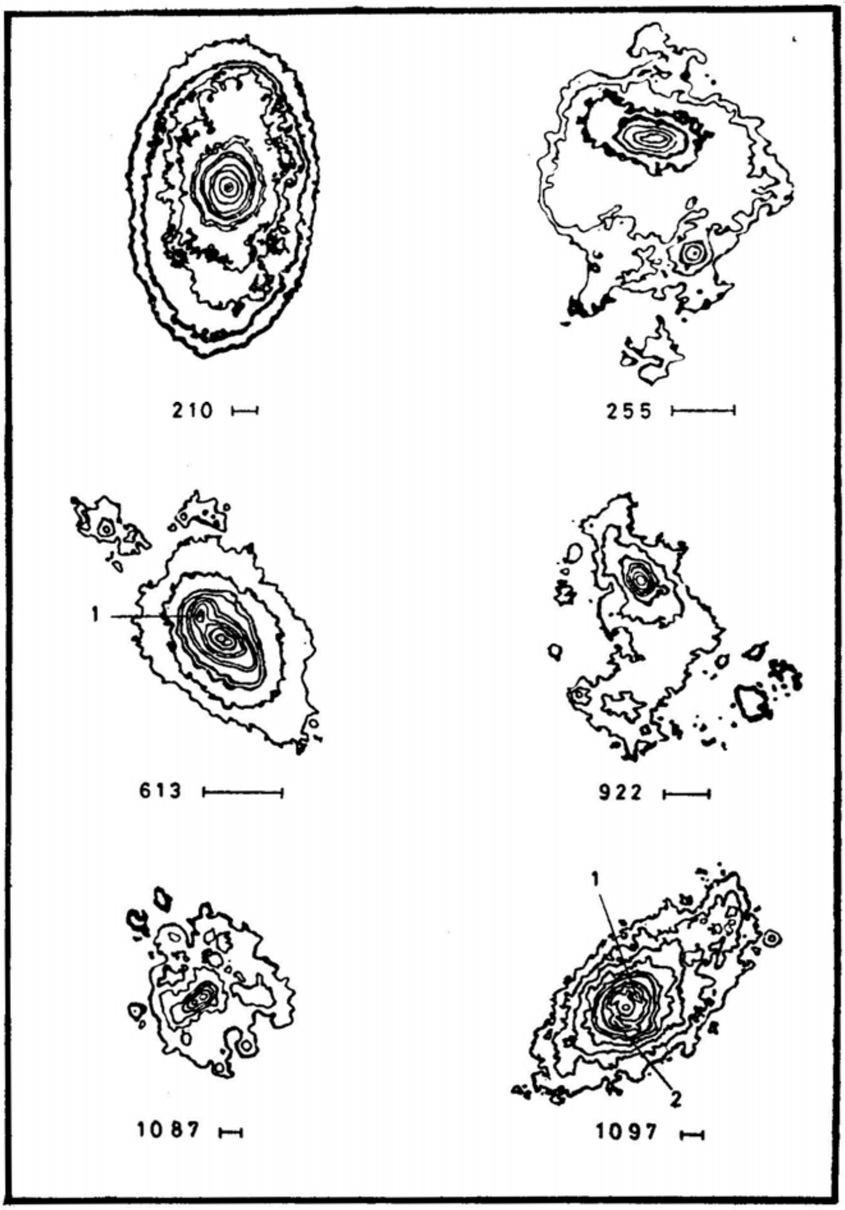

Figure 5a. The equidensity contours of S-P galaxies NGC 210, 255, 613, 922, 1087 and 1097. The lengths of the bars correspond to 10 seconds of arc in the sky. North is at the top and west is to the right. The relative brightness levels of different contours numbered centre outwards are listed in Table 2. The outermost two contours of NGC 210 are obtained from a published print and are not calibrated for intensity. The numbers in NGC 613 and 1097 designate regions discussed in Section 5.

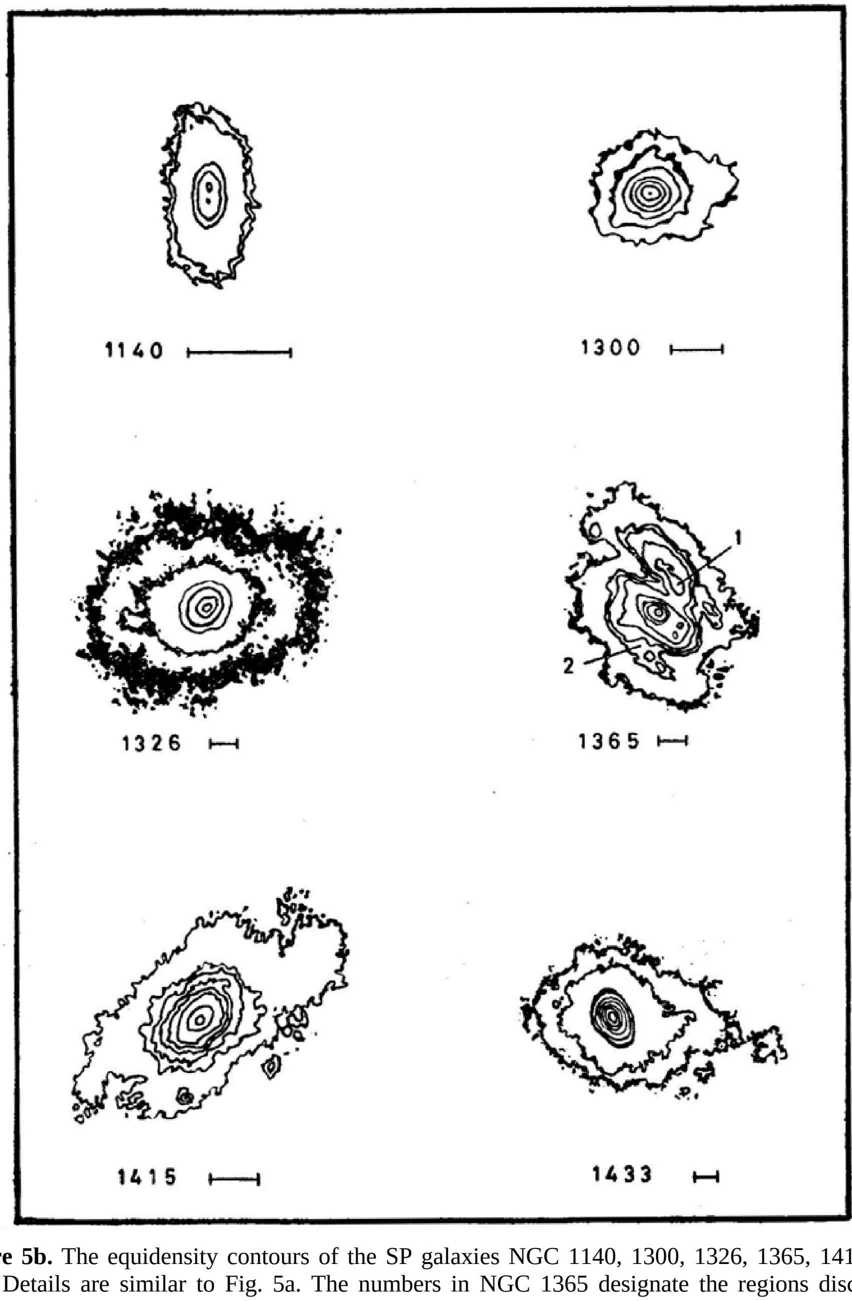

Figure 5b. The equidensity contours of the SP galaxies NGC 1140, 1300, 1326, 1365, 1415 and 1433 Details are similar to Fig. 5a. The numbers in NGC 1365 designate the regions discussed in Section 5.

33 μm×33 μm (0·5×0·5 arcsec^2). Two different exposures were used in general. The internal accuracy was determined to be 0·05 mag which is partly due to the uncertainties of centering the scan path on the nucleus.

The equal intensity contours so obtained have been reproduced in Fig. 5. The intensities relative to the peak intensity have been listed in Table 2 for all the galaxies. The isophotes are designated outwards from the innermost contour. Some of the

Table 2. Equivalent luminosity profiles of the central regions of S-P galaxies.

NGC 210

No.	r^* arcsec	log I
1	0·61	0·747
2	1·25	0·569
3	2·74	0·140
*	3·03	0·121
4	4·33	−0·208
*	4·87	−0·247
5	6·21	−0·367
*	6·65	−0·526
6	7·41	−0·593
7	8·62	−0·628
8	10·79	−0·682
9+	11·75	−0·685
10	20·36	−0·738
11	25·65	−0·757

NGC 255

No.	r^* arcsec	log I
1	1·17	0·976
2	2·01	0·880
3	2·95	0·692
4	4·22	0·538
5+	6·96	0·308
6	14·77	0·052
7	19·41	−0·009

NGC 613

No.	r^* arcsec	log I
1	0·33	0·985
2	0·73	0·895
3	1·41	0·833
4	2·13	0·807
5	2·71	0·698
6	3·89	0·559
7	5·16	0·547
8+	5·79	0·480
9	7·96	0·350
10	11·71	0·100

NGC 922

No.	r^* arcsec	log I
1	1·95	0·815
2	2·46	0·630
3	3·58	0·450
4	4·28	0·280
5+	5·96	0·210
6	11·90	0·135
7	24·11	0·075

NGC 1087

No.	r^* arcsec	log I
1	1·11	0·943
2	1·62	0·828
3+	1·95	0·785
4	2·77	0·642
5	3·88	0·550
6	5·61	0·422
*	8·63	0·405

NGC 1097

No.	r^* arcsec	log I
1	1·71	0·715
2	5·65	0·425
*	6·82	0·298
3	10·27	0·137
*	10·98	0·090
4	12·53	0·059
*	13·55	−0·003
5	17·07	−0·115
6+	18·87	−0·135
7	23·55	−0·205
8	29·54	−0·280
9	39·92	−0·300
10	51·94	−0·396

NGC 1140

No.	r^* arcsec	log I
1	0·34	0·959
2	1·97	0·725
3	2.69	0·544
4	6·43	0·135
5+	7·36	0·107

NGC 1300

No.	r^* arcsec	log I
1	0·00	1·000
2	2·83	0·701
3	4·36	0·597
4	5·61	0·482
5	8·44	0·373
6+	12·01	0·193
7	19·17	0·111

NGC 1326

No.	r^* arcsec	log I
1	1·23	0·893
2	3·10	0·724
*	4·50	0·555
3	5·68	0·380
4+	8·05	0·190
5	15·83	0·002
6	29·17	−0·148

NGC 1365

No.	r^* arcsec	log I
1	0·00	1·000
2	1.00	0·851
3	2·11	0·641
4	2·75	0·544
5	5·69	0·376
6+	8·46	0·214
*	9·12	0·193
7	11·38	0·124
8	13·24	0·083
9	19·97	0·017

NGC 1415

No.	r^* arcsec	log I
1	1·81	0·670
2	2·62	0·583
*	2·82	0·560
3	3·15	0·368
*	3·50	0·345
4	6·45	0·242
5	7·38	0·192
6+	9·22	0·152
7	11·46	0·142
8	21·76	0·042

NGC 1433

No.	r^* arcsec	log I
1	2·31	0·820
*	2·61	0·798
2	4·50	0·635
*	4·68	0·620
3	5·46	0·575
*	6·03	0·561
4	8·12	0·499
*	8·37	0·438
5	10·74	0·310
6+	13·07	0·213
7	30·48	0·119
8	43·80	0·069

The contours marked with an asterisk (*) are not shown in Figure 5. The + signs designate the contours at which the luminosity profile changes slope.

Table 2. continued

No.	r^* arcsec	log I
NGC 1530		
1	1·49	0·889
*	2·13	0·810
*	3·04	0·693
2+	4·03	0·643
3	7·36	0·583
*	8·26	0·563
*	10·15	0·513
4+	13·37	0·491
5	34·76	0·403
NGC 1672		
1	0·40	0·965
2	3·01	0·947
*	3·62	0·776
*	4·84	0·628
3	5·73	0·556
*	8·33	0·487
4+	8·84	0·297
5	19·38	0·132
6	36·78	0·122
NGC 1808		
1	0·51	0·958
2	1·70	0·783
3+	4·73	0·630
4	6·60	0·263
5+	10·96	0·153
NGC 2196		
1	0·47	0·922
2	2·11	0·597
3	5·54	0·504
4	9·07	0·367
5+	18·80	0·056
6	34·58	0·006
NGC 2903		
1	0·40	0·950
2	1·45	0·833
3	2·92	0·728
4	5·05	0·652
5	6·23	0·600
6	8·89	0·450
7	12·25	0·385
8+	13·58	0·380
NGC 2935		
1	0·32	0·980
2	0·78	0·870
3	2·42	0·702
4	3·07	0·602
5	3·35	0·503
6	4·51	0·419
7	5·24	0·297
8	5·83	0·262
9+	11·05	0·092
10	16·25	0·065
NGC 2997		
1	0·69	0·897
2	1·47	0·759
3	2·68	0·614
4	4·37	0·567
5	5·29	0·457
*	6·22	0·422
6	8·77	0·292
7+	15·67	0·177
NGC 3177		
1	0·45	0·838
2	1·55	0·588
3	2·54	0·513
4+	8·09	0·383
NGC 3310		
1	1·62	0·676
*	1·77	0·522
2	2·57	0·322
3+	4·60	0·215
4	8·69	0·188
5	9·48	0·082
6	10·01	0·066
7	11·19	0·007
8	12·67	−0·013
9+	17·77	−0·039
NGC 3351		
1	0·46	0·956
2	1·29	0·906
*	1·80	0·832
3	2·51	0·778
*	3·76	0·565
4	4·15	0·488
5	5·01	0·408
6	6·02	0·328
7	7·65	0·278
8+	10·95	0·178
NGC 3627		
1	1·61	0·825
2	1·94	0·762
*	3·43	0·584
3	3·64	0·569
4	6·54	0·377
5+	7·71	0·353
6	11·14	0·227
7	13·06	0·175
8+	20·14	0·142
9	22·56	0·102
*	43·51	−0·043
*	58·36	−0·063
NGC 3955		
1	1·51	0·973
2	2·24	0·925
3	4·98	0·858
4	5·78	0·790
5	10·92	0·680
6+	12·66	0·665
NGC 4064		
1	0·86	0·985
2	2·62	0·910
*	3·33	0·889
3	3·50	0·855
4	4·13	0·805
5+	8·19	0·732
6	10·99	0·690
NGC 5236		
1	3·38	0·625
2	5·40	0·370
3	7·36	0·090
4+	11·31	−0·135
NGC 7741		
1	0·42	0·965
2	1·76	0·948
3	3·40	0·900
4	5·11	0·872
*	6·61	0·860
5+	7·04	0·835

The contours marked with an asterisk (*) are not shown in Figure 5. The + signs designate the contours at which the luminosity profile changes slope.

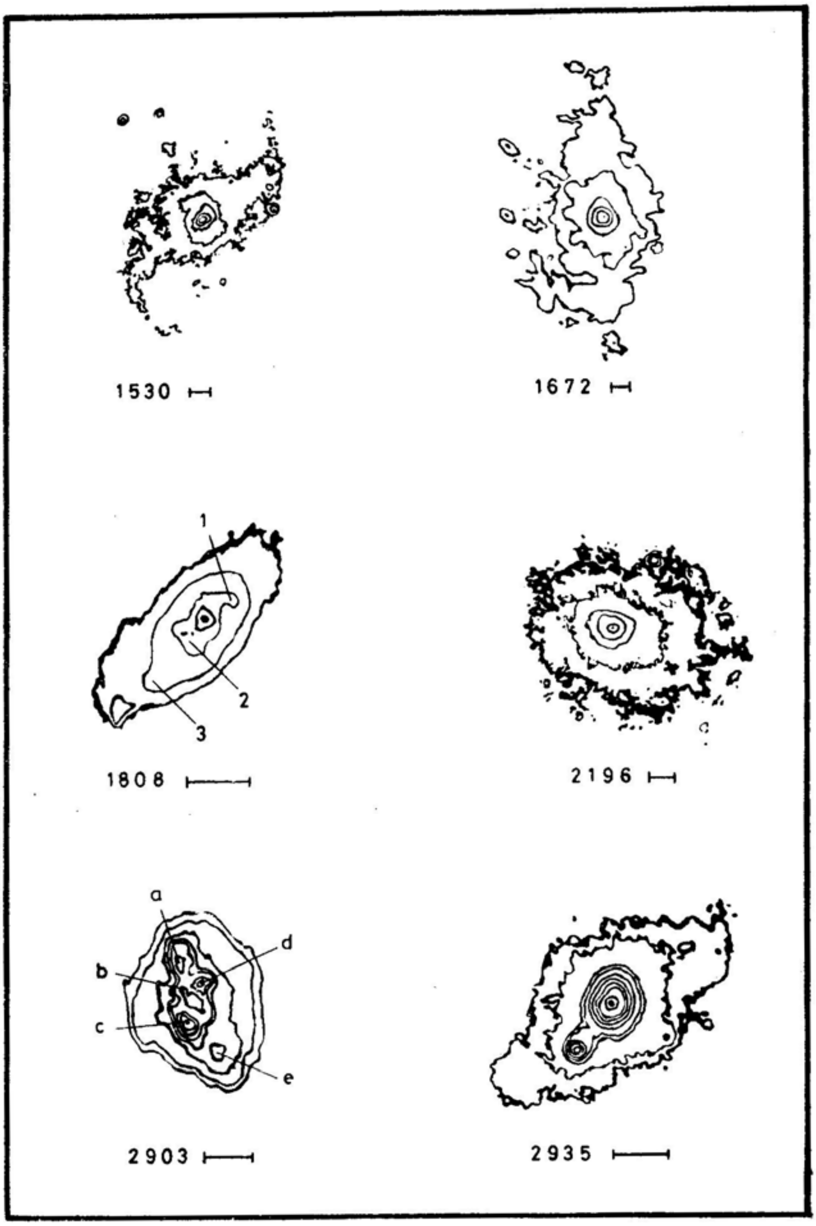

Figure 5c. The equidensity contours of the S-P galaxies NGC 1530, 1672, 1808, 2196, 2903 and 2935. Details are similar to Fig. 5a. The numbers in NGC 1808 and the letters in NGC 2903 designate regions discussed in Section 5.

contours obtained have not been reproduced in the figure to avoid overcrowding; their parameters appear in the table without any numerical designation. Listed also in Table 2 are the equivalent radii $r^* = (A/\pi)^{1/2}$ where A is the area of a particular isophote in square seconds of arc. The equivalent radius can be treated as an average radius when a single contour represents a given intensity level. Some galaxies of

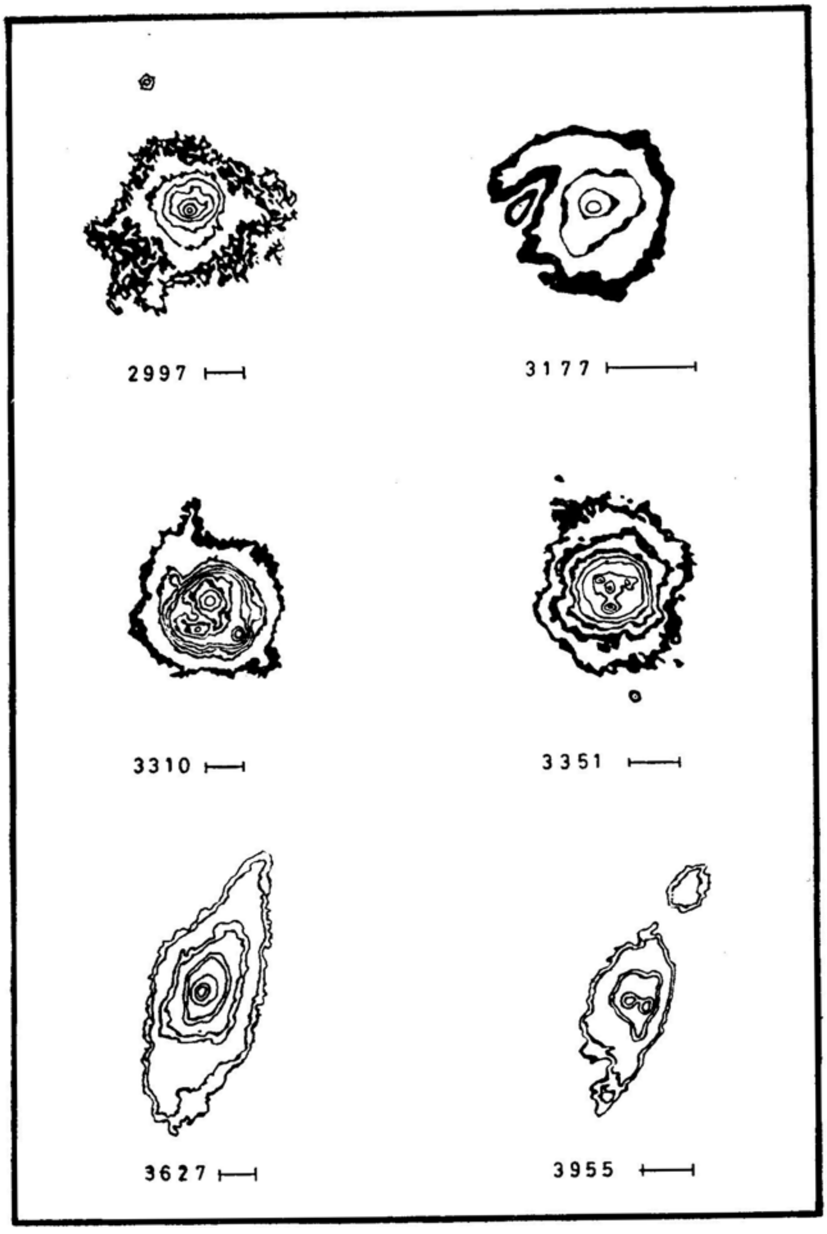

Figure 5d. The equidensity contours of the SP galaxies NGC 2997, 3177, 3310, 3351, 3627 and 3955. Details are similar to Fig. 5a.

class σ exhibit distinct hot-spots even in the integrated light and hence possess different unconnected contours at a given intensity level; in such a case the equivalent radius is related only to the total area, with the surface brightness above a given value. Smooth curves through the points listed in Table 2 appear in Fig. 6. The photometric noise was smoothened whenever present. This noise arises whenever third order isophotes were used and a few times even in the second order isophotes.

Its effect is seen in some of the isophotes in Fig. 5 that appear similar to each other in pairs (*e.g.* NGC 1140). It is desirable to use the mean isophote in such situations.

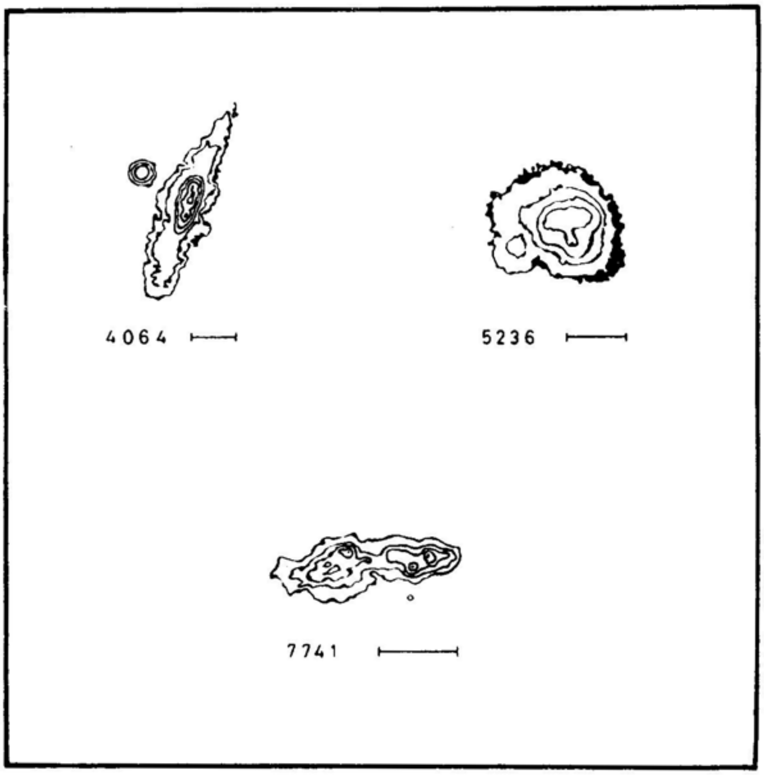

Figure 5e. The equidensity contours of the S-P galaxies NGC 4064, 5236 and 7741. Details are similar to Fig. 5a.

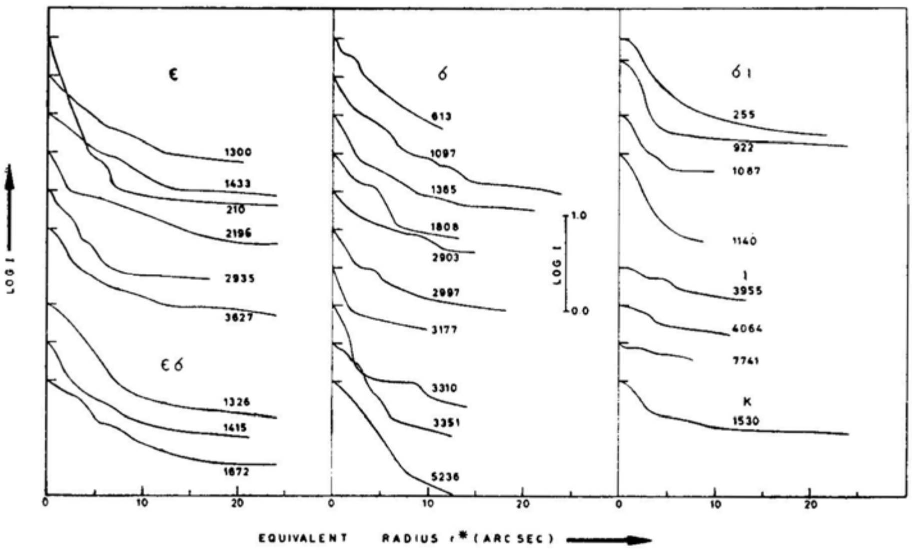

Figure 6. The relative equivalent luminosity profiles for the 27 S-P galaxies. The relative intensity scale is shown in the central frame.

The luminosity profiles in Fig. 6 are only on a relative scale of intensity. As already mentioned in Section 2, we have used the entire band (4000Å-8700Å) of the image tube response in our observations so as to integrate the contribution from the hot spots as well as the stellar population, and to reduce the contrast of the dust lanes. It is hence not possible to establish an accurate zero point for the luminosity profiles. We have, however, compared our profiles with the inner overlapping regions of the blue luminosity profiles of Sérsic (1968) whenever available (Table 4 in Section 6). We have also compared the profiles of Sérsic with the photoelectric *B* magnitudes of Alcaino (1976) with a 5·5 arcsec aperture. The agreement is generally good between the profiles (except that the blue profiles are slightly steeper than ours) and also between the profiles of Sérsic and the photometry of Alcaino. The mean surface brightness seen through a 5·5 arcsec aperture is 1·4±0.6 mag fainter than the peak surface brightness obtained by overlapping our profiles with those of Sérsic. The agreement is not good in the case of NGC 1672: the peak surface brightness is 1·6 mag fainter than the average surface brightness through the 5·5 arcsec aperture. The discrepancy probably results partly from the poor seeing on our photographs of this highly southern object and partly from overexposure of inner regions in Sérsic's photometry. A peak brightness of 18·0 mag arcsec^{-2} is a more likely value.

5. Colour distribution

Six galaxies were photographed in two spectral bands as explained in Section 2. We denote these bands by *BL* (4000Å–4600Å) and *IR* (7000Å–8700Å). We chose one galaxy of class ϵ (NGC 210) and five of class σ (NGC 613,1097,1365,1808 and 2903). The photographs were scanned to derive radial profiles in a single direction. The profiles have been obtained in two different directions for NGC 2903 because in this case the hot spots are extremely distinct. The profiles in *BL*, *IR* and in the (*BL-IR*) colour are presented in Fig. 7. The intensities as well as the colours are in relative units. The scans cover the perinuclear regions and the extreme points are barely outside the perinuclear component.

The colours at the extremities of the profiles do not agree with each other in the cases of NGC 1097, 1365 and the P.A. 168° profile of NGC 2903. The south-eastern regions of NGC 1097 and 1365 are redder than the north-eastern regions while in NGC 2903 it is the north-eastern region that is redder. The most prominent feature in all the profiles is, however, a red nucleus. Relative to the region surrounding the bright perinuclear formations (a bar or a lens) the nuclei are redder by Δ (*BL-IR*)=0·8 mag in NGC 210 and 1365, by ~ 0·4 mag in NGC 613, 1097 and 1808, while the nucleus of NGC 2903 is 0·6 mag redder. The observations of NGC 2903 correspond to the nucleus identified by Prabhu (1980). The nuclei of NGC 1097 and 1808 are not very prominent in the colour profiles partly since the entire perinuclear formation is red. The perinuclear region of NGC 1365 also exhibits some degree of reddening. The ridge 2 (*cf.* Figs 5 and 7) south-east of the nucleus and visible in the blue is not visible in the red. The hot spots are generally bluer by –0·2 to –0·4 mag in all the galaxies (*cf.* 1 in NGC 613, 1 in NGC 1365 and *c* in NGC 2903), a fact that suggests that the hot spots that appear neutral or redder are reddened by dust (*e.g.* all the hot spots in NGC 1097, 1808 and *a*, *b* in NGC 2903).

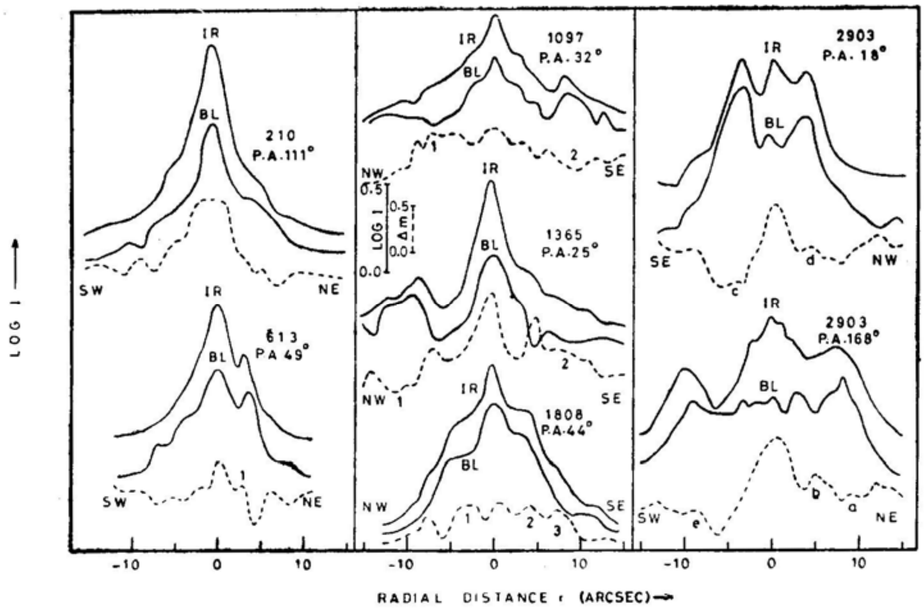

Figure 7. The intensity scans across the central regions of different S-P galaxies. The continuous ines are in *1R* (7000Å–8700Å) and*BL* (4000Å–4600Å) bands while the dotted lines show the *BL-IR* intensity difference on a magnitude scale. The scales are shown in the central frame. The zero point is arbitrary. Note the faintness of the nucleus of NGC 2903 in *BL*. Numbers and letters designate individual regions discussed in the text.

6. Geometrical and photometric properties

The geometrical and photometric properties derived from the photographs and the luminosity profiles appear in Table 3. The galaxies are grouped according to the classification of the central regions. The galaxy type in column 2, the luminosity index in column 3 and the axial ratio in column 4 are all taken from de Vaucouleurs, de Vaucouleurs and Corwin (1976). The heliocentric radial velocities in column 5 are also taken either from the same source or from Sandage (1978) when not available in the former. The radial velocity of NGC 4250 is from Kelton (1980) and that of NGC 3956 is based on a low dispersion plate obtained by the author at the Kavalur Observatory. The semimajor axis a in seconds of arc (column 6) and the axial ratio ρ (column 7) are derived from direct measurements on the plates. The measurements were performed at the points where the surface brightness drops off sharply. All Sérsic-Pastoriza galaxies have by definition, such a sharp drop in luminosity; at the edge of the perinuclear component that it is fairly easy to measure the sizes without any exposure-dependent systematic errors. The contours nearest to such a drop are marked in Table 2. The sizes of the star-like nuclei are also measured in several cases and appear in Table 3 with a subscript n after the NGC designation. The perinuclear component in class κ is too faint and hence could not be measured in all the cases. The length of the semimajor axis was converted to a linear scale assuming a uniform Hubble flow with a constant H_0=50 km s^{-1} Mpc^{-1} and appear as a_{kpc} in column 8. We propose that the apparent nucleus of NGC 7769 consists of

Table 3. Classification of central regions of S-P galaxies and their geometrical and photometric properties.

NGC	Type	Λ	Log R	V_0	log a	log ρ	a_{kpc}	log L (kpc)	m_b-m_p	$m_b-m_p^0$
1	2	3	4	5	6	7	8	9	10	11
Class κ:										
1530	SBT3		0·23		1·325	0·22			1·35	0·98
1530 n					0·743	0·06				
3504 n	RSXS2		0·09	1479	0·701	0·15	0·72			
3611	SAS1P		0·07	1603	1·028	0·12	1·66			
3611 n					0·559	0·00	0·56			
4151 n	PSXT2*		0·13	1002	0·747	0·01	0·54			
4212 n	SA4S	0·9	0·16	1947	0·656	0·00	0·86			
4250 n	LXR+		0·11	2106b	0·521	0·02	0·68			
7769	RSAT3		0·01	4570	0·559	0·02	1·61			
Class ϵ:										
210	SXS3	0·4	0·16	1700	1·149	0·15	2·32	1·25	4·30	4·28
1300	SBT4	0·5	0·18	1422	0·911	0·12	1·12	1·33	2·25	2·10
1433	SBR1		0·05	802	1·212	0·35	1·27	1·10	2·17	2·01
2196	PSAS1	0·3	0·10	2080	0·822	0·11	1·34	1·64	2·50	2·39
2935	PSXS3	0·4	0·08	1939	0·980	0·18	1·80	1·21	2·27	2·13
3627	SXS3	0·6	0·30	583	1·511	0·37	1·83	1·24	2·57	2·46
3627 n					1·036	0·16	0·61			
4124	LAR+		0·42	1551a	1·293	0·29	2·95			
4245	SBRO*	0·5	0·10	882	1·033	0·10	0·92			
4245 n					0·540	0·04	0·30			
5850	SBR3	0·4	0·04	2354	1·071	0·11	2·69			
6951	SXT4	0·6	0·06	1627	0·877	0·22	1·19			
7410	SBS1		0·43	1634	0·591	0·05	0·62			
Class $\epsilon\sigma$:										
1326	RLBR+		0·12	1167	1·085	0·13	1·38	1·42	2·90	2·82
1415	RSXSO	0·5	0·24	1399	1·048	0·29	1·52	1·30	2·37	2.24
1672	SBS3	0.5	0·09	1076	0·971	0·01	0·98	1·16	2·17	2·01
2763	SBR6P	1·3	0·04	1634	0·957	0·21	1·44			
4258	SXS4		0·36	537	1·235	0·36	0·89			
5248	SXT4	0·5	0·12	1102	1·243	0·26	1·87			
5597	SXS6		0·06	2573a	0·822	0·12	1·66			
6907	SBS4	0·6	0·06	3238a	0·735	0·11	1·71			
7552	PSBS2		0·15	1636	0·934	0·15	1·36			
Class σ:										
613	SBT4	0·6	0·10	1462	0·952	0·25	1.27	1.28	2·40	2.27
1097	SBS3	0.5	0.15	1227	1.048	0.01	1.33	1.51	3.25	3.19
1365	SBS3	0.5	0.25	1502	1.240	0.28	2.53	1.35	2.50	2.39
1808	RSXS1		0.25	769	1.299	0.33	1.48	0.85	2.20	2.05
1808 n					0.656	0.19	0·34			
2903	SXT4	0.6	0.28	467	1.293	0·46	0·89	0·73	1·63	1·35
2997	SXT5	0·6	0·10	805	1·240	0.31	1·36	0·97	2·07	1·90
3177	SAT3	0·7	0·09	1123	1·170	0·15	1·61	0·54	1·45	1·12
3177 n					0·877	0·03	0·82			
3310	SXR4P	0·7	0·09	1063	1·325	0·17	2·18	1·14	2·65	2·55

Table 3. *Continued*

NGC 1	Type 2	Λ 3	Log R 4	V_0 5	log a 6	log ρ 7	a_{kpc} 8	log L (kpc) 9	$m_b - m_p$ 10	$m_b - m_p^0$ 11
3310 n					0·656	0·00	0·47			
3351	SBR3	0·6	0·16	673	1·120	0·04	0·86	0·86	2·17	2·01
5236	SXS5	0·7	0·04	337	1·187	0·11	0·50	0·93	3·77	3·74
5728	SXR1*	0·4	0·24	2879a	0·877	0·08	2·10			
Class $\sigma\iota$:										
255	SXT4	0·7	0·05	1873	1·044	0·56	3·01	1·56	2·65	2·55
922	SBS6P	1·0	0·04	3010a	0·895	0·30	2·29	1·27	1·67	1·41
1087	SXT5	1·0	0·17	1844	0·980	0·39	1·71	0·99	1·47	1·15
1140	I 9		0·23	1503	0·985	0·31	1·41	1·12	2·45	2·33
4369	RSAT1		0·01	1066	1·092	0·33	1·28			
Class ι:										
925	SXS7	1·1	0·21	716	1·272	0·68	1·30			
3206	SBS6		0·15	1245	1·011	0·25	1·24			
3346	SBT6	0·9	0·05	980a	0·942	0·45	0·83			
3955	I 0		0·39	1118	1·204	0·17	1·73	0·96	0·83	0·14
3956	SAS5*	1·2	0·45	726c	1·286	0·33	1·36			
4064	SBS1*P	0·6	0·36	959	1·116	0·26	1·21	0·68	0·67	−0·16
7741	SBS6	0·9	0·15	1018	1·088	0·75	2·41	0·36	0·25	−1·47

References to radial velocities: (a) Sandage (1978)
(b) Kelton (1980)
(c) Prabhu (Unpublished)

the entire perinuclear region that appears star-like owing to its great distance. On the other hand the nucleus of the nearby galaxy, NGC 5236, is so well resolved that it appears like the perinuclear component.

Derivation of photometric properties for a two component system is extremely complex and is further complicated when a bar or a lens is present (Kormendy 1980). Hence, we will not attempt a decomposition of the observed profile into different components, but directly intercompare the observed profiles of different galaxies. We assume in the following that the bars and lenses are equivalent (Kormendy 1979) and that the outermost parts of all the luminosity profiles presented in Section 4 are dominated by this component. We assume further that the luminosity profiles of all the bars have similar shape and can be matched with each other after proper scaling in length and intensity. We have converted the observed profiles to a linear scale in size (H_0=50 km s^{-1} Mpc^{-1}) and scaled them to match the bar dominated region. We compared these scaling factors with the bar lengths published by Kormendy (1979) or measured by us on published photographs for eight galaxies (NGC 613,1097,1300, 1365, 1433, 2997, 3351 and 5236). The relationship was linear and provided the necessary zero point. The estimates of the bar lengths L derived from this relation are listed for 26 galaxies in column 9 of Table 3. We prefer this scale length to the actual bar length L_0 since L is a photometrically derived parameter and is less affected by subjective errors of measurement.

We proceed to obtain the peak central surface brightness relative to the surface brightness of the bar just outside the perinuclear component. These values, m_b—m_p

appear on a magnitude scale in column 10 of Table 3. If the contribution of the central surface brightness of the bar to m_p is removed using the relationship

$$m_p^0 = -2{\cdot}5 \log [\mathrm{dex}(-0{\cdot}4 m_p) - \mathrm{dex}(-0{\cdot}4\ m_b)],$$

we obtain the peak surface brightness of the central formation m_p^o. The value of $m_b - m_p^o$ appear in column 11 of Table 3.

We can draw a few important statistical conclusions from the photometric and structural parameters in Table 3.

6.1 *Sizes of the Nuclei and the Perinuclear Components*

The histogram in Fig.8 shows the distribution of the structures of different semi-major axes. Mean size of the star-like nuclei is 0·8±0·35 kpc while that of the perinuclear components (hatched area) is 1·56±0·65 kpc. If the perinuclear component is barlike (*cf.* Section 6.2) oriented randomly in the plane of the galaxy the

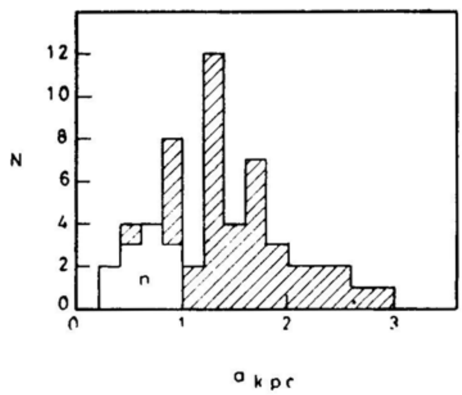

Figure 8. Histogram showing the distribution of the semi major axes of the central substructures in different S-P galaxies.

above average is an underestimate while the dispersion is an overestimate. There is no significant correlation between the size of the perinuclear component and the bar length. The correlation coefficient is 0·19 if the major axis is used, and improves to 0·33 if the geometric mean of the semimajor and semiminor axes is used.

6.2 *Shapes of the Nuclei and the Perinuclear Components*

The isophotes in Fig. 5 show that the position angles of the major axes and the ellipticities of the perinuclear formations differ quite often from the similar quantities for the outer regions. Most striking examples are NGC 1433 and NGC 2935. Such configurations arise in either of the following situations: (a) if the perinuclear formation is barlike (b) if the perinuclear formation is a disk with its plane tilted with respect to the plane of the parent galaxy. We favour the first of these hypotheses as the latter faces the angular momentum problem.

A more quantitative evidence for the barlike structure of the perinuclear formations comes from the distribution of the axial ratios of the formations with respect to the axial ratios of the parent galaxies. We assume that the parent galaxy is a disk with an axial ratio R resulting from its inclination to the line of sight. With ρ as the observed axial ratio of the perinuclear component we expect the following relations to hold for different geometrical structures:

thin disk:	$\log \rho = \log R$
thick disk or oblate spheroid:	$\log \rho < \log R$
sphere:	$\log \rho = 0.$

If the geometrical structure is a prolate spheroid with the major axis oriented randomly in the plane of the disk of the galaxy, the relationship between $\log \rho$ and $\log R$ would be very weak.

We plot in Fig. 9 the inner and the outer axial ratios for all the observed galaxies.

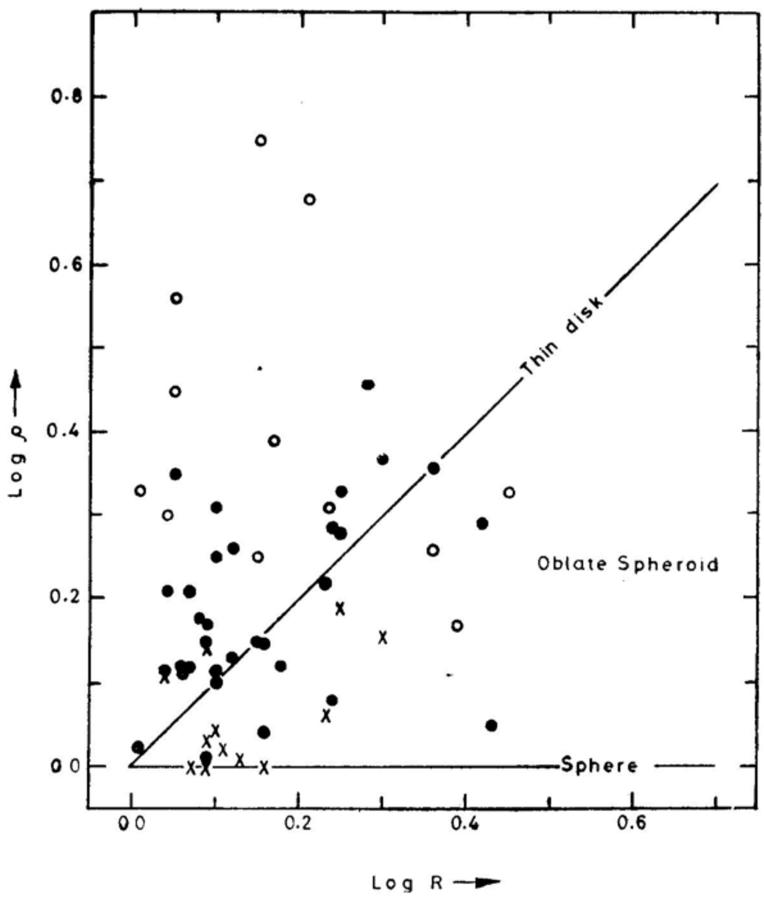

Figure 9. The distribution of the axial ratios of the central substructures (ρ) and the axial ratios of the parent galaxies (R) on a logarithmic scale. The filled circles are the perinuclear formations of classes κ, ϵ, $\epsilon\sigma$ and σ. The open circles represent classes $\sigma\iota$ and ι. Crosses denote the nuclei. The expected positions for thin disks and spheres are shown by straight lines. The oblate spheroids should be contained by these lines.

The perinuclear formations of classes $\sigma\iota$ and ι are represented by open circles while for the remaining classes a filled circle is used. The crosses represent the star-like nuclei. The straight lines for thin disk and spheres are shown. The oblate spheroids are included by these lines. The prolate spheroids may lie anywhere in the diagram . The longer the major axis with respect to the minor axis, the higher above the ‘ thin disk ’ line would be the mean position of prolate spheroids. It is obvious from the figure that the perinuclear formations of classes $\sigma\iota$ and ι are certainly barlike. It is highly likely that the formations of classes $\epsilon, \epsilon\sigma\iota$, σ and κ possess barlike distortions too judging from the large scatter among the points representing these objects. The mean departures from the ‘ thin disk ’ line for these systems are:

$$\log \rho - \log R = 0{\cdot}03 \pm 0{\cdot}13 \text{ for } \kappa, \epsilon, \epsilon\sigma \text{ and } \sigma \quad (n = 33)$$

$$= 0{\cdot}21 \pm 0{\cdot}27 \text{ for } \sigma\iota \text{ and } \iota \quad (n = 12).$$

The description in Section 3 of the regularity in the structure of the perinuclear component supports the view that the scatter diagram in Fig. 9 does not result from the stochastic distribution of hot spots in the central regions, but indicates a real departure of the structure from cylindrical symmetry. All the axial ratios of the parent galaxies have mean errors in log R smaller than 0·045 and often better than 0·025. Hence the errors in log R do not contribute significantly to the scatter. Thus an overwhelming part of the scatter in the figure is real.

The nuclei are generally close to the ‘ sphere ’ line in Fig. 9 and lie within the region of the oblate spheroids with the exceptions of NGC 3504 and 5236. They have a mean axial ratio of

$$\log \rho = 0{\cdot}06 \pm 0{\cdot}07 \qquad (n = 12).$$

They are probably spherical or oblate in shape. It should be borne in mind, though, that image smearing due to seeing makes them appear more circular than what they actually are.

6.3 *Brightness of the Perinuclear Formations*

Sorensen, Matsuda and Fujimoto (1976) have suggested that the bar potential in a barred galaxy dissipates the angular momentum of the gas in the disk and condenses it to the centre. They expect this mechanism to be more efficient as compared to the dissipation of the angular momentum by the spiral density wave. The observation that the overwhelming majority of Sérsic-Pastoriza galaxies are barred or intermediate supports this view. There are seven galaxies listed in Kormendy (1979) with bars exceeding a length of about 20 kpc: NGC 613, 1097, 1300, 4593, 5383, 5850 and 7479. Note that all but the last one is in the list of Sérsic (1973).

If the supply of gas to the inner regions of S-P galaxies is caused by the bar, we would expect a correlation between the length of the bar and the central activity. We list in Table 4 the lengths of the bars for seven galaxies for which we have the approximate photometric zero point as obtained in Section 4. We have also added NGC 4314 for which photometric parameters are taken from Benedict (1980). The bar

Table 4. Central surface brightness of the bars and the perinuclear formations.

NGC	Bar length L_0 (arcmin)	$\log L_0$ (kpc)	m_p mag arcsec^{-2}	$m_b - m_p$ mag	m_b mag arcsec^{-2}	m_p^0
1	2	3	4	5	6	7
613	2·3 K	1·29	17·7	2·4	20·1	17·8
1097	3·0 K	1·39	16·9	3·3	20·2	17·0
1365	3·0 T	1·40	16·7	2·5	19·2	16·8
1433	2·8 T	1·12	18·1	2·2	20·3	18·2
1672	3·0 T	1·27	19·9	2·2	22·1	20·0
			18·0a		20·2a	18·1a
2997	2·0 T	0·98	18·7	2·1	20·8	18·8
4314	2·1 T	1·03	18·2b	2·0b	20·2	18·3
5236	5·0 T	0·98	15·1	3·8	18·9	15·1
			18·9	1·6c	20·5c	18·6

Notes: K Kormendy (1979)
T This work
a Corrected as mentioned in Section 4
b Benedict (1980)
c Talbot, Jensen and Dufour (1979)

lengths in column 2 are either taken from Kormendy (1979) or measured on published photographs. Columns 3 and 4 give the absolute length of the bar L_0 (kpc) and the peak surface brightness m_p of the central region of the galaxy. The difference between the central surface brightness of the bar and the peak surface brightness m_b—m_p, in column 5 is taken from Table 3. The central surface brightness of the bar m_b appears in column 6. The peak surface brightness of the perinuclear component m_p^0 is derived as explained earlier in this section.

We have listed two values each of m_p, m_b and m_p^0 for NGC 1672 and 5236. The effect of poor resolution on NGC 1672 is discussed in Section 4 and the second value for this galaxy is a value corrected for this effect. NGC 5236 is a counter example for the same effect. It is the closest galaxy in our sample and hence provides a very high spatial resolution. The entire region observed by us has the dimensions of the star-like nuclei in the remaining galaxies. Thus the peak brightness is that of the nuclear region alone. The perinuclear region dominates the profile after r^*~10 arcsec, and has a central brightness of 18·9 mag arcsec^{-2}. We have not been able to observe the bar in this galaxy which has a surface brightness of 20·5 mag arcsec^{-2} as seen from the surface photometry of Talbot, Jensen and Dufour (1979). The values with these assumptions appear in the second row for NGC 5236.

We plot in Fig. 10a the values of corrected peak surface brightness m_p^0 against the logarithmic bar length. A correlation is evident in the sense that longer bars have brighter perinuclear components. The corrected values for NGC 1672 and 5236 are shown by filled squares. The straight line

$$m_p^0 = 23{\cdot}90 - \log L_0 \text{ (kpc)},$$

fits the observed points well. The relation implies, that the peak surface brightness of the perinuclear component varies as the square of the bar length. Since the area

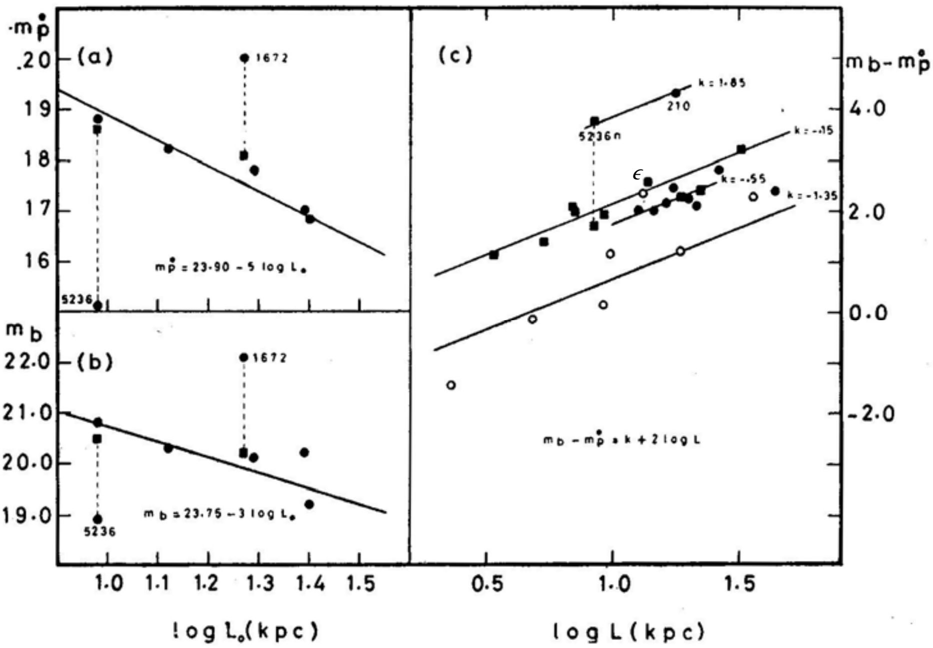

Figure 10. The distribution of (a) the central brightness m_p^0 of the perinuclear formations and (b) the central brightness m_b of the bars (both in equivalent blue mag arcsec^{-2}) with the length of the bar L_0 (kpc) of the parent galaxies. The straight lines corresponding to $m_p^0 = 23{\cdot}90–5 \log L_0$ and $m_b = 23{\cdot}75–3 \log L_0$ are shown. The filled squares denote the corrected values for NGC 1672 and 5236. (c) the distribution of the difference $m_b—m_p^0$ with the estimated length of the bar L (kpc) of the bar (see text for details). The value for NGC 5236 denoted by 5236n corresponds to the nucleus before the correction is applied. The corrected value is joined by dotted line. The filled circles represent the classes ϵ and $\epsilon\sigma$, the filled squares σ, and the open circles $\sigma\iota$ and ι. The straight lines $m_b — m_p^0 = k+2 \log L$ for k = 1·85, –0·15. –0·55 and –1·35 are shown.

of the disk swept by the bar varies as the square of bar length, the above relation agrees with the mechanism suggested by Sorensen, Matsuda and Fujimoto (1976).

Fig. 10b shows the relationship between the central surface brightness of the bar and the length of the bar. We draw a mean line

$$m_b = 23{\cdot}75 — 3 \log L_0 \text{ (kpc)}$$

with the realistic values of NGC 1672 and 5236. Kalloglyan (1977) and Kormendy (1979) have shown that the mean surface brightness of the bars is nearly constant for all barred galaxies. The above relation would then imply that intensity falls more rapidly in the longer bars than in the shorter ones.

The above two relations are derived from rather scanty data. We support these conclusions from the additional photometric data in Table 2. We plot in Fig. 10c, the difference $m_b – m_p^0$ for 26 galaxies against log L. The relationship

$$m_b – m_p^0 = k + 2 \log L \text{ (kpc)}$$

which conforms with the previous two relations fits the points well with

k = 1·85 for NGC 210 and the nucleus of NGC 5236

= – 0.15 for class σ

= – 0.55 for classes $\epsilon\sigma$ and ϵ

= – 1.35 for classes $\sigma\iota$ and ι.

The difference in the zero points for different classes and the anomalous behaviour of NGC 210 and 5236 are discussed in the following section.

7. Discussion and conclusions

The central regions of Sérsic-Pastoriza galaxies contain bright substructures of two different scale lengths: (a) a nucleus of radius 300–900 pc generally redder than its surroundings and (b) a perinuclear formation of radius 1·3–2·4 kpc. There is a range in which the relative strength of the two components varies. The perinuclear formation is very faint in class κ while the nucleus is very faint in class ι. The classes ϵ, $\epsilon\sigma$ and σ contain both the components. While the perinuclear formation of class σ contains giant complexes of the H II regions, the members of class ϵ do not contain significant amount of ionized gas. The class $\epsilon\sigma$ is intermediate between σ and ϵ while the class $\sigma\iota$ is intermediate between σ and ι.

The parent galaxies of classes ϵ, $\epsilon\sigma$ and σ appear morphologically different from those of classes $\sigma\iota$ and ι. The former group contains more *B* and *AB* spirals (90 per cent against 63) and is more luminous ($\Lambda \sim 0{\cdot}5$ against 1·0) as compared with the latter group. The position of class κ is not very clear because of insufficient statistics on luminosity. The structures of this class appear quite often in SA galaxies too. These remarks suggest that the classes ϵ, $\epsilon\sigma$ and σ belong to a single group of events which differ from the objects of other classes. The burst of star formation giving rise to bright H II regions in class σ may cease eventually and the perinuclear formation may change into the one similar to the class ϵ. The perinuclear formations of classes $\sigma\iota$ and ι are prolate as seen from the scatter in log ρ —log R diagram (Fig. 9). Ovoidal and barlike distortions are highly probable even in the classes ϵ, $\epsilon\sigma$ and σ.

Since the bursts of star formation in the central regions of S-P galaxies are of a transient nature, the mechanism for the supply of gas has been an important problem (Wakamatsu and Nishida 1980). Two possible mechanisms are: (a) mass loss from stars in the nuclear region and (b) infall of gas from bar-disk region as suggested by Sorensen, Matsuda and Fujimoto (1976).

The observation that the central brightness of the perinuclear component increases linearly with the square of the bar length (Fig. 10a) supports the mechanism (b). The high specific angular momentum in the perinuclear component also supports this view against the mechanism (a) (Wakamatsu and Nishida 1980). The mechanism (a) may operate in the formation of some nuclei, probably in class κ which ccur often in SA galaxies too (NGC 3611, 4212, 4369).

Since the bursts of star formation are transient in nature we should be able to see different evolutionary stages in different galaxies. An evolution from class σ towards ϵ is very likely as suggested by the lack of H_a emission from class ϵ structures. The brightness of the perinuclear component decreases as the massive stars evolve and die. Thus the $\epsilon\sigma$ and ϵ structures fall below the line for σ in Fig. 10c.

The galaxies with lower luminosity have less gas in the bar-disk region and hence the gas infall would be lower in these cases. Thus $\sigma\iota$ and ι structures result which exhibit the same activity to a much smaller degree (Fig. 10c). Once the gas condenses to the centre, its dynamics may be ruled more by the bar potential than by the disk and halo. Hence, the $\sigma\iota$ and ι structures appear more prolate than the systems of other classes, We have thus been able to separate the activity of differing degree ($\sigma\iota$ and ι) and also in different stages of evolution (from σ towards ϵ). The objects of different classes should be compared with appropriate theoretical models.

The anomalous behaviour of NGC 210 and the nucleus of NGC 5236 in Fig. 10c invites comments. The magnitude difference for NGC 5236n corresponds to the difference between the peak surface brightness of the nucleus and the peak surface brightness of the perinuclear region. Thus it does not belong to the set of values represented in the figure. However, it opens a new question for future investigations, whether the activity in the nucleus is also related to the bar, probably through the perinuclear formation. NGC 210 contains, on the other hand, a well defined perinuclear component typical of class ϵ. It is the brightest, and one of the largest perinuclear formations in our sample. Unfortunately, it is not a well studied galaxy. Detailed surface photometry of NGC 210 and radio observations on its H I content and its environment will help to clarify the situation. This galaxy merits being on the search list for compact IR, X-ray and radio nucleus.

An important off-shoot of the present investigations is the dependence of the central surface brightness of the bar on the size of the bar. The central surface brightness of the bar increases directly with the bar length with an exponent close to unity. Incorporating the observations of Kalloglyan (1977) and Kormendy (1979) that the mean surface brightness of the bars is constant for all barred galaxies, we conclude the surface brightness of the larger bars falls steeper than that of the shorter ones.

Acknowledgements

The material presented in this paper constitutes a major part of the doctoral thesis submitted to the Madurai Kamaraj University. It is indeed a great pleasure to express my deep gratitude to Dr M. K. V. Bappu, my thesis supervisor, for impressing upon me the importance of Sérsic's list, for the design of the instrumentation used in this investigation at the Kavalur Observatory, and for constant encouragement. Thanks are also due to several friends and colleagues at the Indian Institute of Astrophysics whose assistance has been invaluable and was readily available at the crucial moments.

References

Alcaino, G, 1976, *Astr. Astrophys. Suppl. Ser.*, **26**, 261.
Alloin, D., Kunth, D. 1979, *Astr. Astrophys.*, **71**, 335.

Benedict; G. F. 1980, *Astr. J.*, **85,** 513.
Burbidge, E. M. 1962, in *The Distribution and Motion of Interstellar Matter in Galaxies,* Ed. L . Woltjer, W. A. Benjamin, Inc., New York, p. 123.
Burbidge, E. M., Burbidge, G. R. 1960, *Astrophys. J.*, **132,** 30.
Burbidge, E. M., Burbidge, G. R. 1968, *Astrophys. J.*, **151,** 99.
de Vaucouleurs, G. 1977, in *IAU Coll. 37: L'Evolution des Galaxies et ses implications cosmologiques,* CNRS, p. 301.
de Vaucouleurs, G., de Vaucouleurs, A. 1961, *Mem. R. astr. Soc.*, **68,** 69.
de Vaucouleurs, G., de Vaucouleurs, A., Corwin, H. G. 1976, *Second Reference Catalogue of Bright Galaxies,* University of Texas Press, Austin.
Geyer, E. H. 1978, in *Modern Techniques in Astronomical Photography,* Eds R. M. West and J. L. Heudier, European Southern Observatory, Geneva, p. 297.
Glass, I. S. 1976, *Mon. Not. R. astr. Soc.*,**175,** 191.
Griffiths, R. E., Feigelson, E., van Speybroeck, L. 1979, *Bull. Am. astr. Soc.*, **11,** 466.
Kalloglyan, A. T. 1971, *Astrophys.*, **7**, 109.
Kelton, P. W. 1980, *Astr. J.*, **85,** 89.
Kleinmann, D. E., Low, F. J. 1970, *Astrophys. J.*, **161,** L203.
Kleinmann, D. E., Wright, E. L. 1974, *Astrophys. J.*, **191,** L19.
Kormendy, J 1979, *Astrophys. J.*, **227,** 714.
Kormendy, J. 1980, in *Two Dimensional Photometry*, Eds P. Crane and K. Kjar, European Southern Observatory, Geneva, p. 191.
Ku, W. H.-M., Chanan, G. A., Helfand, D. S., Long, K. S. 1979, *Bull. Am. astr. Soc.*, **11,** 466.
Morgan, W. W. 1958, *Publ. astr. Soc. Pacific,* **70,** 364.
Morgan, W. W., Walborn, N. R., Tapscott, J. W. 1971, in *Nuclei of Galaxies,* Ed. D. S. K. O'Connell North Holland Pub. Co., Amsterdam, p. 27.
Oka, S., Wakamatsu, K., Sakka, K., Nishida, M., Jugaku, J. 1974, *Publ. astr. Soc. Japan,* **26,** 289.
Osmer, P. S., Smith, M. G., Weedman, D. W. 1974, *Astrophys. J.*, **192,** 279.
Pastoriza, M. G. 1975, *Astrophys. Sp. Sci*, **33,** 173.
Prabhu, T. P. 1978, *Kodaikanal Obs. Bull. Ser. **A***, **2,** 105.
Prabhu, T. P. 1979, *PhD thesis,* Madurai Kamaraj University.
Prabhu, T, P. 1980, *Astrophys. Sp. Sci.*, **68,** 519.
Rieke, G. H., Lebofsky, M. J. 1978, *Astrophys. J.*, **220,** L38.
Rieke, G. H., Low, F. J. 1972, *Astrophys. J.,* **176,** L95.
Sandage, A. 1978, *Astr. J.*, **83,** 904.
Sérsic, J. L. 1968, *Atlas de Galaxies Australes,* Observatorio Astronomico, Cordoba.
Sérsic, J. L. 1973, *Publ. astr. Soc. Pacific,* **85,** 103.
Sérsic, J. L., Pastoriza, M. G., 1965, *Publ. astr. Soc. Pacific,* **77,** 287.
Sorensen, S. A., Matsuda, T., Fujimoto, M. 1976, *Astrophys. Sp. Sci.,* **43,** 491.
Talbot, R. J., Jensen, E. B., Dufour, R. J. 1979, *Astrophys. J.*, **229,** 91.
Telesco, C. M., Harper, D. A. 1980, *Astrophys. J.,* **235,** 392.
Turnrose, B. E. 1976, *Astrophys. J.,* **210,** 33.
van der Kruit, P. C. 1973, *Astr. Astrophys.,* **29,** 231.
Véron, M. P., Véron, P., Zuiderwijk, E. J. 1980, *ESO Scientific Preprint,* No. 109.
Véron, P., Lindblad, P. O., Zuiderwijk, E. J., Véron, M. P., Adam, G. 1979, *Astr. Astrophys.,* **87,** 245.
Véron, P., Véron, M. P., Bergeron, J., Zuiderwijk, E. J. 1980, *ESO Scientific Preprint* No. 83.
Wakamatsu, K., Nishida, M. T. 1980, *Publ. astr. Soc. Japan,* (in press).
Ward, M. J., Wilson, A. S., Disney, M. J., Elvis, M., Maccacaro, T. 1978, *Astrophys. J.,* **223,** 788.

J. Astrophys. Astr. (1980) **1,** 155–164

Supernovae and the Ap Phenomenon

R. Rajamohan and Ashok K. Pati *Indian Institute of Astrophysics, Bangalore 560034*

Received 1980 August 22; accepted 1980 October 23

Abstract. We put forward evidence that relates the phenomenon of the chemically peculiar stars of the upper main sequence to Supernovae explosions in young clusters. In the Upper Scorpius region we find that a supernova shell has interacted with dense clouds and that the peculiar stars lie close to or along the edges of interaction.

We argue that the stars at or near the cloud faces are capable of acquiring this enriched material which is sufficiently slowed down. The magnetic accretion process of Havnes and Conti provides the mechanism of acquisition. This process with the associated magnetic braking accounts for the build-up in abundance anomalies and the slowing down of rotation with age.

Key words: Supernovae—clusters—peculiar stars

1. Introduction

Several hypotheses to explain the origin of peculiar stars exist. Catalano (1975) has reviewed critically the various hypotheses. None of the theories proposed have been able to account for the bewildering range of phenomena associated with the peculiar stars such as the range in abundance anomalies, spectral and magnetic field variations and their low rotational velocities.

The peculiar stars can be broadly divided into a magnetic and a non-magnetic sequence ranging from early F to early B stars (Wolff and Wolff 1975). The magnetic sequence consists of the Si Cr Eu Sr stars with variations in line intensity and magnetic fields suggesting a patchy surface distribution of anomalous abundances, the most anomalous being in the region of the magnetic poles. The non-magnetic sequence, in order of increasing temperature, are the Am stars, the Hg-Mn stars, the He-weak and the He-rich stars. However, these categories are not clearly defined and as spectroscopic resolution increases, one finds the characteristically overabundant elements of one group also enhanced in the others (Cowley 1975).

Among the different mechanisms proposed to explain the origin of peculiar stars, the diffusion theory proposed by Michaud (1970) is widely accepted. However, several authors have suggested that a nuclear origin of the abundance anomalies cannot be ruled out and there may be some relation between supernova events and the peculiar stars (Guthrie 1968; Blake, Schramm and Kuchowicz 1974; Kuchowicz 1975). High dispersion studies indicate that at present there is no single theory which can account for the complexity of chemical abundance patterns observed in these objects (Cowley 1975).

In what follows we suggest that supernova explosions in clusters and associations together with the magnetic accretion hypothesis of Havnes and Conti (1971) and Havnes (1974, 1975) provides the most natural explanation for the wide range of phenomena associated with these stars.

2. The Upper Scorpius region

The ring-like emission nebulosity in Upper Scorpius seen in the deep sky narrow band H-alpha photographs of Sivan (1974) is shown bounded by dashed lines in Fig. 1, which also shows the position of the H I shell and the gas clouds in this region. The velocities of various H I features from 21-cm observations by Johnson (1971) and Sancisi and Van Woerden (1970) are marked by their values. The positions of the peculiar stars found by Garrison (1967) are indicated by arrows. Table 1 lists all the peculiar stars in the Upper Scorpius region which are members of the Scorpio-Centaurus association. Table 2 lists members of the group suspected to be peculiar.

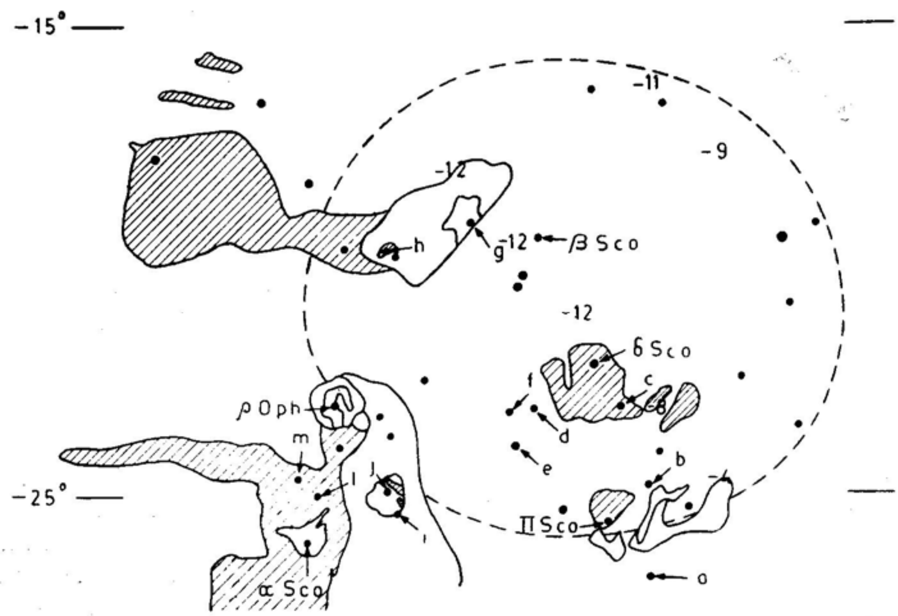

Figure 1. A schematic diagram of the Upper Scorpius region showing: (a) the peculiar stars marked by lower case letters, (b) the H I velocities by their values, (c) the position of the narrow band H-alpha emission ring by the dashed line. (d) Nebulosities in the region as depicted by Johnson (1970); shaded portions are brighter in the red Palomar Sky Survey prints and unshaded portions are brighter in the blue.

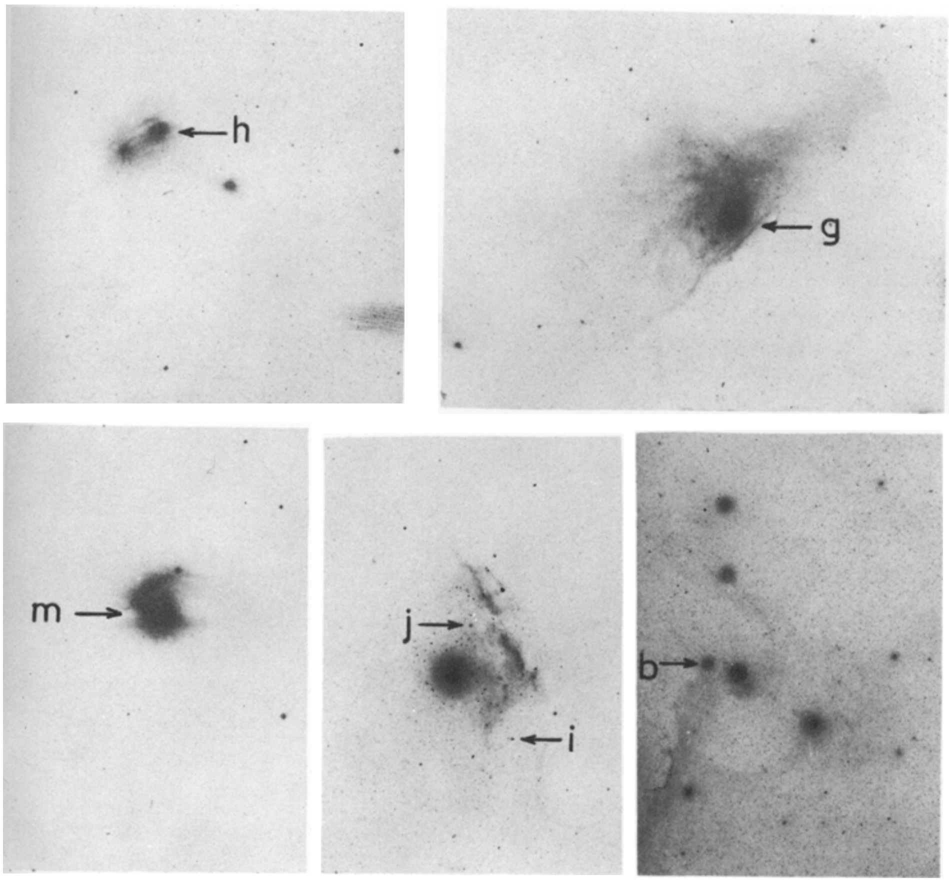

Figure 2. Enlargements of the regions around some of the peculiar stars shown in Fig. 1.

RAJAMOHAN AND PATI

Table 1. Peculiar stars in the Upper Scorpius region.

HD Number	Spectral type	V Sin i	Indicated in Fig. 1 as	Remarks
*142250	B6Vp	$\leqslant$ 50	a	SiII strong
*142301	B8p	$\leqslant$ 50	b	Q (ST) > Q (*UBV*)
*142884	B9p	210	c	SiII strong, Q (ST) > Q (*UBV*)
*144334	B8p	$\leqslant$ 50	d	Q (ST) > Q (*UBV*)
*144661	B7IIIp	75	e	Q (ST) > Q (*UBV*)
*144844	B9IV	185	f	Q (ST) > Q (*UBV*)
145102	B9p	$\leqslant$ 50		SiII strong
*145501B	B9p	—	g	Q (ST) > Q (*UBV*)
*146998	A7p (Sr-Cr)	—	i	
*147010	Ap	$\leqslant$ 50	h	Star very peculiar. See Garrison (1967) for a description.
*147105	A5p (Sr)	—	j	
147890	B9·5p	$\leqslant$ 50	—	SiII strong, Q (ST) > Q (*UBV*)
148199	Ap	$\leqslant$ 50	—	SiII strong, Q (ST) > Q (*UBV*)
*148321	A5mp (Sr)	100	l	
150035	A5p	—	—	CaII K is weak
151346	B7p	—	—	Q (ST) > Q (*UBV*)

Table 2. Stars suspected to be peculiar in Upper Scorpius region.

HD Number	Spectral type	V Sin i	Indicated in Fig. 1 as	Remarks
139160	B8Vp	165	—	The lines with the exception of Balmer lines appear weak
139365	B2.5V	135	—	Ionised Si, Mg weak; H-strong for He-type given
*142096	B2.5V	200	—	Ionised Si, Mg weak; H-strong for He-type given
145482	B2V	230	—	Spectrum indicates low luminosity at B2
*147889	B2V	100	—	Low luminosity at B2, SiII slightly enhanced
*147933	B2IV	295	—	Q(ST) > Q(*UBV*)
*147934	B2V	290	—	Q(ST) > Q(*UBV*)
*148605	B2V	250	m	Low luminosity at B2

V Sin *i* values are mean values from the determinations of Rajamohan (1976) and Slettebak (1968).

Stars marked with asterisks in Tables 1 and 2 are seen to lie at or close to the points of interaction of the shell (*i.e.* within the shell thickness) with the dense clouds in the region. These interaction edges are admittedly not very well defined in all cases. Some of the clearly defined edges are illustrated in Fig. 2, where the filaments are sometimes seen to loop around the peculiar stars.

To determine whether the peculiar stars have a distribution near or away from such interaction edges which is different from that of the normal stars or not, a chi-squared test (with continuity corrections) was carried out. All the stars in the region which are members of the Scorpio-Centaurus association (Garrison 1967) were included. Two cases were considered: Case 1, where only the stars listed in Table 1 were taken to be peculiar, giving χ_c^2 = 2·99 (P = 0·09); Case 2 where the stars in both Table 1 and

Table 2 were taken to be peculiar, giving χ_c^2 = 4·46 (P = 0·04). We give below the contingency tables:

	Case 1		Case 2	
	Normal stars	Peculiar stars	Normal stars	Peculiar stars
Away from edges of interaction	48	5	45	8
At or close to edges of interaction	34	11	29	16

It is apparent that the peculiar stars tend to lie at the edges of interaction of the shell with the dense clouds in the region.

The nebulosity (IC 4592) around ν Sco (star ‘ g ’ in Fig. 1) has a very sharp edge as seen in Figs 1 and 2. Parts of this edge show a motion with respect to the stars of about 0·2 arcsec yr^{-1} (Johnson 1966), which at the average distance to the Upper Scorpius stars corresponds to 165 km s^{-1}. This large velocity can partly be explained in terms of an interaction of the type discussed in subsequent sections.

2.1 *Positions, Distances and Sizes*

There exists a spur of neutral hydrogen, which projects from the galactic plane through this area (McGee, Murray and Milton 1963) and as seen from the H II region produced in it by ζ Oph (not shown in Fig. 1) it appears to b e at the same distance as the latter (~ 170 pc), which is a member of the Scorpio-Centaurus association. Radio maps have also been made of this region by Sancisi and Van Woerden (1970). The maps show several H I features with velocities ranging from –9 to –12 km s^{-1} scattered over the area. The positions of these features are marked by their values in Fig. 1. Sancisi (1974) suggests that the structure and velocities of these features point to an expanding, dense, semispherical shell about 5 pc thick with a volume density of 30 cm^{-3} or higher and an expansion velocity of about 3 km s^{-1}.

The good agreement between the H I emission features and the interstellar sodium (Hobbs 1969) and calcium (Wallerstein 1967) lines for stars in the corresponding areas suggests that the H I shell is at about the same distance as these stars *i.e.* 170 pc (Blaauw 1964). The luminous and dark nebulae in this region are listed by Johnson (1970) along with the stars associated with them. These stars are all members of the Scorpio-Centaurus association (Garrison 1967, Bertiau 1958) and the clouds would hence appear to be at the same distances.

The sizes of the radio shell and the emission ring agree fairly well. Sivan (1974) estimates an angular size of 840 arcmin by 720 arcmin (which is 42 pc by 36 pc at 174 pc) for the latter while Sancisi and Van Woerden (1970) estimate a size of 15 pc by 45 pc and Sancisi (1974) gives an average radius of 13 pc for the radio shell. This discrepancy could partly be explained by the fact that most of the radio observations are on the eastern and northern side of the shell where the features are strong and sharp while the features on the western half are in general low and broad.

2.2 *The Ages of the Dense Shell and the Stars*

Estimates of the age of the Scorpio-Centaurus stars vary from $4{\cdot}5\times10^6$ (Maeder 1972) to 10^7 years (Blaauw 1964). Sancisi (1974) derives 1×10^6 years for the shell using a 'snow-plow ' model for the expansion.

The large amount of kinetic energy and momentum associated with the expanding shell system points to the occurrence of a supernova explosion (Sancisi 1974). The size of the shell is smaller than similar younger shells seen elsewhere because the ambient density here is probably an order of magnitude higher. Also we find that the star ζ Oph, considered a runaway star, has a motion which can be traced back to the approximate centre of this shell with time scales that match.

Using Chevalier's (1974) relation between the energy of a SN explosion (E_o) in an uniform medium of density n_o, the time elapsed since the explosion (t) and the radius of the remnant (R) we obtain the following values of t:

	$E_c(10^{50}$ erg)	n_0 (cm^{-3})	R (pc)	$t(10^5$ yr)
1	3	10	20	4·7
2	3	30	20	11·3
3	3	100	20	29·7
4	3	100	15	11·7
5	3	30	15	4·5
6	10	10	20	2
7	10	30	20	4·8

Values of n_o in the third and fourth rows are rather high. If we then compare the other vaues of t with the age of the stars, it becomes evident that at least one supernova could have occurred in this region.

3. The origin of peculiarities

We suggest now a likely development of events which could apply to other similar regions *e.g.* I Orion association where Kutner *et al* (1977) find that the Barnard loop has interacted with the molecular cloud complexes. The Barnard loop, has been interpreted by Reynolds and Ogden (1978) as part of an expanding shell of a supernova remnant.

The stars of the Scorpio-Centaurus association were formed out of large cloud complexes by one or more possible ways (Kerr 1976, Thaddeus 1976). On an average, stars formed from clouds by some shock or compression mechanism would be found at distances from the cloud which increase with time, the youngest stars being closest to the cloud. If one of the massive stars evolves fast and explodes as a supernova, the material ejected could, in a short time (compared to the apparent motion of the stars relative to the cloud) reach the young stars at the ' shocked ' face of the cloud. This material, rich in heavy elements and slowed down to a few km s^{-1} by interaction with the cloud, could get accreted on to the surfaces of the stars at a rate depending on their magnetic field strengths.

3.1 *The Supernovae Remnant*

The pre-supernova models of massive stars upto the collapse stage (Weaver, Zimmerman and Woosley 1978) show large enhancements for elements like Ne, Mg, Si for a 15 $M_\odot$ star. Weaver, Zimmerman and Woosley (1978) point out that during the early collapse stage about 0·15 $M_\odot$ of ^{56}Ni and ^{54}Fe+2p are produced as the collapse proceeds; this is followed by explosive silicon burning in a shell during core expansion, resulting in the ejection of material. They indicate that a 25 $M_\odot$ star can eject about 6·2 $M_\odot$ of heavy (Z>2) elements while a 15 $M_\odot$ star can eject about 1·1 $M_\odot$. Thermonuclear reactions in such supernova envelopes, caused by an intense shockwave can produce heavy element enhancements (Schramm 1973; Truran 1967).

Chevalier (1974) has discussed the evolution of the pressure, the hydrogen number density, the gas velocity and the temperature of the remnants with time (from 2×10^4 yr to $2·5 \times 10^5$ yr) for an initial ambient density n_0 (cm^{-3}) and an initial magnetic field B_0 (gauss). For n_0=1 and $B_0 = 3 \times 10^{-6}$, the velocity and temperature of the shell, after it forms, decrease rapidly with time. For higher values, n_0=100 and $B_0 = 1 \times 10^{-5}$, the cooling in the shell is not impeded. The ionizing radiation even in the high density cases does not impede shell formation. If the remnant interacts with a dense cloud, the kinetic energy drops sharply and most of it goes into heating up the material. The interface between the high and low density regions remains sharp. This is seen to be true for nebulosities closer to the explosion in Fig. 1 and Fig. 2 and we also notice that some of the peculiar stars are lined up along these sharp edges.

3.2 *Acquisition of Anomalies*

The magnetic accretion process (Havnes and Conti 1971; Havnes 1974, 1975) seems to be a promising mechanism for the acquisition of anomalies on the surfaces of peculiar stars. The predictions of this theory agree well with the observed abundances for the Si Sr Cr Eu stars (Havnes 1974). Also, the increase in abundance of metals with temperature is seen at least for Fe, Cr, Mn (Adelman 1973). The very large observed overabundances of Eu could be produced by this mechanism if the medium around the star was well-enriched in it. In the present scenario, this could occur if the supernova exploded in a non-uniform medium with dense clouds around and the ejecta remaining as clumpy density and abundance inhomogeneities. The large over-abundances of elements with high ionization potentials (*e.g.* Hg and Pt) is a difficulty with this theory. However, such a difficulty could be overcome if the heavy elements in the supernova ejecta are locked up in grains. The possibility of grain formation in Supernovae ejecta is discussed in detail by Schramm (1978).

Havnes (1975) considers magnetic fields at or below the detectable limit and finds that even then, large overabundances could be produced, the times required for the Hg-Mn stars being, on the average, larger than that for the magnetic stars. If, in his models one uses a largely enriched environment, the time scales could be reduced by a factor of 10 or even 100. The detailed model requires magnetospheric radii for various ionized species stemming from an interaction of the kind suggested here.

3.3 *Rotation and Magnetic Fields*

There is no apparent reason to believe that the Ap and Am stars are born differently from normal A and B stars. However, the rotational velocities of normal and peculiar stars in clusters are different. Rajamohan (1978) has given arguments to show that all main sequence single stars in clusters which are normal are also fast rotators. A summary of the rotational behaviour of peculiar stars in clusters is given by Abt (1979). Abt (1979) discusses the frequency of occurrence and the slowing down with age of rotation of peculiar stars in open clusters. The rotational velocities of Ap (Si) stars decrease sharply with age, the Am stars showing a more gradual decrease. The Hg-Mn stars also suggest a decrease but the data are insufficient to be sure. Abt also finds that these objects on the average show increased frequencies with age after an intial threshold period which is shortest for the Ap (Si) stars (*i.e.* those with the strongest magnetic fields). Any theory of the origin of peculiar stars must also be able to account for this bimodal behaviour of rotation of cluster members. Synchronisation in closely spaced binary systems cannot completely account for the slow rotation of these different groups. Even for Am stars, where the binary frequency is as high as 80 per cent, tidal effects are incapable of synchronising the orbital and rotational periods within the main sequence lifetimes of these stars (Rajamohan and Venkatakrishnan 1979, 1980). They find that rotation alone as a criterion suggests that even amongst binaries we have a normal and a peculiar sequence. It would seem that the major angular momentum losses seem to occur for the peculiar sequence in the premain sequence phase of their evolution. The differences in the magnetic and the non-magnetic sequence of peculiar stars then, apparently reflects the initial differences in the magnetic field strengths.

Dolginov (1975) has proposed a mechanism (the ‘ battery effect ’) for enhancing the observable magnetic fields as well as the abundance anomalies of peculiar stars. Any patchy abundance anomalies on the surface of the star is capable of producing a large toroidal magnetic field. Circulation of matter in this field (*e.g.* due to slow meridional circulation or tidal interaction in binary systems) even with low velocities like 10^{-4} to 10^{-5} cm s^{-1} can produce poloidal fields comparable to the toroidal one within the star’s lifetime. The chemical anomaly is supported and amplified by this field. Thus, material accreted onto the surface of the star would accelerate the operation of this process, enhancing both the magnetic field and the abundance anomalies.

From arguments given by Mestel (1975) the magnetic accretion mechanism is reasonably efficient for slowing down early-type stars; an increase in the density of the environment will improve the efficiencies of capture and braking.

This linking-up of processes provides for a fairly efficient acquisition of anomalous abundances and magnetic braking. If angular momentum loss is associated with magnetic braking, older clusters should show more slow rotating and slower rotating peculiar stars than younger clusters. This is indeed seen to be true (Abt 1979).

4. Discussion and conclusions

We see good evidence for a supernova in Upper Scorpius, which accounts well for the origin of the peculiar stars there. Similar situations probably arise in I Orion

OB (Reynolds and Ogden 1978) and CMa R1 (Herbst and Assousa 1977) and probably other areas. Supernova induced star formation seems possible in young star clusters. Can a supernova trigger the formation of a star which subsequently accretes the enriched material? Perhaps this is possible provided a newly formed star, after reaching the main sequence has an enriched environment for at least 10^4 yr, this lower limit depending on the relative velocity between the star and the material, the density and the time taken to reach the main sequence, van Rensbergen, Hammerschlag-Hensberge and van den Heuvel (1978) suggest that spectral anomalies in peculiar stars may develop in the pre-main-sequence stage itself. Considering the significant convection which may be present during this stage, the peculiarity developed, if any would be small. It would seem that stars would necessarily have to accrete the enriched material after arrival on the main sequence. Stars formed out of the enriched material itself would have a more or less uniform distribution of elements throughout the star and hence would not show up the large patchy enhancements seen on the surface.

The diffusion process (Michaud 1975 and references therein) seems to account for large overabundances in a relatively short time ($\sim 10^4$ yr). The difficulty with this process is that it requires slow rotation to start with. Also, any convection or rapid rotation results in abundances not being enhanced. However, this process could be important in maintaining the anomalies at the surface, once they are acquired.

Though the large majority of peculiar stars are slow rotators, there are exceptions where the stars are fast rotators (*e.g.* CU Vir, 56 Ari) or exhibit instabilities such as pulsation (*e.g.* Przybylski's star, 21 Com). It is generally thought that rapid rotation leads to mixing and in such cases it is not clear how the abundance anomalies could persist on the surface of the star. If pulsations are laminar then anomalies on the surface could persist, whether they were initially produced by the diffusion mechanism or by the accretion mechanism.

We have considered enriched material being accreted onto early-type stars. Is enriched material seen in spectra of nebulae in the region described? Swings and Preston (1978) have obtained slit spectrograms of the Antares Nebula around the B companion of α Sco. They find that the nebula is [Fe II] rich; Fe II, Si II and Ti II are also present while [Ni II] and [Cu II] are identified here for the first time. Lines characteristic of low density nebulae like [O II], [N II] are absent. It would seem, therefore, that this material is enriched in the metals and possibly in the heavy elements. This is probably again the supernova material lingering around the vicinity of these stars. Reeves (1972) has shown that the heavy elements enriched by the supernova can spread very fast ($\sim 10^6$ yr) but would take more than 10^8 years to mix completely with the general background.

The scenario presented above seems to explain a wide variety of observed phenomena in young clusters and associations. We interpret the blue stragglers in clusters as stars that are much more magnetic than others. The magnetic fields provide a way for reducing the central temperature and hence increase its main sequence life time relative to a non-magnetic star of the same mass. Indeed Pendl and Seggewiss (1975)'s observations that the percentage of Ap stars among blue stragglers is very much larger than that in the field further supports the phenomenon outlined above.

Acknowledgements

We are grateful to Drs M. K. V. Bappu and O. Havnes for helpful discussions. We thank one of the referees for many useful comments and suggestions. We are indebted to Mr T. P. Prabhu for help in preparation of the figures.

References

Abt, H. A. 1979, *Astrophys. J.*, **230**,485.
Adelman, S. J. 1973, *Astrophys. J.*, **183**, 95.
Bertiau, F. C. 1958, *Astrophys. J.*, **128,** 533.
Blaauw, A. 1964, *A. Rev. Astr. Astrophys.*, **2**, 213.
Blake, J. B., Schramm, D. N., Kuchowicz, B. 1974, *Bull. Am. astr. Soc*, **6**, 282.
Catalano, F. A. 1975, in *IAU Coll. 32: Physics of Ap-Stars,* Eds W. W. Weiss, H. Jenkner and H. J. Wood, Universitatssternwarte Wien, p. 63.
Chevalier, R. A. 1974, *Astrophys. J.*, **188,** 501.
Cowley, C. R. 1975, *in IAU Coll. 32:* Physics *of Ap-Stars,* Eds W. W. Weiss, H. Jenkner and H. J, Wood, Universitatssternwarte Wien, p. **275.**
Dolginov, A. Z. 1975, in *IAU Coll. 32:* Physics *of Ap-Stars,* Eds W. W. Weiss, H. Jenkner and H. J. Wood, Universitatssternwarte Wien, p. 43.
Garrison, R. F. 1967, Astrophys. *J.*, **147,** 1003.
Guthrie, B. N. G. 1968, *Publ R. Obs. Edinburgh,* **6**, 145.
Havnes, O. 1974, *Astr. Astrophys.*, **32,** 161.
Havnes, O. 1975, in *IAU Coll. 32: Physics of Ap-Stars,* Eds W. W. Weiss, H. Jenkner and H. J. Wood, Universitatssternwarte Wien, p. 135.
Havnes, O., Conti, P. S. 1971, *Astr. Astrophys.*, **14,** 1.
Herbst, W., Assousa, G. E. 1977, *Astrophys. J.*, **217,** 473.
Hobbs, L. M. 1969, *Astrophys. J.*, **157,** 135.
Johnson, H. M. 1966, *Astrophys. J.*, **144,** 635.
Johnson, H. M. 1970, *Astrophys. J.*, **160,** 193.
Johnson, H. M. 1971, *Astrophys. J.*, **164,** 67.
Kerr, F. J. 1976, in *IAU in Symp. 75: Star Formation,* Eds T. De Jong and A. Maeder, D. Reidel, Dordrecht, p. 3.
Kuchowicz, B. 1975, in *IAU Coll. 32: Physics of Ap-Stars,* Eds W. W. Weiss, H. Jenkner and H. J. Wood, Universitatssternwarte Wien, p. 169.
Kutner, M. L., Tucker, K. D., Chin, G., Thaddeus, P. 1977, *Astrophys. J.*, **215,** 521.
Maeder, A. 1972, in *IAU Coll. 17: Age des Etoiles,* Eds G. Cayrel and A. M. Delplace, Paris-Meudon Observatory, p. XXIV-1.
McGee, R. X., Murray, J. D., Milton, J. A. 1963, *Austr. J. Phys.*, **16,**136.
Mestel, L. 1975, in *IAU Coll. 32: Physics of Ap-Stars,* Eds W. W. Weiss, H. Jenkner and H. J. Wood, Universitatssternwarte Wien, p. 1.
Michaud, G. 1970, *Astrophys. J.*, **160,** 641.
Michaud, G. 1975, in *IAU Coll. 32: Physics of Ap-Stars,* Eds W. W. Weiss, H. Jenkner and H. J. Wood, Universitatssternwarte Wien, p. 81.
Pendl, E. S., Seggeswiss, W. 1975, in *IAU Coll.* 32: *Physics of Ap-Stars,* Eds W. W. Weiss, H. Jenkner and H. J. Wood, Universitatssternwarte Wien, p. 357.
Rajamohan, R. 1976, *Pramana,* **7,**160.
Rajamohan, R. 1978, *Mon. Not. R. astr. Soc.*, **184,** 743.
Rajamohan, R., Venkatakrishnan, P. 1979, in *.IAU Symp. 88: Close Binary Stars,* Eds M. J. Plavec, D. M. Popper and R. K. Ulrich, D. Reidel, Dordrecht, p. 27.
Rajamohan, R., Venkatakrishnan, P. 1980, In preparation.
Reeves, H. 1972, *Astr. Astrophys.*, **19**, 215.
Reynolds, R. J., Ogden, P. M. 1978, *Wisconsin Astrophys,* No. 81.
Sancisi, R. 1974, in *IAU Symp. 60*: *Galactic Radio Astronomy,* Eds F. J. Kerr and S. C. Simonson, D. Reidel, Dordrecht, p. 115.
Sancisi, R., Van Woerden, H. 1970, *Astr. Astrophys.*, **5**, 135.

Schramm, D. N. 1973, in *Explosive Nucleosynthesis,* Eds D. N. Schramm and W. D. Arnett, University Texas Press, p. 84.

Schramm, D. N. 1978, in *Protostars and Planets,* Ed. T. Gehrels, Univ. of Arizona Press, p. 384.

Sivan, J. P. 1974, *Astr. Astrophys. Suppl. Ser.,* **16,** 163.

Slettebak, A. 1968, *Astrophys. J.,* **151,** 1043.

Swings, J. P., Preston, G. W. 1978, *Astrophys. J.,* **220,** 883.

Thaddeus, P. 1976, in *IAU Symp. 75: Star Formation,* Eds T. De Jong and A. Maeder, D. Reidel, Dordrecht, p. 37.

Truran, J. W. 1967, in *Supernovae and their Remnants,* Eds P. J. Brancazio and A. G. W. Cameron, Gordon and Breach, New York, p. 111.

van Rensbergen, W., Hammerschlag-Hensberge, G., van den Heuvel, E.P.J. 1978, *Astr. Astrophys.,* **64,**131.

Wallerstein, G. 1967, *Astrophys. Lett.,* **1,** 31.

Weaver, T. A., Zimmerman, G. B., Woosley, S. E. 1978, *Astrophys. J.,* **225,** 1021.

Wolff, S. C, Wolff, R. J. 1975, in *IAU Coll. 32: Physics of Ap-Stars,* Eds W. W. Weiss, H. Jenkner and H. J. Wood, Universitatssternwarte Wien, p. 503.

J. Astrophys. Astr. (1980) **1,** 165–175

Convective Instability in the Solar Envelope

D. Narasimha, S. K. Pandey* and S. M. Chitre *Tata Institute of Fundamental Research, Bombay 400005*

Received 1980 September 9; accepted 1980 November 5

Abstract. The characteristics of the most unstable fundamental mode and the first harmonic excited in the convection zone of a variety of solar envelope models are shown to be in reasonable agreement with the observed features of granulation and supergranulation.

Key words: sun—granulation—supergranulation—convective instability

1. Introduction

The existence of preferred length-scales in the solar atmosphere is a well established observational phenomenon which has a satisfactory explanation based on convective motions in the sub-photospheric layers of the Sun (Beckers and Canfield 1976). A considerable amount of effort has been invested in the investigation of polytropic atmospheres (Skumanich 1955; Böhm and Richter 1959). The fluid mechanical equations for an ideal gas with constant coefficients of viscosity and heat conductivity were set up by Spiegel (1965) for studying the convective instability. He found that for a layer of sufficiently small vertical extent the problem of compressible convection was essentially similar to the Boussinesq approximation. In order to understand the length scales and lifetimes observed on the solar surface Böhm (1963) calculated the linear growth rates of convective modes by perturbing the equilibrium solar convection zone model of Böhm-Vitense (1958). In this study the growth rates were found to increase monotonically with the wave number well past the observed cut-off and the size-distribution of the observed cells on the solar surface could not be satisfactorily explained by Böhm's calculations. Later Böhm (1976) attempted to include the effects of turbulent conductivity and viscosity on the convective modes. This investigation which was restricted to the problem of the onset of instability indicated that the fundamental mode with a wavelength of ~ 1500 km could be identified with the granulation by choosing the parameter α occurring in the expression for turbulent

* On leave of absence from Government Digvijai College, Rajnandgaon 491441

viscosity to be of order unity; for a larger value of α the first harmonic with a wavelength of ~ 30,000 km was identified with supergranulation.

Any reasonable theoretical model must account for the distinct peaks exhibited by the cellular structures observed on the solar surface. The work of Antia, Chitre and Pandey (1980; hereinafter referred to as Paper I) was an attempt to explain the observed motions on the solar surface in terms of linear convective modes excited in a realistic solar envelope model (Spruit 1977) by incorporating the mechanical and thermal effects of turbulence through the eddy transport coefficients (Unno 1967).

In the absence of a satisfactory theory of time-dependent compressible convection the effects of turbulence on the mean flow were parametrized through turbulent transport coefficients calculated in the framework of the mixing-length formalism of Böhm-Vitense (1958). Since in the convection zone the turbulent heat conductivity is orders of magnitude larger than the radiative conductivity, the turbulence is expected to have a significant influence on the growth rates both through the modulation of the heat flux and through the Reynolds stresses. This was indeed borne out by the detailed computations of Paper I and it was demonstrated that the most rapidly growing fundamental mode and the first harmonic are in reasonable accord with the scales of motion corresponding to granulation and supergranulation.

The stability analysis in the earlier calculation of Antia, Chitre and Pandey (1980) was performed under certain approximations. In order to make the problem tractable certain simplifying assumptions were introduced, like the neglect of the perturbation of the urbulent thermal conductivity in the expression for the convective flux and of the perturbation in the adiabatic term occurring in the superadiabatic temperature gradient. Moreover, the effect of variation of the degree of ionization in the convective elements was not taken into consideration. This situation is remedied in the present work to find that all these effects in combination lead to a damping of the convective growth rates. The turbulent Prandtl number which is a measure of the relative importance of turbulent viscosity over the turbulent heat conductivity is treated as a free parameter in the investigation. Thus, in order to bring the scales of the most unstable modes in accord with granulation and supergranulation it is necessary to lower the value of the Prandtl number compared to the value found appropriate in the earlier calculation reported in Paper I.

2. Governing equations

We adopt the usual hydrodynamical equations for the conservation of mass, momentum and energy as being applicable to a thermally conducting viscous fluid layer. In the notation of Paper I these equations take the following form:

$$\frac{\partial \rho}{\partial t} + \nabla \cdot (\rho \mathbf{v}) = 0,$$

$$\rho \frac{\partial \mathbf{v}}{\partial t} + \rho (\mathbf{v} \cdot \nabla) \mathbf{v} = -\nabla P + \rho \mathbf{g} - \tfrac{2}{3} \mu \nabla (\nabla \cdot \mathbf{v}) - \tfrac{2}{3} (\nabla \cdot \mathbf{v}) \nabla \mu + \nabla \cdot [\mu (\nabla \mathbf{v} + \mathbf{v} \nabla)],$$

$$\rho C_P \left[\frac{\partial T}{\partial t} + (\mathbf{v} \cdot \nabla) T - \nabla_{ad} \frac{T}{P} \left(\frac{\partial P}{\partial t} + (\mathbf{v} \cdot \nabla) P \right) \right] = -\nabla \cdot \mathbf{F} + \Phi,$$

where Φ is the rate of viscous dissipation given by

$$\Phi = \tfrac{1}{2}\,\mu\,(\nabla \mathbf{v} + \mathbf{v}\nabla)\cdot(\nabla \mathbf{v} + \mathbf{v}\nabla) - \tfrac{2}{3}\,\mu\,(\nabla\cdot\mathbf{v})^2.$$

We treat the medium as a perfect gas undergoing ionization and we include the contribution to the pressure due to radiation. In the foregoing equations μ is the coefficient of dynamic viscosity, C_P the specific heat at constant pressure, ∇_{ad} is the logarithmic adiabatic gradient $(\partial \ln T/\partial \ln P)_{ad}$ and F is the total heat flux which is the sum of the radiative flux, F^R and the convective flux, F^C.For the computation of the radiative flux we use the Eddington approximation (Ando and Osaki 1975) and write

$$\mathbf{F}^R = -\frac{4}{3\kappa\rho}\nabla J,$$

where

$$J = \sigma T^4 + \frac{C_P}{4\kappa}\left\{\left[\frac{\partial T}{\partial t} + (\mathbf{v}\cdot\nabla)\,T\right] - \nabla_{ad}\frac{T}{P}\left[\frac{\partial P}{\partial t} + (\mathbf{v}\cdot\nabla)\,P\right]\right\}$$

is the intensity of radiation and κ the mean Rosseland opacity. The convective flux is computed in the usual mixing length formalism by writing

$$\mathbf{F}^C = -K_t\left[\nabla T - \nabla_{ad}\frac{T}{P}\nabla P\right],$$

where the coefficient of turbulent heat conductivity is taken to be of the form

$$K_t = \alpha\,\rho\,C_P\,WL.$$

Here α is the efficiency factor which is of order unity, L is the mixing length and the mean convective velocity W is given by

$$W = \left[\beta\,\frac{g}{H_P}\,Q\,L^2\,(\nabla - \nabla_{ad})\right]^{1/2}.$$

H_P is the pressure scale-height, β represents the effect of viscous braking on the convective elements and the factor

$$Q = -\frac{T}{\rho}\left(\frac{\partial\rho}{\partial T}\right)_P$$

takes into account the variation of the degree of ionization in the moving element. The turbulent dynamic viscosity is chosen to have the expression,

$$\mu_t = P_t\,\alpha\,\rho\,WL,$$

where the turbulent Prandtl number P_t is treated as a free parameter in the present investigation.

We have adopted a number of equilibrium solar envelope models in order to study the instability of convective modes. The requirement for the models is that the physical run of variables should match with the interior solutions and they should also be consistent with the solar evolution generating the present radius and luminosity of the sun. In the solar envelope model due to Spruit (1977) the mixing length parameters take the form:

$$\alpha = \tfrac{1}{2},\ \beta = \tfrac{1}{8},\ Q = 1 \text{ and } L = z + 459 \text{ km},$$

z measured downwards from the top of the convection zone. We have also generated a model with the above set of parameters for $Q \neq 1$. Moreover, we have computed the solar convection zone models with the following sets of mixing-length parameters:

$$\alpha = \tfrac{1}{2},\ \beta = \tfrac{1}{4},\ Q \neq 1,\ L = 1{\cdot}5\ H_P,$$

$$\alpha = \tfrac{1}{2},\ \beta = \tfrac{1}{4},\ Q \neq 1,\ L = H_\rho\ (H_\rho, \text{ density scale-height}),$$

$$\alpha = \tfrac{1}{2}, \beta = \tfrac{1}{8},\ Q \neq 1, L = 1{\cdot}25\ H_\rho.$$

For the atmosphere we have adopted the empirical temperature-optical depth (T—τ) relationship given by Vernazza, Avrett and Loceser (1976), with the upper boundary chosen a little below the temperature minimum where $\tau = 7\times10^{-4}$. The lower boundary for the layer is fixed at a depth of $3{\cdot}3 \times 10^5$ km. There is a penetration of convective elements into these overlying stable layers. Clearly the velocity does not drop abruptly to zero at the boundary of the convection zone ($\tau \simeq 1$), and there is an overshoot of convective motion into the bounding regions. The height variation of the convective velocity field given by Canfield (1976) suggests that the amplitude of granular velocities is an exponentially decreasing function with a scale height ~150 km. In order to estimate the coefficient of dynamic viscosity in the atmosphere we assume a Kolmogoroff spectrum with turbulent velocities proportional to one-third power of the scale-length. We ensure the continuity of the viscosity coefficient across the interface between the convection zone and the atmosphere. After taking into account the almost exponential decrease of density with height, we find the viscosity coefficient drops exponentially with a scale height of approximately 25 km.

We adopt the spherical geometry and assume that any physical quantity can be expressed as

$$f(r, \theta, \phi, t) = f_0(r) + f_1(r)\ Y_l^m(\theta, \phi) \exp(\omega t),$$

where the subscripts 0 and 1 respectively refer to the equilibrium and perturbed quantities, (r, q, ϕ) are the spherical polar coordinates with the radial coordinate r measured from the centre of the Sun, $Y_l^m(\theta, \phi)$ are the spherical harmonics and ω is the growth rate. We linearize the governing equations in the usual manner to get the following system of equations:

$$\omega\, \rho_1 + \nabla \cdot (\rho_0\, \mathbf{v}) = 0,$$

$$\omega\, \rho_0\, \mathbf{v} = \rho_1\, \mathbf{g} - \nabla P_1 - \tfrac{2}{3}\, \mu_t\, \nabla(\nabla \cdot \mathbf{v}) - \tfrac{2}{3}\,(\nabla \cdot \mathbf{v})\, \nabla \mu_t + \nabla \cdot [\mu_t\, (\nabla\, \mathbf{v} + \mathbf{v}\, \nabla)],$$

$$\rho_0\, C_P \left[\omega\, T_1 + (\mathbf{v} \cdot \nabla) T_0 - \nabla_{ad} \frac{T_0}{P_0}(\omega\, P_1 + (\mathbf{v} \cdot \nabla)\, P_0)\right] = -\nabla \cdot \mathbf{F}_1,$$

$$\mathbf{F}_1 = -\frac{4}{3\kappa_0\, \rho_0}\, \nabla J_1 - \mathbf{F}_0^R \frac{\kappa_1}{\kappa_0} - \mathbf{F}_0^R \frac{\rho_1}{\rho_0}$$

$$-K_{t0}\left(\nabla T_1 - \nabla_{ad} \frac{T_0}{P_0}\, \nabla P_1 - \left(\nabla_{ad} \frac{T}{P}\right)_1 \nabla P_0\right) - K_{t1}\left(\nabla T_c - \nabla_{ad} \frac{T_c}{P_0}\, \nabla\, P_0\right),$$

where

$$J_1 = 4\sigma T_0^3\, T_1 + \frac{C_P}{4\kappa_0}\left[\omega\, T_1 + (\mathbf{v} \cdot \nabla)\, T_0 - \nabla_{ad} \frac{T_0}{P_0}\, (\omega\, P_1 + (\mathbf{v} \cdot \nabla)\, P_0)\right],$$

$$\kappa_1 = \left(\frac{\partial \kappa}{\partial P}\right)_T P_1 + \left(\frac{\partial \kappa}{\partial T}\right)_P T_1,$$

$$\rho_1 = \left(\frac{\partial \rho}{\partial P}\right)_T P_1 + \left(\frac{\partial \rho}{\partial T}\right)_P T_1$$

Here

$$\mathbf{F}_0^R = -\frac{16\sigma T_0^3}{3\kappa_0\, \rho_0}\, \nabla\, T_0$$

is the radiative flux in the steady state and the velocity v is assumed to have the form,

$$\mathbf{v} = \left(v_r\, (r),\, v_h\, (r) \frac{\partial}{\partial \theta},\, v_h\, (r)\, \frac{1}{\sin\, \theta}\, \frac{\partial}{\partial \phi}\right) Y^m\, (\theta, \phi)\, \exp\, (\omega t).$$

In deriving these equations we have incorporated the perturbation in the turbulent heat conductivity K_t including the variation in the specific heat at constant pressure, C_P, the perturbation in the adiabatic term ($\nabla_{ad}\ T/P$) occurring in the superadiabatic temperature gradient and also included the factor Q in the expression for the convective velocity arising from the variation of the degree of ionization. We have, however, neglected the effect due to viscous dissipation in the energy equation which is liable to influence to certain extent the length scales of most unstable modes, especially the higher harmonics.

The total system of equations governing the perturbations is of the sixth order and we therefore require three boundary conditions at each interface. We have emphasized in Paper I that the exact conditions are not very important for convective growth rates since the boundary conditions are applied a little beyond the convection zone where in any case the amplitude of the modes falls off very rapidly. Consequently the convective growth rates turn out to be insensitive to the particular choice of the boundary conditions. For the purpose of the present analysis we have selected free boundary conditions, that is, the Lagrangian perturbation in the pressure and the tangential components of the viscous stress tensor vanish at the surface to give

$$\omega P_1 - g \rho_0 v_r = 0,$$

$$v_r + r \frac{dv_h}{dr} - v_h = 0.$$

Furthermore, we impose the thermal boundary condition which demands that the radiation does not come in from infinity, and this gives

$$\omega F_r - \frac{2 F_0^R}{r} v_r - \frac{J_1 F_0^R \omega}{\sigma T_0^4} - \frac{4 F_0^R v_r}{T_0} \frac{d T_0}{dr} = 0.$$

The boundary conditions at the lower interface are found to have no effect whatsoever on the convective growth rates since the eigenfunctions decay exponentially with depth in these regions. We therefore adopt the rigid conditions with no momentum flux and with the temperature maintained constant at the interface; that is, we take

$v_r = 0$, $v_h = 0$ and $T_1 = 0$.

The numerical scheme for solving this generalised eigenvalue problem is the same as that adopted in Paper I.

3. Numerical results and discussion

We attempt to account for the observed motions on the solar surface in terms of linear convective modes excited in the subphotospheric convection zone. For this purpose we shall first compute a variety of solar envelope models by integrating the standard equations of stellar structure. The mixing-length theory first developed, in the context of stellar structure, by Böhm-Vitense (1958) still remains the only viable method for treating convective transport in the model calculations. In so far as the choice of the mixing-length itself is concerned there is no compelling reason why it should be a constant multiple of the pressure scale height or the density scale height, or should be proportional to the distance from the boundary of the convection zone. We have therefore selected different sets of mixing-length parameters and the characteristic physical values for five models, I—V are summarised in Table 1. It is clear that at the base of the convection zone all the models essentially converge

Table 1. Physical parameters for various models, ρ_b, T_b denote the density and temperature at the base of the convection zone measured from the level $\tau = 1$ and $V_{\max}$ the maximum convective velocity km s^{-1}. L is the mixing-length, H_p, the pressure scale height and H_ρ the density scale height. The parameter $Q \neq 1$ except in Spruit's model (IV).

Model	Mixing-length parameters α	β	L	ρ_b (g cm^{-3})	T_b (K)	Z_0 (km)	$V_{\max}$ (km s^{-1})
I	1/2	1/4	$1{\cdot}5\ H_p$	0·234	$2{\cdot}178 \times 10^6$	$1{\cdot}90 \times 10^5$	3·19
II	1/2	1/4	H_ρ	0·226	$2{\cdot}174 \times 10^6$	$1{\cdot}86 \times 10^5$	3·61
III	1/2	1/8	$1{\cdot}25\ H_\rho$	0·243	$2{\cdot}180 \times 10^6$	$1{\cdot}90 \times 10^5$	3·06
IV	1/4	1/8	$z + 459$ km $Q = 1$ (Spruit 1977)	0·228	$2{\cdot}179 \times 10^6$	$1{\cdot}92 \times 10^5$	3·85
V	1/4	1/8	$z + 459$ km	0·260	$2{\cdot}180 \times 10^6$	$1{\cdot}96 \times 10^5$	3·85

Table 2. Approximate *e*-folding times and preferred horizontal wavelengths corresponding to the most unstable fundamental mode (*C*1) and the first harmonic (*C*2) for a variety of models with different mixing-length parameters over a range of turbulent Prandtl numbers P_t.

Model	Mixing-length parameters α	β	L	P_t	Fundamental mode (*C*1) *e*-folding time (min)	Fundamental mode (*C*1) Preferred horizontal wave-length (km)	First harmonic (*C*2) *e*-folding time (h)	First harmonic (*C*2) Preferred horizontal wavelength (km)
I	1/2	1/4	$1{\cdot}5\ H_p$	1/10	5·5	1900	0·4	2900
				1/4	6·3	2150	0·6	3400
				1/3	6·7	2300	0·8	4400
				1	9·3	2900	4·1	8000
				$1\frac{1}{3}$	11·0	3100	39·0	11500
II	1/2	1/4	H_ρ	1/10	5·3	1900	0·3	2500
				1/4	6·0	2200	0·4	3150
				1/3	6·2	2300	0·5	3550
				1	9·0	2900	2·1	6600
				$1\frac{1}{2}$	10·7	3300	40·1	9100
III	1/2	1/8	$1{\cdot}25\ H_\rho$	1/10	5·9	2100	0·3	2800
				1/4	6·4	2250	0·5	3250
				1/3	6·8	2450	0·6	4150
				1	9·7	3000	3·1	7400
				$1\frac{1}{3}$	11·0	3200	21·0	8800
IV	1/4 $Q = 1$	1/8 (Spruit 1977)	$z + 459$ km	1/10	6·0	1900	0·6	3100
				1/4	7·0	2200	1·5	4800
				1/3	7·5	2350	2·8	5500
				1/2	8·6	2450	15·0	9000
				1	12·0	3100	—	—
V	1/4	1/8	$z + 459$ km	1/10	7·0	1800	1·2	3700
				1/4	8·7	2200	7·7	8400
				1/3	9·6	2400	32·0	11000
				1	19·0	3400	—	—

to the same radiative interior solution. Having obtained the run of the equilibrium physical quantities with depth, the system of linearized equations is solved with the boundary conditions described earlier. The real growth rate ω is then computed as a function of the angular node number l which is related to the wavelength

$$\lambda = \frac{2\pi}{k_H} = \frac{2\pi R_\odot}{[l\,(l+1)]^{1/2}},$$

k_H being the horizontal wave number and R the solar radius. For a given value of l there exists a series of eigenvalues ω, which are classified according to the number of velocity nodes in the radial direction. Thus the fundamental mode ($C1$) which has the largest eigenvalue has no node in the radial velocity component, while the successive harmonics, $C2$, $C3$,.. have one extra node in the radial direction. It is of interest to enquire whether the resulting unstable convective modes for these models exhibit preferred length scales and time scales which are in some reasonable accord with the observed features on the solar surface.

In Table 2 we have summarised for various envelope models the time scales and scales of motion corresponding to the most unstable fundamental mode ($C1$) and the first harmonic ($C2$) for a number of turbulent Prandtl numbers, 0.1 P_t, 1.5. The *e*-folding times and the horizontal wavelengths for the maximally growing fundamental mode lie in the range 5–19 min and 1,900–3,400 km respectively over the range of the turbulent Prandtl numbers considered. The fundamental mode is evidently not very sensitive to the variation in different parameters, but the first harmonic is critically affected both by the choice of the mixing-length parameters and the value of the turbulent Prandtl number. The effect of turbulent viscosity on the convective growth rates of $C1$ and $C2$ modes is displayed in Fig. 1. Here we have shown for a typical solar envelope model with the mixing-length parameters, $\alpha = \frac{1}{2}$, $\beta = \frac{1}{4}$, L=l·5 H_P, the growth rate ω (in s^{-1}) as a function of the horizontal wave number for four values of the turbulent Prandtl number $P_t = 0, \frac{1}{3}, 1, 1\frac{1}{3}$. It is readily seen that for each value of the Prandtl number there is a maximal growth rate, and the damping influence of turbulent viscosity is clearly seen from the trend of the preferred length scales as well as the associated *e*-folding times to increase with P_t. For non-zero values of P_t, the maximum in the growth rates is found to shift to lower *l's for* successive harmonics, but for the inviscid case (P_t =0) all the modes peak at about the same value of $l(\lesssim 3000)$. Thus, without the inclusion of viscosity in the problem it would not be possible to produce different scales of motion observed on the solar surface. An important effect brought about by viscosity is that the modes are highly damped for higher values of the harmonic number and for a given value of l only the first few harmonics turn out to be unstable.

An inspection of Table 2 immediately shows that for each of the models which we have investigated there exists a value of the turbulent Prandtl number for which the time scales and the associated wavelengths of the most unstable fundamental mode and the first harmonic can be made to agree reasonably well with the observed life-times and cell-sizes of granulation and supergranulation. Thus, for models I—III the choice of $P_t \sim 1\frac{1}{3}$ yields, for the most unstable $C1$ mode, time scale ~10 min and length scale ~ 3000 km which are fairly close to the characteristic scales corresponding to granulation. The time scale for the most rapidly growing $C2$ mode, ~30 hrs, is in accordance with the typical observed lifetime of supergranules, but the related wavelength tends to be on the lower side of the usually quoted diameters of super-

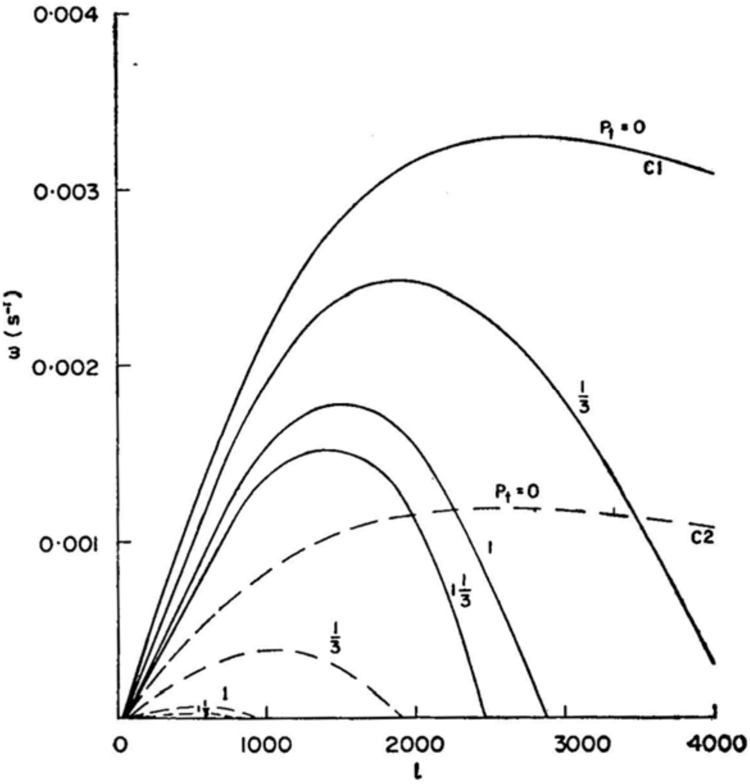

Figure 1. The growth rate ω (s^{-1}) of the fundamental mode ($C1$), shown by the full curves and the first harmonics ($C2$) shown by the broken curves, is displayed against the horizontal harmonic number l for a range of turbulent Prandtl numbers P_t = 0,1/3,1, 4/3.

granules ranging upwards of 10,000 km with a peak around 30,000 km. In models IV and V the value of $P_t \gtrsim \frac{1}{3}$ produces satisfactory lifetimes for granulation and supergranulation. But, while the preferred wavelength for the fundamental mode comes close to the granular cell-size, the corresponding wavelength for the first harmonic is somewhat on the shorter side.

In the earlier work of Antia, Chitre and Pandey (1980), with the choice of the turbulent Prandtl number P_t~1·5 the *e*-folding time and the associated wavelength for the most unstable fundamental mode and the first harmonic turned out to be not too far from the observed features of granulation and supergranulation respectively. The computation was based on Spruit's solar envelope model and there were some approximations introduced to make the calculation tractable. This situation has been remedied and the present investigation incorporates the additional terms arising from the perturbation of the turbulent heat conductivity, K_t and the adiabatic gradient, (∇_{ad} T/P). We have also taken account of the Q-factor in the mean convective velocity which was taken to be unity in the previous calculation. With the change in the degree of ionization in the moving convective elements, the value of Q varies between 1 and 2 and this leads to a damping of the convective modes because of the effective increase in the magnitude of turbulent heat conductivity. There is another difference in the way the viscosity is treated in the overlying atmosphere. In the present study we have taken a Kolmogoroff spectrum for the penetrative motion with turbulent velocities being proportional to one-third power of the scale length and also assumed a velocity profile from the observations of the motion at various heights. With the near-exponential decrease of the density in the atmospheric layers, the effective viscosity scale height in the regions above the convection zone turns out to be ~25 km, while in the earlier work we had assumed the viscosity scale height to be 10 km. The larger viscosity scale height has a more pronounced stabilizing effect on the convective modes, as in this case the effect of viscous damping in the overlying layers persists to a larger extent. All these effects combine to lower the resulting convective growth rates.

The influence of the new terms incorporated in the present investigation is shown ($\alpha = \frac{1}{2}$, $\beta = \frac{1}{4}$, $L = 2\ H_P$, $P_t = \frac{1}{4}$.) Case (a) corresponds to the earlier calculation of Antia, Chitre and Pandey (1980) where the perturbation in the turbulent conductivity, K_t and the perturbation of ($\nabla_{ad}\ T/P$) in the superadiabatic temperature gradient term are neglected. The dimensionless convective growth rates for $C1$ and $C2$ modes are displayed for the horizontal harmonic number l = 100, 500, 1000, 1500, 2000 and 3000 with the Q-factor taken to be unity. In case (b) the perturbations in K_t and ($\nabla_{ad}\ T/P$) are fully included, but the Q-factor is again set to unity, to find that the growth rates are lowered over those in case (a). In case (c) the perturbations in K_t and ($\nabla_{ad}\ T/P$) as well as the variation of the Q-factor are taken into account. The resulting growth rates are seen to be drastically reduced and in order to bring the time scales of the most unstable modes close to the observed solar motions it becomes necessary to lower the value of the turbulent Prandtl number over the corresponding value (P_t ~1·5) found suitable in Paper 1.

We cannot show an overwhelming preference for any particular solar envelope model from the computed eigenvalue spectrum of the convective modes. In fact, it turns out that for a given set of parameters α and β, it is always possible to construct an envelope model which, for a selected value of the mixing-length L and the turbulent Prandtl number gives convective modes in reasonable accord with the characteristic features associated with the observed solar velocity fields. However,

Table 3. Convective growth rates in units of $(3263\ \mathrm{s})^{-1}$ corresponding to the fundamental mode and the first harmonic for the solar envelope model with the mixing-length parameters: α =1/2. ß = 1/4, L/H_p=2·0 are listed for various values of the horizontal harmonic number.

(a)	$Q=1$;	$(K_t)_1$,	$(\nabla_{ad}\ T/P)_1$ are suppressed			
	l = 100	500	1000	1500	2000	3000
$C1$	0·34	3·23	5·79	6·76	6·50	3·52
$C2$	0·08	0·81	1·16	0·77	—	—
(b)	$Q=1$;	$(K_t)_1$,	$(\nabla_{ad}\ T/P)_1$ are included			
	l = 100	500	1000	1500	2000	3000
$C1$	0·25	2·59	4·81	5·75	5·61	3·04
$C2$	0·03	0·50	0·76	0·39	—	—
(c)	$Q\neq1$;	$(K_t)_1$,	$(\nabla_{ad}\ T/P)_1$ are included			
	l=100	500	1000	1500	2000	3000
$C1$	0·16	1·83	3·52	4·13	3·79	1·05
$C2$	0·01	0·20	0·12	—	—	—

any consistent solar envelope model should yield, for the same choice of the turbulent Prandtl number, not only the spectrum of most unstable convective modes corresponding to granulation and supergranulation, but should also reproduce the acoustic modes with the characteristics of five minute oscillations. We hope to discuss this problem in a separate communication.

It should be stressed that we have examined the instability of convective modes in the framework of the linearized theory. The linear stability analysis yields the growth rate indicating the manner in which a perturbation begins to grow from an equilibrium state, while the non-linear effects can alone limit the growing amplitudes of these instabilities. The *e*-folding time given by the inverse of the growth rate can only suggest the approximate time scale over which the instability grows until the effects neglected in the linear formulation become important. The lifetime of a granule must necessarily be determined by incorporating the nonlinear effects.

In conclusion, it may be stated that considering the uncertainties in observations as well as in the mixing-length formalism, our numerical results provide a reasonable explanation for granulation and supergranulation in terms of the unstable fundamental mode and the first harmonic excited in the solar convection zone. It should, however, be stressed that we have ignored potentially significant effects in our calculation like the contribution of the turbulent pressure and the presence of the turbulent energy and its dissipation into heat in the equation for conservation of energy. The neglect of these effects is liable to influence the growth rates at larger values of l especially for the higher harmonics. This, along with the extension into the non-linear regime will, hopefully, improve the agreement of the unstable convective modes with observed velocity fields on the solar surface.

Acknowledgement

It is a pleasure to thank Dr H. M. Antia for valuable correspondence.

References

Ando, H., Osaki, Y. 1975, *Publ. astr. Soc. Japan,* **27**, 581.
Antia, H. M., Chitre, S. M., Pandey, S. K. 1980, *Solar Phys.,* (in press).
Beckers, J. M., Canfield, R. C. 1976, in *CNRS Coll. 250: Physique des Mouvements dans les Atmospheres Stellaires,* Eds R. Cayrel and M. Steinberg, CNRS, Paris.
Böhm, K. H. 1963, *Astrophys. J.,* **137**, 881.
Böhm, K. H. 1976, in *CNRS Coll. 250: Physique des Mouvements dans Les Atmospheres Stellaires,* Eds R. Cayrel and M. Steinberg, CNRS, Paris.
Böhm K. H., Richter, E. 1959, *Z. Astrophys.,* **48**, 231.
Böhm-Vitense, E. 1958, *Z. Astrophys.,* **46**,108.
Canfield, R. C. 1976, *Solar Phys.,* **50**, 239.
Skumanich, A. 1955, *Astrophys. J.,* **121,** 408.
Spiegel, E. A. 1965, *Astrophys. J.,* **141,** 1068.
Spruit, H. C. 1977, *PhD thesis,* Utrecht.
Unno, W. 1967, *Publ. astr. Soc. Japan,* **19**,140.
Vernazza, J. E., Avrett, E. H., Loceser, R. 1976, *Astrophys. J. Suppl. Ser.,* **30**, 1.

J. Astrohys. Astr. (1980) **1,** 177–187

NGC 4650 A: A Nearly Edge-on Ring Galaxy?

S. Laustsen *Astronomisk Institut, Aarhus Universitet, DK-8000 Aarhus C., Denmark*
R. M. West *European Southern Observatory, Karl-Schwarzchild-Strasse 2, D-8046 Garching bei München, F.R.G.*

Received 1980 September 22; accepted 1980 October 16

Abstract. The peculiar galaxy NGC 4650 A ($\alpha = 12^{h}\ 42^{m}.\ 1$; = δ—40° 26′; 1950·0) has been studied by means of direct and spectral observations with the ESO 3·6-m telescope. It is interpreted as a prolate, elliptical galaxy surrounded by a warped ring of H II regions, dust and stars. The distance is 47 Mpc (H_0=55 km s^{-1} Mpc^{-1}). The ring is seen nearly edge-on (inclination 85°) and it rotates. It has a diameter of about 21 kpc and is bluer than the elliptical galaxy for which the (M/L_V) ratio is ~12 in solar units. The observed configuration may be the result of interaction with the nearby galaxy, NGC 4650.

Key words: elliptical galaxy—prolate galaxy—ring galaxy—H II regions

1. Introduction

The peculiar galaxy NGC 4650 A (α_{1950} = $12^{h}\ 42^{m}\ 4^{s}{\cdot}6$; δ_{1950} = –40° 26′ 27″) is a member of the Centaurus group of galaxies, sometimes called the Centaurus association or the Centaurus chain of galaxies; some 10 galaxies are lined up in the sky. The central part of the chain is shown in Fig. 1. NGC 4650 A presents itself (Fig. 2) as an object that consists of two, quite different components. The central component is bright and compact and appears as an elliptical galaxy of axial ratio ~3, *i.e.* E6-E7 in the Hubble classification; the major axis is oriented in the NE-SW direction. We shall refer to this as the E component. The outer component is fainter and looks like an amorphous disc with a ring or spiral arms seen almost edge-on and of which the west side is seen in absorption against the bright E component; we call this the S component. It is extended in the NW-SE direction, approximately at right angles to the major axis of the E component.

A first study of the Centaurus group and of NGC 4650 A in particular was made by Sersic (1967) who at the time concluded that it had an active nucleus. In a later study Sérsic and Agüero (1972) obtained spectra of NGC 4650 A showing the H and K lines of Ca II in absorption and the λl3727 line of [O II] in emission. They determined a radial velocity curve of the S component which within the accuracy is confirmed by our measurements. NGC 4650 A is not in the *Atlas of Peculiar Galaxies* by Arp (1966) but it was included by Sérsic together with other galaxies of the Centaurus group in his *Catalogue of Southern Galaxies* (1968).

As will be seen later, we derive for NGC 4650 A a distance of 47 Mpc, *i.e.* a scale of 227 pc per arcsec. This scale will be used throughout the following discussion.

2. Observations

NGC 4650 A was included in the list of peculiar objects for direct photography during the test period of the ESO 3·6-m telescope in 1977, and spectra were obtained with the same instrument in 1978. The observational material is listed in Table 1.

Five direct plates were obtained during moderately good seeing at the prime focus equipped with a Gascoigne one-element corrector. The scale is 18″·9 per mm. Four of these were in the blue (IIIa-J + GG385) with exposure times from 5–90 minutes, while one was in the red (IIIa-F+RG630) with an exposure time of 53 minutes. The appearance of the galaxy on these plates will be discussed in Section 3.

Four spectra were obtained with the Boller and Chivens spectrograph equipped with a Carnegie image tube at the Cassegrain focus of the 3·6-m telescope. The slit positions are shown in Fig. 3 and radial velocities were measured (with the ESO Grant machine in Geneva) at the positions indicated (A—O). The mean dispersion was 114 Å mm^{-1}. Fifteen lines of the helium-argon comparison spectrum were measured (3727–5500 Å) and a polynomial of third order was fitted to give a rms value of ± 0·20 to ± 0·25 Å.

Emission lines were observed in all positions A—O and absorption lines were seen in the positions C, E, F, G, H, J and K. The spectral characteristics are discussed in Section 4.

Table 1. Observational material

Plate No.	Date	Emulsion	Filter	Exposure time	Seeing (arcsec)
Direct plates					
214	1977 Jan 17	IIIa-J	GG385	60m	1·7
284	1977 Jan 24	IIIa-J	GG385	5m	1·3
285	1977 Jan 24	IIIa-J	GG385	90m	1·3
1391	1978 Mar 4	IIIa-J	GG385	20m	1·2
1392	1978 Mar 4	IIIa-F	RG630	53m	1·2
Spectral plates					
B 158	1978 Jan 9	IIIa-J		35m	1·5
B 166	1978 Jan 10	IIIa-J		30m	1·5
B 182	1978 Jan 12	IIIa-J		40m	1·0
B 191	1978 Jan 13	IIIa-J		30m	1·5

Figure 1. The central part of the Centaurus chain of galaxies. The objects are: (1) NGC 4650 A, (2) companion galaxy to NGC 4650, (3) NGC 4650, (4) ESO 322-IG64 (Holmberg *et al.* 1974). North is up and east to the left; the scale is indicated by the 2 arcmin bar. Reproduced from a 90 min IIIa-J+GG385 plate, obtained at the prime focus of the ESO 3.6-m telescope.

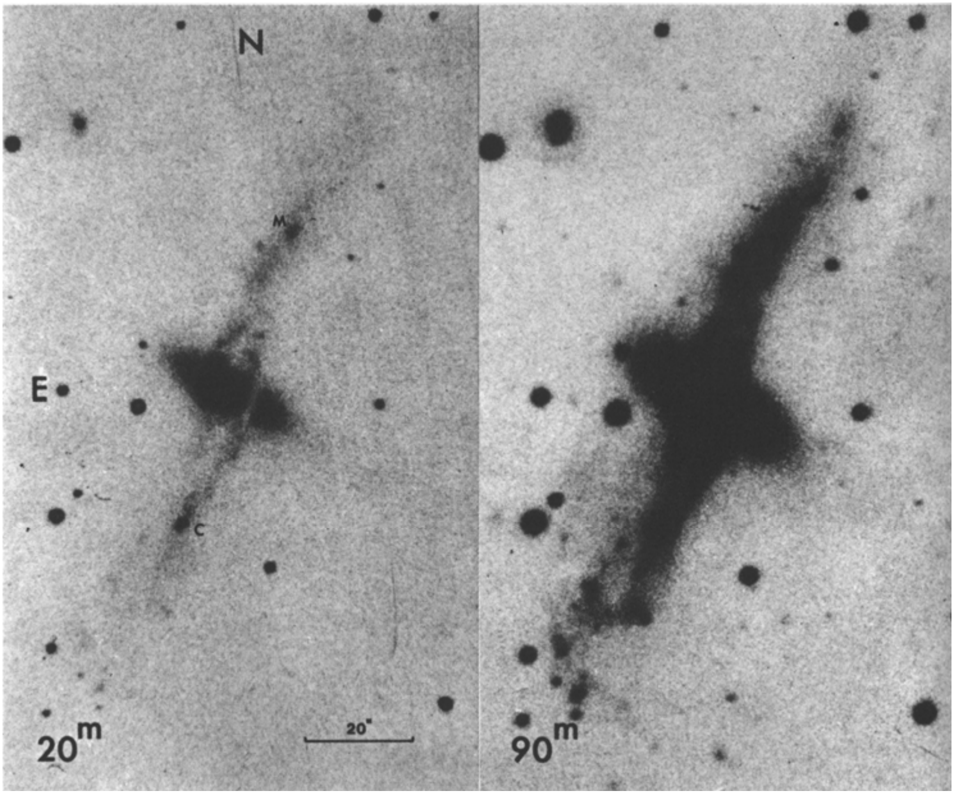

Figure 2. NGC 4650 A, reproduced from a 20 min (left-hand side) and a 90 min (right-hand side) IIIa-J+GG385 plate obtained with the 3.6-m telescope and a Gascoigne corrector in the prime focus. Two knots, C and M are indicated.

3. Morphology and spatial configuration

Concerning the nature of the present object, we can *a priori* list a number of possibilities:

(1) A spiral galaxy with a prolate central bulge.
(2) A collision between a spiral galaxy and an elliptical galaxy.
(3) A ring galaxy.
(4) Star formation due to a collision between a galaxy and an intergalactic cloud.
(5) Ejection of matter from an elliptical galaxy.
(6) Two widely separated galaxies in the same line of sight but with no physical connection.

The appearance of NGC 4650 A on the available direct plates will now be described in some detail. In particular, we shall discuss the morphology and the spatial configuration of the object and try to interpret its probable nature among the possibilities listed above:

5^m *exposure plate:* the nucleus is bright and circular in shape with diameter 3″, or ~700 pc. A search for a second nucleus, on this as well as on other plates, was negative. This may be taken as one reason to assume that we are indeed faced with one object only, and not with a superposition of two galaxies. This is an argument against the possibilities (2) and (6) above. The inner part of the elliptical E component is just visible and the shading by absorption in the S component can be seen as close as 3″ SW of the centre.

20^m *exposure plate:* Figure 2 (left-hand side). The nucleus or central bulge is larger and has become elongated with dimensions 6″ × 4″. The E component is extended to 30″ along the major axis. The S component is clearly visible with its two dense knots in positions C and M. The most striking feature here is the band of absorption due to the S component crossing the E component perpendicularly to its major axis. The band has sharp edges and covers the range from 3″·0 to 6″·0 off the centre on the major axis of the E component on the SW side. The band is about 700 pc wide. On the NE side of the centre we find in the same range, 3″·0 to 6″·0 from the centre, a corresponding band of increased brightness crossing the major axis of the E component; this is particularly obvious when fitting a smooth curve to the profile of a microphotometer tracing along the major axis. From this observation we draw two conclusions. First, the E component has, as would be expected, little or no absorbing material, contrary to the S component. Second, when viewed along the line of sight the E component must be located within the S component. We can therefore assume with good confidence that the two components belong to the same object and have a common centre, *i.e.* we can exclude possibility (6) above.

60^m *exposure plate:* The absorption band has become sharper and a bit narrower, slightly over 2″ or about 500 pc wide. The band of increased brightness on the opposite side is clearly visible. The knot C is well defined and elongated with the dimensions 3″ × 1″·5 or 700 pc×350 pc.

53^m *exposure plate:* This plate exposed in red light was cut short due to technical difficulties, but in the comparison with the 20^m exposure blue plate it clearly demontrates the difference in colour; the S component is considerably bluer than the E component.

90^m *exposure plate:* Figure 2 (right-hand side). The E component extends over 40″ (9 kpc) with an axial ratio of 3. Faint features (wisps) of the S component can be followed to considerable distances, in the south to about 80″ from the centre and in the north to about 100″ from the centre. This brings the total extent of the galaxy to 40 kpc.

The structure of the S component is not obvious from the appearance on our plates but we feel that it is best described by the denser areas forming a more or less regular ring which is seen nearly edge-on. It is, however, not evident what size one should attribute to the major axis of the projected ring. A first approach would be to assume that the major axis is delimited by the points C and M. But the bends of the projected ring at these two points are far too sharp, and there is also much material outside these points, *cf.* Fig. 2.

An apparently more reasonable interpretation is that what we see is the projection of a warped ring of such dimensions that almost all of the material of the S component forms part of the ring. In this case the points C and M become the points in which the projected ring crosses over as a result of warping. A warped ring with unit radius may be described by:

$$(x, y, z) = (\cos v, \sin v, a \sin^n v)$$

where υ is the azimuth angle and the two parameters a and n determine the degree of warping. The ring is ‘ flat ’ along the X-axis, it bends ‘ upwards ” (positive Z) in the ‘ upper ’ half of the (X, Y)-plane (positive Y) and ‘ downwards ’ in the ‘ lower ’ half. The projection onto the tangential plane (the celestial sphere) is determined by two parameters, the angle p in the XY-plane from the X-axis to the line of nodes (Fig. 4), and the inclination i of the XY-plane, relative to the tangential plane.

By varying the values of the four parameters, α, n, p and i, we have tried to obtain the best possible fit to the observed (projected) shape of the S component. After successive appoximations, we find $a = 0{\cdot}3$, $n = 5$, $p = 65°$ and $i = 85°$. After proper scaling and orientation these values reproduce the photographic image rather well as shown in Fig. 5. The diameter of the ring is now determined to 90″–95″, or 21 kpc. It should be noted that in order to obtain the best fit, the centre of the ring has to be slightly displaced to the N of the centre of the E component.

A glance at Fig. 2 gives the immediate impression that the S component is not at right angles to the major axis of the E component. This deviation from perpendicularity is further increased when we take into account the effect of warping. The angle between the line of nodes and the apparent major axis of the E component is close to 75°, *cf.* Fig. 5. It is interesting to note that the neighbouring galaxy in the chain (No. 2 in Fig. 1) is located to a high degree of accuracy on the line through the centre of NGC 4650 A and perpendicular to the line of nodes.

In conclusion, we therefore favour possibility (3) on a morphological basis. We cannot exclude possibilities (1), (4) and (5) but Nos (2) and (6) are unlikely.

4. The spectrum

Four long-slit spectra were obtained of NGC 4650A; the slit positions are indicated in Fig. 3. The lines which could be identified are given in Table 2, together with the measured radial velocities.

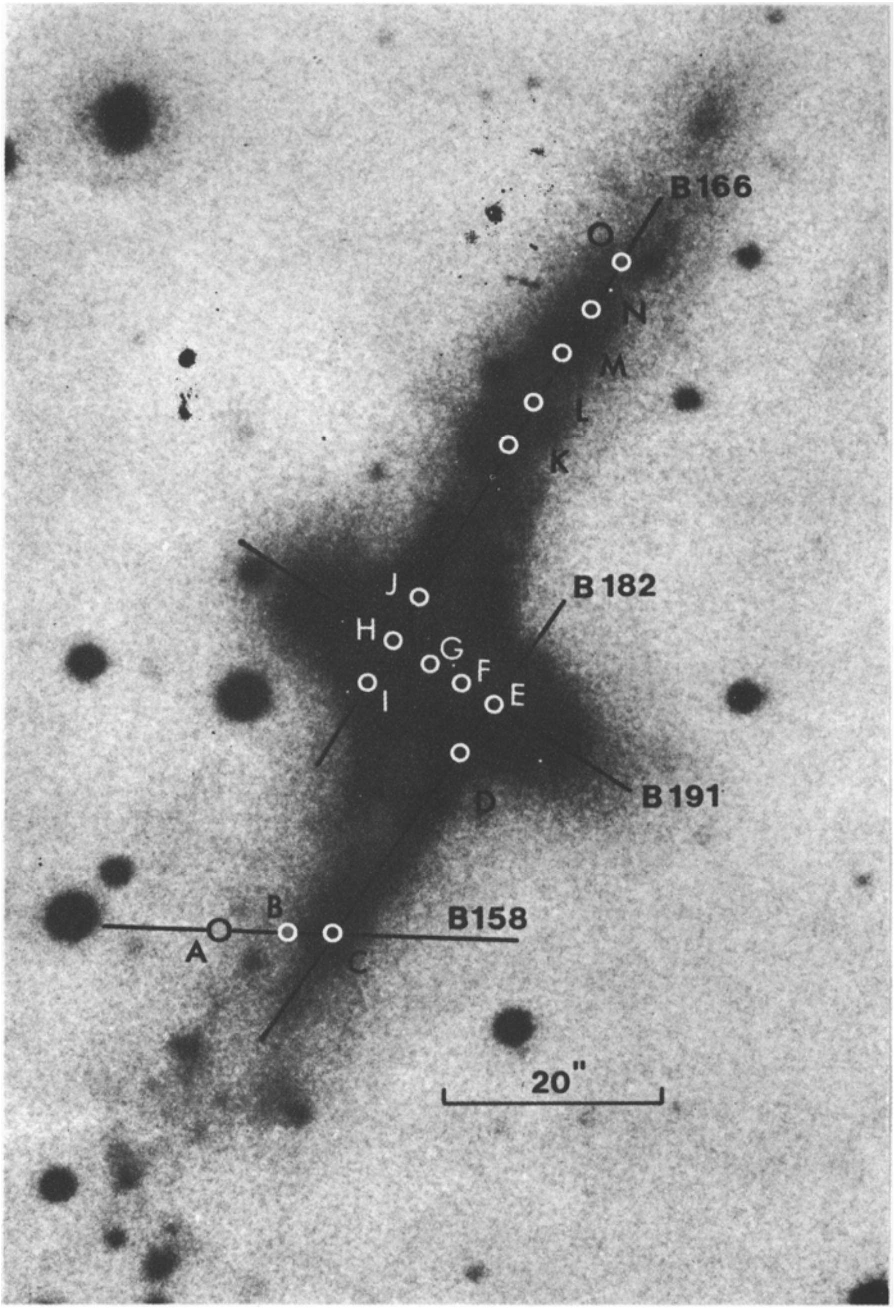

Figure 3. Slit positions in NGC 4650 A. Positions (A-O) indicate where radial velocities were measured. The spectra are identified by their log book no. (*cf.* Table 1).

LAUSTSEN AND WEST

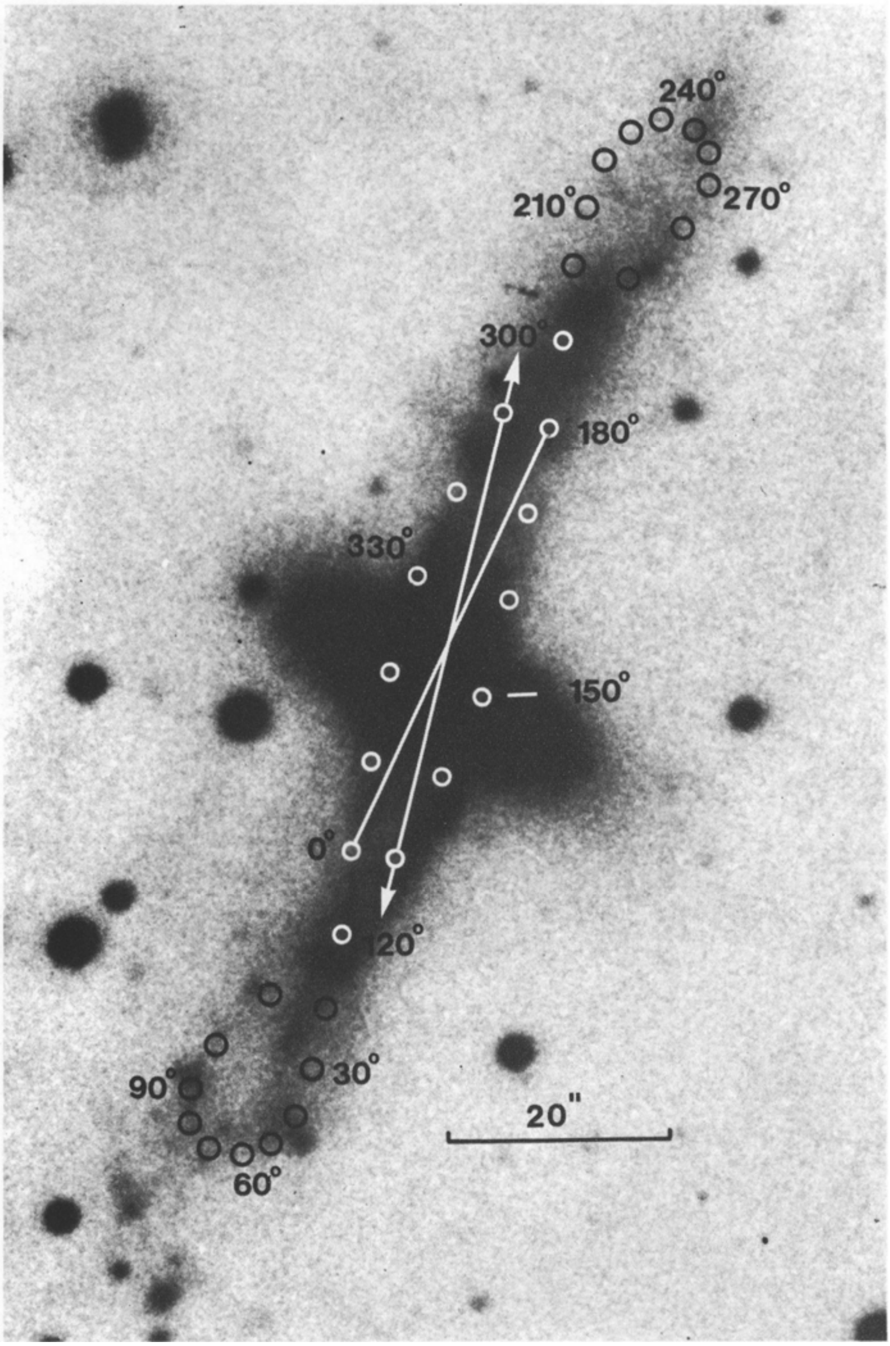

Figure 5. Geometrical interpretation of the S-component. The figure shows the projection of the best fitting ring (a = 0.3, n = 5, i = 85°, p =.65°) superposed on a 90 min exposure.

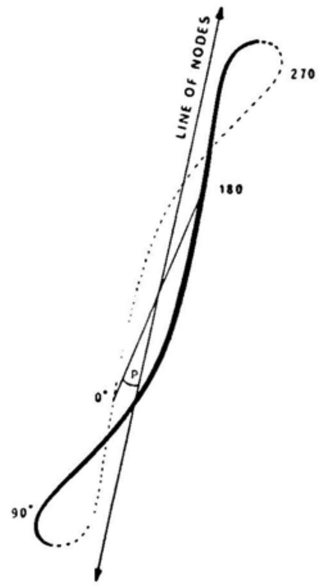

Figure 4. Geometrical interpretation of the S component. As described in the text, a warped ring was fitted to the shape of this component. The figure shows the projection of the best fitting ring (a = 0·3, n = 5, i = 85°, p = 65°) in a perspective drawing. The line of nodes, *i.e.*, the line of intersection of the *XY*-plane with the tangential plane, as well as the line connecting azimuths 0° and 180°, corresponding to the straight diameter in the warped ring, are shown. The part of the ring behind the tangential plane is drawn as a dashed line, while the part in front is fully drawn. The ring warps 'upwards' in the lower part of the figure and 'downwards' in the upper part. The values of the azimuth angle υ in Fig. 5 have been indicated at 10° intervals.

The emission line spectra are all of low excitation, although, certain differences in excitation are noted as listed in Table 2. Most, if not all, of the emission appears to arise in H II regions. The strongest knots are apparently giant H II regions with diameters of the order of 500 pc (~2″).

The absorption line spectrum of the E component (E, G, F) is typical of an elliptical galaxy although the strengths of the Balmer lines in absorption (4340, 4101, 3969) appear somewhat higher than usual, leading to an earlier spectral type (~GO) than most ellipticals (~G4). We note, however, the Mg I triplet (5175) and the Mg *H*-band (5269) as well as the Na I *D*-band, typical of late-type dwarf stars; these lines are normally present in elliptical galaxies.

In the following, further information is given about some of the spectra:

Position C: This knot was observed twice (B158, B182) and the measured velocities are in very good agreement; the mean value is given. I (6562)/I (6583) 1 and 3727 is strong. The absorption lines have about the same velocity as the emission lines but they are very faint and could not be measured with confidence.

Position F: Both [N II] lines are well visible; I (6583) > I (6562)> I (6548). The *G*-band is very broad and diffuse and could not be measured. The *K*-line (3933, Ca II) coincides with the night-sky *H*-line (3969) at 2800 km s^{-1} and was not measured.

Position G: It appears that Hβ consists of a narrow emission line, superimposed on a broader absorption line. The [S II] 6731–6717 lines are barely visible.

Table 2. Spectral lines and radial velocities.

Posi-tion	V_E	$V_{E,\,\mathrm{rel}}$	σ	Emission lines [S II] 6731-6717	[N II] 6583	H I 6562	[N II] 6548	[O III] 5007	[O III] 4959	H I 4861	H I 4340	[O II] 3727	Excitation class
A	2801	− 65	26					*	*	*	(*)	*	3−4
B	2817	− 49	18					*	*	*		*	4
C	2761	−105	15		(*)	(*)		**	**	**	*	**	3−4
D	2823	− 43	31					*		*			
E	2925	59						*					
F	2886	20	10		(*)	(*)	(*)	*	*	(*)		*	4−5
G	2858	− 8	25	(*)	(*)	(*)	(*)	*	*	*		*	3−4
H	2855	− 11	13		(*)	(*)	(*)	**	**	**		**	4−5
I	2821	− 45	7		(*)	(*)		*	*	*		*	3
J	2896	30	30		(*)	(*)		*	*	*		*	3
K	2948	82	18			(*)		*	*	*		(*)	3
L	2943	77	13			(*)		*	*	*		*	
M	2984	118	11			(*)		*	*	*	*	*	3
N	2958	92	24					*	*	*		*	3
O	2978	112	16			(*)		*		*		(*)	3
F,G,H	2866	0	10					*	*	*		*	

* = used for RV-determination
(*) = present, but not used for RV
** = used for RV (two slit positions)

Table 2. *continued*

Position	V_A	$V_{A,\,\mathrm{rel}}$	σ	Absorption lines Na I 5892	Mg H 5269	Mg I 5175	H I 4340	G-band 4304	H I 4101	H I+Ca I 3969	Ca I 3933
A											
B											
C				(*)		(*)				(*)	
D											
E	2755	−34	35			*	*	(*)	(*)	(*)	
F								(*)			(*)
G	2792	3	17	(*)	(*)	(*)	*	(*)	*	*	*
H	2802	13	23	(*)	(*)	(*)	*	(*)	*	**	(*)
I											
J	2829	40								*	(*)
K										(*)	
L											
M											
N											
O											
E,G,H	2789										

Position H: I (6562)/1 (6583)~1.
Position M: The Balmer lines and [O II] 3727 are somewhat stronger than [O III] 5007. The latter appears to be concentrated towards the centre of this knot.
Position *O:* Most outlying point where emission lines could be measured. I (3727)/ I (5007) < 1 , *i.e.* low excitation.

5. Dynamical structure

Radial velocities were determined by means of emission lines for all the positions A-O, and also by means of absorption lines for the positions E, G, H and J. All determinations are listed in Table 2 with the used lines indicated for each position. The correction to be applied for the motion of the earth is + 25 km s^{-1}. Radial velocities determined from absorption lines are systematically smaller than those determined from emission lines for the same positions. This difference is of the order of 100 km s^{-1} and does not appear to be connected with an expansion of the ring. Otherwise we would have expected to find emission line velocities which are smaller than the absorption velocities, especially in the nearer edge of the ring (positions D and E); this is not the case. Part of the discrepancy may be explained as due to systematic errors in the measurement, but it still looks as if there is a real difference. Future, high-resolution spectroscopic observations are necessary to verify this.

The heliocentric systemic velocity V=28 61±11 km s^{-1} was determined by applying all measured lines, emission as well as absorption lines, in the major axis of the E component, *i.e.* in the positions E, F, G and H. It has been adopted for the determination of a cosmological distance. Correction for the solar motion is made according to Yahil, Tammann and Sandage (1977): ΔV = — 285 km s^{-1} giving V_0 = 2576 km s^{-1}. By adopting H_0 = 55 km s^{-1} Mpc^{-1} we derive the distance 47 Mpc and a scale 227 pc $arcsec^{-1}$.

Bergwall *et αl.* (1978) gave V=2870±60 km s^{-1}, in perfect agreement with our value. An earlier determination was made by Sérsic and Agüero (1972) who from three lines found a heliocentric velocity V=2530 km s^{-1} for the central object. de Vaucouleurs and Corwin (1976) applied a correction of —55 km s^{-1} to this giving V=2475 ± 180 km s^{-1}. This is nearly 400 km s^{-1} lower than our value. The most likely explanation is a possible systematic error in the earlier determination.

The measurements in Table 2 have been plotted in Fig. 6. It is seen that the S component rotates; taking into account the projection effects, we find a rotational velocity of ~180 km s^{-1}, 10·5 kpc from the centre. Assuming Keplerian velocity, the enclosed mass becomes 8 10^{10} $M_\odot$ which is a reasonable value for the E component. The mass-to-luminosity ratio is determined on the basis of the photometry by Sérsic and Agüero (1972). With m_v (total)=13·6 and distance modulus (m—M) =33^{m}3, *i.e.* M_v = — 19^{m}7, we get $(M\backslash L)_v$ = 12 in solar units.

There is no measurable rotation along the major axis of the E component, leading to the conclusion that this object is prolate.

6. Discussion

We interpret the present object, NGC 4650 A, as an elliptical galaxy (the E component), surrounded by a warped ring (the S component). The projected size of the central galaxy is 9 kpc. The diameter of the ring is about 21 kpc, but including outlying material, the overall size is almost 40 kpc.

We see only one nucleus in this object and it does not appear to be particularly active, although the emission lines in the spectrum along the major axis of the elliptical galaxy do have a weak maximum near the centre (positions F-G in Fig. 3). There is a little or no rotation along this axis and the spectra that cross the galaxy E and W of the nucleus (in positions E and H) indicate that, the rotation, if any, around the major axis must be slow. Thus the galaxy belongs to the prolate type; other examples are given by Bertola and Galletta (1978). The galaxy has strong, apparently rather broad absorption lines, probably as a result of internal motion, but spectral observations of higher resolution are necessary to confirm this. There is an unexplained difference of ~ 100 km s^{-1} between the absorption and emission line velocities. The mass and the mass-to-luminosity ratio are not untypical for an elliptical galaxy.

The surrounding S component has the geometrical shape of a warped ring, inclined 5° to the line of sight. The spectra show that most of the knots are large H II regions, although there are signs of a stellar component in the form of weak absorption lines. It also contains a significant amount of dust which manifests itself as the strong dust band, W of the centre, seen in Fig. 2 (left-hand side). The emission regions appear to lie on the ring. It is possible that the ring is the edge of a warped disc, but in that case the disc must have low surface brightness, as indicated by the " void " areas, NW and SE of the nucleus, between the denser edges of the S component. The N-part of the ring is receding, relative to the central galaxy, and the S-part is approaching; the velocity curve corresponds to a rotation. On the basis of the present material, there is no unambiguous indication of expansion or contraction of the ring. Similarly, we do not feel that the currently available, somewhat limited data warrant the construction of a dynamical model of the ring. Further spectral observations of higher angular and spectral resolutions are most desirable for a fuller understanding of this peculiar object.

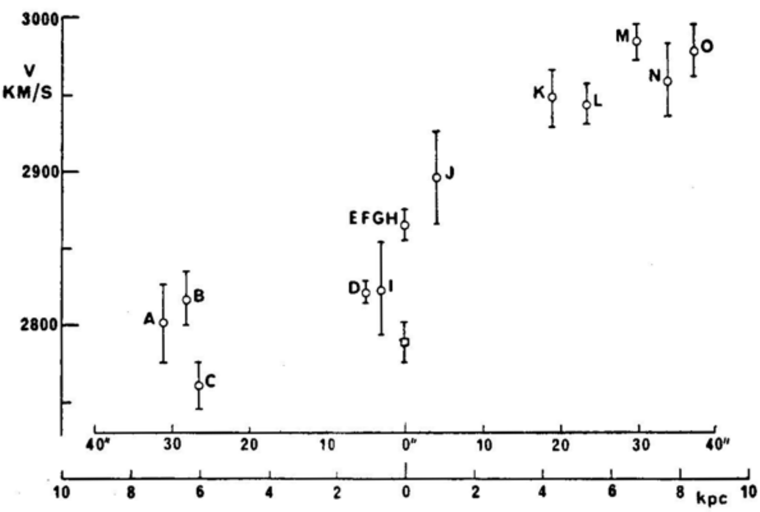

Figure 6. Radial velocity curve of the S component. The measured values, together with the error bars, are shown for emission lines (circles) and absorption lines (square),. The lettering corresponds to the positions in Fig. 3.

At the most, a few dozen ring galaxies are known at this time. Due to the obvious selection effect, most of these are seen nearly face-on; to the best of our knowledge, NGC 4650 A is the hitherto best candidate for an edge-on ring galaxy. Photographs of other ring galaxies may be found in the article of Theys and Spiegel (1976) and detailed investigations of some objects of this class have been carried out by Graham (1974), Fosbury and Hawarden (1977) and Dennefeld, Laustsen and Materne (1979).

Reviews of the various theories of formation of ring galaxies have been written by Chatterjee (1979) and Dennefeld and Materne (1980). It is not clear whether ring galaxies are results of close encounters of galaxies with intergalactic clouds (Freeman and de Vaucouleurs 1974) or with other galaxies (Lynds and Toomre 1976; Theys and Spiegel 1977).

In the case of NGC 4650 A, the nearest neighbour is NGC 4650 or rather its companion (No. 2 in Fig. 1). The radial velocity of NGC 4650 (Bergwall *et αl.* 1978) is within 100 km s^{-1} of that of NGC 4650 A, but the velocity of the companion has not yet been measured. Nevertheless, it is most likely that the three are physically connected (note that the velocity of ESO 322-IG64, No. 4 in Fig. 1, is ~4800 km s^{-1}, *i.e*, they do not belong to the group). The angular distance from NGC 4650 A to galaxy No. 2 is ~ 220″, or about twice the size of the ring of NGC 4650 A. We also remark the apparent alignment of the line of nodes of the ring which is perpendicular to the line connecting NGC 4650 A and NGC 4650. Whether in fact the ring did originate during a close encounter among these galaxies cannot be concluded at this stage. It would be interesting to perform model calculations on this system.

Acknowledgement

It is a pleasure to thank the ESO night assistants, I. Yagnam and M. Pizarro, for cheerful support. We are also happy to acknowledge the help of F. Patard and S. Stillebacher in Geneva and P. E. Rathcke, Åarhus, in connection with the preparation of this article.

References

Arp, H. 1966, *Astrophys. J. Suppl. Ser.,* **14,** 1.

Bergwall, N. A. S., Ekman, A. B. G., Lauberts, A., Westerlund, B. E., Borchkhadze, T. M., Breysacher, J., Laustsen, S., Muller, A. B., Schuster, H.-E., Surdej, J., West, R. M. 1978, *Astr. Astrophys. Suppl. Ser.,* **33,** 243.

Bertola, F., Galletta, G. 1978, *Astrophys, J.*, **226,** L115.

Chatterjee, T. K. 1979, *Bull. astr. Soc. India,* **7,** 32.

Dennefeld, M., Laustsen, S., Materne, J. 1979, *Astr. Astrophys.,* **74,** 123.

Dennefeld, M., Materne, J. 1980, *The Messenger,* **21,** 29.

de Vaucouleurs, G., de Vaucouleurs, A., Corwin, H. G. 1976, *Second Reference Catalogue of Bright Galaxies*, University of Texas Press, Austin.

Fosbury, R. A. E., Hawarden, T. G, 1977, *Mon. Not. R. astr. Soc*., **178,** 473.

Freeman, K. C, de Vaucouleurs, G. 1974, *Astrophys. J.,* **194,** 569.

Graham, J. A. 1974, *Observatory,* **94,** 290.

Holmberg, E. B., Lauberts, A., Schuster, H.E., West, R. M. 1974, *Astr. Astrophys. Suppl. Ser.,* **18,** 463.

Lynds, R., Toomre, A. 1976, *Astrophys. J.,* **209,** 382.

Sérsic, J. L., 1967, *Z.* Astrophys.*,* **67,** 306.

Sérsic, J. L., 1968, *Atlas de Galaxias Australes*, Observatorio Astronomico, Cordoba.
Sérsic, J. L., Agüero, E. L. 1972, *Astrophys. Sp. Sci.*, **19,** 387.
Theys, J. C., Spiegel, E. A. 1976, *Astrophys. J.*, **208,** 650.
Theys, J. C., Spiegel, E. A. 1977, *Astrophys. J.*, **212,** 616.
Yahil, A., Tammann, G. A., Sandage, A. 1977, *Astrophys. J.*, **217,** 903.

J. Astrophys. Astr. (1980) **1,** 189–192

No Detectable Supernova Remnant near the Pulsar PSR 1930 + 22

W. M. GOSS *Kapteyn Astronomical Institute, 9700 AV Groningen, Netherlands*
D. Morris* *Raman Research Institute, Bangalore 560080*

Received 1980 September 22; accepted 1980 October 15

Abstract. No supernova remnant has been found near the third youngest pulsar PSR 1930+22 down to a –limiting brightness temperature of 1·4 K at 610 MHz. This is 6–8 times less than expected of a typical remnant whose age is that of the pulsar (3·6 0× 10^4 years).

Key words: pulsar — supernova remnant

1. Introduction

It is normally assumed that pulsars are formed in supernova explosions. However, so far supernova remnants have only been found associated with the two youngest pulsars PSR 0531+21 and PSR 0833—45. Their spin down ages are 10^3 and 1·1 × l0^4 years, respectively. Any remnants associated with older pulsars (age ≈ 10^6 yr) will probably be too weak to be detected because of their limited lifetime (≈ 10^5 years) and because the proper motion of the pulsars may carry them far from their birth place in 10^6 years.

An exception might be PSR 1930+22 (period 144 ms) which is the third youngest pulsar known at present and at whose age (p/2p=3·6 × 10^4 years) a typical supernova remnant should be detectable.

2. Observations

We have thus observed a field (FWHB=82′) centered on the pulsar position (equinox 1950·0, R.A. 19^h 30^m 12^s·5 ± 0^s·3, dec 22° 15′ 19″ ± 4″, Gullahorn and Rankin 1978). The Westerbork synthesis telescope was used at a frequency of 610 MHz. A full 12^h synthesis was made using the 4+10 antenna array *i.e.* 40 interferometers. The resulting synthesized beam dimensions are (R.A. × dec) 52 5″ × 155·5″. The

*Present address: I. R.A.M., B.P. 391, F 38017 Grenoble, France shortest spacing was 36 m (73 wavelengths) so that the maximum fringe spacing was 47′ are. Thus extended features much greater than 30′ in diameter are significantly resolved out. A 1° diameter source would not be detectable. The first grating ring was at 47′ (R.A.) × 124′ (dec).

3. Results

Previous low resolution radio frequency surveys have detected structure in the neighbourhood of PSR 1930+22. Wendker (1968) reported a non-thermal source (number 26 in his list) and the map of Terzian (1965) shows extended structure to the north (G 57·6+1·6 and G 57·6+1·9) and south of the pulsar.

The present observations show that this emission can be accounted for by a grouping of point sources (number 9, 11 and 12 of Table 1) and one extended triple source (S=l·6 Jy) at R.A. (1950) 19^h 32^m $55^S \pm 2^S$, dec (1950) 21° 50′ ±0′·5 which may be a head-tail source. When all these sources have been subtracted (see Table 1) no detec-

Table 1. Point sources found in the field of PSR 1930+22 at 610 MHz.

W.S.R.T. No.		R.A. (1950.0)	dec (1950.0)	S (mJy)
38	W1	19^h 26^m $48^s{\cdot}8 \pm 0^s{\cdot}4$	22° 38′ 23″ ± 15″	67 ± 28
	W2	19 27 41.9 ± 0·4	21 56 42 ± 20	36 ± 10
	W3	19 27 53·7 ± 0·2	22 52 07 ± 5	180 ± 20
	W4	19 28 04·9 ± 0·4	22 17 17 ± 15	25 ± 4
	W5	19 28 11·3 ± 0·1	22 39 05 ± 5	112 ± 10
	W6	19 28 25·3 ± 0·3	22 45 22 ± 20	35 ± 6
	W7	19 28 58·3 ± 0·2	22 54 54 ± 6	115 ± 20
	W8	19 28 58·7 ± 0·2	21 58 28 ± 5	57 ± 10
	W9	19 29 06·7 ± 0·1	22 25 42 ± 2	252 ± 15
	W10	19 29 07·3 ± 0·5	21 36 43 ± 20	39 ± 6
	W11	19 29 08·1 ± 0·1	22 12 56 ± 2	150 ± 10
	W12	19 29 16.5 ± 0·1	22 37 07 ± 2	430 ± 20
	W13	19 29 40·2 ± 0·3	22 27 19 ± 15	43 ± 6
	W14	19 30 09·1 ± 0·2	21 48 04 ± 10	40 ± 7
	W15	19 30 19·1 ± 0·4	22 12 28 ± 15	18 ± 5
	W16	19 30 26·8 ± 0·2	22 37 54 ± 6	62 ± 7
	W17	19 30 30·7 ± 0·3	21 51 16 ± 20	33 ± 6
	W18	19 30 58·3 ± 0·1	22 42 36 ± 5	100 ± 8
	W19	19 31 11·5 ± 0·2	22 34 25 ± 6	64 ± 6
	W20	19 31 21·7 ± 0·1	21 31 09 ± 2	330 ± 50
	W21	19 31 29·1 ± 0·2	22 19 57 ± 8	39 ± 6
	W22	19 31 32·2 ± 0·2	22 29 12 ± 13	31 ± 7
	W23	19 31 38·4 ± 0·2	22 42 59 ± 10	44 ± 10
	W24	19 31 41·0 ± 0·6	22 20 19 ± 25	27 ± 10
	W25	19 31 53·0 ± 0·5	21 50 52 ± 20	38 ± 10
	W26	19 32 06·2 ± 0·2	21 54 37 ± 7	74 ± 8
	W27	19 32 13·4 ± 0·3	21 40 34 ± 12	49 ± 15
	W28	19 32 23·7 ± 0·3	21 27 01 ± 12	85 ± 25
	W29	19 32 29·9 ± 0·2	22 36 32 ± 8	65 ± 10
	W30	19 33 03·7 ± 0·2	22 42 18 ± 8	87 ± 13
	W31	19 33 36·1 ± 0·3	22 57 02 ± 12	130 ± 35
	W32	19 33 55·1 ± 0·2	21 42 20 ± 9	170 ± 25
	W33	19 34 21·1 ± 0·2	22 39 40 ± 8	240 ± 30

table extended source $\leqslant 1^{\circ}$ in diameter remains. The limiting brightness temperature corresponds to an R.M.S. of σ=1·4 K (2·8 mJy per beam). This limit is determined by ionospheric phase errors. Furthermore, no detectable point source coincides with the pulsar. So we must conclude that the flux of the integrated pulses was below the detection threshold at the time of observation. The expected 610 MHz average flux density is 7·2 mJy $\approx$ 2·6 σ. This implies either a steep spectrum or that the mean flux density is time variable and was low by a factor 2–3 during our observations. The nearest point source (No. 15) is 3′·2 from the pulsar position. None of the sources in Table 1 is a 4C source.

4. Discussion

No extended source—either shell or filled ‘ Plerion ’ type has been detected down to the limit set by the rms noise of 2·8 mJy per beam or 1·4 K brightness temperature.

It only remains to estimate the expected remnant brightness. The most complete semi-empirical theory of shell type remnant evolution is that of Caswell and Lerche (1979). This takes into account the effect of the changing interstellar medium as a function of *z*, the distance from the galactic plane. As principal input we use the remnant age assumed to be $3{\cdot}6 \times 10^4$ years from the rate of slow down of the pulsar. To enable a *z* correction to be made we assume a distance of 8·1 kpc—from the pulsar dispersion measure (Taylor and Manchester 1975). From this follows z=210 pc. The equation (8) of Caswell and Lerche (1979) then yields a shell diameter of 77 pc which corresponds to an angular diameter of 33′. The predicted average surface brightness, from equation (9) is then 12 K at 400 MHz. If a spectral index (flux density) of —0·5 is assumed this corresponds to 4·1 K at 610 MHz. For a typical shell source the peak brightness will be higher than the average by about 2·0 *i.e.* 8·2 K. So this calculation would predict a shell detection with a peak signal to rms noise ratio of about six.

This estimate is uncertain due to the intrinsic scatter of the age-brightness relation and to uncertainties in the *z* distance correction. These uncertainties might easily amount to a factor three.

The evolution of the filled remnants is less well understood but recently Weiler and Panagia (1980) have given analagous formulae to those for shell remnants. They are based on observations of the Crab Nebula, 3C58 and Vela X which they argue is also a filled remnant. They assume adiabatic expansion up to an age $\gtrsim 3 \times 10^4$ yr, and that all such sources have had a similar energy input and expansion velocity. Their formulae (45) and (47) yield a 1 GHz flux density of 2·4 Jy and an angular diameter of 18′. If we assume a spectral index (flux density) of —0·25 this corresponds to an average brightness temperature of 11 K at 610 MHz. This is also well above our rms limit (*i.e.* eight times) for the peak brightness temperature. However, this may be an over-estimate for several reasons. The calculation neglects any influence of the height of the remnant above the galactic plane and also assumes that the observations were made below the cut-off frequency in the spectrum. However, equations (42) and (43) of Weiler and Panagia (1980) predict a critical frequency of 16 GHz, which is well above our observing frequency of 0·61 GHz. Finally the basic assumption that PSR 1930+22 had an energy and an expansion velocity similar to those of the Crab Nebula, 3C58 and Vela X may be unjustified.

The failure to detect any remnant associated with PSR 1930+22, either shell or filled type, is unexpected. Although this may be just the result of an incorrect estimate of the expected remnant brightness there are several possible alternative explanations. According to the suggestion of Radhakrishnan and Srinivasan (1980) no shell remnant is to be expected around a pulsar; however, the lack of any filled remnant is unexpected since according to their theory all young pulsars should make filled remnants. This may indicate that the theory of Weiler and Panagia (1980) over-estimates the lifetime of older remnants at high latitudes—for example their assumption of adiabatic expansion may be in error. Furthermore, their intrinsic properties (energy, expansion velocity) may show a large scatter. For these reasons it may be of interest to search again with higher sensitivity.

Acknowledgements

The Westerbork Radio Observatory is operated by the Netherlands Foundation for Radio Astronomy with the financial support of the Netherlands Organisation for the Advancement of Pure Research. D. M. thanks V. Radhakrishnan for facilities provided at the Raman Research Institute during the preparation of this paper.

References

Caswell, J. L., Lerche, I. 1979, *Mon. Not. R. astr. Soc,* **187,** 201.
Gullahorn, G. E., Rankin, J. M. 1978, *Astr. J.,* **83,** 1219.
Radhakrishnan, V., Srinivasan, G. 1980, *J. Astrophys. Astr.,* **1,** 25.
Taylor, J. H., Manchester, R. N. 1975, *Astr. J.,* **80,** 794.
Terzian, Y. 1965, *Astrophys. J.,* **142,** 135.
Weiler, K., Panagia, N. 1980, *Astr. Astrophys.,* **90,** 269.
Wendker, H. 1968, *Astr, J.,* **73,** 644.

J. Astrophys. Astr. (1980) **1,** 193–196

A New Spectroscopic Facility at Millimetre Wavelengths

(*Report on New Instrumentation Facilities*)

A. Baudry, J. Brillet, J. M. Desbats, J. Lacroix, G. Montignac
E. R. A. du C. N. R. S. no 380, Observatoire de l'Universite de Bordeaux, 33270 Floirac, France

P. Encrenaz, R. Lucas *E. R. A. du C. N. R. S. n° 762, Ecole Normale Superieure, 75231 Paris Cedex 05 et U. S. M. G., CERMO, B. P. 53X, 38041 Grenoble, Cedex, France*

G. Beaudin, P. Dierich, A. Germont, P. Landry, G. Rerat
L. A. du *C. N. R. S. n° 236, Observatoire de Meudon, 92190, Meudon, France*

Received 1980 August 10; accepted 1980 September 16

Abstract. A new millimeter-wave facility is in operation at the Bordeaux Observatory for spectroscopic observations of interstellar and stratospheric molecules. A cooled receiver has been installed on a 2·5m radio telescope. The overall system temperature is in the range 400 to 600 K (single side band) in the operating frequency range 75 to 115 GHz. The relatively broad beam of the telescope (~ 5 arcmin) combined with a sensitive receiver will permit studies of extended molecular cloud complexes.

Key words: instruments—millimeter-wave astronomy

1. Introduction

A new facility for millimeter-wave observations of interstellar and stratospheric molecules has been put into operation at the Bordeaux Observatory under a cooperative effort. The spectroscopic system consists of a multi-channel filter bank and a cooled receiver which has been installed on a 2·5-m Cassegrain telescope. The antenna, with an azimuth-elevation mount, is one of the two antennas of the Bordeaux mm-wave interferometer which has been extensively described by Baudry *et al.* (1975). The interferometer is operated in the continuum at 8·6 mm. Single dish observations of molecules are now possible in the range 75–115 GHz with a 256 channel spectrometer. The relatively broad beam of the telescope, about 5 arcmin at around 90 GHz, combined with the sensitivity of a cooled receiver, are well suited for spectral observations of extended molecular dark clouds. This new spectroscopic receiver has been designed so that it can be used with other telescopes in the near future.

2. The equipment

Fig. 1 is a block-diagram of the receiving system. The receiver includes a cooled (20 K) mixer with a GaAs Schottky diode mounted on an integrated circuit. Several GaAs diodes (made by G. T. Wrixon, Cork University) have been matched to mixer mounts and various diodes can be used on the telescope. The first intermediate frequency is at 4·755 GHz. Image rejection is achieved in the mixer by means of a movable dielectric backshort. Rejection is better than 15 dB. The first stage intermediate frequency amplifier is a cooled parametric amplifier followed by a room temperature FET amplifier. The best system temperature is of the order of 400 K (single side band) at 93 GHz.

The first local oscillator is a klystron phase-locked to a highly stable 8 GHz solid state source; both signals are fed into a harmonic mixer with an intermediate frequency of 300 MHz. The 8 GHz source is itself phase-locked to the output of a 110 MHz synthesizer.

A 256-channel spectrometer has been built following the NRAO design (Mauzy 1974; Pace and Payne 1973). The spectral resolution is 100 kHz per channel. At 90 GHz the overall velocity coverage is thus ~ 85 km s^{-1} with 0·33 km s^{-1} resolution.

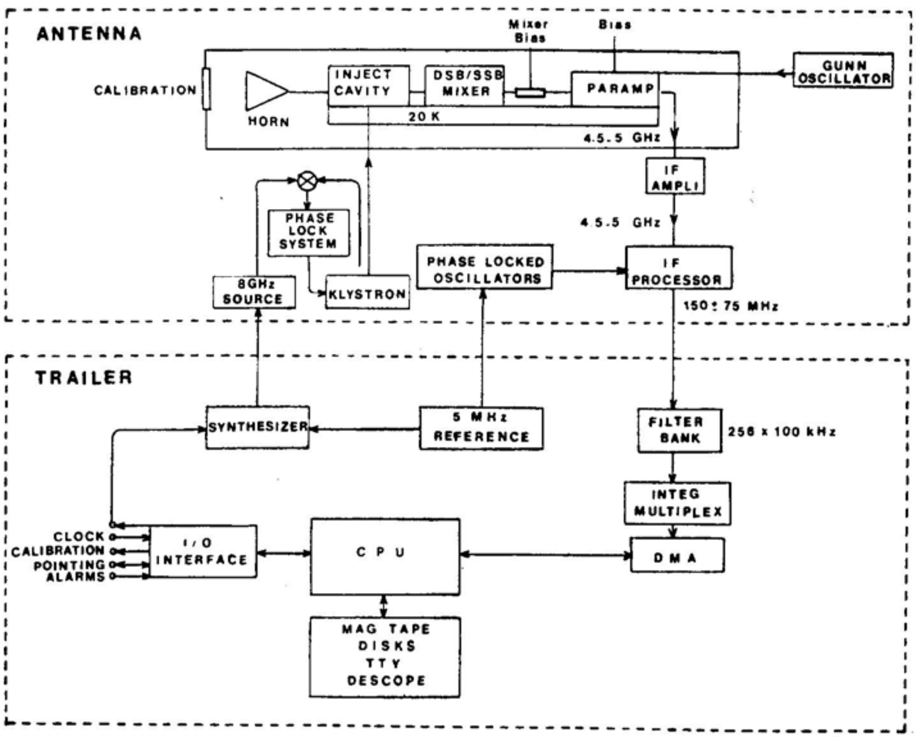

Figure 1. Block diagram of receiving system,

Table 1. Main characteristics of the new spectroscopic millimetre facility.

Antenna diameter	2·5 m
Surface accuracy (rms)	0·05 mm
Beamwidth	5′.4 at 90 GHz
Pointing accuracy	$< \pm 20''$
Frequency coverage	75-115 GHz
System temperature	400 K (SSB) at 93 GHz
Frequency resolution	100 kHz (256 channels)

A PDP 11/34 computer is used for collecting and reducing data in real time and for handling the whole observing procedure. In particular it is linked to another small computer used to drive the 2·5-m telescope. Data are written on disk and/or magnetic tape for further analysis. The PDP 11/34 and its peripheral devices, the back-end, the local oscillator power supply and the stable low frequency oscillators are installed in a controlled-temperature trailer.

The beam width measurement and the focal adjustment were made by observing the centre and the limbs of the solar disk. The pointing has been checked on the sun and on stars by means of a refractor attached to the antenna. It is better than about ± 20″.

The sea level site of the Bordeaux Observatory has been chosen mainly because of the already existing antenna and of the technical assistance available for easy debugging of the system. Table 1 summarises the main characteristics of the new mm-wave facility. Future developments will include a back-end extension with 256×500 kHz analog filters and a spectrum line expander.

3. Preliminary observation

Preliminary observations have shown that many days or nights are expected to give zenith opacities $\simeq$ 0·1 to 0·2 in the frequency range 80 to 100 GHz. Two modes of operation are currently used: either the receiver is frequency-switched or the antenna is positions-witched. Calibration is obtained by switching between an absorbing movable load in front of the feed horn and the cold sky, in the usual way at millimetre wavelengths.

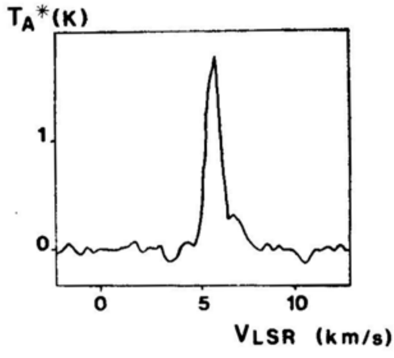

Figure 2. Line profile of HCO^+ observed toward Taurus Molecular Cloud 2 (a = $4^h\,29^m\,43^s$ (1950), δ = +24° 16′.9) at positions $\Delta\ a$, $\Delta\delta$=10′, 8′. Spectral resolution = l00 kHz.

The new spectroscopic system briefly presented in this paper has been designed primarily to study the spatial extent of dark molecular clouds and to investigate part of the large scale structure of the Galaxy by observing molecular species other than CO (the latter is observed by the 1·2-m telescope of the Columbia University, see *e.g.* Cohen and Thaddeus 1977). Our very first spectra were obtained in mid-December 1979 and the present observation programmes are mainly devoted to the $J = 1 \rightarrow 0$ transition of HCN and HCO+ in various galactic clouds. Fig. 2 shows the result of an HCO+ observation made towards Taurus Molecular Cloud 2.

Acknowledgements

Building of the new mm-wave facility would not have been possible without the efficient help of J. P. Busset, J. Delannoy, F. Gérard, B. Lazareff, S. Lebourg, C. Rosolen, G. Trennec, N. Weliachew and the machineshops at the Ecole Normale Supérieure, and the Bordeaux and Meudon observatories. This mm-wave project was largely supported by INAG.

Reference

Baudry, A., Bocchia, R., Delannoy, J., Gérard, F., Lacroix, J., Montignac, G., Poumeyrol, F., Robillot, J. M. 1975, *L' Interférométre Millimetrique Solaire de Bordeaux,* CNRS, Paris.

Cohen, R. S., Thaddeus, P. 1977, *Astrophys. J.*, **217,** L155.

Mauzy, B. 1974, *NRAO Electron. Div. Internal Report* No. 146.

Pace, C, Payne, J. 1973, *NRAO Electron. Div. Internal Report* No. 134.